WA School of Mines: Minerals, Energy and Chemical Engineering

Faculty of Science and Engineering

Engineering of Perovskite Oxides for Electrochemical Water Splitting

Xiaomin Xu

0000-0002-0067-3331

This thesis is presented for the Degree of

Doctor of Philosophy

of

Curtin University

August 2020

Declaration

To the best of my knowledge and belief this thesis contains no material previously published by any other person except where due acknowledgment has been made.

This thesis contains no material which has been accepted for the award of any other degree or diploma in any university.

Signature:

Date: 27/08/2020

Abstract

Electrochemical water splitting represents a viable process that can address humanity's growing concerns over climate change caused by the excessive use of conventional fossil fuels, because it can produce hydrogen as a cleaner fuel using electricity generated from renewable energy sources (e.g., solar and wind). However, the implementation of water electrolysis is often hindered by the energy losses associated with the slow kinetics of the two half-reactions involved, i.e., the hydrogen evolution reaction (HER) at the cathode and the oxygen evolution reaction (OER) at the anode. To make these processes more energy-efficient and cost-effective, active electrocatalysts made of inexpensive, Earth-abundant elements are urgently needed. Among many candidates, ABO_3 perovskite oxides have recently emerged as promising low-cost alternatives for catalyzing both the HER and OER. This study centers on the engineering of perovskite oxides towards increased electrocatalytic HER/OER performance. Novel perovskite oxides consisting of non-precious elements are synthesized using facile chemical approaches such as sol–gel process and high-temperature reduction. Their physicochemical properties are investigated using a set of materials characterization techniques based on diffraction, microscopy, spectroscopy, and others. The electrocatalytic performance is assessed in a rotating disk electrode-based, three-electrode configuration using electrochemical testing methods ranging from cyclic voltammetry, linear sweep voltammetry, to chronopotentiometry. By fine-tuning the chemical compositions and structures, perovskite oxides with improved HER/OER catalytic performance are developed. Of importance, correlations are established between the electrocatalytic activity and the perovskite electronic structure (e.g., crystal symmetry, transition metal oxidation state, oxygen vacancy, and metal–oxygen covalency). This thesis is expected to offer a deepened understanding of the structure–activity relationship of the perovskite oxide electrocatalysts in the water-splitting reactions.

Acknowledgements

This thesis would not have been possible without the expertise and enthusiastic support of many other brilliant scientists. First, I would like to express my deepest gratitude to my supervisor, Prof. Zongping Shao, who has the substance of a genius: he continuously and convincingly guided me to conduct independent research, develop critical thinking, and make wise plans. I also appreciate his insight, support, and feedback over the past three and a half years, which has encouraged me to complete this thesis and to further pursue a research career.

In addition, I would like to thank my co-supervisors, Prof. Moses Tadé and Dr. Chao Su, for all the support they have given me, both in research and in life. I am grateful to Prof. Shaomin Liu for serving as the chairperson of my thesis committee and for providing useful suggestions on my research. I would also like to thank Prof. San Ping Jiang, Prof. Shaobin Wang, and Dr. Chunyan Fan for their help, support, and encouragement.

I wish to show my gratitude to Prof. Wei Wang, Prof. Wei Zhou, Dr. Lei Ge, Dr. Yubo Chen, Dr. Mengran Li, and Prof. Zhiwei Hu for their great help and collaboration. I am indebted to Prof. Martin Saunders, Dr. Alexandra Suvorova, Dr. Jean-Pierre Marcel Veder, Dr. Matthew Rowles, and Ms. Veronica Avery for their technical support in materials characterizations. I would also like to pay my special regards to Prof. Ryan O'Hayre for the fruitful discussion.

To my friend and colleague Mr. Yijun Zhong, I owe a special thanks. We have been studying and working together ever since we went to college in Nanjing in 2009. It has always been a pleasure to work alongside you on those long days in the lab. I also share my thanks to my other colleagues, Dr. Yu Liu, Mr. Paulo Sérgio Barros Julião, Ms. Pengyun Liu, Mr. Yasir Arafat, Ms. Hira Fatima, for their help and support during my research. Additionally, I would like to thank all the visiting scholars in our research group that I have had the opportunity to work with, including Dr. Huangang Shi, Dr. Jiafeng Cao, Prof. Li Yang, Prof. Dalei Sun, Prof. Yong Jiao, Prof. Wenting An, and Dr. Muhammad Azhar. I would also like to thank my undergraduate student Mr. Chun Hei Chiu for working with me.

I would like to recognize the invaluable assistance from all the technical officers, including Dr. Roshanak Doroushi, Mr. Xiao Hua, Miss Jennifer Wang, Mr. Araya Abera, Mr. Jason Wright, Ms. Ann Carroll, Mr. Andrew Chan, Mrs. Melina Miralles, and Ms. Karen Haynes, without which my research activities would not have been as smooth.

I also sincerely acknowledge the financial support for my PhD study from the Australian Government Research Training Program (RTP) Scholarship.

Thank you to all of my friends, both old and new, for the roles you have played in my time at Curtin University and well before. Your support has helped a great deal in handling the highs and lows of my PhD journey.

Finally, my deepest thanks and love to my family. Thank you to my wife, Yangli. Your wholehearted love and your unwavering support through the long and late nights of writing is the reason I have been able to complete this thesis. Thank you to my parents, Zhengfang and Juliang, for your unconditional love and for always being so supportive to the academic path I have chosen. Thank you to my grandmother, Amei, for always believing in me. I love you all deeply and truly.

List of publications

Published papers and book chapters:

1. **Xiaomin Xu**, Yangli Pan, Yijun Zhong, Lei Ge, San Ping Jiang, Zongping Shao*, From scheelite $BaMoO_4$ to perovskite $BaMoO_3$: Enhanced electrocatalysis toward the hydrogen evolution in alkaline media, **Composites Part B: Engineering**, 198 (2020): 108214.
2. Yangli Pan[#], **Xiaomin Xu**[#] ([#] Equal contribution), Yijun Zhong, Lei Ge*, Yubo Chen, Jean-Pierre Marcel Veder, Daqin Guan, Ryan O'Hayre, Mengran Li, Guoxiong Wang, Hao Wang, Wei Zhou, Zongping Shao*, Direct evidence of boosted oxygen evolution over perovskite by enhanced lattice oxygen participation, **Nature Communications**, 11 (2020): 2002.
3. **Xiaomin Xu**, Yangli Pan, Yijun Zhong, Ran Ran, Zongping Shao*, Ruddlesden–Popper perovskites in electrocatalysis, **Materials Horizons**, 7 (2020): 2519–2565.
4. **Xiaomin Xu**, Yangli Pan, Lei Ge, Zongping Shao*, (2020) Perovskite materials in electrocatalysis. In: Arul N., Nithya V. (eds) Revolution of Perovskite. Materials Horizons: From Nature to Nanomaterials. **Springer**, Singapore.
5. **Xiaomin Xu**, Yijun Zhong, Zongping Shao*, Double perovskites in catalysis, electrocatalysis, and photo(electro)catalysis, **Trends in Chemistry**, 1 (2019): 410–424.
6. **Xiaomin Xu**, Wei Wang, Wei Zhou, Zongping Shao*, Recent advances in novel nanostructuring methods of perovskite electrocatalysts for energy-related applications, **Small Methods**, 2 (2018): 1800071.
7. Hainan Sun, **Xiaomin Xu**, Zhiwei Hu, Liu Hao Tjeng, Jie Zhao, Qin Zhang, Hong-Ji Lin, Chien-Te Chen, Ting-Shan Chan, Wei Zhou*, Zongping Shao*, Boosting the oxygen evolution reaction activity of a perovskite through introducing multi-element synergy and building an ordered structure, **Journal of Materials Chemistry A**, 7 (2019): 9924–9932.
8. Hainan Sun, **Xiaomin Xu**, Gao Chen, Yupeng Zhou, Hong-Ji Lin, Chien-Te Chen, Ran Ran, Wei Zhou*, Zongping Shao*, Smart control of composition for double perovskite electrocatalysts toward enhanced oxygen evolution reaction, **ChemSusChem**, 12 (2019): 5111–5116.
9. Yijun Zhong, **Xiaomin Xu**, Wei Wang, Zongping Shao*, Recent advances in

metal-organic framework derivatives as oxygen catalysts for zinc-air batteries, **Batteries & Supercaps**, 2 (2019): 272–289.

10. Wei Wang#, Meigui Xu#, **Xiaomin Xu**, Wei Zhou, Zongping Shao*, Perovskite oxide-based electrodes for high-performance photoelectrochemical water splitting: A review, **Angewandte Chemie International Edition**, 59 (2020): 136–152.
11. Hainan Sun, Zhiwei Hu, **Xiaomin Xu**, Juan He, Jie Dai, Hong-Ji Lin, Ting-Shan Chan, Chien-Te Chen, Liu Hao Tjeng, Wei Zhou*, Zongping Shao*, Ternary phase diagram-facilitated rapid screening of double perovskites as electrocatalysts for the oxygen evolution reaction, **Chemistry of Materials**, 31 (2019): 5919–5926.
12. Yasir Arafat, Muhammad Rizwan Azhar, Yijun Zhong, **Xiaomin Xu**, Moses O Tadé, Zongping Shao*, A porous nano-micro-composite as a high-performance bi-functional air electrode with remarkable stability for rechargeable zinc–air batteries, **Nano-Micro Letters**, 12 (2020): 130.
13. Shaghraf Javaid, Yunguo Li, Dechao Chen, **Xiaomin Xu**, Yingping Pang, Wei Chen, Fei Wang, Zongping Shao, Martin Saunders, Jean-Pierre Veder, Guohua Jia*, Franca Jones*, Spontaneous formation of heterodimer Au–Fe_7S_8 nanoplatelets by a seeded growth approach, **The Journal of Physical Chemistry C**, 123 (2019): 10604–10613.
14. Daqin Guan, Jing Zhou, Zhiwei Hu*, Wei Zhou*, **Xiaomin Xu**, Yijun Zhong, Bo Liu, Yuhui Chen, Meigui Xu, Hong-Ji Lin, Chien-Te Chen, Jian-Qiang Wang, Zongping Shao*, Searching general sufficient-and-necessary conditions for ultrafast hydrogen-evolving electrocatalysis, **Advanced Functional Materials**, 29 (2019): 1900704.

Manuscripts in preparation:

1. **Xiaomin Xu**, Zongping Shao*, et al., Fe-based perovskites for catalyzing the hydrogen evolution reaction in alkaline solutions, In Preparation.
2. **Xiaomin Xu**, Zongping Shao*, et al., An unusually stabilized Co-based perovskite for highly efficient oxygen evolution, In Preparation.
3. **Xiaomin Xu**, Zongping Shao*, et al., Alkali-metal-doped perovskites for efficient oxygen evolution in alkaline solutions, In Preparation.

Table of Contents

Chapter 1 Introduction

1.1 Background*

Moving into the 2020s, humanity continues to face formidable challenges from energy and the environment. According to the International Energy Agency,[1] world primary energy demand in 2017 reached 5.8×10^8 TJ (terajoule, 1 TJ = 10^{12} J), of which fossil fuels (oil, coal, and natural gas) have a major share of more than 80% (about 81%). Projections indicate that with the growth in population and economy, this energy demand will further increase to 7.4 or 8.1×10^8 TJ in 2040 under the "New Policies Scenario" or "Current Policies Scenario", respectively, with a corresponding increase in carbon dioxide (CO_2) emissions from 32.6 Gt (gigatonne, 1 Gt = 10^9 *t* = 10^{12} kg) in 2017 to 35.9 or 42.5 Gt in 2040.[1] As a consequence, great concerns have been raised regarding the environmental issues associated with the continued use of fossil fuels, for example, global warming.

One way to address the energy and environmental problems is to utilize renewable energy sources, such as solar and wind, to power our planet.[2] For instance, solar power is by far the most abundant source of renewable energy. It is approximated that the Earth's surface receives 1.2×10^5 TJ of solar energy at every second,[3] meaning that with just 1–2 hours of direct sunlight, one could collect enough energy to satisfy the global energy demand for one entire year. However, solar or wind supplies power only when the sun shines or wind blows. To overcome the problem of energy supply intermittency, energy storage technologies will be required.

* *This Background section contains text extracts form published works of the author. These text extracts are reprinted (adapted) with permission from Xiaomin Xu, Yangli Pan, Yijun Zhong, Ran Ran, Zongping Shao, Ruddlesden–Popper perovskites in electrocatalysis, Materials Horizons, 2020, 7, 2519–2565. Copyright (2020) The Royal Society of Chemistry; and Xiaomin Xu, Wei Wang, Wei Zhou, Zongping Shao, Recent advances in novel nanostructuring methods of perovskite electrocatalysts for energy-related applications, Small Methods, 2018, 2, 1800071. Copyright (2018) WILEY-VCH Verlag GmbH & Co. KGaA, Weinheim.*

The existing energy storage technologies, with many commercial installations worldwide, are largely based on mechanical energy storage, such as pumped-storage hydroelectricity (i.e., pumped hydro),[4] compressed air energy storage,[5] and flywheels.[6] According to statistics, the world's total installed capacity of pumped hydro was about 1.3×10^5 MW (megawatt, 1 MW = 10^6 W) in 2010, accounting for 99% of the worldwide storage capacity.[7,8] When coupled with the renewable energy sources, these mechanical energy storage technologies, in particular pumped hydro, can bring about reduced emissions.[9] Nonetheless, these currently available technologies can be dependent on limited resources or geographic locations and thus may not be affordable for or accessible to all users.[10] As an alternative, electrochemical energy storage represents an excellent platform for the integration of renewable resources. For example, battery technologies including sodium-sulfur batteries, redox-flow batteries, and lithium-ion batteries have been commercialized in grid storage, stationary storage, and portable electronics and electric vehicles, respectively.[8] Despite their different operational characteristics, these battery technologies face several common challenges for further development, including the enhancement in performance, reduction in cost, and improvement in safety.

Recently, electrochemically storing renewable energy in chemical products of global importance has been proposed to be a feasible and promising option.[11] For instance, the electrochemical reduction of water (H_2O), nitrogen (N_2), and CO_2,[12-14] which are universal feedstocks provided by the Earth's atmosphere, can produce a large variety of energy carriers (hydrogen (H_2), ammonia (NH_3), and carbon-containing species such as carbon monoxide (CO), hydrocarbons, and alcohols) that enable the storage of renewables-derived electricity in the form of chemical energy. These electrochemical transformations can be facilely realized using an electrolysis cell under (near) ambient conditions, allowing the on-site production of chemicals at a reduced capital cost. Furthermore, the chemicals produced can be employed as sustainable fuels in electrochemical devices such as fuel cells to generate electrical energy,[15,16] which offers a cleaner alternative for power generation compared to the combustion of fossil fuels.

Among the various electrochemical conversions, the electrochemical reduction of water, which is more often called the electrochemical water splitting or water electrolysis, is considered a key approach for renewable energy conversion and storage

because it can convert the electricity generated from renewable energy sources into hydrogen as a carbon-neutral fuel. In water splitting, water is split into oxygen and hydrogen according to the equation $H_2O \rightarrow 1/2O_2 + H_2$. This reaction is a thermodynamically uphill process that necessitates an energy input of 286 kJ mol^{-1} at room temperature and pressure. As an equivalent of this energy input, a minimum theoretical voltage of 1.229 V (often approximated to 1.23 V) is required to drive the water splitting at room temperature.[12] However, the practical operation of water electrolysis is often hampered by the slow kinetics of the two half-reactions, namely the hydrogen evolution reaction (HER) at the cathode and the oxygen evolution reaction (OER) at the anode. To further accelerate these reactions, additional energy input, which manifests as a need for a potential larger than their equilibrium potential (i.e., 0 and 1.23 V vs. the reversible hydrogen electrode for HER and OER, respectively), is required. This gap of potential applied is normally termed the overpotential (η). In order to lower this overpotential and make the water-splitting process more energy-efficient, electrocatalysts have to be introduced to the water electrolysis system, on both the anode and the cathode. The state-of-the-art electrocatalysts for the OER and HER often involve noble metals, for example, platinum for the cathodic HER,[17] and iridium or ruthenium (or their oxides) for the anodic OER.[18] Due to the low abundance and prohibitive cost of these catalysts, increasing research efforts are focusing on nonprecious metal-based alternatives.

Among many candidates, perovskite oxides have emerged as a large family of functional materials that show great potential for catalyzing the OER,[19-22] as well as the HER in alkaline media.[23-25] **Figure 1.1** gives a schematic representation of the perovskite oxide structure in an ideal cubic symmetry. With a formula generally expressed as $ABO_{3-\delta}$, the A-site is typically a rare-earth or an alkali whereas the B-site is often a transition metal, occupying the 12-fold and 6-fold coordination sites, respectively. Compared to other catalytic materials, perovskite oxides feature low cost, facile synthesis, and easiness for scale-up. More importantly, perovskite oxides are known for their compositional and structural tunability. The perovskite structure can allow the incorporation of almost 90% of the elements within the "Periodic Table of Elements" by partial substitution of elements at A- or/and B-, or O-site.[26] Meanwhile, the oxygen nonstoichiometry (δ) can vary within a large range. Such flexibility in composition and structure gives rise to the tunable electronic structure of perovskites,

exhibiting diverse physical and chemical properties that can be utilized to design highly efficient electrocatalysts toward both the OER and HER.

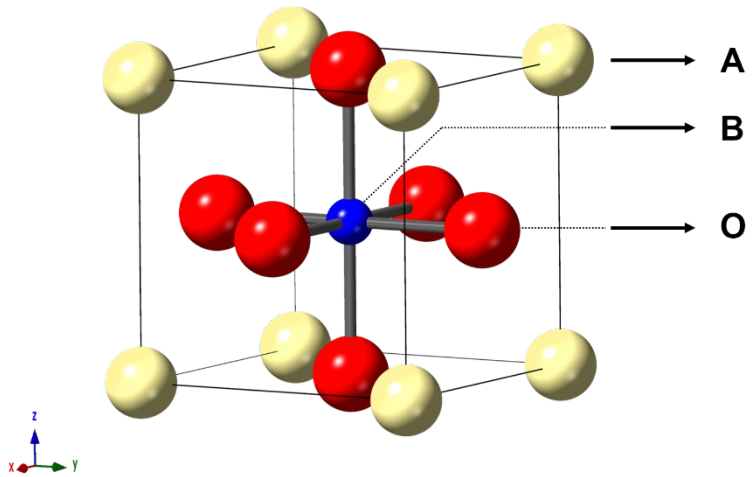

Figure 1.1 A schematic showing the crystalline structure of the ABO_3 perovskite with an ideal cubic symmetry.

1.2 Research objectives

While recent years have witnessed great progress in the development of perovskite-based water splitting electrocatalysts, there is much room for further advances in terms of activity improvement, stability enhancement, and cost reduction. This thesis aims to develop non-precious metal-based perovskite oxides as the electrocatalysts for facilitating the HER and OER kinetics in electrochemical water splitting. Taking advantage of the compositional and structural diversity, strategies are adopted to tune the chemical composition and engineer the crystal structure of perovskites oxides, which serve as useful means to modify their electronic structures. Based on these strategies, perovskites with new compositions, reduced costs, and improved performance are designed and fabricated. Their functionality in the electrocatalytic HER/OER is evaluated and the structure–activity relationship is investigated. The specific objectives of this thesis are listed as follows.

- To summarize the current research status of perovskite oxides as the electrocatalysts for electrochemical water splitting.
- To expand the compositional space of perovskite oxides and to investigate the efficacy of molybdenum-based perovskite oxides as electrocatalysts for the HER.

- To explore iron-based perovskite oxides as alternatives to cobalt-based ones for catalyzing the HER and to study their structure–activity correlations.
- To boost the electrocatalytic OER performance of an existing cobalt-based perovskite oxide through stabilizing an unusually obtained phase structure and to investigate the structural effects on the OER electrocatalysis.
- To improve the activity and stability of iron-based OER perovskite catalysts by alkali-metal substitution and to understand the origins of the enhanced performance.

1.3 Thesis organization

This thesis consists of eight chapters. Chapter 1 introduces the research background and outlines the thesis structure. Chapter 2 provides a literature review on the recent progress of perovskite-based water-splitting catalysts. Chapter 3 details the experimental methodologies used in this thesis. Chapters 4–7 offer the results and discussion of the experimental studies. Chapter 8 presents the conclusions and provides perspectives for future research. The specific contents of these chapters are also summarized as follows.

Chapter 1: Introduction

This chapter provides the global energy context under which the research in this thesis is conducted. It also briefly introduces the background of electrochemical water splitting, the two half-reactions involved, and the perovskite oxides. The thesis objectives and organization are also provided.

Chapter 2: Literature review

This chapter presents a thorough review on the fundamentals and applications of perovskite oxides as the electrochemical water splitting catalysts. The materials design strategies to tune the perovskite structure are also discussed.

Chapter 3: Methodologies and characterizations

This chapter summarizes the materials synthesis, characterizations, and electrochemical measurements used throughout the experimental studies involved in this thesis.

Chapter 4: From scheelite $BaMoO_4$ to perovskite $BaMoO_3$: Enhanced electrocatalysis toward the hydrogen evolution in alkaline media

This chapter evaluates the use of a molybdenum based $BaMoO_3$ perovskite oxide, synthesized from the conversion of a $BaMoO_4$ scheelite oxide under a reductive condition, as the HER electrocatalyst in alkaline media. The activity improvement is discussed based on considerations of structural changes.

Chapter 5: Fe-based perovskites for catalyzing the hydrogen evolution reaction in alkaline solutions

This chapter focuses on iron-based perovskites as the HER electrocatalysts, using an alkaline-earth metals Ba and Sr co-doped $La_{1-x}(Ba_{0.5}Sr_{0.5})_xFeO_{3-\delta}$ series (x = 0.0, 0.2, 0.5, 0.8, and 1.0) as the research target. The effect of the Ba/Sr substitution on the phase structure, Fe oxidation state, and Fe–O bond covalency is discussed and correlated with the catalytic activity.

Chapter 6: An unusually stabilized Co-based perovskite for highly efficient oxygen evolution

This chapter reports a new methodology for the stabilization of a cobalt-based cubic-structured perovskite from a hexagonal-structured perovskite and evaluates their electrocatalytic activity for the OER in alkaline solutions. The influence of this phase transformation on the perovskite electronic structure and the OER activity is explored.

Chapter 7: Alkali-metal-doped perovskites for efficient oxygen evolution in alkaline solutions

This chapter concerns a new doping strategy using alkali metals as the dopants and addresses the unsatisfactory performance of iron-based perovskite OER electrocatalysts. Utilizing a model catalyst of $LaFeO_3$, monovalent Na^+ was doped into the system to partially replace trivalent La^{3+}. The changes induced by the Na-doping, including Fe valence, Fe–O covalency, and oxygen vacancy content, are discussed and related to the electrocatalytic performance.

Chapter 8: Conclusions and perspectives

This chapter concludes with the major achievements of this thesis and proposes some interesting topics of further research.

1.4 References

(1) IEA (2018), World Energy Outlook 2018, IEA, Paris. https://www.iea.org/reports/world-energy-outlook-2018.

(2) Gray, H. B. Powering the planet with solar fuel. *Nat. Chem.* **2009**, *1*, 7.

(3) Blankenship, R. E.; Tiede, D. M.; Barber, J.; Brudvig, G. W.; Fleming, G.; Ghirardi, M.; Gunner, M. R.; Junge, W.; Kramer, D. M.; Melis, A. et al. Comparing photosynthetic and photovoltaic efficiencies and recognizing the potential for improvement. *Science* **2011**, *332*, 805–809.

(4) Rehman, S.; Al-Hadhrami, L. M.; Alam, M. M. Pumped hydro energy storage system: A technological review. *Renew. Sustain. Energy Rev.* **2015**, *44*, 586–598.

(5) Budt, M.; Wolf, D.; Span, R.; Yan, J. A review on compressed air energy storage: Basic principles, past milestones and recent developments. *Appl. Energy* **2016**, *170*, 250–268.

(6) Mousavi G, S. M.; Faraji, F.; Majazi, A.; Al-Haddad, K. A comprehensive review of flywheel energy storage system technology. *Renew. Sustain. Energy Rev.* **2017**, *67*, 477–490.

(7) Wu, F.-B.; Yang, B.; Ye, J.-L. *Grid-Scale Energy Storage Systems and Applications*; Academic Press, **2019**.

(8) Dunn, B.; Kamath, H.; Tarascon, J.-M. Electrical energy storage for the grid: A battery of choices. *Science* **2011**, *334*, 928–935.

(9) Denholm, P.; Kulcinski, G. L. Life cycle energy requirements and greenhouse gas emissions from large scale energy storage systems. *Energy Convers. Manag.* **2004**, *45*, 2153–2172.

(10) Soloveichik, G. L. Battery technologies for large-scale stationary energy storage. *Annu. Rev. Chem. Biomol. Eng.* **2011**, *2*, 503–527.

(11) Seh, Z. W.; Kibsgaard, J.; Dickens, C. F.; Chorkendorff, I.; Nørskov, J. K.; Jaramillo, T. F. Combining theory and experiment in electrocatalysis: Insights into materials design. *Science* **2017**, *355*, eaad4998.

(12) Roger, I.; Shipman, M. A.; Symes, M. D. Earth-abundant catalysts for electrochemical and photoelectrochemical water splitting. *Nat. Rev. Chem.* **2017**, *1*, 0003.

(13) Voiry, D.; Shin, H. S.; Loh, K. P.; Chhowalla, M. Low-dimensional catalysts for hydrogen evolution and CO_2 reduction. *Nat. Rev. Chem.* **2018**, *2*, 0105.

(14) Suryanto, B. H. R.; Du, H.-L.; Wang, D.; Chen, J.; Simonov, A. N.; MacFarlane, D. R. Challenges and prospects in the catalysis of electroreduction of nitrogen to ammonia. *Nat. Catal.* **2019**, *2*, 290–296.

(15) Wang, X. X.; Swihart, M. T.; Wu, G. Achievements, challenges and perspectives on cathode catalysts in proton exchange membrane fuel cells for transportation. *Nat. Catal.* **2019**, *2*, 578–589.

(16) Pan, Z. F.; An, L.; Zhao, T. S.; Tang, Z. K. Advances and challenges in alkaline anion exchange membrane fuel cells. *Prog. Energy Combust. Sci.* **2018**, *66*, 141–175.

(17) Tavakkoli, M.; Kallio, T.; Reynaud, O.; Nasibulin, A. G.; Johans, C.; Sainio, J.; Jiang, H.; Kauppinen, E. I.; Laasonen, K. Single-shell carbon-encapsulated iron nanoparticles: Synthesis and high electrocatalytic activity for hydrogen evolution reaction. *Angew. Chem. Int. Ed.* **2015**, *54*, 4535–4538.

(18) Lee, Y.; Suntivich, J.; May, K. J.; Perry, E. E.; Shao-Horn, Y. Synthesis and activities of rutile IrO_2 and RuO_2 nanoparticles for oxygen evolution in acid and alkaline solutions. *J. Phys. Chem. Lett.* **2012**, *3*, 399–404.

(19) Suntivich, J.; May, K. J.; Gasteiger, H. A.; Goodenough, J. B.; Shao-Horn, Y. A perovskite oxide optimized for oxygen evolution catalysis from molecular orbital principles. *Science* **2011**, *334*, 1383–1385.

(20) Hong, W. T.; Risch, M.; Stoerzinger, K. A.; Grimaud, A.; Suntivich, J.; Shao-Horn, Y. Toward the rational design of non-precious transition metal oxides for oxygen electrocatalysis. *Energy Environ. Sci.* **2015,** *8*, 1404–1427.

(21) Bockris, J. O. M.; Otagawa, T. Mechanism of oxygen evolution on perovskites. *J. Phys. Chem.* **1983**, *87*, 2960–2971.

(22) Bockris, J. O. M. The electrocatalysis of oxygen evolution on perovskites. *J. Electrochem. Soc.* **1984**, *131*, 290–302.

(23) Xu, X.; Chen, Y.; Zhou, W.; Zhu, Z.; Su, C.; Liu, M.; Shao, Z. A perovskite electrocatalyst for efficient hydrogen evolution reaction. *Adv. Mater.* **2016**, *28*, 6442–6448.

(24) Guan, D.; Zhou, J.; Hu, Z.; Zhou, W.; Xu, X.; Zhong, Y.; Liu, B.; Chen, Y.; Xu, M.; Lin, H.-J. et al. Searching general sufficient-and-necessary conditions

for ultrafast hydrogen-evolving electrocatalysis. *Adv. Funct. Mater.* **2019**, *29*, 1900704.

(25) Guan, D.; Zhou, J.; Huang, Y.-C.; Dong, C.-L.; Wang, J.-Q.; Zhou, W.; Shao, Z. Screening highly active perovskites for hydrogen-evolving reaction via unifying ionic electronegativity descriptor. *Nat. Commun.* **2019**, *10*, 3755.

(26) Zhu, L.; Ran, R.; Tadé, M.; Wang, W.; Shao, Z. Perovskite materials in energy storage and conversion. *Asia-Pac. J. Chem. Eng.* **2016**, *11*, 338–369.

Chapter 2 Literature review*

2.1 Abstract

Electrocatalysis-based technologies are central to enabling the vision of a sustainable energy future. One major challenge is to develop nonprecious, high-efficient electrocatalysts that can promote the electrocatalytic processes. Perovskite materials have recently been extensively studied as alternative electrocatalysts to noble metal-based materials owing to their low cost, tunable structure, and high catalytic activity. This chapter discusses perovskite materials in electrocatalysis for several important reactions, including the oxygen reduction reaction, oxygen evolution reaction, and hydrogen evolution reaction. The electrocatalytic mechanisms are first introduced to offer a fundamental understanding of the electrocatalysis occurring on the surface of perovskite catalysts. Following this is a detailed description of the rational design of perovskite materials toward efficient electrocatalysis. Several activity descriptors for theoretically guiding the catalyst design are presented while many other practical parameters that can influence the catalyst behavior are also highlighted. In addition, concerns for the catalyst stability under realistic electrochemical conditions are expressed. In an effort to realize global energy sustainability, several key applications of perovskite materials in electrocatalysis-related energy devices, for example, metal–air batteries and water electrolyzers, are presented, with an emphasis on how to enable the widespread penetration of these energy technologies.

2.2 Introduction

Driven by pressing concerns over the growing energy demands, depleting fossil fuels, and impending climate change, one grand challenge facing humanity today is how to power the planet with renewable energy sources (e.g., wind and solar). Renewable energy is plentiful but tends to be intermittent in nature as the wind is not always blowing and the sun is not always shining. One prospective option to address the issue of energy supply intermittency is to develop electrochemical devices that can utilize electricity produced from renewable energy to enable the transformations between electrical energy and chemical energy. For example, in water electrolyzers, water molecules are split into hydrogen, which is a clean energy carrier that can be used in fuel cells to generate electricity. In fuel cells or metal–air batteries, the oxidation of hydrogen or metals is coupled with the reduction of oxygen to convert chemical energy into electrical energy. Unfortunately, these energy conversion technologies have low efficiency because of the sluggish kinetics of several key reactions involved. For instance, the overall efficiency of water electrolysis is dominated by the hydrogen evolution reaction (HER) at the cathode and the oxygen evolution reaction (OER) at the anode [1]. Likewise, the efficiency of rechargeable metal–air batteries is strongly dependent on the oxygen reduction reaction (ORR) during discharge and the OER during charge [2]. Increasing the efficiency of these devices would therefore necessitate the role of electrocatalysis to modify the rate of the relevant chemical reactions via the assistance of electrocatalysts that are active and stable.

The term “electrocatalysis” is generally referred to as a type of catalysis that leads to the change of the rate of an electrochemical reaction taking place at the interface between an electrode and an electrolyte. Despite its high relevance to renewable energy technologies, our current knowledge about the fundamental mechanisms underlying electrocatalysis is still inadequate. For instance, mechanistic insights into the OER is limited to theoretical understanding only, due to the complexity in this multi-step four-electron reaction which lacks experimental observation on the details of electrode interfaces under realistic operating conditions. Nonetheless, years of intense academic research have seen significant breakthroughs in the development of electrocatalysts that can substantially lower the overpotential associated with the electrochemical reactions. While noble metal-based materials (e.g., Pt-, Ir-, and Ru-based materials) normally show optimum catalytic activity [3,4], their widespread

penetration into clean energy devices is hindered by their low abundance and high cost, which does not conform to the vision of a sustainable energy future. Hence tremendous efforts have been devoted to the search for a wide range of inexpensive alternatives that consist of Earth-abundant elements. These include metals [5], oxides [6-8], (oxy)hydroxides [9,10], chalcogenides [11], non-metal carbon materials [12], and metal-organic frameworks [13], to name just a few.

Of all the candidates, perovskite materials have recently emerged as a new family of low-cost, high-efficient nonprecious metal catalysts for catalyzing relevant reactions including the ORR, OER, and HER [14]. Perovskites are known for their versatility in chemical, crystal, and electronic structures [15]. With a nominal formula generally expressed as ABO_3, the perovskite chemical structure can accommodate nearly 90% of the elements within the "Periodic Table of Elements" by partial substitution of elements at A or/and B sites, while also allowing a changeable stoichiometry at the O site [16]. In addition, a range of perovskite derivatives with varied crystal structures, including double perovskite, layered perovskite, and quadruple perovskite, further add to the diversity of the perovskite family. This flexibility gives rise to the tunability in the electronic structure of perovskites, making them ideally suited for the study of the structure-performance relationship in electrocatalysis. In oxygen electrocatalysis, a veritable explosion of research activity targeting the development perovskite catalysts has been observed. On the other hand, the role of perovskites in the field of hydrogen electrocatalysis is less explored and has been gaining growing attention until recently. In this chapter, we mainly focus on perovskite materials for the electrocatalysis toward the ORR, OER, and HER reactions. Considering that perovskite oxides are typically stable in alkaline media and can dissolve in acids, this chapter will primarily deal with those that work in alkaline environments unless otherwise stated. The electrocatalytic mechanisms are first introduced to offer a clear picture of the reactions taking place on perovskite catalysts. This is followed by a detailed discussion on the rational design of perovskite materials toward efficient electrocatalysis, which focuses on both catalytic activity and stability. In the context of the pursuit of a sustainable future of energy, we also present applications of perovskite materials in electrocatalysis-related energy devices which can enable efficient use of renewable energy.

2.3 Mechanisms in electrocatalysis on perovskite materials

Fundamental insights into the reaction mechanisms is a vital step toward understanding electrocatalysis on catalyst surfaces. Due to the complex interaction at the electrode interface, there is no single governing mechanism that unifies all electrocatalytic reactions. Even for the same reaction of interest, the mechanisms can differ with catalyst chemistries. Taking the OER in alkaline media as an example, one-metal-site mechanisms have been proposed for noble metals [17], dimeric molecules [18], and perovskite oxides [19], whereas distinct two-metal-site mechanisms have been introduced for the oxygen evolving complex of photosystem II [20] and electrodeposited oxides [21]. In this section, only the conventional mechanisms (which are considered the most favorable) underlying the oxygen and hydrogen electrocatalysis on perovskite surfaces are highlighted.

2.3.1 Oxygen electrocatalysis

Conventionally, the ORR reaction in alkaline solutions can be written as $O_2 + 2H_2O + 4e^- \rightarrow 4OH^-$. Previous experimental and computational studies show that the ORR on perovskite oxides is a consecutive, four-step, proton-coupled electron transfer process taking place on single surface metal sites [22,23]. These four sequential steps are 1, hydroxide displacement; 2, peroxide formation; 3, oxide formation; and 4, hydroxide regeneration as shown in **Figure 2.1a** [22]. In these reaction pathways, molecular O_2 or H_2O from the electrolyte and electron interact with surface metal sites to generate four different oxygenated adsorbates including OO*, OOH*, O*, and OH* (* denotes a reactive site on the catalyst surface), which is accompanied by the oxidation and reduction (redox) of surface metal sites whose oxidation state changes between n+ and n+1. Energetically, the ORR reaction kinetics are largely determined by the binding energy of oxygen and the surface metal sites; too weak of an oxygen binding energy leads to the first OH*-to-OO* displacement step being the rate-determining step (RDS), whereas too strong of an oxygen binding energy renders the last O*-to-OH* transition step being rate-limiting [23]. An optimal perovskite catalyst binds to oxygen neither too weakly nor too strongly, which is commonly referred to as the Sabatier principle. For perovskite oxide surfaces that follow the same one-metal-site mechanism, the binding energies of the different reactive oxygen adsorbates involved in the ORR are highly correlated due to scaling relations [24,25], which is the origin of the nonzero theoretical overpotential observed among many catalysts.

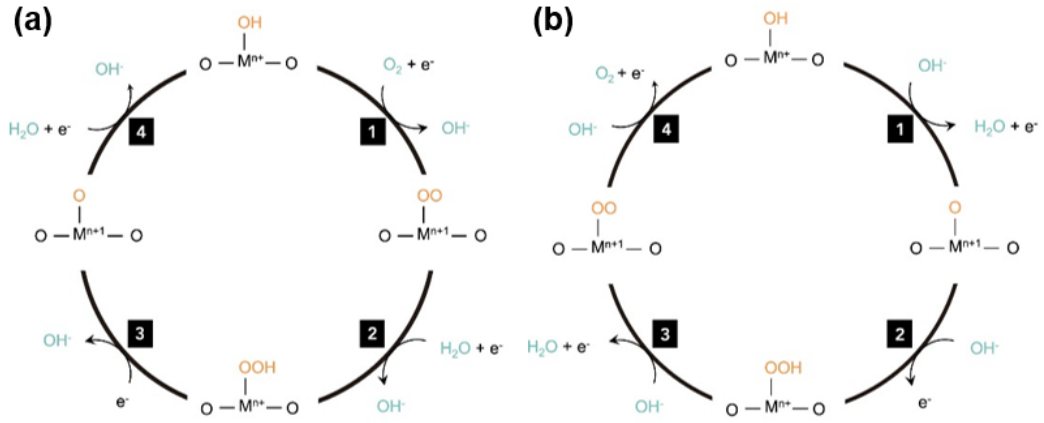

Figure 2.1 (a) Four-step ORR mechanism on the surface of perovskite oxide catalysts in alkaline solutions. (b) Four-step OER mechanism on the surface of perovskite oxide catalysts in alkaline solutions. (Reprinted with permission from Ref. [22]. Copyright 2017 Elsevier Inc.)

In a similar vein, the OER reaction on perovskite oxides in alkaline media, which can be written as $4OH^- \rightarrow O_2 + 2H_2O + 4e^-$, proceeds via four proton-coupled electron transfer steps including 1, hydroxide deprotonation; 2, peroxide formation; 3, peroxide deprotonation; and 4, hydroxide regeneration (**Figure 2.1b**) [22]. In this mechanism, hydroxyl ions (OH^-) from the electrolyte interacts with surface metal sites, resulting in the redox of the metal (with the oxidation state switching between n+ and n+1). The reactive intermediates generated for the OER in base are the same as those for the ORR, which are however in a different sequence of O*, OOH*, OO*, and OH*. Similar to the ORR, the OER reaction kinetics are primarily controlled by the oxygen binding strength on surface metal sites. For metal sites that bind oxygen too weakly, the second O*-to-OOH* peroxide formation step is rate-limiting. On the other hand, for metal sites that bind oxygen too strongly, the RDS may be the third OOH*-to-OO* peroxide deprotonation step [26]. The binding strength of the surface oxygen adsorbates is found to obey a scaling relation [27], analogous to the case of perovskites for the ORR, again hampering the development of a perovskite OER catalyst with zero overpotential. While the conventional OER mechanism considers surface metal as the sole reactive site, novel mechanisms that involve the participation of lattice oxygen have recently been proposed [28-32].

Note that the intermediate adsorbates on perovskite oxide surfaces in the above-mentioned ORR/OER mechanisms are not identical to those on metal surfaces in relevant mechanisms proposed based on density functional theory (DFT) calculations. Despite having similar elementary reaction steps, the ORR on metal surfaces involves a series of intermediates in the order of O_2*, OOH*, O*, and OH* [24], whereas the OER on metal surfaces involves a sequence of intermediates of OH*, O*, OOH*, and O_2* [17]. This difference can be rationalized from the different surface properties of metal surfaces and perovskite oxide surfaces, the latter being able to adsorb negatively charged species (such as OH^-) in alkaline conditions at the initial stage of electrocatalysis [33]. Such difference also points to the diversity in reaction mechanisms that have been proposed for oxygen electrocatalysis, which again highlights the complexity of the oxygen chemistries on catalyst surfaces. To date, due to the underdeveloped time-resolved techniques, experimentally accessing the reaction intermediates on perovskite oxide surfaces remains a formidable challenge. Theoretically, to gain a better mechanistic understanding of the oxygen electrocatalysis, interested readers can resort to the pioneering DFT works by Rossmeisl et al. [17,27,34] and Nørskov et al. [24,35,36].

2.3.2 Hydrogen electrocatalysis

The overall reaction of the HER in basic solutions can be written as $2H_2O + 2e^- \rightarrow H_2 + 2OH^-$. Generally, the alkaline HER is a two-step electron transfer process, and may occur via either the Volmer-Heyrovsky mechanism or the Volmer-Tafel mechanism [37,38]:

Volmer reaction:	$* + H_2O + e^- \rightarrow H^* + OH^-$	(1)
Heyrovsky reaction:	$H^* + H_2O + e^- \rightarrow H_2 + OH^- + *$	(2)
Tafel reaction:	$2H^* \rightarrow H_2 + 2*$	(3)

Both reaction pathways include the same Volmer reaction, which involves adsorption of molecular H_2O on the empty reactive sites, electrochemical reduction of adsorbed H_2O into adsorbed hydrogen atoms (H*) and OH^-, desorption of OH^- to refresh the catalyst surface and formation of H* for H_2 evolution.

While the conventional HER mechanism has been well established based on experimental and theoretical results on metal catalysts [39], little is known about the HER process on oxide surfaces, especially in alkaline environments [40,41]. Back in the 1990s, Goodenough et al. first experimentally observed the evolution of hydrogen on $Sr_{1-x}NbO_{3-\delta}$ ($0.05 \leq x \leq 0.3$) perovskite oxides in strong acids [19]. Based on

electrochemical measurements, they proposed a possible HER reaction pathway and pointed out that the reactive site for the HER on perovskite oxides appears to be not the surface metal, but rather the surface oxygen anion. This is not unexpected considering that binding with positively charged metal cations would be kinetically unfavorable for H atoms. Very recently, Xu et al. showcased the efficacy of a $Pr_{0.5}(Ba_{0.5}Sr_{0.5})_{0.5}Co_{0.8}Fe_{0.2}O_{3-\delta}$ perovskite oxide in catalyzing the HER in bases, and proposed a reaction mechanism for the alkaline HER as shown in **Figure 2.2** [42], similar to that for the HER in acids [19]. Note that the O site at the initial reaction state is not protonated here for the sake of simplicity. In this pathway, molecular H_2O from the electrolyte and electron interact with a bridging oxygen site to form an adsorbed H* intermediate, where one adjacent surface metal can be reduced or oxidized (with the oxidation state switching between n+1 and n). However, it remains difficult to determine whether the second step proceeds via the Heyrovsky reaction or the Tafel reaction.

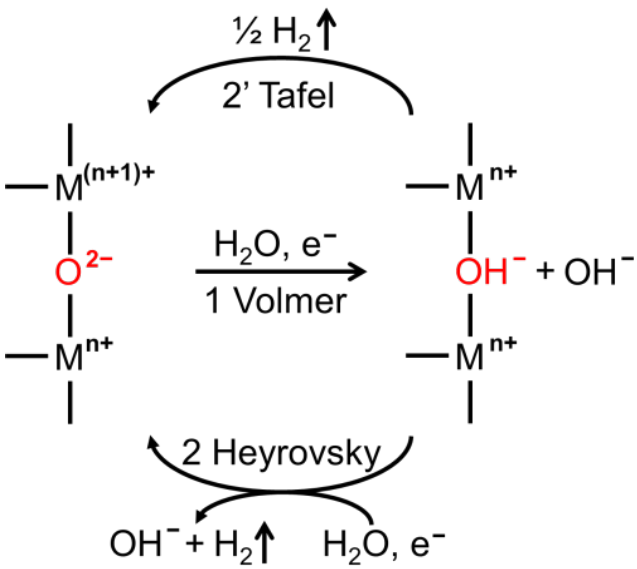

Figure 2.2 Two-step HER mechanism on the surface of perovskite oxide catalysts in alkaline solutions. (Reprinted with permission from Ref. [42]. Copyright 2016 John Wiley and Sons)

Unlike in the case of the ORR/OER with multiple reaction intermediates, the two-electron HER involves only one intermediate (H*). Thus, no scaling relation is observed and an ideal zero overpotential can be achieved on advanced catalysts (e.g.,

Pt) [11], which represents a goal for optimizing the perovskite electrocatalysts. The rate of the overall HER reaction is mainly dependent on the binding strength of the H* intermediate, which is more commonly referred to as the hydrogen adsorption free energy (ΔG_H) [43]. An optimal HER catalyst should bind to hydrogen neither too weakly nor too strongly, having a ΔG_H value close to zero.

2.4 Rational design of perovskite materials toward efficient electrocatalysis

While the proposed reaction mechanisms can offer a fundamental understanding of the electrochemical processes occurring on perovskite materials, they do not have the power to screen perovskites with remarkable catalytic effects ("activity"). Given the large number of perovskite candidates and their many physical properties influencing the catalytic activity, it is necessary to realize the rational design of perovskite materials toward efficient electrocatalysis. Generally, the activity of an electrocatalyst can be improved by either increasing the intrinsic activity of each reactive site or increasing the number of reactive sites (extrinsic activity) [44]. A combination of these two strategies can lead to further enhancement in activity. To rationalize the design of improved perovskite catalysts, property–activity relationships that govern the intrinsic activity, which are often referred to as "activity descriptors", have been developed [45]. This section describes several important activity descriptors that have shown predictive power in discovering advanced perovskite catalysts, with a special emphasis on descriptors for the OER. Nonetheless, these descriptors have their limitations and do no hold universally for all perovskite materials across all catalytic reactions. Thus, specific design strategies that aim to increase the intrinsic or extrinsic activity (or both) are discussed, focusing on a range of parameters that can be tuned in perovskite oxides to promote the catalytic performance of the ORR, OER, and HER. In addition to high activity, robust stability represents another important issue for efficient electrocatalysts. To facilitate improved catalyst design, major concerns over the stability of perovskite materials during electrocatalytic processes are included in this section.

2.4.1 Activity descriptors

As mentioned earlier, the reaction rate of the OER is primarily determined by the strongly correlated binding energy of oxygen intermediates. Based on this understanding, Rossmeisl et al. utilized DFT calculations to establish the difference

between the adsorption free energy of the O* and OH* intermediates ($\Delta G_{O*} - \Delta G_{OH*}$) as a universal activity descriptor for the OER on perovskite oxide surfaces [27], with highest activity expected at a moderate binding of the oxygen intermediates. However, because of the experimental challenge in unambiguously distinguishing reaction intermediates, it is not straightforward to identify active perovskite catalysts using this descriptor. Directly related to the term $\Delta G_{O*} - \Delta G_{OH*}$ is the redox potential of transition metal cations prior to the catalytic OER, which has recently been proposed as a simpler activity descriptor [22]. Unfortunately, this approach is limited by the difficulty in the assignment of the redox transition in perovskite oxides preceding the OER. Alternatively, activity descriptors from both molecular orbital theory and band theory have proved fruitful in guiding the design of perovskite materials as efficient electrocatalysts [23,26,46].

2.4.1.1 Activity descriptors from molecular orbital theory

In the perovskite oxide structure, the B-site transition metal is six-fold coordinated to the oxygen to form an octahedron. In this octahedral environment, the transition metal d orbitals hybridize with the O 2p orbitals, forming π-bonding and π*-antibonding (called t_{2g} orbital) where d_{xy}, d_{yz}, and d_{xz} orbitals have a weak spatial overlap with adjacent O 2p orbitals, and σ-bonding and σ*-antibonding (called e_g orbital) where $d_{x^2-y^2}$ and d_{z^2} orbitals have a strong spatial overlap with nearby O 2p orbitals. Molecular orbitals depicting the metal-oxygen electronic states can be used to explain the electrocatalytic phenomena in perovskite materials. Bockris and Otagawa were the first to use the d-electron number (both t_{2g} and e_g electrons) of transition metal cations as an activity descriptor to clarify the OER activity observed on ABO_3 (B = Ni, Co, Fe, Mn, Cr, V) perovskites [47,48]. They found an inverse trend between the OER overpotential and the number of transition metal d electrons, which was concluded to play a major role in determining the binding strength of the OH* adsorbate via the filling of the metal–OH antibonding orbitals. Similar to this finding, recent DFT calculations showed that the binding energy of possible OER adsorbates has a scaling relationship with the transition metal d-electron number and oxidation state of perovskite oxides [49].

In contrast to the d-electron descriptor from Bockris and Otagawa, a more appropriate activity descriptor from molecular orbital principles is the filling of e_g orbital of surface

transition metal cations reported by Shao-Horn and co-workers [26]. Based on the consideration that the e_g orbital has a higher overlap with a surface-anion adsorbate than does the t_{2g} orbital, the occupancy of e_g orbital can more directly influence the binding of adsorbed oxygen intermediates on surface transition metals and thus the OER activity. Through a systematic evaluation of more than 10 perovskite oxides with varying B-site elements in basic solutions, they demonstrated a volcano relationship between the OER activity (in terms of the overpotential needed to afford a 50 μA cm_{ox}^{-2} specific current density) and the e_g filling of B-site ions (**Figure 2.3a**) [26,45]. For the left/right branch of the volcano, perovskites having too little/much e_g orbital occupancy can result in too strong/weak interaction with oxygen intermediates, both leading to unfavorable OER activity. Sitting at the top of the volcano plot are perovskites with e_g filling close to unity, offering optimum binding of reaction intermediates and high OER performance. This observation is consistent with the Sabatier principle. The volcano trend is observed on a number of perovskite oxides, over a voltage span of 0.3 V, and across four orders of magnitude, rendering e_g-filling as a universally applicable descriptor of OER activity. This descriptor has allowed the identification of a range of active perovskite OER catalysts, including $Ba_{0.5}Sr_{0.5}Co_{0.8}Fe_{0.2}O_{3-\delta}$ (BSCF) [26], $SrNb_{0.1}Co_{0.7}Fe_{0.2}O_{3-\delta}$ [50], $Ca_2Mn_2O_5$ [51], $Ca_{0.9}Yb_{0.1}MnO_{3-\delta}$ [52], and $CaCu_3Fe_4O_{12}$ [53]. More recently, the application of the e_g-filling descriptor has been successfully extended to the screening of oxides with structures other than perovskite, for example, spinel [54] and rock salt [55] structures, for efficient OER electrocatalysts.

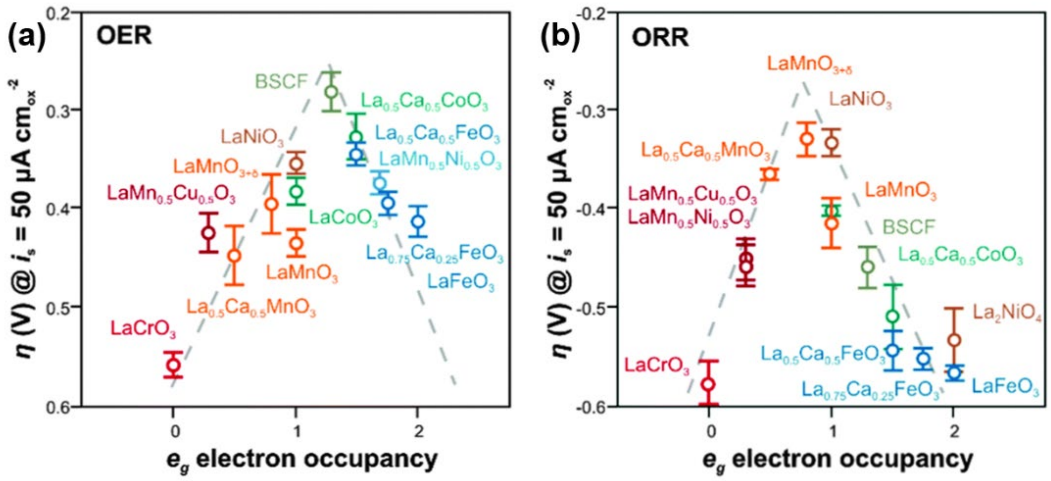

Figure 2.3 The volcano relationship between (a) the OER activity or (b) the ORR activity in alkaline solutions, defined by the overpotential at a 50 μA cm_{ox}^{-2} specific current density, and the transition metal e_g electron occupancy on perovskites. (Reprinted with permission from Ref. [45]. Copyright 2015 Royal Society of Chemistry)

In a similar fashion, plotting the ORR activity (in terms of the overpotential required to give a 50 μA cm_{ox}^{-2} specific current density) of 15 perovskite oxides in alkaline media versus the e_g occupancy of surface transition metal cations can also obtain a volcano relationship as shown in **Figure 2.3b** [23,45]. Again, the perovskite ORR activity peaks at a near-unity filling of the e_g orbital for $LaNiO_3$, $LaCoO_3$, and $LaMnO_3$, outperforming $LaCrO_3$ (e_g^0) with too low an e_g occupancy at the left branch of the volcano and $LaFeO_3$ (e_g^2) with too high an e_g filling at the right branch. The e_g-filling descriptor has seen success in discovering many efficient perovskite ORR catalysts, such as $LaNi_{0.25}Co_{0.75}O_{3-\delta}$ [56], $LaNi_{1-x}Mg_xO_3$ [57], $LaNi_{1-x}Fe_xO_3$ [58], and $La_{0.8}Sr_{0.2}Mn_{0.6}Ni_{0.4}O_3$ [59]. In the case where an identical e_g occupancy of B-site cations is observed in different perovskite materials, the transition metal–oxygen covalency is found to serve as a secondary activity descriptor [23,26]. For example, the ORR/OER activity of $LaMnO_3$, $LaCoO_3$, and $LaNiO_3$ (all having an electronic state of e_g^1) increases with the extent of the covalent mixing between transition metal ions and oxygen atoms in the order of $LaMnO_3 < LaCoO_3 < LaNiO_3$.

Despite the usefulness of the molecular orbital-based e_g-filling as a universal descriptor for picking perovskite ORR/OER catalysts, this descriptor has its own limitations. On the one hand, molecular orbital theory only considers the transition metal as the reactive site, thus cannot efficiently capture the metal–oxygen covalency of highly covalent perovskite systems where both metal and oxygen can function as reactive sites [29,30]. On the other hand, the estimation of the e_g electron number, which is based on the transition metal oxidation state and spin state extracted from ex situ measurements, remains ambiguous. For instance, there has been an ongoing debate over the spin state of cobalt-based perovskites [60-64].

2.4.1.2 Activity descriptors from band theory

The success of the e_g-filling descriptor highlights the importance of catalyst electronic structure on the ORR/OER. In addition to molecular orbital theory, band theory can also offer insightful understanding of the electronic structure of catalyst materials. For example, previous theoretical works have correlated the catalytic activity of metal or alloy surfaces with the metal d-band center [65]. As for perovskite oxides, band descriptions (such as band width) have also been developed to describe the trend in oxygen electrocatalysis [66,67]. Very recently, Grimaud et al. reported a correlation between the computed O p-band center relative to the Fermi level and the OER activity of cobalt-based perovskites [46]. As depicted in **Figure 2.4a**, the electronic structure characteristics of perovskite oxides are more accurately captured by the more delocalized O p-band while the transition metal d-character is still reflected through hybridized density of states. The O p-band center of several double perovskite and single perovskite oxides, which was obtained from DFT calculations, was found to scale linearly with the OER performance (**Figure 2.4b**) [45,46]; the closer the O p-band center to the Fermi level, the greater the OER activity. Despite acting as an alternative activity descriptor, the computed O p-band center remains to be verified by experimental investigations into the metal and oxygen states. Moreover, the universality of this activity descriptor needs to be testified on perovskite systems beyond cobalt-containing ones.

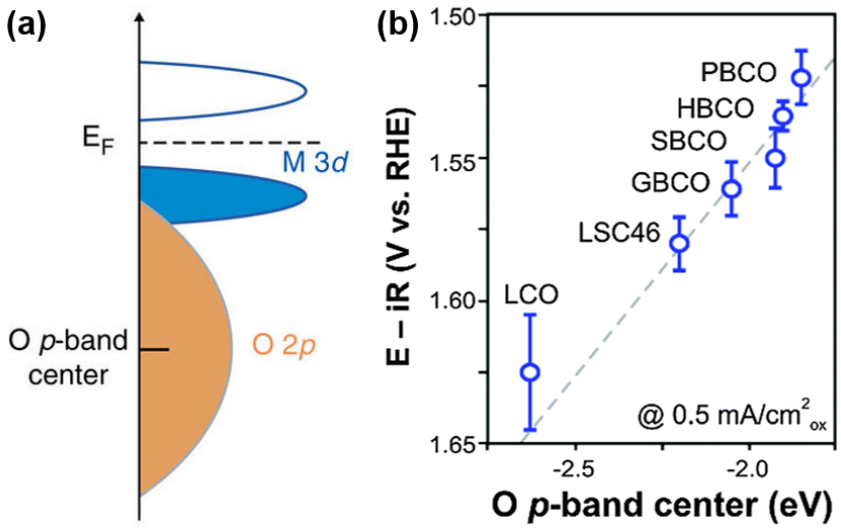

Figure 2.4 (a) A schematic representation of the density of states for perovskite oxides, illustrating the O 2p and transition metal 3d bands. (Reprinted with permission from

Ref. [46]. Copyright 2013 Springer Nature) (b) The relationship between the OER activity in alkaline solutions, defined by the potential at a 0.5 mA cm_{ox}^{-2} specific current density, and the O p-band center relative to the Fermi level for cobalt-based perovskite oxides including $PrBaCo_2O_{5+\delta}$ (PBCO), $HoBaCo_2O_{5+\delta}$ (HBCO), $SmBaCo_2O_{5+\delta}$ (SBCO), $GdBaCo_2O_{5+\delta}$ (GBCO), $La_{0.4}Sr_{0.6}CoO_{3-\delta}$ (LSC46), and $LaCoO_3$ (LCO). (Reprinted with permission from Ref. [45]. Copyright 2015 Royal Society of Chemistry)

2.4.2 Design strategies

In spite of the success in the establishment of activity descriptors, they appear to be not explicit enough in guiding catalyst design and could present a challenge in transforming into more practical design strategies toward active perovskite electrocatalysts. In practice, the activity of a perovskite catalyst can be increased by two means. One is to take into account the electronic effects, aiming to intrinsically increase the activity of each reactive site. This can be achieved by regulating the physical/chemical properties related to the perovskite electronic structures, such as composition, oxygen vacancy, and crystal structure. The other is to consider the geometric effects that can extrinsically increase the number of reactive sites. This involves the search for novel methods to synthesize perovskite nanostructures or composites. This section covers catalyst design strategies based on these parameters, with special attempts to illustrate how each parameter can be separately tuned in perovskites for improved electrocatalysis. Note that these parameters are actually correlated to one another. For instance, changing the composition could affect the oxygen vacancy or crystal structure [29]. Moreover, there are cases when the intrinsic and extrinsic activity can be increased simultaneously. One example is that downsizing the perovskite oxides could also bring about changes in their electronic structure [68]. Considering the huge quantity of perovskites that have been studied thus far, it appears to be impractical to mention them all and thus only typical examples are given here. Other catalyst design parameters, such as strain [69-71] and conductivity [52,71-74], can also influence the electrocatalytic performance of perovskites. However, they are not included here given that they are currently less explored.

2.4.2.1 Composition

Perovskite materials are known for their flexibility in chemical compositions. Elemental substitution on the A- or/and B-site can alter the electronic structure of the B-site transition metal, thereby modifying the electrocatalytic activity. Generally, a complex doped perovskite oxide can be described using the formula of $A_{1-x}A'_xB_{1-y}B'_yO_3$, where A′ and B′ represent the A- and B-site dopants at a doping level of x and y, respectively. For the A-site substitution, A′ is typically a rare-earth or an alkaline-earth metal. Hyodo et al. investigated the effect of rare-earth elements on the ORR activity of $LnMnO_3$ (Ln = lanthanides) in alkaline solutions, and found an activity order of La > Pr > Nd > Sm > Gd > Y > Dy > Yb, consistent with the decreasing order of the Ln^{3+} ionic radius [75]. Partial replacement of lanthanides by alkaline-earth metals can further change the catalytic performance. For example, the ORR activity of $Pr_{0.8}A'_{0.2}MnO_3$ (A′ = Ca, Sr, Ba) perovskites was reported to increase in the order of $PrMnO_3$ < $Pr_{0.8}Ba_{0.2}MnO_3$ < $Pr0_{.8}Sr_{0.2}MnO_3$ < $Pr_{0.8}Ca_{0.2}MnO_3$ [76]. The effects of A-site doping on the ORR activity were also observed in other perovskite systems, such as $La_{1-x}Ca_xMnO_3$ [77], $La_{1-x}Sr_xMnO_3$ [78,79], and $La_{1-x}Ca_xCoO_3$ [80]. Similar studies have also been conducted in the OER (e.g., $La_{1-x}Sr_xCoO_3$ [29,73,81], and $La_{1-x}Sr_xFeO_3$ [82]) and HER (e.g., $Pr_x(Ba_{0.5}Sr_{0.5})_{1-x}Co_{0.8}Fe_{0.2}O_{3-\delta}$ [42]).

Compared to the A-site doping, the B-site doping can more directly affect the catalytic activity of perovskite oxides because the B-site transition metal is considered the reactive site in conventional ORR/OER mechanisms. Sunarso et al. studied the influence of transition metals on the ORR activity of $LaBO_3$ (B = Cr, Mn, Fe, Co, and Ni) in alkaline media, and found that the diffusion-limited current density of the ORR decreases in the order of $LaCoO_3$ > $LaMnO_3$ > $LaNiO_3$ > $LaFeO_3$ > $LaCrO_3$ [83], analogous to that reported by Shao-Horn et al. [26]. For the B-site substitution, B′ can be a redox-active transition metal or a redox-inert element or both. For instance, partial substitution of Ni in $LaNiO_3$ with Fe [58] or Mg [57] could give rise to $LaNi_{0.8}Fe_{0.2}O_3$ or $LaNi_{0.85}Mg_{0.15}O_3$ with improved ORR activity. In particular, incorporating catalytically inactive components into the B-site can help tune the electronic structure of the original redox-active metal and thus contribute to enhanced catalytic performance. Notably, this aspect has been extensively studied on a multitude of perovskite systems involving a range of elements as dopants, such as Sc [84,85], Ti [86], Nb [50,84,87], Mo [87], W [88], Sn [89], Bi [85], Si [90], P [91-93], S [91].

Moreover, the accommodation of multiple dopants in the B-site can also alter the catalytic behavior [84,85,89]. For example, Xu et al. evaluated the OER activity of a series of iron and tin co-doped $BaCo_{0.9-x}Fe_xSn_{0.1}O_{3-\delta}$ (x = 0.2, 0.3, 0.4, denoted as BCFSn-721, BCFSn-631, and BCFSn-541, respectively) [89]. Having negligible variance in physicochemical properties like surface area, morphology, crystal structure, oxygen nonstoichiometry, and surface Co oxidation state, the $BaCo_{0.9-x}Fe_xSn_{0.1}O_{3-\delta}$ series offer a good activity comparison in terms of the concentration of different dopants. As shown in **Figure 2.5**, the OER activity increases with a higher amount of Co occupying the B-site. This indicates the intrinsically better OER performance of transition metal Co ions relative to Fe ions in a perovskite structure, similar to the finding observed on $SrB_{0.9}Ti_{0.1}O_{3-\delta}$ (B = Co, Fe) perovskites [86]. A much improved OER activity was also found on the most active $BaCo_{0.7}Fe_{0.2}Sn_{0.1}O_{3-\delta}$ compared to the non-doped and the Fe or Sn single-doped counterparts, suggesting that a synergistic effect of the two dopants may be at work.

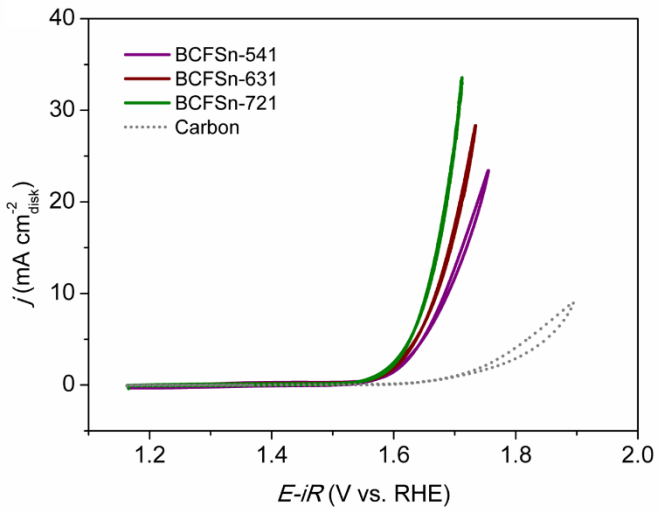

Figure 2.5 The OER activity of a series of $BaCo_{0.9-x}Fe_xSn_{0.1}O_{3-\delta}$ perovskites (x = 0.2, 0.3, 0.4, denoted as BCFSn-721, BCFSn-631, and BCFSn-541, respectively) evaluated by cyclic voltammograms in 0.1 M KOH solution. The negligible OER activity of a carbon background is shown for reference. (Reprinted with permission from Ref. [89]. Copyright 2015 John Wiley and Sons)

The effect of composition can be more complicated where both the A and B sites are doped with foreign elements [94-96]. In this scenario, a systematic investigation, more often case-by-case, is needed to study the relationship between composition and activity before locating an optimal composition. Apart from cation doping, the composition of perovskites can be further altered by introducing A-site cation deficiency [97-99]. For example, Zhu et al. synthesized several A-site-deficient $La_{1-x}FeO_{3-\delta}$ perovskites and obtained the optimal OER activity at a deficiency of x = 0.05 [97].

2.4.2.2 Oxygen vacancy

A stricter way of describing the formula of perovskite oxides would actually be $ABO_{3\pm\delta}$ because many perovskite oxides have an oxygen stoichiometry that deviates from the nominal value of 3. While the effect of oxygen excess (i.e., oxygen stoichiometry of $3+\delta$) in perovskites is merely studied in electrocatalysis, that of oxygen vacancy (i.e., oxygen stoichiometry of $3-\delta$) has attracted plenty of research interest. Mefford et al. found that the OER activity of the $La_{1-x}Sr_xCoO_{3-\delta}$ series correlated strongly with the oxygen vacancy concentration (δ), with the highest activity obtained on $SrCoO_{2.7}$ with the largest vacancy content (**Figure 2.6a**) [29]. Based on this, they proposed a lattice oxygen-mediated (LOM) OER mechanism that takes into consideration the involvement of lattice oxygen species and the role of surface oxygen vacancies (**Figure 2.6b**). The validity of this LOM mechanism was further supported by DFT modelling. Later, the participation of lattice oxygen in the OER was experimentally verified by in situ ^{18}O isotope labelling mass spectrometry [30]. Different from the classically studied mechanism which only concerns surface metal sites, the LOM mechanism considers the importance of transition metal–oxygen covalency in triggering the reaction [29,30]. These studies thus point to the critical role of oxygen vacancy, which cannot be ignored in the fundamental understanding of reaction mechanisms as well as the rational design of advanced perovskite electrocatalysts.

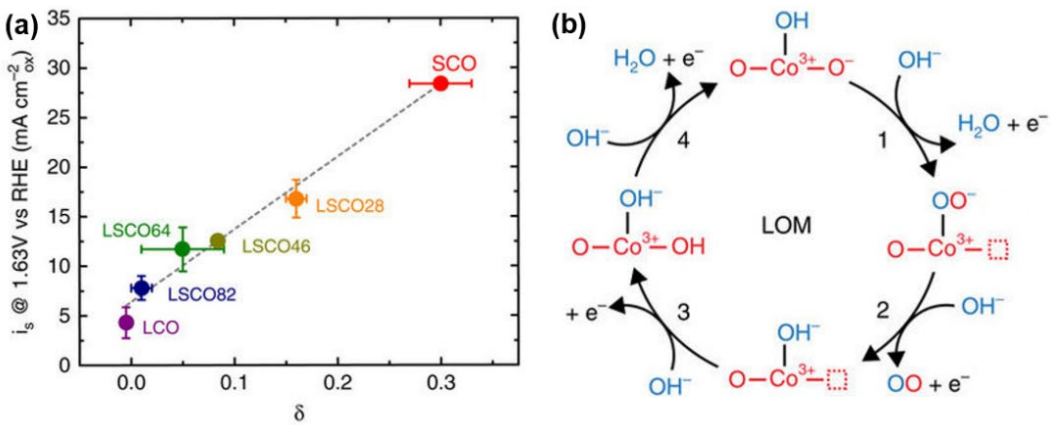

Figure 2.6 (a) Correlation of the OER activity of $La_{1-x}Sr_xCoO_{3-\delta}$ with the oxygen vacancy concentration (δ), where $La_{1-x}Sr_xCoO_{3-\delta}$ is denoted as LSCO(1−x)x, that is, LSCO82 for $La_{0.8}Sr_{0.2}CoO_{3-\delta}$. (b) Lattice oxygen-mediated (LOM) OER mechanism for perovskites in alkaline solutions. (Reprinted with permission from Ref. [29]. Copyright 2016 Springer Nature)

Normally, oxygen vacancy is inherent in most of the perovskite oxides, and often varies accordingly with any compositional change in order to maintain charge neutrality within the perovskite structure. For perovskites with a specific composition, there are generally two approaches to creating oxygen vacancy. One is to control the synthetic procedures, in which thermal reduction during the formation of perovskite crystallinity may be crucial to the generation of oxygen vacancy. For example, flame spray method was reported to synthesize BSCF perovskite with an oxygen deficiency up to ~0.75 [100], much higher than that synthesized from other methods such as sol−gel process ($\delta \approx 0.44$) [42] and solution combustion method ($\delta \approx 0.4$) [26]. The highly oxygen-deficient BSCF was found to show a 55-fold enhancement in the OER current density relative to the sol–gel produced BSCF. The other route to increase the amount of oxygen vacancy is to conduct post-treatment on an existing perovskite, typically via reduction in H_2 or vacuum. For instance, oxygen-stoichiometric $CaMnO_3$ was converted into oxygen-deficient $CaMnO_{2.5}$ (δ = 0.5) after a low-temperature reductive annealing process in 5% H_2/Ar while the orthorhombic crystal structure was preserved [51]. With the introduction of oxygen defects, $CaMnO_{2.5}$ displayed a significantly improved OER activity compared to $CaMnO_3$. Under a much harsher reductive treatment in vacuum, Chen et al. prepared $BaTiO_{3-\delta}$ perovskite with

abundant oxygen vacancies, showing enhanced performance in both the OER and ORR [101].

It should be noted, however, that increasing the number of oxygen defect sites does not necessarily lead to increased catalytic activity. This is because oxygen vacancy is not the sole factor that influences electrocatalysis. When oxygen vacancy changes, the metal electronic states (e.g., oxidation state and coordination) and metal–oxygen covalency change concomitantly. Wang et al. studied the HER activity of a series of H_2-redution treated $NdBaMn_2O_{6-\delta}$ double perovskites with various oxygen vacancy contents (δ = 0.35, 0.54, and 0.80) [102]. The best activity was obtained for the sample with a moderate oxygen vacancy of δ = 0.54, which they attributed to a combination of several factors including a distorted structure, a near-unity e_g occupancy, and an optimized O p-band center. This suggests that optimized catalytic activity may be achieved on perovskites with a moderate number of oxygen vacancy. A similar trending was also found in the $CaMnO_{3-\delta}$ perovskites ($0 < \delta \leq 0.5$) in the electrocatalysis of ORR/OER [103]. Therefore, caution needs to be exercised in the development of oxygen-deficient perovskite catalysts.

2.4.2.3 Crystal structure

The crystal structure of perovskite oxides, both bulk and surface, is closely related to the electrocatalytic activity. For a perovskite with a specific nominal composition, its bulk crystal structure can vary with the synthesis conditions. For example, heat-treating a $La_{0.7}Sr_{0.3}MnO_3$ precursor at 650, 750, and 850 °C led to the formation of tetragonal, cubic, and orthorhombic phase structure, respectively [104]. Electrochemical measurements indicated that the tetragonal $La_{0.7}Sr_{0.3}MnO_3$ exhibited the highest ORR activity. Another way to alter the bulk crystal structure is via post-treatment. For instance, crystalline $LaNiO_{3-\delta}$ perovskite, which has a rhombohedral phase at room temperature, transformed into a cubic-phase $LaNiO_{3-\delta}$ after being quenched from 800 °C to room temperature [105]. Such a phase transition contributed to a significant improvement in the ORR/OER catalytic activity. Apart from the quenching process, reductive annealing in H_2 can also change the perovskite bulk structure. In this respect, a cubic-phase $Pr_{0.5}Ba_{0.5}MnO_{3-\delta}$ perovskite was reported to convert into a tetragonal-phase $PrBaMn_2O_{5+\delta}$ layered perovskite after H_2 treatment, showing greatly enhanced activity toward both the ORR and OER [106].

While conventional research has mostly focused on crystalline perovskites for electrocatalysis, it has recently been shown that amorphous perovskites also exhibit considerable catalytic performance. For example, Trudel and co-workers developed a photochemical thin-film deposition technique to synthesize a series of amorphous perovskite oxides such as $LaCoO_{3-\delta}$ [107], $La_{0.7}Ca_{0.3}CoO_{3-\delta}$ [108], and BSCF [109], all showing favorable OER activity. In addition, magnetron sputtering deposition was used by Chen et al. to obtain amorphous BSCF nanofilms with exceptional OER performance [110]. The good catalytic activity may originate from the coordinately unsaturated surface metal sites of amorphous perovskites [111]. More research efforts are required to gain a better understanding of the origin of the catalytic activity of perovskite materials with an amorphous structure.

The surface crystal structure of perovskite materials can also influence the electrocatalytic performance. BSCF perovskite, which was crystallized from a conventional sol–gel process by calcination at 950 °C for 5 h, was found to have a surface amorphous oxide layer with a thickness of around 20 nm [112]. After heat-treatment in argon (Ar) atmosphere, this amorphous layer gigantically grew to a thickness of 180–200 nm, deactivating the catalytic performance of BSCF toward the ORR. However, a same Ar-treatment to pristine $Ba_{0.5}Sr_{0.5}Co_{0.2}Fe_{0.8}O_{3-\delta}$ with also a ≈20 nm thick amorphous layer did not lead to further amorphization while offering an increased amount of oxygen vacancy, which resulted in a notable improvement in ORR activity. This suggests a composition-dependent behavior upon treatment in Ar between the changes in perovskite surface structure and catalytic activity.

The surface crystal structure of perovskites with an identical composition can differ with the calcination conditions. For example, the BSCF perovskite calcined at 1050 °C for 5 h exhibited a nanoscale-thick spinel-phase layer between the bulk particle and the amorphous layer on the outermost surface [113]. This spinel layer could be removed by an oxygenation process via heat-treatment in oxygen atmosphere (**Figure 2.7**), giving rise to enhanced ORR/OER performance of the BSCF catalyst.

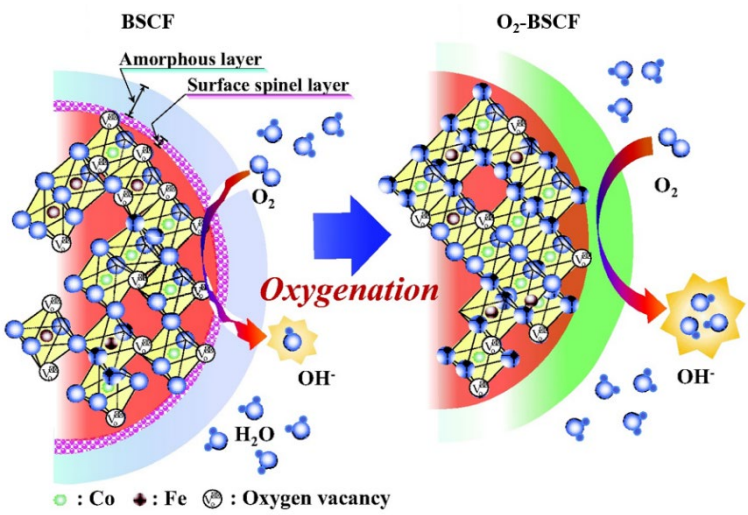

Figure 2.7 A schematic representation of the effect of heat treatment in oxygen on the BSCF perovskite. (Reprinted with permission from Ref. [113]. Copyright 2014 John Wiley and Sons)

These studies highlight the tunability of perovskite structures in both the bulk and surface, which is achieved using experimental procedures that are performed ex situ. It should also be noted that perovskite structures can undergo in situ changes under realistic electrochemical conditions. For example, the structure transformation from $BaNiO_3$ to $BaNi_{0.83}O_{2.5}$ over the OER testing in alkaline media led to an improved catalytic performance [114]. To some extent, this is more of a stability issue, and thus will be discussed later in more detail in the section of stability concerns.

2.4.2.4 Nanostructure

Previous understanding of the electrocatalytic role of perovskites is mainly gained from bulk-sized materials, which are prepared from conventional sol–gel process [115], solid-state reaction [116], and high-pressure synthesis [117]. These bulk perovskites normally have a large particle size, a small surface area, and a featureless morphology, which can only offer limited catalytic capability. This is because a substantial proportion of inactive atoms in the bulk of perovskites are often not catalytically active toward reactions occurring at the surface. To address this issue, nanostructuring has been proposed as a technically viable approach [14]. Once a perovskite material is downsized to the nanoscale, an increase in surface area and also the number of reactive

sites can be expected. Although a linearly increased number of reactive sites may not be necessarily achievable considering the accessibility issue of reactive sites, the increase in surface area does provide a greater number of reactive sites, thus contributing to an improved catalytic activity, more often on a catalyst mass basis. This has already been proved by the increased OER activity observed on the ball-milled BSCF catalyst [26], which has a particle size much reduced compared to the bulk BSCF.

Perovskite nanostructures can be attained by tailoring the synthetic parameters of conventional preparation methods. For example, Cho and co-workers developed an intriguing pattern of perovskite phase existence and particle growth by altering the calcination temperatures and lanthanum-dopant concentrations during the sol–gel synthesis of $La_x(Ba_{0.5}Sr_{0.5})_{1-x}Co_{0.8}Fe_{0.2}O_{3-\delta}$ perovskites [118]. At a reduced temperature calcination of 700 °C and a La doping content of x = 0.7, $La_{0.7}(Ba_{0.5}Sr_{0.5})_{0.3}Co_{0.8}Fe_{0.2}O_{3-\delta}$ perovskite with a particle size as small as 50 nm was obtained, showing a substantial improvement in the alkaline ORR/OER activity. This approach, however, requires the perovskite A-site to contain a lanthanide component, and thus may not be broadly extended to other perovskite oxides. Alternatively, a range of synthetic methods have been used to synthesize nanostructured perovskites, including precipitation method, hydrothermal synthesis, templating approach, and electrospinning [14]. In addition, several deposition-based techniques, such as physical vapor deposition (PVD), chemical vapor deposition (CVD), and electrodeposition, have also been developed to fabricate nanosized perovskite materials. The as-obtained perovskites possess plenty of morphological features, including nanowire [119], nanofiber [120], nanorod [121], nanotube [122], nanosphere [123], nanocube [124], among others. These morphologies can lead to the different catalytic behaviors of nanostructured perovskites. For instance, compared to $LaCoO_3$ dense particles synthesized by a sol–gel route, $LaCoO_3$ porous particles and hollow nanospheres synthesized by a hydrothermal method showed an increased OER activity in an alkaline electrolyte (**Figure 2.8**).

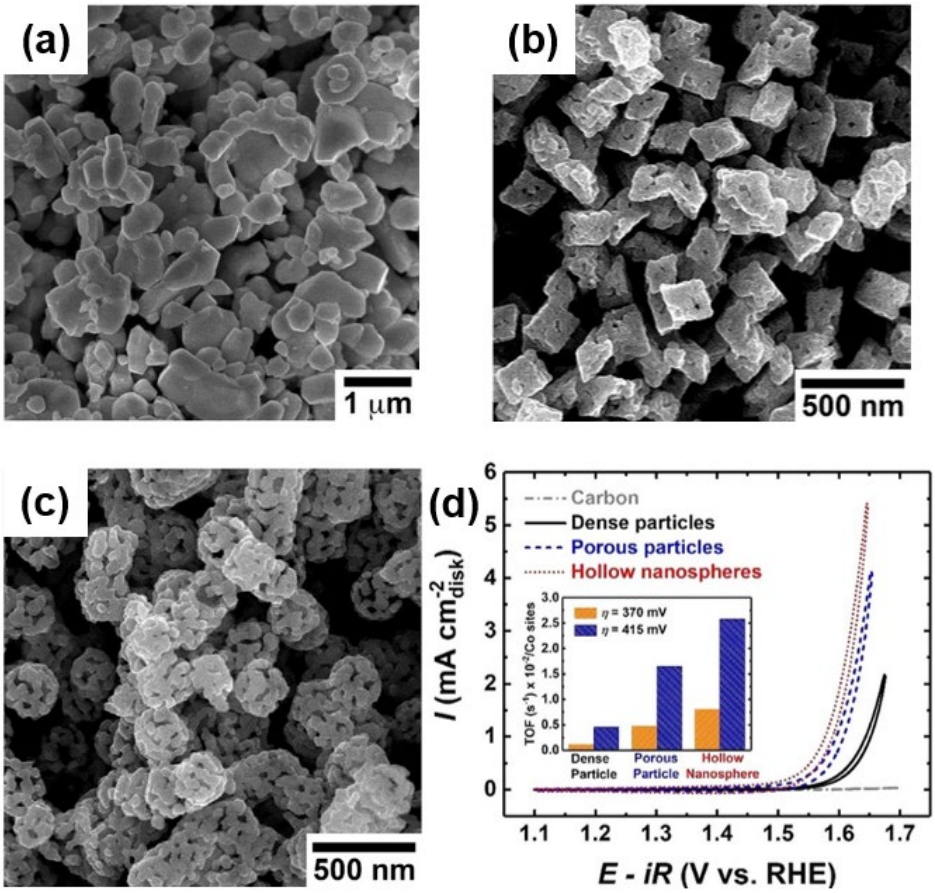

Figure 2.8 Scanning electron micrographs of $LaCoO_3$ (a) dense particles, (b) porous particles, and (c) hollow nanospheres. (d) The OER activity of $LaCoO_3$ dense particles, porous particles, and hollow nanospheres evaluated by cyclic voltammograms in 0.1 M KOH solution. (Reprinted with permission from Ref. [123]. Copyright 2017 American Chemical Society)

Note that the improved catalytic performance of nanostructured perovskites may not be just a surface area effect. While $LaCoO_3$ porous particles and hollow nanospheres had a higher surface area than the dense particles, their increased OER activity was also attributed to the presence of amorphous surface structures formed during the hydrothermal synthesis [123]. Moreover, nanostructuring can further bring about a nanosize effect, that is, reducing the nanostructure size can tune the electronic state of perovskites. For example, Zhou et al. obtained $LaCoO_3$ nanoparticles with sizes of 60, 80, and 200 nm, and bulk $LaCoO_3$ particles by annealing a sol–gel precursor at 600, 700, 800, and 1000 °C, respectively [68]. Surprisingly, the best OER activity was

observed on the 80 nm $LaCoO_3$, which was ascribed to its optimal e_g filling of Co ions (~1.2) based on Shao-Horn's activity descriptor [26]. The nanosize effect can still be at play when the perovskite size is further reduced. For instance, Zhao et al. found that the OER activity of an electrospun double perovskite nanofiber with a diameter as low as 20 nm is intrinsically higher than those with larger diameters, which was presumably due to the favorable surface electronic structure and the possible presence of heterostructures [125]. It is therefore important to understand the electrocatalytic processes on nanostructured perovskites, both experimentally and theoretically. Such understanding, combined with that gained from bulk perovskite materials, can better guide the development of improved perovskite electrocatalysts.

2.4.2.5 Composite

Forming composites with other materials, including carbons, metals, and metal oxides, among others, can also extrinsically increase the catalytic activity of perovskite materials. In particular, perovskite/carbon composites have attracted the most research interest [126]. The inclusion of carbon into a perovskite oxide was first used to remove any possible electrical conductivity limitations within some intrinsically insulating or semiconducting perovskites [127]. However, recent investigations have suggested that carbon could serve more than just the role of a conductive support [128-134]. For example, in the electrocatalytic ORR, carbon in perovskite/carbon composites was found to participate in the ORR mechanistic pathway by catalyzing the reduction of O_2 to HO_2^- [128-133]. In addition, carbon could act as a reducing agent to modify the electronic structure of perovskites. For example, acetylene black (a type of conductive carbon), when composited with BSCF, was found to reduce the cobalt cations to a lower oxidation state, which contributed to a greatly improved ORR/OER activity [134]. These observations highlight the important roles of carbon in perovskite/carbon composites, which can be utilized to design improved perovskite-based hybrid catalysts.

Perovskite/carbon composites can be simply obtained using physical mixing, showing enhanced bifunctional activity toward the ORR and OER [135-138]. A more intimate combination between perovskites and carbons is expected to further improve the ORR/OER bifunctionality. This can be realized by means of advanced chemical synthesis, such as the CVD process [139-143], hydrothermal method [144,145], and

electrospinning [146]. However, due to the inherent incompatibility between the reductive carbon materials and the oxidative perovskite oxides, it remains challenging to obtain perovskite/carbon composites with a pure-phase perovskite component. For instance, the perovskite structure may not be preserved during the high-temperature CVD process [143]. To address this, modification to the current synthetic conditions are required. In addition, novel fabrication techniques should be developed to synthesize intact perovskite/carbon composites to achieve improved electrocatalysts.

Understanding the origin of enhanced catalytic activity on perovskite/carbon composites is important to the rational design of efficient perovskite catalysts. While conventional research has pointed to a "synergistic effect" between the perovskite and carbon, that is, two is better than one, it does not clarify the true reason behind the improved activity. Recently, Zhu et al. proposed three possible origins to explain the increased activity observed on perovskite/carbon composites (**Figure 2.9**) [126]. First, the ligand effect at the interface can modify the electronic structure and thus lead to increased activity as mentioned earlier [134]. Second, the formation of interfacial heterostructures, in the form of covalent bonds or a new phase, can contribute to enhanced catalytic activity. This can be understood from the fact that strongly coupled perovskite/carbon composites made from chemical synthesis outperformed not only each individual component but also their physical mixtures. Third, the spillover effect can be at work for the improved bifunctionality of perovskite/carbon composites. In the composite, perovskites are considered to be more active toward the OER whereas carbons are more active toward the ORR. During the ORR process, the OH^- generated on the carbon surface spills over to the perovskite surface, which promotes the ORR by releasing more reactive sites on the carbon surface, leading to increased ORR activity. In a similar way, during the OER process, O_2 produced on the perovskite surface spills over to the carbon surface, which facilitates the OER by releasing more reactive sites on the perovskite surface, giving rise to enhanced OER activity.

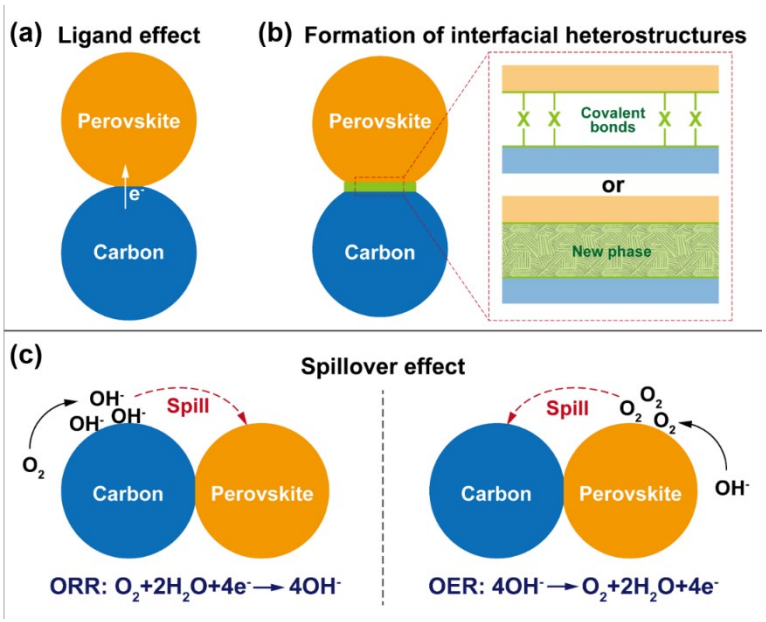

Figure 2.9 A schematic illustration of three possible origins that may clarify the improved activity on perovskite/carbon composites. (a) Ligand effect. (b) Formation of interfacial heterostructures. (c) Spillover effect. (Reprinted with permission from Ref. [126]. Copyright 2017 John Wiley and Sons)

Despite the contribution to improved electrocatalysis, perovskite/carbon composites might suffer from carbon corrosion, a common issue for carbon-based materials especially in the case of the OER. This issue, although less severe in alkaline media as compared to acidic media [147], can still lead to the reduction of reactive sites and even degradation of catalysts under elevated potentials during the OER testing. One way to mitigate the carbon corrosion is by using graphitized carbon or nitrogen-doped carbon with improved corrosion resistance [148,149].

Very recently, perovskites have also been hybridized with other conducting substrates, for example, Ni foam, via advanced synthetic methods such as hydrothermal method [150] and electrodeposition [151]. Similarly, due to the reductive nature of Ni foam, the difficulty in fabricating perovskite/Ni foam composites lies in the acquisition of pure oxidative perovskites in a high-temperature annealing process. Annealing under nonoxidative atmosphere can stabilize the Ni foam while also facilitating the formation of a perovskite phase if the precursor of perovskites is finely tuned. For example, Li et al. used electrodeposition to deposit a perovskite hydroxide precursor on Ni foam,

which could convert into crystallized perovskite oxide upon a moderate annealing treatment in Ar [151]. Taking advantage from both the catalytically active perovskites and the 3D porous, highly conductive Ni foam, perovskite/Ni foam composites possess great potential in practical applications.

In addition to forming composites with conductive materials, perovskites can also be coupled with metal nanoparticles. Such hybrid materials are often synthesized by exsolution, a chemical process that is almost exclusive to perovskite oxides. Under heat treatment in a reductive atmosphere (e.g., H_2), an active metal initially incorporated in the perovskite lattice can go through a reduction process and then exsolve in the form of metal nanoparticles on the surface of the perovskite [152]. These metal nanoparticles can act as additional catalytic sites while also changing the original perovskite electronic structure, thus leading to a different behavior in electrocatalysis. For example, Ni nanoparticle-decorated $La_{0.4}Sr_{0.4}Ti_{0.9}O_{3-\delta}$ composite, which was constructed from the $La_{0.4}Sr_{0.4}Ti_{0.9}Ni_{0.1}O_{3-\delta}$ parent perovskite using a facile exsolution process, can synergistically catalyze the alkaline HER at a significantly improved efficiency [153]. In the hybrid catalyst, $La_{0.4}Sr_{0.4}Ti_{0.9}O_{3-\delta}$ facilitates water dissociation whereas Ni nanoparticles favors hydrogen adsorption for the recombination into H_2. In a similar fashion, a Ag nanoparticle-modified $(PrBa)_{0.95}Mn_2O_{5+\delta}$ double perovskite obtained from exsolution exhibited favorable ORR activity in alkaline electrolytes, which is due likely to the strong coupling between the perovskite and Ag nanoparticles [154]. Apart from metal nanoparticles, other nanomaterials, such as metal alloys [155-158], metal/metal oxide hybrids [159,160], can also exsolve from the perovskite lattice by carefully tuning the perovskite composition and H_2-reduction condition. These advantages of the exsolution process can bring about ample opportunities for making perovskite derived composites with increased electrocatalytic performance.

Other catalytically active materials, such as hydroxides [161] and metal oxides [162-165], can also composite with perovskite oxides using either an infiltration process or chemical synthesis. These composite materials showed enhanced catalytic performance with respect to the sole perovskite component. To obtain optimized activity, both the perovskite oxide and the additive functional material should be cautiously selected. For example, BSCF, which is considered the benchmark perovskite OER catalyst, was composited with the benchmark ORR catalyst, commercial Pt/C, and obtained a substantially improved catalytic activity in both the

ORR and OER [166]. However, these two components were physically mixed, which may not be able to unleash the full potential of their high activity. Future efforts should be devoted to the design of strongly coupled perovskite-based materials, either through experimentally developed synthetic methods or through theoretically established modelling approaches.

2.4.3 Stability concerns

Compared to the significant advances in the establishment of design principles for improvement in catalytic activity, much less attention is placed on the stability of an electrocatalyst, which is actually of more relevance to realistic device-based applications. This is especially the case when it comes to perovskite OER catalysts. Even under ambient conditions, most of perovskite oxides will become amorphous during the OER, which is often accompanied by the leaching of A- or B-site cations into the electrolyte. For instance, amorphization was observed in the bulk and surface of highly active perovskite catalysts (e.g., BSCF), leading to the structural evolution from corner-sharing octahedra to edge-sharing octahedra [167,168]. This phenomenon is more pronounced near the catalyst surface region than in the bulk, as evidenced from ex situ X-ray absorption spectroscopic measurements (XAS) [168].

Understanding the changes occurring at the catalyst surface is therefore critical for the design of enduring perovskite electrocatalysts. This can be partially achieved through an improved understanding of the interaction between perovskite oxides and water electrolytes under a modelling system similar to the OER. For example, using in situ environmental transmission electron microscopy, Shao-Horn et al. observed structural oscillations on BSCF upon its interaction with water vapor under electron irradiation [169]. A more direct and viable way to access the changes on perovskite oxides is to use operando XAS measurements during realistic OER conditions, which was first reported by Fabbri and co-workers. **Figure 2.10** shows an anodic polarization of a flame spray-synthesized BSCF nanocatalyst (BSCF-FS), where shift of the Co K-edge position, which was extracted from operando X-ray absorption near-edge structure (XANES) spectra, is recorded in line with the OER current [100]. It is noticeable that upon the onset of the oxygen evolution at 1.425 V versus the reversible hydrogen electrode (RHE), the Co K-edge shifts toward higher energy, corresponding to an increase in the Co oxidation state. Such change was not observed in a reverse cathodic

polarization scan, indicating that the oxidation of Co is mostly an irreversible process. Further operando extended X-ray absorption fine-structure (EXAFS) tests revealed the formation of a self-assembled surface layer consisting of OER-active metal (oxy)hydroxides, which is considered to be the origin of the significantly enhanced OER performance (in both activity and stability) based on an OER mechanism coupled with lattice oxygen participation.

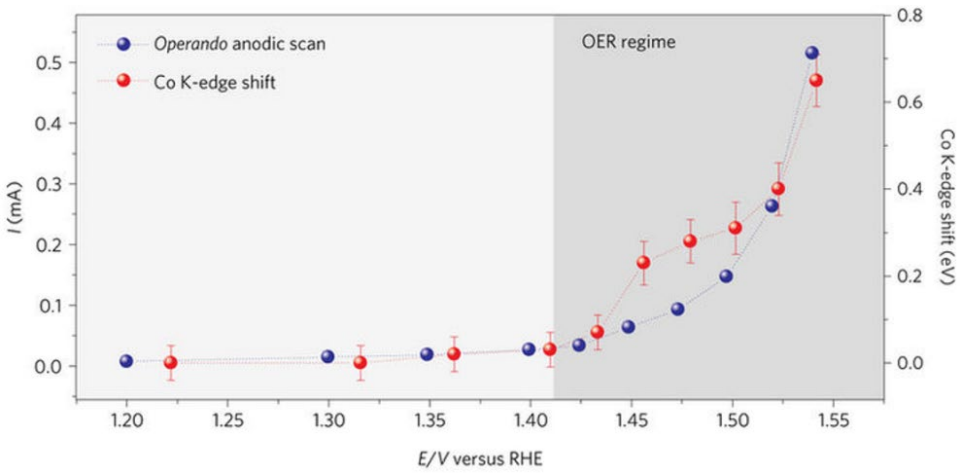

Figure 2.10 OER current and shift of the Co K-edge position (taken from Operando XANES spectra) collected in situ during an anodic polarization of the BSCF-FS perovskite catalyst in 0.1 M KOH alkaline solution. (Reprinted with permission from Ref. [100]. Copyright 2017 Springer Nature)

These operando observations point to an important conclusion with respect to both catalyst activity and stability. Active perovskite OER catalysts can experience drastic changes in local chemical/electronic structures. This is substantially different from the previously mentioned activity descriptors which rely on ex situ physical properties (e.g., e_g-filling number) to guide catalyst design. On the other hand, a perovskite oxide initially considered to be 'instable' could actually evolve into a 'stable' catalyst through operando changes, in which case the original perovskite can be seen as a 'precursor' (or 'pre-catalyst') of a real active catalyst [100]. A similar phenomenon was also found in acidic electrolytes on a $SrIrO_3$ perovskite, which transformed in situ during electrochemical testing into a highly active and stable $IrO_x/SrIrO_3$ catalyst [170].

It is noteworthy that the extent of changes on perovskite surfaces varies with different materials compositions and chemistries, which may relate to the different concentrations of oxygen vacancy in perovskites [100]. Shao-Horn et al. has earlier correlated the computed O p-band center with the perovskite stability under alkaline OER conditions, and arrived at the conclusion that an optimum position of the O p-band center leads to high catalyst stability [46]. It is also important to note that not all perovskites are capable of evolving into active and durable catalysts. For example, several nickel-based and iron-based perovskite materials were found to lose activity upon prolonged OER tests under alkaline media [82,171]. Based on these considerations, a case-by-case investigation into the stability (and activity) of a specific perovskite material can be necessary in the evaluation of its electrocatalytic performance.

Sometimes the stability issue is of more interest to the industry than to the academia. The research community currently tends to report 'stable' perovskite catalysts, more often simply from the viewpoint of electrochemical stability, without looking further into the catalyst structure either ex situ or in situ. Also, the catalyst degradation phenomena under OER testing and their origins are less explored [172-174]. In industrial settings, more rigid requirements are placed on the catalyst stability. For instance, the alkaline water electrolysis would require a catalyst to stably operate at temperatures of around 80 °C, under which condition perovskite OER catalysts may undergo changes even harsher than those at room temperature. To bridge this gap between the fundamental and applied research, more efforts should be devoted to understanding the changes in perovskites (e.g., degradation mechanisms) during the OER, which will also aid the establishment of an improved catalyst design principle that combines both catalytic activity and stability. The same holds true for perovskites in the ORR and HER electrocatalysis, although attention to these fields is still lacking.

2.5 Perovskite materials for electrocatalysis-related applications

The ORR/OER reactions are technologically relevant to metal–air batteries, whereas the OER/HER reactions hold key to the overall efficiency of a water electrolyzer. Over the years, a plethora of perovskite materials have been used in these devices [14,175]. While conventional mechanistic understanding of electrocatalysis is gained mostly from bulk perovskite materials, they may not favor practical applications because of

their rather low catalytic activity, which is due to their huge particle sizes, low surface areas, and few morphological features. Comparatively speaking, nanosized and nanostructured perovskites are more suited for practical use because they offer increased reactive sites, improved accessibility of reactive sites, and better diffusion of gas reactants/products. In addition, the cost of an electrocatalyst can be more of concern for real-world devices. Also of importance is the catalyst stability, and very often a compromise has to be made between stability and activity. This section discusses the use of perovskite nanocatalysts made of Earth-abundant elements in metal–air batteries and water electrolyzers.

2.5.1 Metal–air batteries

Metal–air batteries are efficient energy conversion devices that can offer a theoretical specific energy even higher than that of the commercially available Li-ion batteries [176]. In general, a metal–air battery is composed of a metal anode, an electrolyte, and an air cathode. Among various anode candidates, Li and Zn are two of the most widely studied anode materials. The corresponding metal–air batteries are typically referred to as Li–air batteries and Zn–air batteries, respectively. Despite a major difference in electrolyte (i.e., normally nonaqueous electrolyte for Li–air batteries and aqueous electrolyte for Zn–air batteries), these two types of metal–air batteries suffer from one common scientific issue, that is, the slow kinetics of the ORR/OER reactions that determine the overall energy efficiency. At the cathode of a metal–air battery, oxygen is reduced upon discharge (ORR) and is evolved upon charge (OER). Therefore, an efficient, rechargeable metal–air battery would necessitate a bifunctional electrocatalyst that promotes both the ORR and OER.

Porosity is an important factor for achieving the practical use of perovskite catalysts in metal–air batteries. Zhang and co-workers reported the application of a three-dimensionally ordered macroporous $LaFeO_3$ perovskite (3DOM-LFO) as a cathode catalyst in a nonaqueous Li–air battery (**Figure 2.11a**) [177]. The 3DOM-LFO catalyst had an interconnected, well-ordered, honeycomb-like pore structure (**Figure 2.11b**), which was inherited from the polystyrene sphere template during a templating synthesis. Such a porous nanostructure could facilitate the diffusion of O_2/electrolyte during discharge/charge processes while offering significantly enhanced surface area for catalytic ORR/OER reactions, both contributing to improved performance and

cycle stability of the rechargeable Li–air battery compared to the nanoparticulate $LaFeO_3$ catalyst. Porous one-dimensional (1D) nanostructures possess high surface-to-volume ratios and abundant porosity, which can favor the availability of catalytic sites as well as the diffusion of O_2 gas when used as cathode catalysts for Li–air batteries. For example, a porous nanotubular $La_{0.75}Sr_{0.25}MnO_3$ perovskite fabricated by electrospinning was found to show a significant increase in both ORR/OER electrocatalysis and battery performance in a nonaqueous electrolyte [178]. Another useful way to obtain a porous cathode catalyst is via the growth of perovskites on 3D porous substrates (e.g., Ni foam). Pham et al. used hydrothermal synthesis to grow perovskite $LaNi_{0.9}Cu_{0.1}O_3$ nanosheet arrays on the surface of a 3D microporous Ni foam [150]. This composite was directly applied as a binder-free cathode, and exhibited notable ORR/OER activity and cycling performance in a nonaqueous Li–air battery.

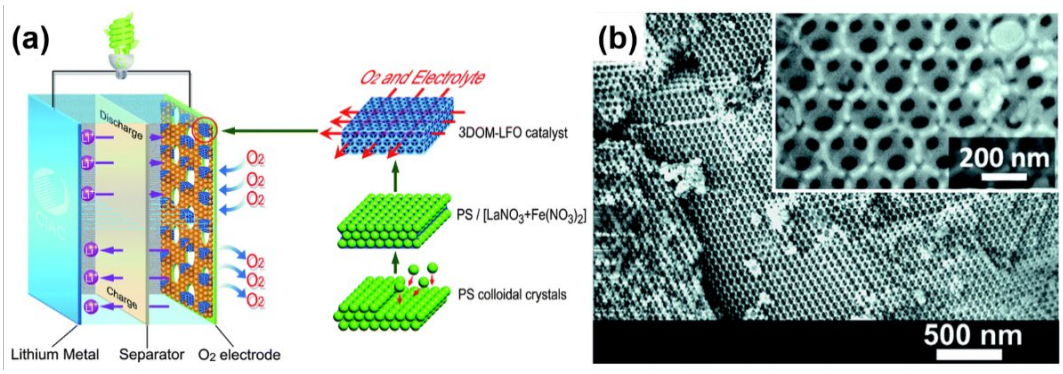

Figure 2.11 (a) A schematic representation of the synthesis of a 3DOM-LFO perovskite and its application as a cathode catalyst in a rechargeable Li–air battery. (b) Scanning electron micrographs of the 3DOM-LFO catalyst, showing an interconnected, well-ordered, honeycomb-like pore structure. (Reprinted with permission from Ref. [177]. Copyright 2013 Royal Society of Chemistry)

It should be noted that the oxygen electrocatalysis in nonaqueous Li–air batteries, which follows the reaction of $O_2 + 2Li^+ + 2e^- \leftrightarrow Li_2O_2$, is quite different from that in aqueous solutions. Therefore, the design principles for advanced perovskite catalysts working in alkaline water may not be able to extend to the system of nonaqueous Li–air batteries. Despite the success of several perovskite nanocatalysts, little understanding is gained about the reaction mechanisms in nonaqueous electrolytes.

While some attempts were made to evaluate the ORR/OER in nonaqueous solutions [119,124,150,177,178], more systematic investigations, rather than trial-and-error approaches, are needed in order to design better perovskite catalysts for nonaqueous Li–air batteries. By contrast, Zn–air batteries commonly adopt an aqueous alkaline electrolyte considering the stability of zinc anode and the manufacturing cost of the battery configuration. Although a higher concentration of potassium hydroxide solution (e.g., 6 M KOH) is used in Zn–air batteries, the oxygen electrocatalysis at the cathode follows the same reaction of $O_2 + 2H_2O + 4e^- \leftrightarrow 4OH^-$ as that in fundamental research. Therefore, the conventionally studied ORR/OER on perovskite materials in alkaline media is considered more relevant to the application in Zn–air batteries.

Recent years have witnessed the development of a myriad of perovskite nanomaterials for use in Zn–air batteries. Among the many candidates, perovskite/carbon composites have received more research attention, due primarily to their significantly increased electrical conductivity compared to the sole perovskites. For instance, a $LaNiO_3$ nanorod/reduced graphene oxide hybrid synthesized using a hydrothermal method showed much enhanced conductivity relative to the $LaNiO_3$ nanorod, thereby leading to higher ORR/OER activity in alkaline solutions and also better cycle performance in rechargeable Zn–air batteries [144]. Prabu et al. reported perovskite $LaTi_{0.65}Fe_{0.35}O_{3-\delta}$ nanoparticles embedded both at the surface of and within nitrogen-doped carbon nanorods, which were prepared via electrospinning followed by calcination under Ar atmosphere [146]. Compared to $LaTi_{0.65}Fe_{0.35}O_{3-\delta}$ nanotubes without carbon, which were obtained after calcination under air, the $LaTi_{0.65}Fe_{0.35}O_{3-\delta}$/carbon nanocomposite afforded increased catalytic sites, improved electrical conductivity, and highly promoted kinetics toward both the ORR and OER, resulting in an exceptionally higher Zn–air battery performance.

Although the above-mentioned perovskite/carbon composites can give rise to an improvement in Zn–air battery performance, they are produced at a small scale using bench-based hydrothermal method or electrospinning technique, which may present a hurdle toward their widespread application. Recently, CVD has emerged as a versatile process to achieve scaled-up production of nanohybrids of perovskites and carbons (especially carbon nanotubes (CNTs)), in which transition-metal-containing perovskites are applied as substrates for the catalytic growth of CNTs. Chen and co-workers reported the CVD synthesis of a core–corona structured bifunctional catalyst

(CCBC) and its application as a cathode catalyst in a rechargeable Zn–air battery (**Figure 2.12a**) [139]. This CCBC composite is comprised of a highly OER-active $LaNiO_3$ derived core component and a highly ORR-active nitrogen-doped CNTs (NCNTs) corona with a bamboo-like structure (**Figure 2.12b**). Owing to the strong coupling effect between these two active components, an optimized CCBC-2 catalyst, which was obtained by tuning the CVD synthetic parameters, exhibited outstanding discharge and charge performance comparable to that of the benchmark catalysts in the ORR (i.e., Pt/C) and OER (i.e., $LaNiO_3$) (**Figure 2.12c**). In addition, the CCBC-2 catalyst showed excellent cycling stability for 75 charge–discharge cycles (**Figure 2.12d**). Using a similar CVD method, the same researchers also obtained an intertwined core–corona structured bifunctional catalyst composed of $LaNiO_3$ nanoparticles encapsulated by NCNTs, showing bifunctionality toward the ORR/OER in rechargeable Zn–air batteries [140]. The CVD process was further extended to the synthesis of perovskite/CNTs composites involving other perovskite oxides, such as $LaMn_{0.9}Co_{0.1}O_3$ [141] and $La_{0.5}Sr_{0.5}Co_{0.8}Fe_{0.2}O_3$ [142], and good Zn–air battery performance was achieved. However, the physcial origin of the catalysts' high activity and stability is less understood. Moreover, the crystalline structure of the perovskite oxides might be destroyed after the CVD synthesis because of the presence of carbon serving as a reducing agent [143], which calls for more research inputs into the preparation of intact perovskites hybridized with conductive carbons.

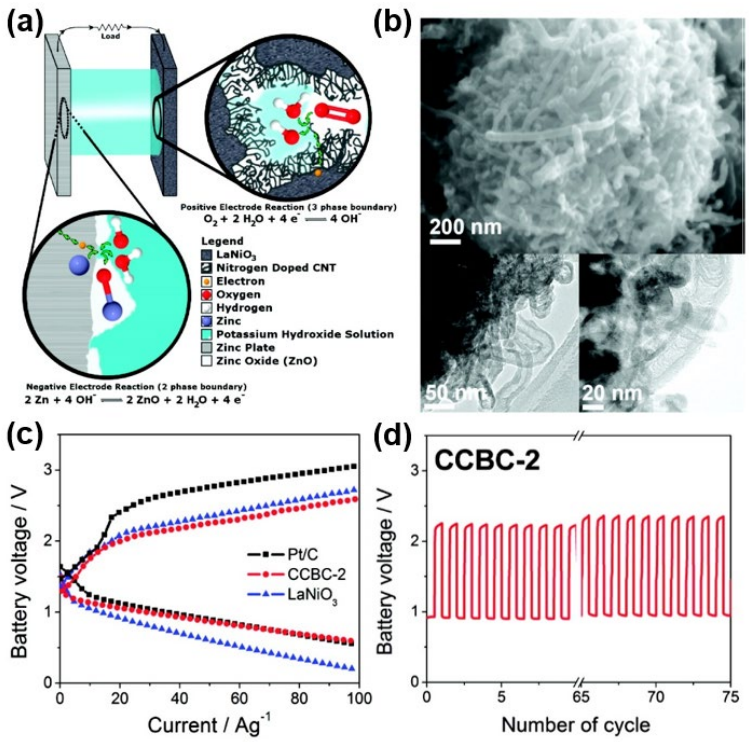

Figure 2.12 (a) A schematic representation of a Zn–air battery and the reactions taking place on the electrodes. (b) Scanning electron micrograph and transmission electron micrograph images of the CCBC catalyst. (c) Discharge and charge polarization curves of the CCBC-2 catalyst in comparison to Pt/C and $LaNiO_3$. (d) Charge–discharge cycling performance of the CCBC-2 catalyst. (Reprinted with permission from Ref. [139]. Copyright 2012 American Chemical Society)

While much progress has been made experimentally in fabricating perovskite catalysts for metal–air batteries, theoretically less is known about the relationship between structure, morphology, and performance under operational conditions. This gap has to be bridged if perovskites are to be developed as practical electrocatalysts in real-world batteries. Stability remains to be another concern. Currently, lab-based metal–air batteries that adopt perovskite cathode catalysts can only sustain around 100 cycles of charge–discharge tests, which is far from the requirement of battery technologies. Another long-term goal would be to develop metal–air batteries that can work in ambient air [179], as the present catalyst performance is recorded in laboratory pure oxygen environment. This, however, could take more efforts from scientists, engineers, and the industry.

2.5.2 Water electrolyzers

A water electrolyzer is one of the simplest systems for generating high-purity hydrogen. It is also a key component for the 'indirect' solar-to-hydrogen production, converting the electricity generated from renewable solar energy (via solar panels) into chemical energy in hydrogen [180]. In water electrolysis, water is split into hydrogen and oxygen following the equation of $H_2O \rightarrow H_2 + 1/2O_2$. This reaction is a thermodynamically uphill process that necessitates an energy input of 286 kJ mol^{-1} at room temperature and pressure, corresponding to a theoretical minimum cell voltage of 1.23 V. However, the two half reactions of water splitting, namely the OER at the anode and the HER at the cathode, have sluggish kinetics and can cause large energy losses. For example, commercial water electrolyzers generally operate at a much higher cell voltage of 1.8–2.0 V [181]. The implementation of the water electrolysis technology would thus require highly active and stable OER/HER electrocatalysts to lower the large water-splitting overpotentials and to make the whole process more energy-efficient. While the state-of-the-art Ir-/Ru-based compounds [4] and Pt-group metals [3] offer the highest OER and HER activity, respectively, they suffer from low Earth abundance and high capital cost, hampering their commercial viability. It is thus appealing to develop perovskite materials as alternatives that contain Earth-abundant, low-cost transition metals while still offering high catalytic activity. In addition, industrial electrolyzers work in strong alkaline electrolytes in order to avoid the corrosion from acids and reduce the total cost [182], where perovskites appear to be readily suited given the fundamental understanding of their electrocatalytic roles in alkaline media.

Ever since the first report by Xu. et al. [42], showing that perovskite oxides can catalyze the HER in basic solutions, several works have focused on using perovskites as bifunctional catalysts toward both the HER and OER and the overall water splitting. A typical example was given by Zhu et al. [183], who reported the electrospinning synthesis of perovskite $SrNb_{0.1}Co_{0.7}Fe_{0.2}O_{3-\delta}$ nanorods (SNCF-NR) and their application as HER/OER catalysts in an alkaline water-splitting cell (**Figure 2.13a**). Owing to the porous 1D nanostructure, SNCF-NR showed significantly enhanced HER and OER activity compared to the bulk-sized SNCF. When loaded on a Ni foam substrate (mass loading: 3 mg cm^{-2}) and used as the cathode and anode in a water electrolyzer containing 1 M KOH electrolyte, the SNCF-NR//SNCF-NR couple

delivered a voltage of ~1.68 V to reach a geometric current density of 10 mA cm^{-2} (η_{10}) (**Figure 2.13b**), a figure of merit associated with solar-to-hydrogen production [184]. Although inferior to the state-of-the-art Pt/C cathode and IrO_2 anode couple at this voltage, the SNCF-NR//SNCF-NR couple began to overtake at elevated voltages (> 1.78 V). The alkaline water electrolysis performance can be increased by coupling perovskite materials with nanocarbons. For instance, Hua et al. ultrasonically attached electrospun $La_{0.5}(Ba_{0.4}Sr_{0.4}Ca_{0.2})_{0.5}Co_{0.8}Fe_{0.2}O_{3-\delta}$ perovskite nanorods to reduced graphene oxide nanosheets and obtained a comparable η_{10} value of ~1.66 V in an overall water splitting test [185]. Further improvement in performance can be attained by introducing additional reactive sites other than perovskites. For example, Hua et al. conducted H_2 treatment on A-site-deficient double perovskite nanowires, $(PrBa_{0.8}Ca_{0.2})_{0.95}(Co_{1.5}Fe_{0.5})_{0.95}Co_{0.05}O_{5+\delta}$, and obtained Co/CoO_x nanoparticles exsolved on the surface [159]. Since metal/metal oxide components are expected to show catalytic activity [38,186], their synergistic coupling to perovskite oxides gave rise to a significantly enhanced performance for the HER/OER electrocatalysis and the overall water electrolysis (η_{10} = 1.62 V).

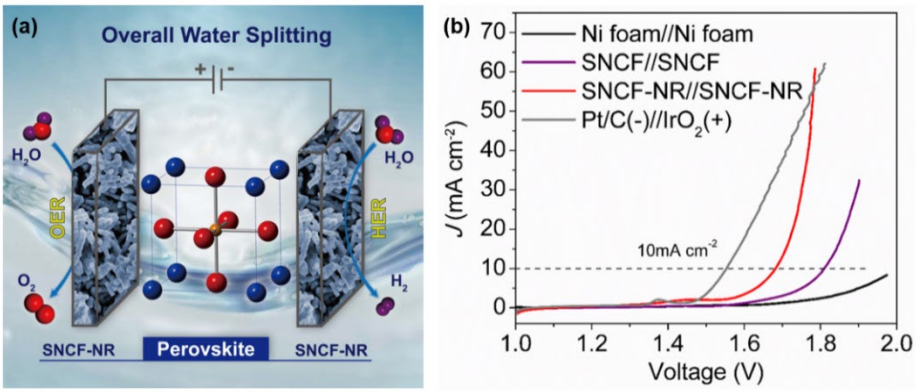

Figure 2.13 (a) A schematic representation of a water electrolyzer using $SrNb_{0.1}Co_{0.7}Fe_{0.2}O_{3-\delta}$ nanorods (SNCF-NR) as both the cathode and anode. (b) Polarization curves of SNCF-NR//SNCF-NR, SNCF//SNCF, Ni foam//Ni foam, and Pt/C(−)//IrO_2(+) for overall water splitting in 1 M KOH. (Reprinted with permission from Ref. [183]. Copyright 2016 John Wiley and Sons)

Despite the attempts at developing bifunctional perovskite materials for catalyzing both the OER and HER, the currently available perovskites only show moderate

catalytic activity toward the HER [42,102,159,183,185], posing an inevitable overpotential of around 0.2 V for the alkaline water electrolysis. One straightforward way to circumvent this issue is to replace the perovskite-based cathode with the state-of-the-art Pt metal. For example, Chen et al. used magnetron sputtering, which is one popular type of PVD synthesis, to deposit amorphous BSCF nanofilms onto Ni foam substrates (mass loading: 38.7 μg cm^{-2}) as highly active OER catalysts [110]. When combined with a Pt–Ni foam cathode, which was also obtained by magnetron sputtering deposition at a Pt mass loading of 38.7 μg cm^{-2}, the BSCF//Pt couple showed significantly reduced voltage for overall water splitting compared to the BSCF//BSCF couple (**Figure 2.14a**). This is mainly attributed to the intrinsically higher HER activity of Pt relative to BSCF [42]. The cell voltage was further reduced to a η_{10} value of 1.57 V for the BSCF//Pt couple when the mass loading of BSCF on Ni foam was increased to 154.8 μg cm^{-2}. It is noteworthy that this high performance was achieved on electrodes with an ultralow catalyst mass loading, almost 20 times lower than that of SNCF-NR (3 mg cm^{-2}), which may have strong implications for practical use.

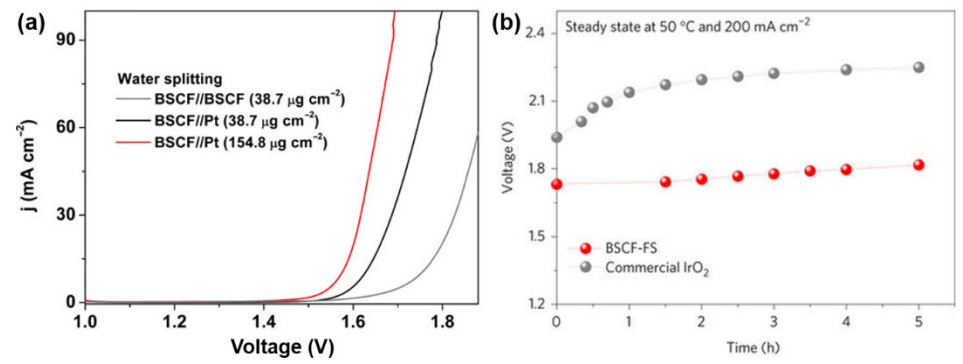

Figure 2.14 (a) Polarization curves of BSCF//BSCF (both at 38.7 μg cm^{-2}), BSCF//Pt (both at 38.7 μg cm^{-2}), and BSCF//Pt (BSCF at 154.8 μg cm^{-2} and Pt at 38.7 μg cm^{-2}) for overall water splitting in 1 M KOH. (Reprinted with permission from Ref. [110]. Copyright 2017 American Association for the Advancement of Science) (b) Voltage versus time at 50 °C and a steady-state current density of 200 mA cm^{-2} obtained for membrane electrode assemblies (MEAs) having BSCF-FS and IrO_2 as the anode electrocatalyst. (Reprinted with permission from Ref. [100]. Copyright 2017 Springer Nature)

The aforementioned perovskite catalysts are evaluated in a simple, lab-based, room-temperature electrolysis cell, without taking into consideration the configuration of water electrolyzers. A more rational practice was recently reported by Fabbri et al. [100], who employed an alkaline membrane water electrolysis cell to assess the performance of BSCF-FS as an anode OER catalyst in comparison to the state-of-the-art IrO_2. Membrane electrode assemblies (MEAs) containing Pt as the cathode, and BSCF-FS or commercial IrO_2 as the anode were assembled with a 3 mg cm^{-2} catalyst loading. Compared to the IrO_2-based MEA, the BSCF-FS-based MEA presented a lower and more stable cell voltage at steady-state conditions of more relevance to industrial settings, that is, a higher temperature of 50 °C and a larger current density of 200 mA cm^{-2} (**Figure 2.14b**). Such measurement offers more solid evidence to the viability of perovskite BSCF-FS nanocatalyst as a low-cost alternative to IrO_2 for efficient water electrolysis.

While much progress has been made in the application of perovskite materials as electrocatalysts for water electrolyzers, there is still room for activity increase, especially in the case of the HER. However, bifunctionality of perovskites for both the HER and OER may appear to be a formidable challenge considering the substantially different reaction processes on perovskite oxide surfaces. Nonetheless, it should be noted that the development of perovskite HER catalysts is still in its infancy. An improved understanding of the reaction mechanism on perovskite surfaces, together with optimized catalyst design strategies, may help facilitate the location of highly active perovskite HER catalysts. At present, a water electrolyzer based on a perovskite OER catalyst coupled with a Pt HER catalyst seems to be a more practical option. Once again, the major concern remains to be the operational stability. The current understanding of catalyst stability is based on short-term electrochemical testing for no more than tens of hours, which is far from satisfactory. In addition, the testing conditions in research laboratories are found to deviate from those in industry. In this sense, application-oriented research should be more extensively carried out for longer lifetimes at conditions more of industrial interest, for example, a temperature of 80 °C and a current density of ~0.5–2 A cm^{-2} [187]. Provided a combination of inputs into both fundamental and applied research, an operative water electrolyzer based on perovskite electrocatalysts can be expected.

2.6 References

1. Wang J, Cui W, Liu Q, Xing Z, Asiri AM, Sun X (2016) Recent progress in cobalt-based heterogeneous catalysts for electrochemical water splitting. Adv Mater 28 (2):215-230. doi:10.1002/adma.201502696

2. Cheng FY, Chen J (2012) Metal-air batteries: From oxygen reduction electrochemistry to cathode catalysts. Chem Soc Rev 41 (6):2172-2192. doi:10.1039/c1cs15228a

3. Mohammad T, Kallio T, Reynaud O, Nasibulin AG, Johans C, Sainio J, Jiang H, Kauppinen EI, Laasonen K (2015) Single-shell carbon-encapsulated iron nanoparticles: Synthesis and high electrocatalytic activity for hydrogen evolution reaction. Angew Chem Int Ed 54 (15):4535-4538. doi:10.1002/anie.201411450

4. Lee Y, Suntivich J, May KJ, Perry EE, Shao-Horn Y (2012) Synthesis and activities of rutile IrO_2 and RuO_2 nanoparticles for oxygen evolution in acid and alkaline solutions. J Phys Chem Lett 3 (3):399-404. doi:10.1021/jz2016507

5. Tian N, Zhou Z-Y, Sun S-G (2008) Platinum metal catalysts of high-index surfaces: From single-crystal planes to electrochemically shape-controlled nanoparticles. J Phys Chem C 112 (50):19801-19817. doi:10.1021/jp804051e

6. Fabbri E, Habereder A, Waltar K, Kotz R, Schmidt TJ (2014) Developments and perspectives of oxide-based catalysts for the oxygen evolution reaction. Catal Sci Technol 4 (11):3800-3821. doi:10.1039/C4CY00669K

7. Gupta S, Kellogg W, Xu H, Liu X, Cho J, Wu G (2016) Bifunctional perovskite oxide catalysts for oxygen reduction and evolution in alkaline media. Chem Asian J 11 (1):10-21. doi:10.1002/asia.201500640

8. Chen DJ, Chen C, Baiyee ZM, Shao ZP, Ciucci F (2015) Nonstoichiometric oxides as low-cost and highly-efficient oxygen reduction/evolution catalysts for low-temperature electrochemical devices. Chem Rev 115 (18):9869-9921. doi:10.1021/acs.chemrev.5b00073

9. Burke MS, Enman LJ, Batchellor AS, Zou S, Boettcher SW (2015) Oxygen evolution reaction electrocatalysis on transition metal oxides and (oxy)hydroxides: Activity trends and design principles. Chem Mater 27 (22):7549-7558. doi:10.1021/acs.chemmater.5b03148

10. Yin H, Tang Z (2016) Ultrathin two-dimensional layered metal hydroxides: An emerging platform for advanced catalysis, energy conversion and storage. Chem Soc Rev 45 (18):4873-4891. doi:10.1039/C6CS00343E
11. Benck JD, Hellstern TR, Kibsgaard J, Chakthranont P, Jaramillo TF (2014) Catalyzing the hydrogen evolution reaction (HER) with molybdenum sulfide nanomaterials. ACS Catal 4 (11):3957-3971. doi:10.1021/cs500923c
12. Hu C, Dai L (2016) Carbon-based metal-free catalysts for electrocatalysis beyond the ORR. Angew Chem Int Ed 55 (39):11736-11758. doi:10.1002/anie.201509982
13. Wang W, Xu X, Zhou W, Shao Z (2017) Recent progress in metal-organic frameworks for applications in electrocatalytic and photocatalytic water splitting. Adv Sci 4 (4):1600371. doi:10.1002/advs.201600371
14. Xu X, Wang W, Zhou W, Shao Z (2018) Recent advances in novel nanostructuring methods of perovskite electrocatalysts for energy-related applications. Small Methods 2 (7):1800071. doi:10.1002/smtd.201800071
15. Hwang J, Rao RR, Giordano L, Katayama Y, Yu Y, Shao-Horn Y (2017) Perovskites in catalysis and electrocatalysis. Science 358 (6364):751-756. doi:10.1126/science.aam7092
16. Zhu L, Ran R, Tadé M, Wang W, Shao Z (2016) Perovskite materials in energy storage and conversion. Asia-Pac J Chem Eng 11 (3):338-369. doi:10.1002/apj.2000
17. Rossmeisl J, Logadottir A, Nørskov JK (2005) Electrolysis of water on (oxidized) metal surfaces. Chem Phys 319 (1):178-184. doi:10.1016/j.chemphys.2005.05.038
18. Mavros MG, Tsuchimochi T, Kowalczyk T, McIsaac A, Wang L-P, Voorhis TV (2014) What can density functional theory tell us about artificial catalytic water splitting? Inorg Chem 53 (13):6386-6397. doi:10.1021/ic5002557
19. Goodenough JB, Manoharan R, Paranthaman M (1990) Surface protonation and electrochemical activity of oxides in aqueous solution. J Am Chem Soc 112 (6):2076-2082. doi:10.1021/ja00162a006
20. Haumann M, Liebisch P, Müller C, Barra M, Grabolle M, Dau H (2005) Photosynthetic O_2 formation tracked by time-resolved x-ray experiments. Science 310 (5750):1019-1021. doi:10.1126/science.1117551
21. Gerken JB, McAlpin JG, Chen JYC, Rigsby ML, Casey WH, Britt RD, Stahl SS (2011) Electrochemical water oxidation with cobalt-based electrocatalysts from pH 0–14: The thermodynamic basis for catalyst structure, stability, and activity. J Am Chem Soc 133 (36):14431-14442. doi:10.1021/ja205647m

22. Kuznetsov DA, Han B, Yu Y, Rao RR, Hwang J, Román-Leshkov Y, Shao-Horn Y (2018) Tuning redox transitions via inductive effect in metal oxides and complexes, and implications in oxygen electrocatalysis. Joule 2 (2):225-244. doi:10.1016/j.joule.2017.11.014
23. Suntivich J, Gasteiger HA, Yabuuchi N, Nakanishi H, Goodenough JB, Shao-Horn Y (2011) Design principles for oxygen-reduction activity on perovskite oxide catalysts for fuel cells and metal–air batteries. Nature Chem 3:546-550. doi:10.1038/nchem.1069
24. Nørskov JK, Rossmeisl J, Logadottir A, Lindqvist L, Kitchin JR, Bligaard T, Jónsson H (2004) Origin of the overpotential for oxygen reduction at a fuel-cell cathode. J Phys Chem B 108 (46):17886-17892. doi:10.1021/jp047349j
25. Fernández EM, Moses PG, Toftelund A, Hansen HA, Martínez JI, Abild-Pedersen F, Kleis J, Hinnemann B, Rossmeisl J, Bligaard T, Nørskov JK (2008) Scaling relationships for adsorption energies on transition metal oxide, sulfide, and nitride surfaces. Angew Chem Int Ed 47 (25):4683-4686. doi:10.1002/anie.200705739
26. Suntivich J, May KJ, Gasteiger HA, Goodenough JB, Shao-Horn Y (2011) A perovskite oxide optimized for oxygen evolution catalysis from molecular orbital principles. Science 334 (6061):1383-1385. doi:10.1126/science.1212858
27. Man IC, Su H-Y, Calle-Vallejo F, Hansen HA, Martínez JI, Inoglu NG, Kitchin J, Jaramillo TF, Nørskov JK, Rossmeisl J (2011) Universality in oxygen evolution electrocatalysis on oxide surfaces. ChemCatChem 3 (7):1159-1165. doi:10.1002/cctc.201000397
28. Rong X, Parolin J, Kolpak AM (2016) A fundamental relationship between reaction mechanism and stability in metal oxide catalysts for oxygen evolution. ACS Catal 6 (2):1153-1158. doi:10.1021/acscatal.5b02432
29. Mefford JT, Rong X, Abakumov AM, Hardin WG, Dai S, Kolpak AM, Johnston KP, Stevenson KJ (2016) Water electrolysis on $La_{1-x}Sr_xCoO_{3-\delta}$ perovskite electrocatalysts. Nat Commun 7:11053. doi:10.1038/ncomms11053
30. Grimaud A, Diaz-Morales O, Han B, Hong WT, Lee Y-L, Giordano L, Stoerzinger KA, Koper MTM, Shao-Horn Y (2017) Activating lattice oxygen redox reactions in metal oxides to catalyse oxygen evolution. Nature Chem 9:457-465. doi:10.1038/nchem.2695

31. Yoo JS, Liu Y, Rong X, Kolpak AM (2018) Electronic origin and kinetic feasibility of the lattice oxygen participation during the oxygen evolution reaction on perovskites. J Phys Chem Lett 9 (7):1473-1479. doi:10.1021/acs.jpclett.8b00154
32. Yoo JS, Rong X, Liu Y, Kolpak AM (2018) Role of lattice oxygen participation in understanding trends in the oxygen evolution reaction on perovskites. ACS Catal 8 (5):4628-4636. doi:10.1021/acscatal.8b00612
33. Noh JS, Schwarz JA (1989) Estimation of the point of zero charge of simple oxides by mass titration. J Colloid Interface Sci 130 (1):157-164. doi:10.1016/0021-9797(89)90086-6
34. Rossmeisl J, Qu ZW, Zhu H, Kroes GJ, Nørskov JK (2007) Electrolysis of water on oxide surfaces. J Electroanal Chem 607 (1):83-89. doi:10.1016/j.jelechem.2006.11.008
35. Nørskov JK, Bligaard T, Rossmeisl J, Christensen CH (2009) Towards the computational design of solid catalysts. Nature Chem 1:37-46. doi:10.1038/nchem.121
36. García-Mota M, Vojvodic A, Metiu H, Man IC, Su H-Y, Rossmeisl J, Nørskov JK (2011) Tailoring the activity for oxygen evolution electrocatalysis on rutile TiO_2(110) by transition-metal substitution. ChemCatChem 3 (10):1607-1611. doi:10.1002/cctc.201100160
37. Vilekar SA, Fishtik I, Datta R (2010) Kinetics of the hydrogen electrode reaction. J Electrochem Soc 157 (7):B1040-B1050. doi:10.1149/1.3385391
38. Gong M, Zhou W, Tsai M-C, Zhou J, Guan M, Lin M-C, Zhang B, Hu Y, Wang D-Y, Yang J, Pennycook SJ, Hwang B-J, Dai H (2014) Nanoscale nickel oxide/nickel heterostructures for active hydrogen evolution electrocatalysis. Nat Commun 5:4695. doi:10.1038/ncomms5695
39. Nørskov JK, Bligaard T, Logadottir A, Kitchin JR, Chen JG, Pandelov S, Stimming U (2005) Trends in the exchange current for hydrogen evolution. J Electrochem Soc 152 (3):J23-J26. doi:10.1149/1.1856988
40. Mahmood N, Yao Y, Zhang J-W, Pan L, Zhang X, Zou J-J (2018) Electrocatalysts for hydrogen evolution in alkaline electrolytes: Mechanisms, challenges, and prospective solutions. Adv Sci 5 (2):1700464. doi:10.1002/advs.201700464
41. Zheng Y, Jiao Y, Vasileff A, Qiao SZ (2018) The hydrogen evolution reaction in alkaline solution: From theory, single crystal models, to practical electrocatalysts. Angew Chem Int Ed 57 (26):7568-7579. doi:10.1002/anie.201710556

42. Xu X, Chen Y, Zhou W, Zhu Z, Su C, Liu M, Shao Z (2016) A perovskite electrocatalyst for efficient hydrogen evolution reaction. Adv Mater 28 (30):6442-6448. doi:10.1002/adma.201600005
43. Parsons R (1958) The rate of electrolytic hydrogen evolution and the heat of adsorption of hydrogen. T Faraday Soc 54:1053-1063. doi:10.1039/TF9585401053
44. Seh ZW, Kibsgaard J, Dickens CF, Chorkendorff I, Nørskov JK, Jaramillo TF (2017) Combining theory and experiment in electrocatalysis: Insights into materials design. Science 355 (6321):eaad4998. doi:10.1126/science.aad4998
45. Hong WT, Risch M, Stoerzinger KA, Grimaud A, Suntivich J, Shao-Horn Y (2015) Toward the rational design of non-precious transition metal oxides for oxygen electrocatalysis. Energy Environ Sci 8 (5):1404-1427. doi:10.1039/C4EE03869J
46. Grimaud A, May KJ, Carlton CE, Lee Y-L, Risch M, Hong WT, Zhou J, Shao-Horn Y (2013) Double perovskites as a family of highly active catalysts for oxygen evolution in alkaline solution. Nat Commun 4:2439. doi:10.1038/ncomms3439
47. Bockris JO, Otagawa T (1983) Mechanism of oxygen evolution on perovskites. J Phys Chem 87 (15):2960-2971. doi:10.1021/j100238a048
48. Bockris JOM, Otagawa T (1984) The electrocatalysis of oxygen evolution on perovskites. J Electrochem Soc 131 (2):290-302. doi:10.1149/1.2115565
49. Calle-Vallejo F, Inoglu NG, Su H-Y, Martinez JI, Man IC, Koper MTM, Kitchin JR, Rossmeisl J (2013) Number of outer electrons as descriptor for adsorption processes on transition metals and their oxides. Chem Sci 4 (3):1245-1249. doi:10.1039/C2SC21601A
50. Zhu Y, Zhou W, Chen Z-G, Chen Y, Su C, Tadé MO, Shao Z (2015) $SrNb_{0.1}Co_{0.7}Fe_{0.2}O_{3-\delta}$ perovskite as a next-generation electrocatalyst for oxygen evolution in alkaline solution. Angew Chem Int Ed 54 (13):3897-3901. doi:10.1002/anie.201408998
51. Kim J, Yin X, Tsao K-C, Fang S, Yang H (2014) $Ca_2Mn_2O_5$ as oxygen-deficient perovskite electrocatalyst for oxygen evolution reaction. J Am Chem Soc 136 (42):14646-14649. doi:10.1021/ja506254g
52. Guo YQ, Tong Y, Chen PZ, Xu K, Zhao JY, Lin Y, Chu WS, Peng ZM, Wu CZ, Xie Y (2015) Engineering the electronic state of a perovskite electrocatalyst for synergistically enhanced oxygen evolution reaction. Adv Mater 27 (39):5989-5994. doi:10.1002/adma.201502024

53. Yagi S, Yamada I, Tsukasaki H, Seno A, Murakami M, Fujii H, Chen H, Umezawa N, Abe H, Nishiyama N, Mori S (2015) Covalency-reinforced oxygen evolution reaction catalyst. Nat Commun 6:8249. doi:10.1038/ncomms9249
54. Wei C, Feng Z, Scherer GG, Barber J, Shao-Horn Y, Xu ZJ (2017) Cations in octahedral sites: A descriptor for oxygen electrocatalysis on transition-metal spinels. Adv Mater 29 (23):1606800. doi:10.1002/adma.201606800
55. Jin YZ, Li Z, Wang JQ, Li R, Li ZQ, Liu H, Mao J, Dong CK, Yang J, Qiao SZ, Du XW (2018) Tuning spin state of rock-salt-based oxides by manipulation of crystallinity for efficient oxygen electrocatalysis. Adv Energy Mater 8(22):1703469. doi:10.1002/aenm.201703469
56. Kalubarme RS, Park GE, Jung KN, Shin KH, Ryu WH, Park CJ (2014) $LaNi_xCo_{1-x}O_{3-\delta}$ perovskites as catalyst material for non-aqueous lithium-oxygen batteries. J Electrochem Soc 161 (6):A880-A889. doi:10.1149/2.012406jes
57. Du Z, Yang P, Wang L, Lu Y, Goodenough JB, Zhang J, Zhang D (2014) Electrocatalytic performances of $LaNi_{1-x}Mg_xO_3$ perovskite oxides as bi-functional catalysts for lithium air batteries. J Power Sources 265:91-96. doi:10.1016/j.jpowsour.2014.04.096
58. Zhang D, Song Y, Du Z, Wang L, Li Y, Goodenough JB (2015) Active $LaNi_{1-x}Fe_xO_3$ bifunctional catalysts for air cathodes in alkaline media. J Mater Chem A 3 (18):9421-9426. doi:10.1039/c5ta01005e
59. Wang Z, You Y, Yuan J, Yin YX, Li YT, Xin S, Zhang D (2016) Nickel-doped $La_{0.8}Sr_{0.2}Mn_{1-x}Ni_xO_3$ nanoparticles containing abundant oxygen vacancies as an optimized bifunctional catalyst for oxygen cathode in rechargeable lithium-air batteries. ACS Appl Mater Interfaces 8 (10):6520-6528. doi:10.1021/acsami.6b00296
60. Goodenough JB (1958) An interpretation of the magnetic properties of the perovskite-type mixed crystals $La_{1-x}Sr_xCoO_{3-\lambda}$. J Phys Chem Solids 6 (2):287-297. doi:10.1016/0022-3697(58)90107-0
61. Korotin MA, Ezhov SY, Solovyev IV, Anisimov VI, Khomskii DI, Sawatzky GA (1996) Intermediate-spin state and properties of $LaCoO_3$. Phys Rev B 54 (8):5309-5316. doi:10.1103/PhysRevB.54.5309
62. Maris G, Ren Y, Volotchaev V, Zobel C, Lorenz T, Palstra TTM (2003) Evidence for orbital ordering in $LaCoO_3$. Phys Rev B 67 (22):224423. doi:10.1103/PhysRevB.67.224423

63. Haverkort MW, Hu Z, Cezar JC, Burnus T, Hartmann H, Reuther M, Zobel C, Lorenz T, Tanaka A, Brookes NB, Hsieh HH, Lin HJ, Chen CT, Tjeng LH (2006) Spin state transition in $LaCoO_3$ studied using soft X-ray absorption spectroscopy and magnetic circular dichroism. Phys Rev Lett 97 (17):176405. doi:10.1103/PhysRevLett.97.176405
64. Křápek V, Novák P, Kuneš J, Novoselov D, Korotin DM, Anisimov VI (2012) Spin state transition and covalent bonding in $LaCoO_3$. Phys Rev B 86 (19):195104. doi:10.1103/PhysRevB.86.195104
65. Hammer B, Nørskov JK (1995) Electronic factors determining the reactivity of metal surfaces. Surf Sci 343 (3):211-220. doi:10.1016/0039-6028(96)80007-0
66. Egdell RG, Goodenough JB, Hamnett A, Naish CC (1983) Electrochemistry of ruthenates. Part 1.-Oxygen reduction on pyrochlore ruthenates. J Chem Soc, Faraday Trans 1 79 (4):893-912. doi:10.1039/F19837900893
67. Matsumoto Y, Sato E (1986) Electrocatalytic properties of transition metal oxides for oxygen evolution reaction. Mater Chem Phys 14 (5):397-426. doi:10.1016/0254-0584(86)90045-3
68. Zhou SM, Miao XB, Zhao X, Ma C, Qiu YH, Hu ZP, Zhao JY, Shi L, Zeng J (2016) Engineering electrocatalytic activity in nanosized perovskite cobaltite through surface spin-state transition. Nat Commun 7:11510. doi:10.1038/ncomms11510
69. Petrie JR, Cooper VR, Freeland JW, Meyer TL, Zhang Z, Lutterman DA, Lee HN (2016) Enhanced bifunctional oxygen catalysis in strained $LaNiO_3$ perovskites. J Am Chem Soc 138 (8):2488-2491. doi:10.1021/jacs.5b11713
70. Petrie JR, Jeen H, Barron SC, Meyer TL, Lee HN (2016) Enhancing perovskite electrocatalysis through strain tuning of the oxygen deficiency. J Am Chem Soc 138 (23):7252-7255. doi:10.1021/jacs.6b03520
71. Stoerzinger KA, Choi WS, Jeen H, Lee HN, Shao-Horn Y (2015) Role of strain and conductivity in oxygen electrocatalysis on $LaCoO_3$ thin films. J Phys Chem Lett 6 (3):487-492. doi:10.1021/jz502692a
72. Lee D-G, Gwon O, Park H-S, Kim SH, Yang J, Kwak SK, Kim G, Song H-K (2015) Conductivity-dependent completion of oxygen reduction on oxide catalysts. Angew Chem Int Ed 54 (52):15730-15733. doi:10.1002/anie.201508129
73. Cheng X, Fabbri E, Nachtegaal M, Castelli IE, El Kazzi M, Haumont R, Marzari N, Schmidt TJ (2015) Oxygen evolution reaction on $La_{1-x}Sr_xCoO_3$ perovskites: A combined experimental and theoretical study of their structural, electronic, and

electrochemical properties. Chem Mater 27 (22):7662-7672. doi:10.1021/acs.chemmater.5b03138

74. Pramana SS, Cavallaro A, Li C, Handoko AD, Chan KW, Walker RJ, Regoutz A, Herrin JS, Yeo BS, Payne DJ, Kilner JA, Ryan MP, Skinner SJ (2018) Crystal structure and surface characteristics of Sr-doped $GdBaCo_2O_{6-\delta}$ double perovskites: Oxygen evolution reaction and conductivity. J Mater Chem A 6 (13):5335-5345. doi:10.1039/C7TA06817D

75. Hyodo T, Hayashi M, Miura N, Yamazoe N (1996) Catalytic activities of rare-earth manganites for cathodic reduction of oxygen in alkaline solution. J Electrochem Soc 143 (11):L266-L267. doi:10.1149/1.1837229

76. Hyodo T, Hayashi M, Mitsutake S, Miura N, Yamazoe N (1997) Praseodymium–calcium manganites ($Pr_{1-x}Ca_xMnO_3$) as electrode catalyst for oxygen reduction in alkaline solution. J Appl Electrochem 27 (6):745-745. doi:10.1023/a:1018404308209

77. Hu J, Wang L, Shi L, Huang H (2014) Preparation of $La_{1-x}Ca_xMnO_3$ perovskite–graphene composites as oxygen reduction reaction electrocatalyst in alkaline medium. J Power Sources 269:144-151. doi:10.1016/j.jpowsour.2014.07.004

78. Tulloch J, Donne SW (2009) Activity of perovskite $La_{1-x}Sr_xMnO_3$ catalysts towards oxygen reduction in alkaline electrolytes. J Power Sources 188 (2):359-366. doi:10.1016/j.jpowsour.2008.12.024

79. Stoerzinger KA, Lü W, Li C, Ariando, Venkatesan T, Shao-Horn Y (2015) Highly active epitaxial $La_{(1-x)}Sr_xMnO_3$ surfaces for the oxygen reduction reaction: Role of charge transfer. J Phys Chem Lett 6 (8):1435-1440. doi:10.1021/acs.jpclett.5b00439

80. Hammouche A, Kahoul A, Sauer DU, De Doncker RW (2006) Influential factors on oxygen reduction at $La_{1-x}Ca_xCoO_3$ electrodes in alkaline electrolyte. J Power Sources 153 (2):239-244. doi:10.1016/j.jpowsour.2005.05.028

81. Lal B, Raghunandan MK, Gupta M, Singh RN (2005) Electrocatalytic properties of perovskite-type $La_{1-x}Sr_xCoO_3$ ($0 \leq x \leq 0.4$) obtained by a novel stearic acid sol–gel method for electrocatalysis of O_2 evolution in KOH solutions. Int J Hydrogen Energy 30 (7):723-729. doi:10.1016/j.ijhydene.2004.07.002

82. She S, Yu J, Tang W, Zhu Y, Chen Y, Sunarso J, Zhou W, Shao Z (2018) Systematic study of oxygen evolution activity and stability on $La_{1-x}Sr_xFeO_{3-\delta}$ perovskite electrocatalysts in alkaline media. ACS Appl Mater Interfaces 10 (14):11715-11721. doi:10.1021/acsami.8b00682

83. Sunarso J, Torriero AAJ, Zhou W, Howlett PC, Forsyth M (2012) Oxygen reduction reaction activity of La-based perovskite oxides in alkaline medium: A thin-film rotating ring-disk electrode study. J Phys Chem C 116 (9):5827-5834. doi:10.1021/jp211946n

84. Zhou W, Zhao M, Liang F, Smith SC, Zhu Z (2015) High activity and durability of novel perovskite electrocatalysts for water oxidation. Mater Horiz 2 (5):495-501. doi:10.1039/C5MH00096C

85. Sun H, Chen G, Zhu Y, Liu B, Zhou W, Shao Z (2017) B-site cation ordered double perovskites as efficient and stable electrocatalysts for oxygen evolution reaction. Chem Eur J 23 (24):5722-5728. doi:10.1002/chem.201700507

86. Su C, Wang W, Chen Y, Yang G, Xu X, Tadé MO, Shao Z (2015) $SrCo_{0.9}Ti_{0.1}O_{3-\delta}$ as a new electrocatalyst for the oxygen evolution reaction in alkaline electrolyte with stable performance. ACS Appl Mater Interfaces 7 (32):17663-17670. doi:10.1021/acsami.5b02810

87. Sun H, Chen G, Sunarso J, Dai J, Zhou W, Shao Z (2018) Molybdenum and niobium codoped B-site-ordered double perovskite catalyst for efficient oxygen evolution reaction. ACS Appl Mater Interfaces 10 (20):16939-16942. doi:10.1021/acsami.8b03702

88. Chen G, Hu Z, Zhu Y, Chen Z-G, Zhong Y, Lin H-J, Chen C-T, Tjeng LH, Zhou W, Shao Z (2018) Ultrahigh-performance tungsten-doped perovskites for the oxygen evolution reaction. J Mater Chem A 6 (21):9854-9859. doi:10.1039/C8TA02864H

89. Xu X, Su C, Zhou W, Zhu Y, Chen Y, Shao Z (2016) Co-doping strategy for developing perovskite oxides as highly efficient electrocatalysts for oxygen evolution reaction. Adv Sci 3 (2):1500187. doi:10.1002/advs.201500187

90. Xu X, Chen Y, Zhou W, Zhong Y, Guan D, Shao Z (2018) Earth-abundant silicon for facilitating water oxidation over iron-based perovskite electrocatalyst. Adv Mater Interfaces 5(11):1701693. doi:10.1002/admi.201701693

91. Zhu Y, Zhou W, Sunarso J, Zhong Y, Shao Z (2016) Phosphorus-doped perovskite oxide as highly efficient water oxidation electrocatalyst in alkaline solution. Adv Funct Mater 26 (32):5862-5872. doi:10.1002/adfm.201601902

92. Shen Y, Zhu Y, Sunarso J, Guan D, Liu B, Liu H, Zhou W, Shao Z (2018) New phosphorus-doped perovskite oxide as an oxygen reduction reaction electrocatalyst in an alkaline solution. Chem Eur J 24 (27):6950-6957. doi:10.1002/chem.201705675

93. Li Z, Lv L, Wang J, Ao X, Ruan Y, Zha D, Hong G, Wu Q, Lan Y, Wang C, Jiang J, Liu M (2018) Engineering phosphorus-doped $LaFeO_{3-\delta}$ perovskite oxide as robust bifunctional oxygen electrocatalysts in alkaline solutions. Nano Energy 47:199-209. doi:10.1016/j.nanoen.2018.02.051

94. Yuasa M, Tachibana N, Shimanoe K (2013) Oxygen reduction activity of carbon-supported $La_{1-x}Ca_xMn_{1-y}Fe_yO_3$ nanoparticles. Chem Mater 25 (15):3072-3079. doi:10.1021/cm401276y

95. Malkhandi S, Trinh P, Manohar AK, Manivannan A, Balasubramanian M, Prakash GKS, Narayanan SR (2015) Design insights for tuning the electrocatalytic activity of perovskite oxides for the oxygen evolution reaction. J Phys Chem C 119 (15):8004-8013. doi:10.1021/jp512722x

96. Zhen DX, Zhao BT, Shin HC, Bu YF, Ding Y, He GH, Liu ML (2017) Electrospun porous perovskite $La_{0.6}Sr_{0.4}Co_{1-x}Fe_xO_{3-\delta}$ nanofibers for efficient oxygen evolution reaction. Adv Mater Interfaces 4 (13):1700146. doi:10.1002/admi.201700146

97. Zhu Y, Zhou W, Yu J, Chen Y, Liu M, Shao Z (2016) Enhancing electrocatalytic activity of perovskite oxides by tuning cation deficiency for oxygen reduction and evolution reactions. Chem Mater 28 (6):1691-1697. doi:10.1021/acs.chemmater.5b04457

98. Liu H, Ding X, Wang L, Ding D, Zhang S, Yuan G (2018) Cation deficiency design: A simple and efficient strategy for promoting oxygen evolution reaction activity of perovskite electrocatalyst. Electrochim Acta 259:1004-1010. doi:10.1016/j.electacta.2017.10.172

99. Xue Y, Miao H, Sun S, Wang Q, Li S, Liu Z (2017) $(La_{1-x}Sr_x)_{0.98}MnO_3$ perovskite with A-site deficiencies toward oxygen reduction reaction in aluminum-air batteries. J Power Sources 342:192-201. doi:10.1016/j.jpowsour.2016.12.065

100. Fabbri E, Nachtegaal M, Binninger T, Cheng X, Kim BJ, Durst J, Bozza F, Graule T, Schaublin R, Wiles L, Pertoso M, Danilovic N, Ayers KE, Schmidt TJ (2017) Dynamic surface self-reconstruction is the key of highly active perovskite nano-electrocatalysts for water splitting. Nature Mater 16 (9):925-931. doi:10.1038/nmat4938

101. Chen CF, King G, Dickerson RM, Papin PA, Gupta S, Kellogg WR, Wu G (2015) Oxygen-deficient $BaTiO_{3-x}$ perovskite as an efficient bifunctional oxygen electrocatalyst. Nano Energy 13:423-432. doi:10.1016/j.nanoen.2015.03.005

102. Wang J, Gao Y, Chen D, Liu J, Zhang Z, Shao Z, Ciucci F (2018) Water splitting with an enhanced bifunctional double perovskite. ACS Catal 8 (1):364-371. doi:10.1021/acscatal.7b02650

103. Du J, Zhang TR, Cheng FY, Chu WS, Wu ZY, Chen J (2014) Nonstoichiometric perovskite $CaMnO_{3-\delta}$ for oxygen electrocatalysis with high activity. Inorg Chem 53 (17):9106-9114. doi:10.1021/ic501631h

104. Wang G, Xu T, Wen S, Pan M (2015) Structure-dependent electrocatalytic activity of $La_{1-x}Sr_xMnO_3$ for oxygen reduction reaction. Sci China Chem 58 (5):871-878. doi:10.1007/s11426-015-5326-9

105. Zhou W, Sunarso J (2013) Enhancing bi-functional electrocatalytic activity of perovskite by temperature shock: A case study of $LaNiO_{3-\delta}$. J Phys Chem Lett 4 (17):2982-2988. doi:10.1021/jz401169n

106. Zhu Y, Zhou W, Chen Y, Yu J, Xu X, Su C, Tadé MO, Shao Z (2015) Boosting oxygen reduction reaction activity of palladium by stabilizing its unusual oxidation states in perovskite. Chem Mater 27 (8):3048-3054. doi:10.1021/acs.chemmater.5b00450

107. Zhang C, Trudel S, Berlinguette CP (2014) Water oxidation catalysis: Survey of amorphous binary metal oxide films containing lanthanum and late 3d transition metals. Eur J Inorg Chem 2014 (4):660-664. doi:10.1002/ejic.201300765

108. Zhang C, Zhang X, Daly K, Berlinguette CP, Trudel S (2017) Water oxidation catalysis: Tuning the electrocatalytic properties of amorphous lanthanum cobaltite through calcium doping. ACS Catal 7 (9):6385-6391. doi:10.1021/acscatal.7b02145

109. Zhang C, Berlinguette CP, Trudel S (2016) Water oxidation catalysis: an amorphous quaternary Ba-Sr-Co-Fe oxide as a promising electrocatalyst for the oxygen-evolution reaction. Chem Commun 52 (7):1513-1516. doi:10.1039/C5CC09361A

110. Chen G, Zhou W, Guan DQ, Sunarso J, Zhu YP, Hu XF, Zhang W, Shao ZP (2017) Two orders of magnitude enhancement in oxygen evolution reactivity on amorphous $Ba_{0.5}Sr_{0.5}Co_{0.8}Fe_{0.2}O_{3-\delta}$ nanofilms with tunable oxidation state. Sci Adv 3 (6):e1603206. doi:10.1126/sciadv.1603206

111. Yoon C, Cocke DL (1986) Potential of amorphous materials as catalysts. J Non-Cryst Solids 79 (3):217-245. doi:10.1016/0022-3093(86)90224-3

112. Jung JI, Park S, Kim MG, Cho J (2015) Tunable internal and surface structures of the bifunctional oxygen perovskite catalysts. Adv Energy Mater 5 (24):1501560. doi:10.1002/aenm.201501560

113. Jung JI, Jeong HY, Kim MG, Nam G, Park J, Cho J (2015) Fabrication of $Ba_{0.5}Sr_{0.5}Co_{0.8}Fe_{0.2}O_{3-\delta}$ catalysts with enhanced electrochemical performance by removing an inherent heterogeneous surface film layer. Adv Mater 27 (2):266-271. doi:10.1002/adma.201403897

114. Lee JG, Hwang J, Hwang HJ, Jeon OS, Jang J, Kwon O, Lee Y, Han B, Shul Y-G (2016) A new family of perovskite catalysts for oxygen-evolution reaction in alkaline media: $BaNiO_3$ and $BaNi_{0.83}O_{2.5}$. J Am Chem Soc 138 (10):3541-3547. doi:10.1021/jacs.6b00036

115. Jung JI, Jeong HY, Lee JS, Kim MG, Cho J (2014) A bifunctional perovskite catalyst for oxygen reduction and evolution. Angew Chem Int Ed 53 (18):4582-4586. doi:10.1002/anie.201311223

116. Xu X, Pan Y, Zhou W, Chen Y, Zhang Z, Shao Z (2016) Toward enhanced oxygen evolution on perovskite oxides synthesized from different approaches: A case study of $Ba_{0.5}Sr_{0.5}Co_{0.8}Fe_{0.2}O_{3-\delta}$. Electrochim Acta 219:553-559. doi:10.1016/j.electacta.2016.10.031

117. Yamada I, Fujii H, Takamatsu A, Ikeno H, Wada K, Tsukasaki H, Kawaguchi S, Mori S, Yagi S (2017) Bifunctional oxygen reaction catalysis of quadruple manganese perovskites. Adv Mater 29 (4):1603004. doi:10.1002/adma.201603004

118. Jung JI, Risch M, Park S, Kim MG, Nam G, Jeong HY, Shao-Horn Y, Cho J (2016) Optimizing nanoparticle perovskite for bifunctional oxygen electrocatalysis. Energy Environ Sci 9 (1):176-183. doi:10.1039/c5ee03124a

119. Zhao Y, Xu L, Mai L, Han C, An Q, Xu X, Liu X, Zhang Q (2012) Hierarchical mesoporous perovskite $La_{0.5}Sr_{0.5}CoO_{2.91}$ nanowires with ultrahigh capacity for Li-air batteries. Proc Natl Acad Sci U S A 109 (48):19569-19574. doi:10.1073/pnas.1210315109

120. Bu Y, Gwon O, Nam G, Jang H, Kim S, Zhong Q, Cho J, Kim G (2017) A highly efficient and robust cation ordered perovskite oxide as a bifunctional catalyst for rechargeable Zinc-air batteries. ACS Nano 11 (11):11594-11601. doi:10.1021/acsnano.7b06595

121. Lu F, Wang Y, Jin C, Li F, Yang R, Chen F (2015) Microporous $La_{0.8}Sr_{0.2}MnO_3$ perovskite nanorods as efficient electrocatalysts for lithium air battery. J Power Sources 293:726-733. doi:10.1016/j.jpowsour.2015.06.022
122. Vignesh A, Prabu M, Shanmugam S (2016) Porous $LaCo_{1-x}Ni_xO_{3-\delta}$ nanostructures as an efficient electrocatalyst for water oxidation and for a Zinc-air battery. ACS Appl Mater Interfaces 8 (9):6019-6031. doi:10.1021/acsami.5b11840
123. Kim J, Chen X, Shih P-C, Yang H (2017) Porous perovskite-type lanthanum cobaltite as electrocatalysts toward oxygen evolution reaction. ACS Sustainable Chem Eng 5 (11):10910-10917. doi:10.1021/acssuschemeng.7b02815
124. Zhang J, Zhao YB, Zhao X, Liu ZL, Chen W (2014) Porous perovskite $LaNiO_3$ nanocubes as cathode catalysts for Li-O_2 batteries with low charge potential. Sci Rep 4:6005 doi:10.1038/srep06005
125. Zhao B, Zhang L, Zhen D, Yoo S, Ding Y, Chen D, Chen Y, Zhang Q, Doyle B, Xiong X, Liu M (2017) A tailored double perovskite nanofiber catalyst enables ultrafast oxygen evolution. Nat Commun 8:14586. doi:10.1038/ncomms14586
126. Zhu Y, Zhou W, Shao Z (2017) Perovskite/carbon composites: Applications in oxygen electrocatalysis. Small 13 (12):1603793. doi:10.1002/smll.201603793
127. Suntivich J, Gasteiger HA, Yabuuchi N, Shao-Horn Y (2010) Electrocatalytic measurement methodology of oxide catalysts using a thin-film rotating disk electrode. J Electrochem Soc 157 (8):B1263-B1268. doi:10.1149/1.3456630
128. Poux T, Napolskiy FS, Dintzer T, Kéranguéven G, Istomin SY, Tsirlina GA, Antipov EV, Savinova ER (2012) Dual role of carbon in the catalytic layers of perovskite/carbon composites for the electrocatalytic oxygen reduction reaction. Catal Today 189 (1):83-92. doi:10.1016/j.cattod.2012.04.046
129. Poux T, Bonnefont A, Kéranguéven G, Tsirlina GA, Savinova ER (2014) Electrocatalytic oxygen reduction reaction on perovskite oxides: Series versus direct pathway. ChemPhysChem 15 (10):2108-2120. doi:10.1002/cphc.201402022
130. Malkhandi S, Trinh P, Manohar AK, Jayachandrababu KC, Kindler A, Prakash GKS, Narayanan SR (2013) Electrocatalytic activity of transition metal oxide-carbon composites for oxygen reduction in alkaline batteries and fuel cells. J Electrochem Soc 160 (9):F943-F952. doi:10.1149/2.109308jes
131. Li X, Qu W, Zhang J, Wang H (2011) Electrocatalytic activities of $La_{0.6}Ca_{0.4}CoO_3$ and $La_{0.6}Ca_{0.4}CoO_3$-carbon composites toward the oxygen reduction reaction in

concentrated alkaline electrolytes. J Electrochem Soc 158 (5):A597-A604. doi:10.1149/1.3560170

132. Nishio K, Molla S, Okugaki T, Nakanishi S, Nitta I, Kotani Y (2015) Oxygen reduction and evolution reactions of air electrodes using a perovskite oxide as an electrocatalyst. J Power Sources 278:645-651. doi:10.1016/j.jpowsour.2014.12.100

133. Nishio K, Molla S, Okugaki T, Nakanishi S, Nitta I, Kotani Y (2015) Effects of carbon on oxygen reduction and evolution reactions of gas-diffusion air electrodes based on perovskite-type oxides. J Power Sources 298:236-240. doi:10.1016/j.jpowsour.2015.08.070

134. Fabbri E, Nachtegaal M, Cheng X, Schmidt TJ. (2015) Superior bifunctional electrocatalytic activity of $Ba_{0.5}Sr_{0.5}Co_{0.8}Fe_{0.2}O_{3-\delta}$/carbon composite electrodes: Insight into the local electronic structure. Adv Energy Mater 5 (17):1402033. doi:10.1002/aenm.201402033

135. Jin C, Cao X, Zhang L, Zhang C, Yang R (2013) Preparation and electrochemical properties of urchin-like $La_{0.8}Sr_{0.2}MnO_3$ perovskite oxide as a bifunctional catalyst for oxygen reduction and oxygen evolution reaction. J Power Sources 241:225-230. doi:10.1016/j.jpowsour.2013.04.116

136. Park HW, Lee DU, Zamani P, Seo MH, Zazar LF, Chen ZW (2014) Electrospun porous nanorod perovskite oxide/nitrogen-doped graphene composite as a bi-functional catalyst for metal air batteries. Nano Energy 10:192-200. doi:10.1016/j.nanoen.2014.09.009

137. Oh MY, Jeon JS, Lee JJ, Kim P, Nahm KS (2015) The bifunctional electrocatalytic activity of perovskite $La_{0.6}Sr_{0.4}CoO_{3-\delta}$ for oxygen reduction and evolution reactions. RSC Adv 5 (25):19190-19198. doi:10.1039/c4ra16097e

138. Liu G, Chen H, Xia L, Wang S, Ding LX, Li D, Xiao K, Dai S, Wang H (2015) Hierarchical mesoporous/macroporous perovskite $La_{0.5}Sr_{0.5}CoO_{3-x}$ nanotubes: A bifunctional catalyst with enhanced activity and cycle stability for rechargeable lithium oxygen batteries. ACS Appl Mater Interfaces 7 (40):22478-22486. doi:10.1021/acsami.5b06587

139. Chen Z, Yu A, Higgins D, Li H, Wang H, Chen Z (2012) Highly active and durable core–corona structured bifunctional catalyst for rechargeable metal–air battery application. Nano Lett 12 (4):1946-1952. doi:10.1021/nl2044327

140. Lee DU, Park HW, Park MG, Ismayilov V, Chen ZW (2015) Synergistic bifunctional catalyst design based on perovskite oxide nanoparticles and intertwined

carbon nanotubes for rechargeable Zinc-air battery applications. ACS Appl Mater Interfaces 7 (1):902-910. doi:10.1021/am507470f

141. Lee DU, Park MG, Park HW, Seo MH, Ismayilov V, Ahmed R, Chen ZW (2015) Highly active Co-doped $LaMnO_3$ perovskite oxide and N-doped carbon nanotube hybrid bi-functional catalyst for rechargeable Zinc-air batteries. Electrochem Commun 60:38-41. doi:10.1016/j.elecom.2015.08.001

142. Park HW, Lee DU, Park MG, Ahmed R, Seo MH, Nazar LF, Chen ZW (2015) Perovskite-nitrogen-doped carbon nanotube composite as bifunctional catalysts for rechargeable lithium-air batteries. ChemSusChem 8 (6):1058-1065. doi:10.1002/cssc.201402986

143. Elumeeva K, Masa J, Sierau J, Tietz F, Muhler M, Schuhmann W (2016) Perovskite-based bifunctional electrocatalysts for oxygen evolution and oxygen reduction in alkaline electrolytes. Electrochim Acta 208:25-32. doi:10.1016/j.electacta.2016.05.010

144. Hu J, Liu Q, Shi Z, Zhang L, Huang H (2016) $LaNiO_3$-nanorod/graphene composite as an efficient bi-functional catalyst for Zinc-air batteries. RSC Adv 6 (89):86386-86394. doi:10.1039/c6ra16610e

145. Ge X, Goh FWT, Li B, Hor TSA, Zhang J, Xiao P, Wang X, Zong Y, Liu Z (2015) Efficient and durable oxygen reduction and evolution of a hydrothermally synthesized $La(Co_{0.55}Mn_{0.45})_{0.99}O_{3-\delta}$ nanorod/graphene hybrid in alkaline media. Nanoscale 7 (19):9046-9054. doi:10.1039/c5nr01272d

146. Prabu M, Ramakrishnan P, Ganesan P, Manthiram A, Shanmugam S (2015) $LaTi_{0.65}Fe_{0.35}O_{3-\delta}$ nanoparticle-decorated nitrogen-doped carbon nanorods as an advanced hierarchical air electrode for rechargeable metal-air batteries. Nano Energy 15:92-103. doi:10.1016/j.nanoen.2015.04.005

147. Katsounaros I, Cherevko S, Zeradjanin AR, Mayrhofer KJJ (2014) Oxygen electrochemistry as a cornerstone for sustainable energy conversion. Angew Chem Int Ed 53 (1):102-121. doi:10.1002/anie.201306588

148. Hardin WG, Slanac DA, Wang X, Dai S, Johnston KP, Stevenson KJ (2013) Highly active, nonprecious metal perovskite electrocatalysts for bifunctional metal-air battery electrodes. J Phys Chem Lett 4 (8):1254-1259. doi:10.1021/jz400595z

149. Hardin WG, Mefford JT, Slanac DA, Patel BB, Wang X, Dai S, Zhao X, Ruoff RS, Johnston KP, Stevenson KJ (2014) Tuning the electrocatalytic activity of

perovskites through active site variation and support interactions. Chem Mater 26 (11):3368-3376. doi:10.1021/cm403785q

150. Pham TV, Guo HP, Luo WB, Chou SL, Wang JZ, Liu HK (2017) Carbon- and binder-free 3D porous perovskite oxide air electrode for rechargeable lithium-oxygen batteries. J Mater Chem A 5 (11):5283-5289. doi:10.1039/c6ta10751f

151. Li B-Q, Tang C, Wang H-F, Zhu X-L, Zhang Q (2016) An aqueous preoxidation method for monolithic perovskite electrocatalysts with enhanced water oxidation performance. Sci Adv 2 (10):e1600495. doi:10.1126/sciadv.1600495

152. Neagu D, Tsekouras G, Miller DN, Ménard H, Irvine JTS (2013) In situ growth of nanoparticles through control of non-stoichiometry. Nature Chem 5:916-923. doi:10.1038/nchem.1773

153. Zhu Y, Dai J, Zhou W, Zhong Y, Wang H, Shao Z (2018) Synergistically enhanced hydrogen evolution electrocatalysis by in situ exsolution of metallic nanoparticles on perovskites. J Mater Chem A 6:13582-13587. doi:10.1039/C8TA02347F

154. Zhang Y-Q, Tao H-B, Liu J, Sun Y-F, Chen J, Hua B, Thundat T, Luo J-L (2017) A rational design for enhanced oxygen reduction: Strongly coupled silver nanoparticles and engineered perovskite nanofibers. Nano Energy 38:392-400. doi:10.1016/j.nanoen.2017.06.006

155. Sun Y-F, Li J-H, Cui L, Hua B, Cui S-H, Li J, Luo J-L (2015) A-site-deficiency facilitated in situ growth of bimetallic Ni-Fe nano-alloys: A novel coking-tolerant fuel cell anode catalyst. Nanoscale 7 (25):11173-11181. doi:10.1039/C5NR02518D

156. Du Z, Zhao H, Yi S, Xia Q, Gong Y, Zhang Y, Cheng X, Li Y, Gu L, Świerczek K (2016) High-performance anode material $Sr_2FeMo_{0.65}Ni_{0.35}O_{6-\delta}$ with in situ exsolved nanoparticle catalyst. ACS Nano 10 (9):8660-8669. doi:10.1021/acsnano.6b03979

157. Gao Y, Wang J, Lyu YQ, Lam KY, Ciucci F (2017) In situ growth of Pt_3Ni nanoparticles on an A-site deficient perovskite with enhanced activity for the oxygen reduction reaction. J Mater Chem A 5 (14):6399-6404. doi:10.1039/C7TA00349H

158. Wu N, Wang W, Zhong Y, Yang G, Qu J, Shao Z (2017) Nickel-iron alloy nanoparticle-decorated K_2NiF_4-type oxide as an efficient and sulfur-tolerant anode for solid oxide fuel cells. ChemElectroChem 4 (9):2378-2384. doi:10.1002/celc.201700211

159. Hua B, Li M, Sun Y-F, Zhang Y-Q, Yan N, Chen J, Thundat T, Li J, Luo J-L (2017) A coupling for success: Controlled growth of Co/CoO_x nanoshoots on perovskite mesoporous nanofibres as high-performance trifunctional electrocatalysts in alkaline condition. Nano Energy 32:247-254. doi:10.1016/j.nanoen.2016.12.044
160. Song Y, Wang W, Ge L, Xu X, Zhang Z, Julião PSB, Zhou W, Shao Z (2017) Rational design of a water-storable hierarchical architecture decorated with amorphous barium oxide and nickel nanoparticles as a solid oxide fuel cell anode with excellent sulfur tolerance. Adv Sci 4 (11):1700337. doi:10.1002/advs.201700337
161. Liang F, Sunarso J, Mao J, Yang Z, Zhou W (2017) Amorphous $Ni_{0.75}Fe_{0.25}(OH)_2$-decorated layered double perovskite $Pr_{0.5}Ba_{0.5}CoO_{3-\delta}$ for highly efficient and stable water oxidation. ChemElectroChem 4 (3):550-556. doi:10.1002/celc.201600718
162. Gong Y, Zhang X, Li Z, Wang Z, Sun C, Chen L (2017) Perovskite $La_{0.6}Sr_{0.4}Co_{0.2}Fe_{0.8}O_3$ nanofibers decorated with RuO_2 nanoparticles as an efficient bifunctional cathode for rechargeable Li-O_2 batteries. ChemNanoMat 3 (7):485-490. doi:10.1002/cnma.201700071
163. Zhang X, Gong Y, Li S, Sun C (2017) Porous perovskite $La_{0.6}Sr_{0.4}Co_{0.8}Mn_{0.2}O_3$ nanofibers loaded with RuO_2 nanosheets as an efficient and durable bifunctional catalyst for rechargeable Li-O_2 batteries. ACS Catal 7 (11):7737-7747. doi:10.1021/acscatal.7b02153
164. Kim S, Kwon O, Kim C, Gwon O, Jeong HY, Kim KH, Shin J, Kim G (2018) Strategy for enhancing interfacial effect of bifunctional electrocatalyst: Infiltration of cobalt nanooxide on perovskite. Adv Mater Interfaces 5(12):1800123. doi:10.1002/admi.201800123
165. Liu R, Liang F, Zhou W, Yang Y, Zhu Z (2015) Calcium-doped lanthanum nickelate layered perovskite and nickel oxide nano-hybrid for highly efficient water oxidation. Nano Energy 12:115-122. doi:10.1016/j.nanoen.2014.12.025
166. Zhu Y, Su C, Xu X, Zhou W, Ran R, Shao Z (2014) A universal and facile way for the development of superior bifunctional electrocatalysts for oxygen reduction and evolution reactions utilizing the synergistic effect. Chem Eur J 20 (47):15533-15542. doi:10.1002/chem.201403192
167. May KJ, Carlton CE, Stoerzinger KA, Risch M, Suntivich J, Lee Y-L, Grimaud A, Shao-Horn Y (2012) Influence of Oxygen evolution during water oxidation on the surface of perovskite oxide catalysts. J Phys Chem Lett 3 (22):3264-3270. doi:10.1021/jz301414z

168. Risch M, Grimaud A, May KJ, Stoerzinger KA, Chen TJ, Mansour AN, Shao-Horn Y (2013) Structural changes of cobalt-based perovskites upon water oxidation investigated by EXAFS. J Phys Chem C 117 (17):8628-8635. doi:10.1021/jp3126768
169. Han B, Stoerzinger Kelsey A, Tileli V, Gamalski Andrew D, Stach Eric A, Shao-Horn Y (2017) Nanoscale structural oscillations in perovskite oxides induced by oxygen evolution. Nature Mater 16:121-126. doi:10.1038/nmat4764
170. Seitz LC, Dickens CF, Nishio K, Hikita Y, Montoya J, Doyle A, Kirk C, Vojvodic A, Hwang HY, Norskov JK, Jaramillo TF (2016) A highly active and stable $IrO_x/SrIrO_3$ catalyst for the oxygen evolution reaction. Science 353 (6303):1011-1014. doi:10.1126/science.aaf5050
171. Yu J, Sunarso J, Zhu Y, Xu X, Ran R, Zhou W, Shao Z (2016) Activity and stability of Ruddlesden–Popper-type $La_{n+1}Ni_nO_{3n+1}$ (n=1, 2, 3, and ∞) electrocatalysts for oxygen reduction and evolution reactions in alkaline media. Chem Eur J 22 (8):2719-2727. doi:10.1002/chem.201504279
172. Bick DS, Kindsmüller A, Staikov G, Gunkel F, Müller D, Schneller T, Waser R, Valov I (2016) Stability and degradation of perovskite electrocatalysts for oxygen evolution reaction. Electrochim Acta 218:156-162. doi:10.1016/j.electacta.2016.09.116
173. Bick DS, Kindsmueller A, Cho D-Y, Mohamed AY, Bredow T, Laufen H, Gunkel F, Mueller DN, Schneller T, Waser R (2017) Self-assembling oxide catalyst for electrochemical water splitting. arXiv preprint arXiv:170703346
174. Bick DS, Krebs TB, Kleimaier D, Zurhelle AF, Staikov G, Waser R, Valov I (2018) Degradation kinetics during oxygen electrocatalysis on perovskite-based surfaces in alkaline media. Langmuir 34 (4):1347-1352. doi:10.1021/acs.langmuir.7b03733
175. Tan P, Liu M, Shao Z, Ni M (2017) Recent advances in perovskite oxides as electrode materials for nonaqueous lithium-oxygen batteries. Adv Energy Mater 7 (13):1602674. doi:10.1002/aenm.201602674
176. Bruce PG, Freunberger SA, Hardwick LJ, Tarascon J-M (2012) Li–O_2 and Li–S batteries with high energy storage. Nature Mater 11:19-29. doi:10.1038/nmat3191
177. Xu J-J, Wang Z-L, Xu D, Meng F-Z, Zhang X-B (2014) 3D ordered macroporous $LaFeO_3$ as efficient electrocatalyst for Li-O_2 batteries with enhanced rate capability and cyclic performance. Energy Environ Sci 7 (7):2213-2219. doi:10.1039/C3EE42934B

178. Xu J-J, Xu D, Wang Z-L, Wang H-G, Zhang L-L, Zhang X-B (2013) Synthesis of perovskite-based porous $La_{0.75}Sr_{0.25}MnO_3$ nanotubes as a highly efficient electrocatalyst for rechargeable lithium–oxygen batteries. Angew Chem Int Ed 52 (14):3887-3890. doi:10.1002/anie.201210057
179. Zhang T, Zhou H (2013) A reversible long-life lithium–air battery in ambient air. Nat Commun 4:1817. doi:10.1038/ncomms2855
180. Roger I, Shipman MA, Symes MD (2017) Earth-abundant catalysts for electrochemical and photoelectrochemical water splitting. Nat Rev Chem 1:0003. doi:10.1038/s41570-016-0003
181. Zeng K, Zhang D (2010) Recent progress in alkaline water electrolysis for hydrogen production and applications. Progr Energy Combust Sci 36 (3):307-326. doi:10.1016/j.pecs.2009.11.002
182. LeRoy RL (1983) Industrial water electrolysis: Present and future. Int J Hydrogen Energy 8 (6):401-417. doi:10.1016/0360-3199(83)90162-3
183. Zhu Y, Zhou W, Zhong Y, Bu Y, Chen X, Zhong Q, Liu M, Shao Z (2017) A perovskite nanorod as bifunctional electrocatalyst for overall water splitting. Adv Energy Mater 7 (8):1602122. doi:10.1002/aenm.201602122
184. Gorlin Y, Jaramillo TF (2010) A bifunctional nonprecious metal catalyst for oxygen reduction and water oxidation. J Am Chem Soc 132 (39):13612-13614. doi:10.1021/ja104587v
185. Hua B, Li M, Zhang Y-Q, Sun Y-F, Luo J-L (2017) All-in-one perovskite catalyst: Smart controls of architecture and composition toward enhanced oxygen/hydrogen evolution reactions. Adv Energy Mater 7 (20):1700666. doi:10.1002/aenm.201700666
186. Jin H, Wang J, Su D, Wei Z, Pang Z, Wang Y (2015) In situ cobalt–cobalt oxide/N-doped carbon hybrids as superior bifunctional electrocatalysts for hydrogen and oxygen evolution. J Am Chem Soc 137 (7):2688-2694. doi:10.1021/ja5127165
187. Li X, Walsh FC, Pletcher D (2011) Nickel based electrocatalysts for oxygen evolution in high current density, alkaline water electrolysers. Phys Chem Chem Phys 13 (3):1162-1167. doi:10.1039/C0CP00993H

Chapter 3 Methodologies and characterizations*

** This chapter summarizes the materials synthesis, characterizations, and electrochemical measurements. Part of this chapter is reprinted (adapted) with permission from (Xiaomin Xu, Yangli Pan, Yijun Zhong, Lei Ge, San Ping Jiang, Zongping Shao, From scheelite $BaMoO_4$ to perovskite $BaMoO_3$: Enhanced electrocatalysis toward the hydrogen evolution in alkaline media, Composites Part B: Engineering, 2020, 198, 108214). Copyright (2020) Elsevier Ltd.*

3.1 Materials syntheses

3.1.1 Mo-based perovskite

Scheelite-type oxide $BaMoO_4$ was synthesized by a co-precipitation method. Barium chloride dihydrate ($BaCl_2 \cdot 2H_2O$, 99.0%, Chem-Supply Pty Ltd) and ammonium heptamolybdate tetrahydrate ($(NH_4)_6Mo_7O_{24} \cdot 4H_2O$, 81.0–83.0% as MoO_3, Chem-Supply Pty Ltd) were used as the metal sources, which were dissolved separately into ultrapure water (18.2 MΩ cm, Milli-Q) to a metal concentration of 1 M. Ammonium hydroxide solution (NH_4OH, 28.0–30.0%, Chem-Supply Pty Ltd) was then added to both solutions to reach pH = 10. Afterwards, the Ba-containing solution was pipetted slowly into the Mo-containing solution with constant stirring at ambient temperature, during which the co-precipitation reaction occurs according to Equation 1. The resultant precipitate was digested for 24 h, filtered and washed with Milli-Q water, dried in vacuum at 80 °C, and finally heat-treated in air at 600 °C for 10 h to obtain the $BaMoO_4$ product with high crystallinity.

$$Ba^{2+}(aq) + MoO_4^{2-}(aq) \rightarrow BaMoO_4(s) \quad (1)$$

Perovskite-type oxide $BaMoO_3$ was prepared by a reduction process. The as-obtained $BaMoO_4$, loaded into a quartz tube, was heated to 900 °C at a temperature ramping rate of 5 °C min^{-1}, held at this temperature for 3 h, and then cooled to ambient temperature naturally to yield the $BaMoO_3$ product, during which high-purity H_2 (99.999%, BOC) was introduced at a flow rate of 150 ml min^{-1} to serve as a reducing agent. The reduction reaction during this process can be expressed as below:

$$BaMoO_4(s) + H_2(g) \rightarrow BaMoO_3(s) + H_2O(g) \quad (2)$$

3.1.2 Fe-based perovskites $La_{1-x}(Ba_{0.5}Sr_{0.5})_xFeO_{3-\delta}$

Fe-based perovskites $La_{1-x}(Ba_{0.5}Sr_{0.5})_xFeO_{3-\delta}$ (x = 0.0, 0.2, 0.5, 0.8, and 1.0) were prepared by a sol–gel process. In brief, lanthanum nitrate hexahydrate ($La(NO_3)_3 \cdot 6H_2O$, 99.99%, Sigma-Aldrich), barium nitrate ($Ba(NO_3)_2$, ≥99%, Sigma-Aldrich), strontium nitrate ($Sr(NO_3)_2$, ≥99.0%, Sigma-Aldrich), and iron nitrate nonahydrate ($Fe(NO_3)_3 \cdot 9H_2O$, ≥98%, Sigma-Aldrich) were weighed at their stochiometric ratios and dissolved in Milli-Q water under constant stirring. Afterwards, ethylenediaminetetraacetic acid (EDTA, ≥99%, Sigma-Aldrich) and citric acid (CA, 99.5%, Chem-Supply Pty Ltd) were introduced as complexing agents into the solution at a molar ratio of 1:2:1 for EDTA/CA/total metal content. To guarantee complete

complexation, an ammonium hydroxide solution (NH_4OH, 28.0–30.0%, Chem-Supply Pty Ltd) was added to adjust the solution pH to a value close to 6. The mixed solution was then continuously stirred at 150 °C to allow for the evaporation of water and the formation of a clear gel. The gel was baked in a furnace at 250 °C (at a temperature ramping rate of 5 °C min^{-1}) for 5 h to yield a solid precursor, which was further calcined in air at a furnace temperature of 1100 °C (at a temperature ramping rate of 5 °C min^{-1}) for 5 h to obtain the final products. The calcined samples were finely ground using a mortar and pestle prior to use.

3.1.3 Co-based perovskites $BaCo_{0.7}Fe_{0.3}O_{3-\delta}$

The hexagonal-structured $BaCo_{0.7}Fe_{0.3}O_{3-\delta 1}$ perovskite (denoted as *h*-BCF) and $BaCo_{0.8}Fe_{0.2}O_{3-\delta}$ (BCF82) were prepared by a sol–gel process using procedures similar to those for $La_{1-x}(Ba_{0.5}Sr_{0.5})_xFeO_{3-\delta}$, except that the metal sources used are barium nitrate ($Ba(NO_3)_2$, ≥99%, Sigma-Aldrich), cobalt nitrate hexahydrate ($Co(NO_3)_2 \cdot 6H_2O$, ≥98%, Sigma-Aldrich), and iron nitrate nonahydrate ($Fe(NO_3)_3 \cdot 9H_2O$, ≥98%, Sigma-Aldrich), and that the calcination was conducted in air at a furnace temperature of 1000 °C (at a temperature ramping rate of 5 °C min^{-1}) for 10 h to obtain the final products.

The cubic-structured $BaCo_{0.7}Fe_{0.3}O_{3-\delta 2}$ perovskite (denoted as *c*-BCF) was prepared by reducing *h*-BCF in an inert nitrogen atmosphere. The as-prepared *h*-BCF was loaded into a quartz tube, heated to 900 °C at a temperature ramping rate of 5 °C min^{-1}, held at this temperature for 0.5 h, and then cooled to ambient temperature naturally to yield the *c*-BCF product, during which high-purity N_2 (99.999%, BOC) was introduced at a flow rate of 150 ml min^{-1} to serve as a reducing agent. The reduction reaction during this process can be expressed as below:

$$BaCo_{0.7}Fe_{0.3}O_{3-\delta 1}\ (\text{hexagonal}) \rightarrow BaCo_{0.7}Fe_{0.3}O_{3-\delta 2}\ (\text{cubic}) + 1/2(\delta 2 - \delta 1)O_2 \qquad (3)$$

3.1.4 Alkali-metal-doped perovskites $La_{1-x}Na_xFeO_{3-\delta}$

Alkali-metal-doped lanthanum ferrites ($La_{1-x}Na_xFeO_{3-\delta}$, x = 0, 0.05, 0.1, 0.2, and 0.3) were prepared by a modified sol–gel process with a reduced calcination temperature for phase formation. Most of the experimental procedures are similar to those for $La_{1-x}(Ba_{0.5}Sr_{0.5})_xFeO_{3-\delta}$, except that the metal sources used are lanthanum nitrate hexahydrate ($La(NO_3)_3 \cdot 6H_2O$, 99.99%, Sigma-Aldrich), sodium nitrate ($NaNO_3$, 99.0%, Chem-Supply Pty Ltd), and iron nitrate nonahydrate ($Fe(NO_3)_3 \cdot 9H_2O$, ≥98%, Sigma-Aldrich), and that the calcination was conducted in air at a furnace temperature

of 600 °C (at a temperature ramping rate of 2.5 °C min^{-1}) for 3 h to obtain the final products.

3.2 Materials characterizations

X-ray diffraction (XRD): The crystalline structure was investigated by X-ray diffraction (XRD, Bruker D8 Advance) using Cu Kα radiation (λ = 0.15418 nm) at a tube voltage of 40 kV and a tube current of 40 mA. All XRD patterns were collected under ambient conditions. Rietveld refinement of the XRD patterns was performed using the GSAS program and EXPGUI interface to obtain detailed information about the phase structure.[1]

***In situ* X-ray diffraction**: The structural evolution of *h*-BCF in the temperature range from room temperature to 900 °C under an air atmosphere was investigated by *in situ* X-ray diffraction (Rigaku Smartlab 3kW) using Cu Kα radiation (λ = 0.15418 nm) at a tube voltage of 40 kV and a tube current of 40 mA. The sample was loaded on an alumina holder and data were first collected at room temperature. Afterwards, the sample was heated to 900 °C at a temperature ramping rate of 5 °C min^{-1}, and data were collected in the 500–900 °C range with an interval of 50 °C after the sample was settled for 10 min at each temperature point. After data collection at 900 °C, the temperature program was reversed to allow the cooling of the sample and data were recorded at the same temperature range as that of the heating process. Data was also collected when the sample was cooled to room temperature.

Transmission electron microscopy (TEM): The crystalline structure was also gleaned by high-resolution transmission electron microscopy (TEM, FEI Titan G2 80-200) at a 200 kV accelerating voltage. Fast Fourier transform (FFT) patterns were obtained using the Fiji (Fiji Is Just ImageJ) software.[2] High-angle annular dark-field scanning TEM (HAADF-STEM) imaging and energy-dispersive X-ray spectroscopy (EDS) mapping were also performed. The selected-area electron diffraction (SAED) patterns were collected for $La_{1-x}(Ba_{0.5}Sr_{0.5})_xFeO_{3-\delta}$ (x = 0.8) sample. The TEM specimens were prepared by dripping a small portion of the sample powders dispersed in ethanol onto a carbon-coated Cu grid.

Scanning electron microscopy (SEM): The microstructure was studied by field-emission scanning electron microscopy (SEM) using either a Zeiss 1555 or a Zeiss

Neon 40EsB microscope. The SEM specimens were prepared by depositing the sample powders on a double-sided adhesive carbon tape attached to a SEM holder.

N_2 sorption measurements: The specific surface area was calculated by the Brunauer–Emmett–Teller (BET) method using data from the nitrogen sorption measurements conducted at the nitrogen boiling point (−196 °C) on instruments of Micromeritics Tristar 3000, BELSORP-mini II, or Quantachrome AutoSorb-iQ3. The samples were outgassed under vacuum at 200 °C for 5–10 h prior to the measurements.

Inductively coupled plasma-optical emission spectrometry (ICP-OES): The atomic ratio for the sample $La_{1-x}Na_xFeO_{3-\delta}$ (x = 0.2) was analyzed by performing inductively coupled plasma-optical emission spectrometry (ICP-OES) on a PerkinElmer Optima 8300 instrument. The as-prepared powdery sample was dissolved in concentrated nitric acid and then diluted to a certain concentration for the measurement.

Thermogravimetric and differential scanning calorimetry analysis (TG-DSC): To investigate the reduction process from *h*-BCF to *c*-BCF, a combined thermogravimetric and differential scanning calorimetry analysis (TG-DSC) was performed under an argon (Ar) atmosphere on a PerkinElmer TGA 8000 instrument. About 30 mg of the *h*-BCF powder was loaded into an alumina crucible, heated to 900 °C at a temperature ramping rate of 5 °C min^{-1}, and further held under this temperature for 1 h.

Oxygen temperature-programmed desorption (O_2-TPD): The reduction process from *h*-BCF to *c*-BCF was also studied by oxygen temperature-programmed desorption (O_2-TPD), which was performed in pure Ar (15 mL min^{-1}) at a temperature up to 930 °C with a temperature ramping rate of 10 °C min^{-1} and a holding period at 930 °C for 1.5 h. The sample was sieved into 150-mesh granule and about 0.15 g of the granule was used for the O_2-TPD experiment. The effluent gases were analyzed by a mass spectrometer (Hiden, QIC-20) to monitor the desorbed oxygen signal.

Electrical conductivity measurement: The electrical conductivity of $BaMoO_4$ and $BaMoO_3$ was characterized in air at ambient temperature using a four-probe DC method. The $BaMoO_4$ powder was pressed and sintered into dense bar-shaped specimens with an approximate geometric dimension of 2 mm × 6 mm × 20 mm. The $BaMoO_3$ bar was obtained by reducing the $BaMoO_4$ bar under conditions identical to

those for the reduction synthesis of $BaMoO_3$ powder. Two silver wires acting as the current leads were fixed to the top and bottom surfaces of the bar using silver paste and another two silver wires serving as the voltage probes were fixed to the side surfaces of the bar. A constant direct current (DC) was applied to the current leads, and the voltage response at the voltage probes was collected by a source meter (Keithley 2440 5A) using the LabVIEW software (National Instruments). The electrical conductivity was quantified using the relationship given by Equation 4, where l is the shortest distance between the voltage probes, S is the smallest cross-sectional area, and R is the electrical resistance obtained from the current versus voltage plot, respectively.

$$\sigma = \frac{1}{R} \times \frac{l}{S} \tag{4}$$

Raman spectroscopy: The crystalline information was also gathered by Raman spectroscopy, which was performed at room temperature on a Horiba LabRAM HR Evolution Raman microscope using 532 nm laser as the radiation source.

X-ray photoelectron spectroscopy (XPS): The surface chemical composition and electronic state were scrutinized by X-ray photoelectron spectroscopy (XPS, Kratos AXIS Ultra DLD) using a monochromatic Al Kα source ($h\nu$ = 1486.6 eV). The electron binding energy scale was calibrated by referencing the C 1s peak to 284.8 eV. The peak fitting of the XPS data was performed by using the public software package XPSPEAK 4.1.

X-ray absorption spectroscopy (XAS): The electronic state of the samples was also analyzed by X-ray absorption spectroscopy (XAS) performed at synchrotron facilities. The XAS experiments for the $La_{1-x}(Ba_{0.5}Sr_{0.5})_xFeO_{3-\delta}$ samples were conducted at the TLS BL11A beamline of the National Synchrotron Radiation Research Center (NSRRC) in Taiwan. The O *K*-edge soft XAS data were taken in the fluorescence yield mode. To calibrate the photon energy, the O *K*-edge spectra of a NiO sample was simultaneously measured.

The XAS experiments for the $La_{1-x}Na_xFeO_{3-\delta}$ samples were performed at the Soft X-ray (SXR) Beamline at the Australian Synchrotron.[3] The O *K*-edge soft XAS data were collected using a multichannel plate detector in fluorescence yield mode. Data were analyzed using the QANT software package.[4] The photon energy was calibrated by

applying the offset required to shift the concurrently measured reference spectra of MnO powder (for O *K*-edge) to its known energy positions.

3.3 Electrode preparations

The working electrode was prepared by casting a certain aliquot of catalyst dispersion onto a 5-mm-diameter glassy carbon electrode (GCE, Pine Research Instrumentation). Prior to electrode preparation, the GCE was polished to a mirror finish using 0.05 μm α-Al_2O_3 slurries on a polishing cloth and then cleaned by ultrasonication in Milli-Q water.

For $BaMoO_4$ and $BaMoO_3$, the catalyst dispersion was prepared by suspending 10 mg of powder in a mixed solution containing 1 mL of isopropanol and 10 μL of 5 wt% Nafion solution (Nafion® 117 solution, Sigma-Aldrich), followed by ultrasonication for 30 min. Afterwards, 5 μL of this catalyst dispersion was pipetted onto the GCE surface and allowed to dry naturally in air, yielding a loading density of m = 0.253 mg cm^{-2} for the oxide catalyst. Electrodes modified by commercial molybdenum trioxide (MoO_3, 99.5%, Sigma-Aldrich) and molybdenum dioxide (MoO_2, 99.0%, Sigma-Aldrich) were prepared in the same manner to serve as control samples.

For the Fe-based perovskites $La_{1-x}(Ba_{0.5}Sr_{0.5})_xFeO_{3-\delta}$, Co-based perovskites $BaCo_{0.7}Fe_{0.3}O_{3-\delta}$, and alkali-metal-doped perovskites $La_{1-x}Na_xFeO_{3-\delta}$, carbon black (Super P®, Alfa Aesar), which serves as a conductive agent, was added to prepare the catalyst dispersion. 10 mg of perovskite powder was mixed with 2 mg of carbon black in a solution containing 900 μL of absolute ethanol and 100 μL of 5 wt% Nafion solution, followed by ultrasonication for 1 h. Afterwards, 5 μL of this catalyst dispersion was pipetted onto the GCE surface and allowed to dry naturally in air, yielding a loading density of m = 0.255 mg cm^{-2} for the perovskite catalyst.

3.4 Electrochemical measurements

3.4.1 Electrochemical data collection

Electrocatalytic properties of the samples were measured at ambient temperature using a rotating disk electrode configuration (RDE, Pine Research Instrumentation) coupled with an electrochemical workstation (CHI760E, CH Instruments). The electrochemical tests were conducted in a standard three-electrode cell using aqueous potassium hydroxide (KOH) solutions as the alkaline electrolytes. The three-electrode

systems consist of a catalyst-modified GCE as the working electrode, a double junction silver/silver chloride (4 M KCl) (Ag/AgCl, Pine Research Instrumentation) as the reference electrode, and a graphite rod (Pine Research Instrumentation) or a platinum wire (Pine Research Instrumentation) as the counter electrode for the evaluation of the electrocatalytic hydrogen evolution reaction (HER) or oxygen evolution reaction (OER), respectively. For the HER, a 1 M KOH solution was employed as the electrolyte, which was purged with ultrahigh purity Ar (>99.999%, BOC) before and during the HER experiments. For the OER, a 0.1 M KOH solution was used as the electrolyte, which was bubbled with ultrahigh purity O_2 (99.995%, BOC) prior to the OER experiments. The KOH solutions were freshly prepared before each experiment by dissolving high-purity KOH pellets (99.99%, Sigma-Aldrich) into Milli-Q water. The electrocatalytic HER activity was evaluated by performing linear sweep voltammetry (LSV) at a 5 mV s^{-1} scan rate in the potential window of −1.8–−0.9 V vs. Ag/AgCl. The HER stability test was assessed by running 1000 continuous cyclic voltammetry (CV) scans at a 100 mV s^{-1} scan rate in the potential range between −1.5 and −1.1 V vs. Ag/AgCl. The electrocatalytic OER activity was evaluated by performing CV at a slow scan rate of 10 mV s^{-1} in the potential window of 0.2–1.0 or 0.2–1.1 V vs. Ag/AgCl. The OER stability was assessed by running chronopotentiometry with the working electrode held at a constant current density of 5 mA cm_{geo}^{-2}. Throughout these measurements, the working electrode was maintained at a rotation speed of 2000 revolutions per minute (rpm) to readily remove gaseous H_2 or O_2 product generated on the catalyst surface.

3.4.2 Electrochemical data analysis

The measured potentials versus Ag/AgCl were converted to the reversible hydrogen electrode (RHE) by using the following Nernst equation:

$$E_{RHE} = E^0_{Ag/AgCl} + E_{Ag/AgCl} + 0.0591 \times \mathrm{pH} \quad (5)$$

where $E^0_{Ag/AgCl}$ is the standard potential of Ag/AgCl, $E_{Ag/AgCl}$ is the experimentally measured potential versus Ag/AgCl, and E_{RHE} is the converted potential versus RHE, respectively. To compensate for the effect of electrolyte resistance, the potentials reported in this work were further corrected using the below equation:

$$E_{iR\text{-corrected}} = E_{RHE} - iR_s \quad (6)$$

where $E_{\text{iR-corrected}}$ is the corrected potential, i is the current (in A), and R_s is the ohmic electrolyte resistance (~8 Ω for 1 M KOH solution and 45~50 Ω for 0.1 M KOH) obtained from high-frequency alternating current (AC) impedance, respectively. The overpotential (η) is defined as the difference between the corrected potential ($E_{\text{iR-corrected}}$) and the standard equilibrium potential (E^0, which is 0 V or 1.229 V vs. RHE for the HER or OER, respectively) according to the following equation:

$$\eta = |E_{\text{iR-corrected}} - E^0| \tag{7}$$

The as-obtained current was normalized by the geometric area of the GCE, S_{GCE} (0.196 cm^2), to yield the current density j (in mA cm_{geo}^{-2}), as described below:

$$j = 1000 \times i / S_{\text{GCE}} \tag{8}$$

The current density was further normalized by the BET surface area of the perovskite oxides, S_{BET} (in $m^2\ g^{-1}$), to yield the specific activity (SA, in mA cm_{oxide}^{-2}), as shown below:

$$SA = j/(10 \times S_{\text{BET}} \times m) \tag{9}$$

where m is the mass loading of the perovskite oxide catalyst (0.253 or 0.255 mg cm^{-2}).

The polarization data were plotted as the overpotential (η) versus the logarithm of the current density ($\log j$) or the logarithm of the specific activity ($\log SA$) to yield the Tafel plots, whose linear portions at the low overpotential regimes were fitted to the Tafel equation as given below to gain the Tafel slope (b):

$$\eta = a + b\log j \tag{10}$$

or

$$\eta = a + b\log SA \tag{11}$$

3.5 References

(1) Toby, B. EXPGUI, a graphical user interface for GSAS. *J. Appl. Crystallogr.* **2001**, *34*, 210–213.

(2) Schindelin, J.; Arganda-Carreras, I.; Frise, E.; Kaynig, V.; Longair, M.; Pietzsch, T.; Preibisch, S.; Rueden, C.; Saalfeld, S.; Schmid, B. et al. Fiji: an open-source platform for biological-image analysis. *Nat. Methods* **2012**, *9*, 676–682.

(3) Cowie, B. C. C.; Tadich, A.; Thomsen, L. The current performance of the wide range (90–2500 eV) soft X-ray beamline at the Australian Synchrotron. *AIP Conf. Proc.* **2010**, *1234*, 307–310.

(4) Gann, E.; McNeill, C. R.; Tadich, A.; Cowie, B. C. C.; Thomsen, L. Quick AS NEXAFS Tool (QANT): a program for NEXAFS loading and analysis developed at the Australian Synchrotron. *J. Synchrotron Radiat.* **2016**, *23*, 374–380.

Chapter 4 From scheelite $BaMoO_4$ to perovskite $BaMoO_3$: Enhanced electrocatalysis toward the hydrogen evolution in alkaline media*

4.1 Abstract

The discovery of new, inexpensive, and efficient electrocatalysts for the hydrogen evolution reaction (HER) in alkaline solutions holds key to the realization of clean hydrogen production through water electrolysis. While molybdenum (Mo)-based inorganic compounds have been extensively investigated as catalyst candidates toward the alkaline HER, Mo-based oxides, in particular, complex oxides, are rarely explored. Here we report a Mo-containing, metallic $BaMoO_3$ perovskite, which is derived from a scheelite-type, insulating $BaMoO_4$ oxide through a thermal reduction-induced phase transformation, as a potential electrocatalyst for driving the alkaline HER. The $BaMoO_3$ perovskite made of interconnected MoO_6 octahedra is found to be more HER-active than the $BaMoO_4$ scheelite consisting of isolated MoO_4 tetrahedra, showing a significant increase in intrinsic activity by about one order of magnitude, which is due to the stabilized Mo tetravalent state, the increased surface oxygen vacancy concentration, and the improved electrical conductivity of $BaMoO_3$. Importantly, $BaMoO_3$ exhibits a smaller overpotential to deliver a geometric current density of −10 mA cm_{geo}^{-2} when compared with many of the bulk-sized perovskite catalysts comprising other transition metals (e.g., Mn, Fe, Co, and Ni) and the intensively studied Mo-based catalysts (e.g., MoS_2), making it highly promising as an alternative electrocatalyst for the alkaline HER.

4.2 Introduction

Water electrolysis is able to convert electricity to chemical energy stored in the form of hydrogen (H_2), which, unlike the conventional fossil fuels, is regarded as a clean energy carrier, supplying energy without substantial carbon footprints. One critical step involved in the splitting of water is the hydrogen evolution reaction (HER) at the cathode [1-3], which suffers from sluggish kinetics, especially in alkaline solutions, as described by Equation 1. To drive the HER half-reaction, platinum is considered the most efficient electrocatalyst because of its optimal binding to the hydrogen but is limited in widespread use due to its scarcity and prohibitive cost [4, 5]. Molybdenum (Mo) compounds, such as boride [6], carbide [6], phosphide [7], and sulfide [8-10], represent a large group of inexpensive alternatives that afford a suitable hydrogen binding strength and thus exhibit good HER activity. In particular, molybdenum disulfide (MoS_2), known as the very first catalyst material that reopened the fundamental research of the HER electrocatalysis in acidic media [11], has been demonstrated with significant progress in terms of the HER activity over the past decade [12]. However, its catalytic capability in the alkaline media cannot compare with that in the acidic media, which, in principle, is primarily a result of the slower HER kinetics in bases than in acids, often by at least two orders of magnitude [13]. In addition, the pristine MoS_2 is a poor electronic conductor, which requires additional post-treatment or alternative synthetic approach to promote the transformation to or stabilization of a more conducting phase showing enhanced catalytic activity [14, 15]. Therefore, the development of new electrocatalytic materials for efficiently catalyzing the alkaline HER is highly desirable.

$$2H_2O + 2e^- \rightarrow H_2 + 2OH^- \quad (1)$$

Transition metal oxides, as an important class of inorganic compounds, have received considerable attention in the field of electrocatalysis (for instance, the oxygen electrocatalysis) [16] owing to their fascinating physicochemical properties with low cost, high stability, and environmental compatibility. While previously considered as HER-inactive resulting from the inappropriate hydrogen adsorption energy and unsatisfactory electrical conductivity, several unary metal oxides have been rationally designed to allow for increased competitiveness as HER electrocatalysts [17-19]. For example, Gong et al. [17] increased the alkaline HER activity of NiO-based nanostructured materials by constructing heterostructures with Ni metal and coupling

with conductive carbon nanotubes. Qiao and co-workers [18] utilized a strain engineering approach to activate the CoO nanorod catalyst through the introduction of abundant surface oxygen vacancies. In addition, Luo and colleagues [19] prepared a nonstoichiometric, mesoporous MoO_{3-x} oxide using a templating method, which showed favorable alkaline HER performance due to the mesoporous structure, the reduced Mo oxidation state, and the increased electrical conductivity. These endeavors suggest the possibility of making transition metal oxides more catalytically active toward the alkaline HER, both intrinsically and extrinsically, by regulating the electronic structure and/or modifying the material morphology.

Compared to unary metal oxides, multi-metal oxides usually excel in view of the ability to allow for the fine-tuning of their electronic structures and the resultant modulation of the binding with the reaction intermediates, thereby rendering high intrinsic HER activity achievable. Of importance, complex oxides having a perovskite structure, for example, ABO_3 simple perovskites [20] and $AA'B_2O_6$/$A_2BB'O_6$ double perovskites [21] where A is an alkaline-earth or rare-earth metal and B is a transition metal, are known for their compositional and structural flexibility and are therefore well suited for elucidating the structure–property relationships in a variety of catalytic processes such as the oxygen electrocatalysis [22-24], and more recently the alkaline HER electrocatalysis [25-34]. The perovskite structure can stabilize transition metals in their unique oxidation states unusually found in other material structures. For example, palladium (Pd) of mixed trivalent/tetravalent states was stabilized in the $LaFe_{1-x}Pd_xO_{3-\delta}$ perovskite [23], which led to a more than 80 times higher intrinsic activity toward the oxygen reduction as compared to the zerovalent Pd metal. Furthermore, perovskite oxides typically have oxygen defects, often in the form of oxygen vacancies, associated with the changeable transition metal valences or stoichiometries, and such defects can play a decisive role in the electrocatalysis. For instance, the electrocatalytic oxygen evolution reactivity of a silicon-incorporated $SrCo_{1-y}Si_yO_{3-\delta}$ system was found to be significantly higher than that of the parent $SrCoO_{3-\delta}$ [24], due to the formation of extra oxygen vacancies that promoted the lattice oxygen participation during the catalysis. Also importantly, by taking advantage of the nature of the constituent elements in the perovskite structure, the conductivity property of the resultant perovskite oxides can be facilely modulated. This is exemplified by $Ba_{0.5}Sr_{0.5}Co_{0.8}Fe_{0.2}O_{3-\delta}$, which was poorly conductive at room temperature but

experienced a surge in the electrical conductivity upon the partial substitution of barium/strontium with praseodymium in the A-site [30], leading to substantially enhanced performance for the alkaline HER. It is believed that the elegant combination of these unique properties within one single perovskite structure, which is often unattainable in other material systems, can contribute to highly efficient HER electrocatalysis in the alkaline solutions.

In this work, we report a Mo-containing, metallic $BaMoO_3$ perovskite [35-37], which is derived from a scheelite-type, insulating $BaMoO_4$ oxide through a thermal reduction-induced phase transition, as a potential electrocatalyst for facilitating the alkaline HER. While previously investigated as the candidate for the catalytic oxidation of 2-propanol [38] and photocatalytic splitting of water [39], $BaMoO_3$ has not yet been explored as an electrocatalytic material. When evaluated as the alkaline HER electrocatalyst, $BaMoO_3$ exhibits a significantly accelerated HER kinetics as compared with $BaMoO_4$, showing an increase in intrinsic activity by about one order of magnitude, which is likely due to the fact that the $BaMoO_3$ perovskite stabilizes the tetravalent state of Mo, possesses a greater quantity of surface oxygen vacancies, and provides faster electron transport. Notably, $BaMoO_3$ requires a smaller overpotential to reach a given geometric current density of -10 mA cm_{geo}^{-2} when compared with many of the bulk-sized perovskite catalysts comprising other transition metals (for example, Mn, Fe, Co, and Ni) and the intensively explored Mo-based catalysts (including MoS_2), demonstrating its promise as an efficient HER electrocatalyst worthy to be further optimized.

4.3 Results and discussion

4.3.1 Synthesis and structural characterizations

The synthesis of $BaMoO_3$ involves a two-step process. As illustrated in **Figure 4.1**, $BaMoO_4$ was initially prepared through the co-precipitation of Ba^{2+} and MoO_4^{2-} under mildly alkaline conditions, after which $BaMoO_3$ was produced by the thermal reduction of $BaMoO_4$ using H_2 as a reducing agent. Upon thermal reduction, the sample color changes from white for $BaMoO_4$ to dark red for $BaMoO_3$, which, consistent with previous observations [38], suggests that a scheelite-to-perovskite phase transition takes place.

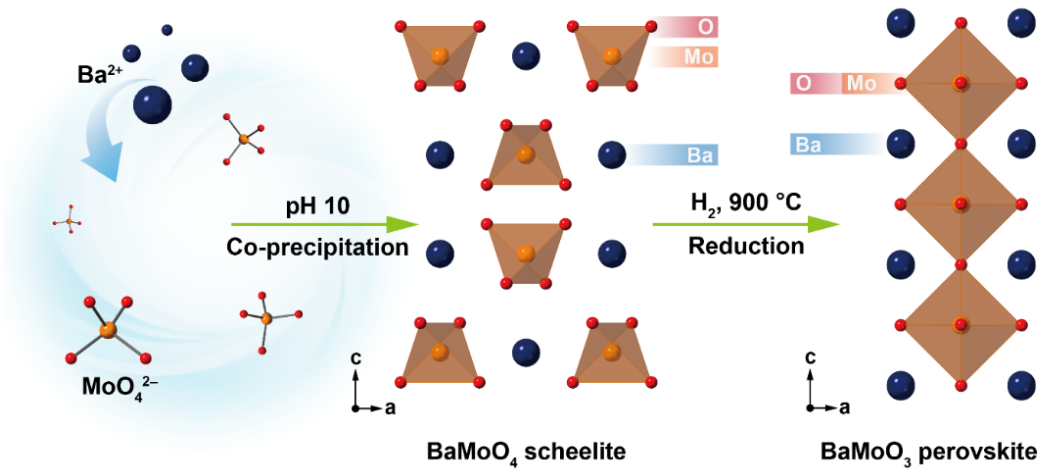

Figure 4.1 Synthesis of $BaMoO_3$ perovskite. A schematic showing the synthesis of $BaMoO_3$ perovskite, involving two steps of co-precipitation synthesis of $BaMoO_4$ scheelite and its subsequent reduction. The atomic arrangements of $BaMoO_4$ and $BaMoO_3$ are viewed along the [010] direction, with *c* axis vertical. In the tetragonal unit cell of the $BaMoO_4$ scheelite, the tetrahedra corresponding to the MoO_4 units are isolated from each other. In the cubic structure of the $BaMoO_3$ perovskite, the octahedra corresponding to the MoO_6 units are interconnected with one another (to illustrate this, the cubic unit cell is triplicated in the *c* direction). For simplicity, the Ba–O coordination is not given.

More direct evidence of the phase transformation comes from the XRD characterization. As shown in **Figure 4.2a**, both $BaMoO_4$ and $BaMoO_3$ exhibited strong, well-defined XRD peaks, indicative of a high level of crystallinity. The XRD peaks of $BaMoO_4$ can be perfectly assigned to the scheelite-type tetragonal structure with a space group of $I4_1/a$, in accord with the International Centre for Diffraction Data (ICDD) Powder Diffraction File (PDF) No. 00-029-0193 [41]. By comparison, the XRD peaks of $BaMoO_3$ align well with those of the perovskite-type cubic structure with a crystal symmetry of $Pm\bar{3}m$ (ICDD PDF No. 01-084-9949 [41]). These phase structures were also verified by a detailed Rietveld refinement analysis (**Figure A.1 and Table A.1, Appendix A**), which gives calculated lattice parameters of $a = 0.5582$ nm and $c = 1.2822$ nm for the tetragonal $BaMoO_4$ and $a = 0.4041$ nm for the cubic $BaMoO_3$. The low-intensity diffraction peak at 2θ of around 40.5° indicates the minor presence of an impurity phase of Mo metal, due likely to the complete reduction of a

fragment of the Mo species [42]. The weight percentage of this Mo impurity phase was quite low, at about 2.5 wt% as determined from the Rietveld refinement.

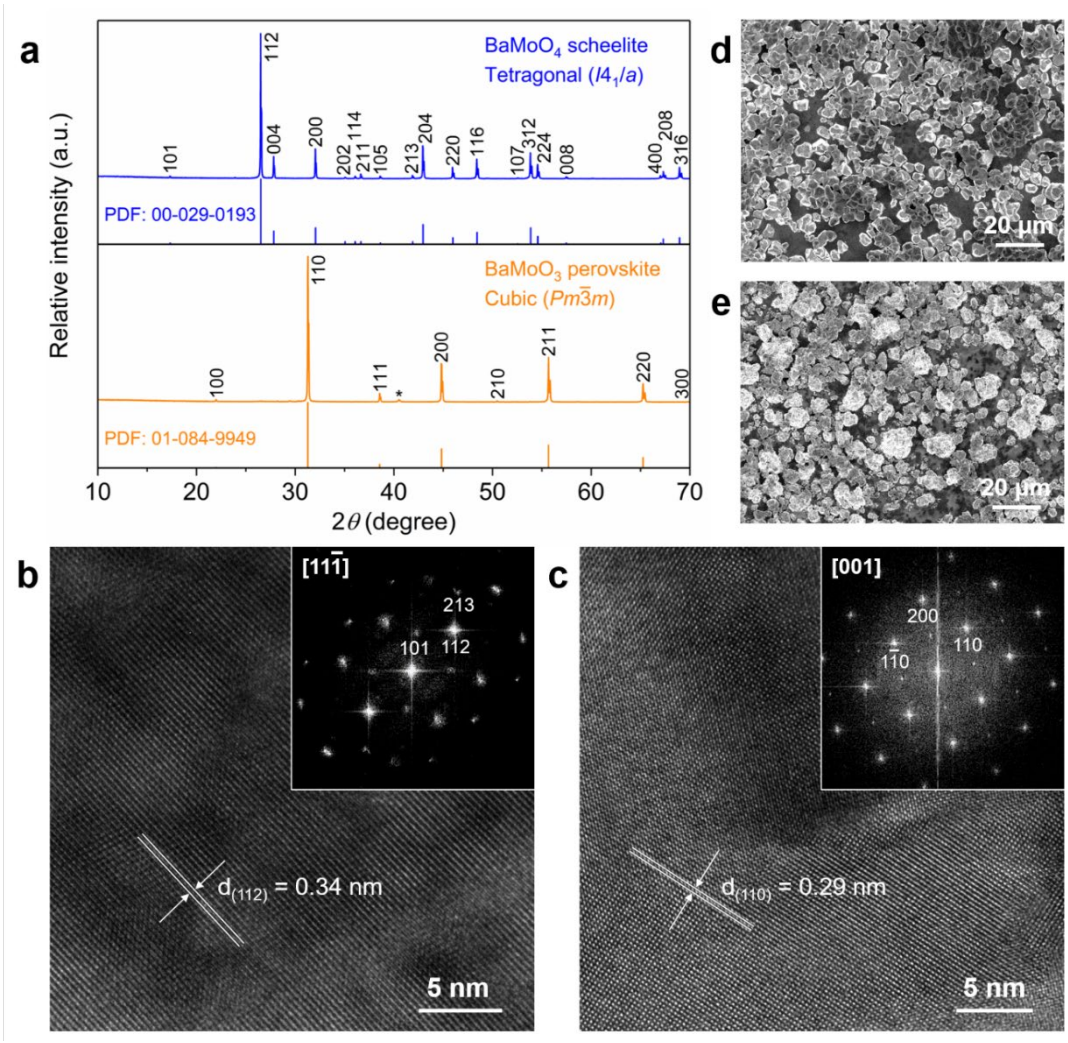

Figure 4.2 Structural characterizations of $BaMoO_3$ perovskite. (a) XRD patterns of $BaMoO_4$ and $BaMoO_3$. The tick marks below the patterns represent the positions of the Bragg reflections of the standards, i.e., the tetragonal phase for $BaMoO_4$ scheelite (space group $I4_1/a$, ICDD PDF No. 00-029-0193) and the cubic phase for $BaMoO_3$ perovskite (space group $Pm\bar{3}m$, ICDD PDF No. 01-084-9949). The peak marked with an asterisk corresponds to the Mo metal phase. (b) High-resolution TEM image of $BaMoO_4$ recorded with the electron beam along the $[11\bar{1}]$ zone axis. (c) High-resolution TEM image of $BaMoO_3$ recorded with the electron beam along the [001] zone axis. Insets in (b) and (c) show the corresponding FFT patterns. (d) SEM image of $BaMoO_4$. (e) SEM image of $BaMoO_3$.

The phase transition is also corroborated by TEM observations. As depicted in **Figure 4.2b** and **c**, lattice fringes with interplanar spacings of 0.34 and 0.29 nm are observed in the high-resolution TEM images, which match the (112) and (110) planes of tetragonal-structured $BaMoO_4$ and cubic-structured $BaMoO_3$, respectively. The distinct crystalline structures of $BaMoO_4$ and $BaMoO_3$ are apparently discernible when one further compares their respective fast Fourier transform (FFT) patterns that reflect the characteristic diffraction spots of the $[11\bar{1}]$ zone axis for $BaMoO_4$ and [001] zone axis for $BaMoO_3$ (insets of **Figure 4.2b** and **c**). As demonstrated in **Figure 4.1**, the two phases are different in that in the tetragonal $BaMoO_4$ scheelite Mo in the hexavalent state (Mo^{6+}) is fourfold coordinated to the O anion forming MoO_4 tetrahedra that are isolated from one another [43], whereas in the cubic $BaMoO_3$ perovskite Mo in the tetravalent state (Mo^{4+}) is sixfold coordinated to the O anion forming MoO_6 octahedra that are corner-shared with each other [42].

The XPS survey spectra reveal that both $BaMoO_4$ and $BaMoO_3$ are composed of Ba, Mo, and O elements (**Figure A.2**). Further, HAADF-STEM imaging and EDS mapping analysis of $BaMoO_3$ suggests that these constituent elements are homogeneously distributed throughout the $BaMoO_3$ sample (**Figure A.3**). The microstructure of $BaMoO_4$ and $BaMoO_3$ was examined by SEM imaging (**Figure 4.2d** and **e**), from which particles with a (sub)micrometer-scale size are seen, signifying their bulk nature. A closer look at the SEM results indicates that the $BaMoO_3$ sample has a somewhat less uniform particle size, which is likely caused by the cracking or sintering of the more uniformly sized $BaMoO_4$ precursor during reduction at elevated temperatures. Nevertheless, both samples exhibit a similar specific surface area, i.e., 0.7 $m^2\ g^{-1}$ for $BaMoO_4$ and 1.2 $m^2\ g^{-1}$ for $BaMoO_3$, as measured from the nitrogen sorption experiments using the BET method.

4.3.2 Evaluation of electrocatalytic performance

The electrocatalytic activity of $BaMoO_4$ and $BaMoO_3$ toward the HER was assessed using a three-electrode configuration in a 1 M KOH solution. **Figure 4.3a** displays the LSV curves where the current is normalized to the geometric area of the GCE substrate and the potential is *iR*-corrected to compensate for the electrolyte resistance. As expected, the bare GCE exhibits negligible HER activity over the potential range of 0.0–−0.7 V vs. RHE [44]. On the contrary, both $BaMoO_4$ and $BaMoO_3$ show a large current response in the same potential range. Noticeably, $BaMoO_3$ displays an earlier

onset potential, as defined to be the potential required to approach a current density of −1 mA cm_{geo}^{-2}, than $BaMoO_4$ does (−0.197 V vs. −0.353 V) and delivers higher current density with the further increase of overpotential (inset of **Figure 4.3a**). When one compares the overpotential required to reach −10 mA cm_{geo}^{-2} (η_{10}), a generic metric related to the production of solar fuels [45], $BaMoO_3$ is found to outperform $BaMoO_4$, showing a reduction in η_{10} by more than 200 mV (i.e., 336 mV vs. 561 mV). Furthermore, the η_{10} value of $BaMoO_3$ is found to be smaller than that of many of the reported bulk-sized, Mo-containing catalysts (e.g., Mo oxide [6] and sulfide [8-10]) and perovskite catalysts (e.g., Mn- [25], Fe- [26, 27], Co- [28-33], and Ni-based [34]) tested under the same alkaline electrolytes (**Figure 4.3b**). This signifies the great promise of $BaMoO_3$ as an efficient catalyst for the alkaline HER.

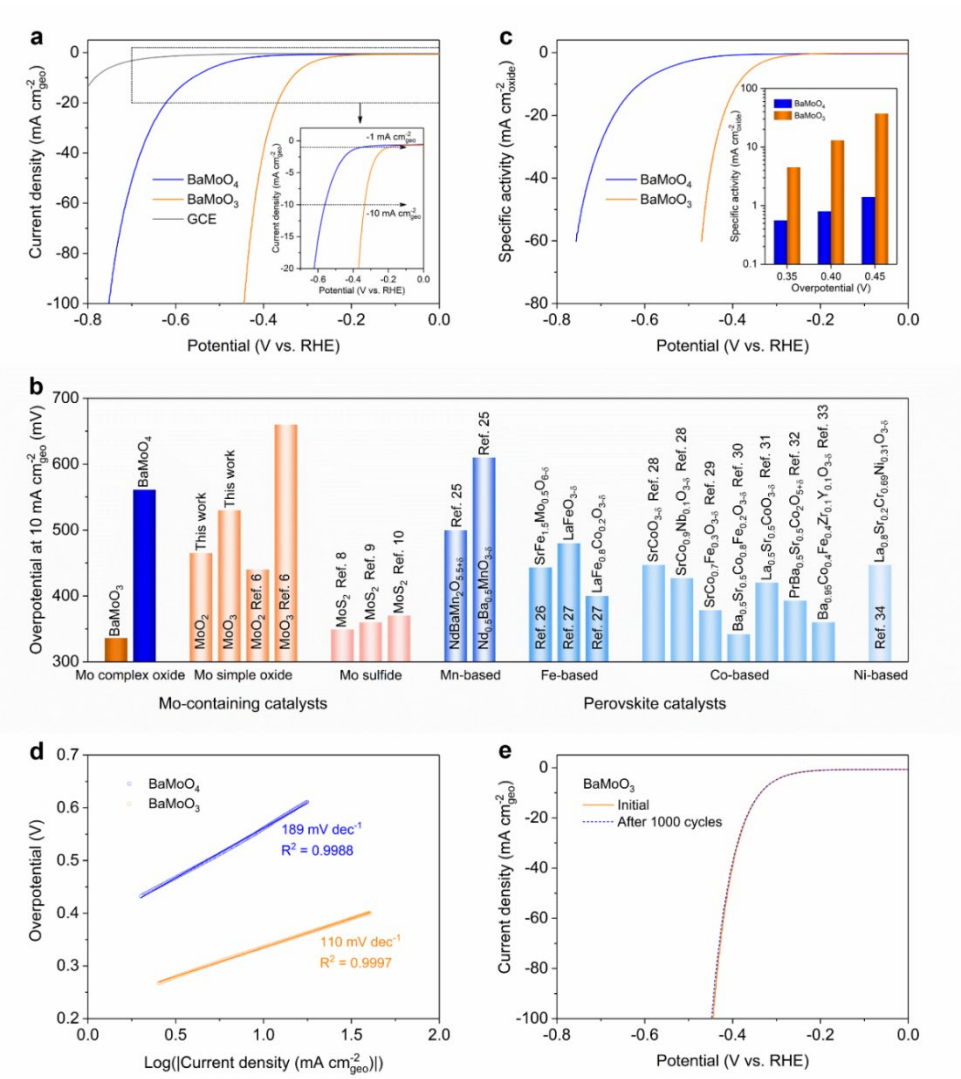

Figure 4.3 Electrocatalytic performance of $BaMoO_3$ perovskite toward the HER in 1 M KOH. (a) LSV curves of $BaMoO_4$ and $BaMoO_3$, where currents are normalized to

the geometric area of GCE (in mA cm_{geo}^{-2}). The LSV curve of GCE is shown for reference. The inset gives an enlargement of the low current density region. (b) A comparison of the HER activity of $BaMoO_4$ and $BaMoO_3$ with other reported bulk-sized, Mo-containing catalysts (e.g., Mo oxide and sulfide) and perovskite catalysts (e.g., Mn-, Fe-, Co-, and Ni-based), using the metric of the overpotential needed to obtain a current density of 10 mA cm_{geo}^{-2}. (c) LSV curves of $BaMoO_4$ and $BaMoO_3$, where currents are normalized to the BET surface area to give the specific activity (in mA cm_{oxide}^{-2}). The inset gives a comparison of the specific activity at select overpotentials. (d) Tafel plots of $BaMoO_4$ and $BaMoO_3$. (e) LSV curves of $BaMoO_3$ before and after 1000 CV cycles.

A comprehensive comparison with literature results is provided in **Table A.2**. It is interesting to note that the $BaMoO_3$ perovskite oxide shows greater HER activity compared to the Mo simple oxides MoO_3 and MoO_2 (**Figure 4.3b, Figure A.4 and A.5**), suggesting that Mo incorporated in a complex oxide framework may perform better than incorporated in a simple oxide structure. It should also be noted that there is still room for the further activity improvement of the $BaMoO_3$ perovskite, as the state-of-the-art perovskite oxide catalysts are reported with even smaller η_{10} values, for example, the well-designed, Co-based $(Gd_{0.5}La_{0.5})BaCo_2O_{5.5+\delta}$ double perovskite having a η_{10} of less than 200 mV [46, 47].

The surface area of an HER electrocatalyst is known to affect its apparent catalytic activity. The HER current of $BaMoO_4$ and $BaMoO_3$ is therefore normalized to their respective BET surface area to obtain the specific activity (**Figure 4.3c**), which serves as a metric for assessing the intrinsic activity [47]. As is obvious from **Figure 4.3c** inset and **Table A.3**, at the select overpotentials of 350, 400, and 450 mV, $BaMoO_3$ showed a significantly higher specific activity than $BaMoO_4$ by approximately one order of magnitude, indicating its greater intrinsic performance.

To elucidate the HER reaction kinetics, Tafel plots were derived from the LSV data and shown in **Figure 4.3d**. The Tafel slope for $BaMoO_3$ was calculated to be 110 mV dec^{-1}, which is much lower than that for $BaMoO_4$ (189 mV dec^{-1}). This manifests the faster HER kinetics on the $BaMoO_3$ perovskite catalyst with respect to the $BaMoO_4$ scheelite catalyst, because a catalyst featuring a smaller Tafel slope tends to give

increased HER currents at smaller increments of overpotential [30]. Furthermore, the Tafel slope of $BaMoO_3$ is lower than that of MoO_3 and MoO_2 (**Figure A.6**) and compares favorably to that of the earlier reported Mo-containing catalysts and perovskite catalysts (**Table A.2**), demonstrating the superior HER kinetics of $BaMoO_3$.

In alkaline media, the HER could take place through either a Volmer–Heyrovsky pathway or a Volmer–Tafel pathway via the below reactions [48]:

(Volmer reaction) $M + H_2O + e^- \leftrightarrow M–H + OH^-$ (2)

(Heyrovsky reaction) $M–H + H_2O + e^- \leftrightarrow H_2 + OH^- + M$ (3)

(Tafel reaction) $2M–H \leftrightarrow H_2 + 2M$ (4)

where M represents an active site onto which the H atom adsorbs. Both pathways involve a Volmer step, in which electron-coupled water dissociation occurs to form the adsorbed M–H intermediate, followed by a Heyrovsky or Tafel step where M–H is transformed into molecular H_2 through different mechanisms. Previous research suggests that the rate-determining step of the alkaline HER could be assigned using the Tafel slope [1]; a Tafel slope near 120, 40, and 30 mV dec^{-1} is anticipated, respectively, for the Volmer, Heyrovsky, and Tafel reaction to be rate-limiting. While the exact catalytic mechanism remains elusive, the Tafel slopes of $BaMoO_4$ and $BaMoO_3$, which are closer to 120 mV dec^{-1} than to 40 or 30 mV dec^{-1}, reveal that they might catalyze the HER following a Volmer–Heyrovsky pathway where the reaction rate is controlled by the Volmer process.

Apart from the catalytic activity, it is also important to examine the electrochemical stability in the assessment of a new type of HER catalyst. For this purpose, the $BaMoO_3$ perovskite catalyst was subjected to 1000 continuous potential cycles. As presented in **Figure 4.3e**, negligible decay is observed for the polarization data recorded before and after the cycling, indicating the good HER stability of $BaMoO_3$ in alkaline electrolytes.

4.3.3 Origins of the activity enhancement

Understanding the origins of the enhanced HER activity observed on the $BaMoO_3$ perovskite relative to the $BaMoO_4$ scheelite is critical to the design of improved electrocatalysts. In complex transition metal oxide catalysts, the transition metal–oxygen building block is assumed to be responsible for the electrocatalytic process

[30]. Therefore, it is believed that the HER activity difference between $BaMoO_4$ and $BaMoO_3$ mainly originates from the intrinsic difference in the respective active site, i.e., disconnected MoO_4 tetrahedra in a tetragonal structure for $BaMoO_4$ and interconnected MoO_6 octahedra in a cubic structure for $BaMoO_3$. From the viewpoint of crystal structure, $BaMoO_3$ with a higher symmetry and better connection of active sites, which offers a collinear covalent bridge of –Mo–O–Mo–O–, is expected to allow for a shorter reaction path and therefore is considered to be more advantageous to the electrocatalysis [46]. More importantly, $BaMoO_3$ has a lower valence state of Mo as compared with $BaMoO_4$ (4+ vs. 6+), which can lead to increased d band filling of Mo and thereby tune the hydrogen adsorption energy in the Volmer process as mentioned earlier [49]. This is directly supported by the similar activity trend of Mo simple oxides in alkaline solutions. As shown in **Figure 4.3b** and **Figure A.5**, MoO_2 with a lower Mo oxidation state delivered greater HER activity than MoO_3, in agreement with literature results [6]. Further evidence comes from the observation that the activity of MoS_2 toward the HER in acidic electrolytes was significantly boosted after a lithium intercalation treatment that caused a reduction in the Mo valence [50].

Considering that the catalyst surface is more relevant to the electrocatalysis [51], high-resolution XPS was conducted to verify the reduced valence of the surface Mo cation in $BaMoO_3$. **Figure 4.4a** shows the Mo 3d core-level XPS spectra of $BaMoO_4$ and $BaMoO_3$. A spin-orbit doublet with peaks at the binding energies of about 232.2 and 235.4 eV was observed in $BaMoO_4$, which can be ascribed to the $3d_{5/2}$ and $3d_{3/2}$ of the Mo cation being at the highest oxidation state (Mo^{6+}) [52]. By comparison, the Mo 3d spectra of $BaMoO_3$ appears to be more complex and can be deconvoluted into four components. The doublet with peaks at 229.2 and 232.4 eV is attributed to Mo^{4+} [50, 53], which, however, only accounts for a small amount of the overall Mo species. This can be explained by the partial oxidation of the $BaMoO_3$ surface during the XPS sample preparation or testing, a phenomenon often encountered on tetravalent Mo-based compounds [53, 54], as evidenced by the doublet (at 231.9 and 235.1 eV) sitting in between the regions of Mo^{4+} and Mo^{6+}. In addition, another doublet with peaks at 227.2 and 230.3 eV is assigned to the metallic molybdenum (Mo^0) [55], in line with the existence of the minor Mo metal phase as detected by XRD. The last doublet was identified at relatively higher binding energies of 234.3 and 237.5 eV, probably associated with the presence of relaxed surface phase, which is complemented by the

emergence of a pair of shoulder peaks at the higher binding energy region of the Ba 3d core lines (**Figure 4.4b**). According to previous reports [56], the appearance of relaxed surface phase is likely caused by the surface defects such as cation defects and oxygen vacancies. Such kind of defects is not unexpected in the $BaMoO_3$ sample obtained from the reduction of $BaMoO_4$, given that a tiny amount of metallic Mo was produced in the same process, which could result in a departure of the Mo stoichiometry from unity and simultaneously lead to the formation of oxygen vacancies to compensate for any possible charge imbalance. This process can be expressed by the following equation, where δ denotes the number of oxygen vacancies.

$$BaMoO_4(s) + (1+\delta)H_2(g) \rightarrow BaMo_{1-\delta/2}O_{3-\delta}(s) + \delta/2Mo(s) + (1+\delta)H_2O(g) \quad (5)$$

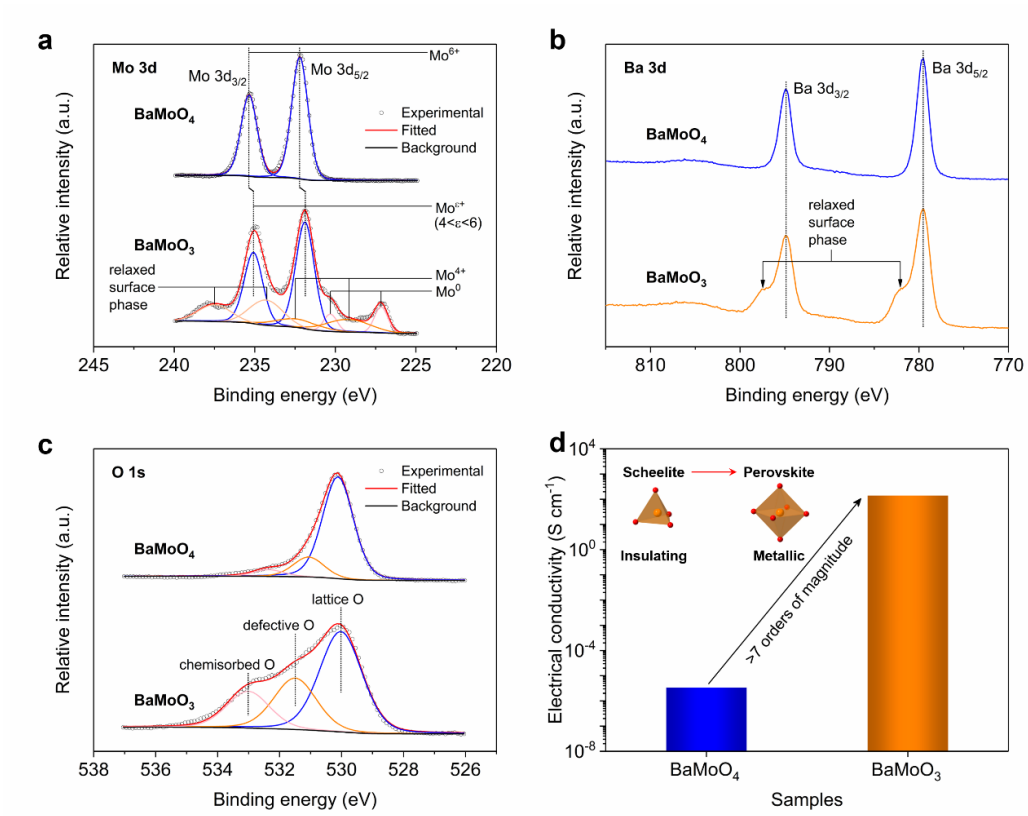

Figure 4.4 Chemical and electrical properties of $BaMoO_3$ perovskite. (a–c) High-resolution XPS spectra of $BaMoO_4$ and $BaMoO_3$. (a) Mo 3d, (b) Ba 3d, and (c) O 1s. (d) Electrical conductivity of $BaMoO_4$ and $BaMoO_3$ measured under ambient conditions. The inset is a schematic illustration of the scheelite-to-perovskite phase transition, along with a change from insulating to metallic conduction.

The formation of oxygen vacancies is thought to be another important factor that contributes to the enhanced HER performance on $BaMoO_3$. Recent theoretical and experimental studies on the transition metal oxide catalysts have suggested that oxygen vacancies on the catalyst surface can facilitate the water dissociation (i.e., the OH–H bond cleavage) [18], a vital step in the Volmer reaction, especially for the alkaline HER [2]. For instance, facile water dissociation was achieved when the surface of a CoO electrocatalyst was enriched with oxygen vacancies by means of strain engineering [18], showing significantly enhanced alkaline HER activity. In our case, the presence of surface oxygen vacancies is also evident in the high-resolution O 1s XPS scans (**Figure 4.4c**), which can be decomposed into three subpeaks that correspond to the lattice oxygen, defective oxygen (i.e., oxygen vacancy), and chemisorbed oxygen, respectively, from low to high binding energies [57]. In addition, after thermal reduction of $BaMoO_4$, the as-obtained $BaMoO_3$ offers a larger formation of surface oxygen vacancies, as indicated by an obvious increase in the concentration of the defective oxygen, which was calculated based on the relative area of the subpeaks (**Table A.4**). It is worth noting that the peak positions for the defective and chemisorbed oxygen shifted to somewhat larger binding energies, which is likely a result of the modification in the coordination environment of Mo with O.

Furthermore, the electrical conductivity of an HER electrocatalyst represents another parameter that is crucial to high catalytic activity. Generally, efficient charge transfer is required for the Volmer reaction to occur. In other words, if the catalyst candidate is not conductive enough to allow for the transfer of electrons to the active sites, the Volmer step will be prevented from proceeding. In fact, the important role of electronic conductivity is widely acknowledged in the HER electrocatalysis on the MoS_2 catalyst [14, 15]. For example, MoS_2 with the semiconducting 2H phase shows limited HER activity due to its high electrical resistance, which can be mitigated through phase transformation to the metallic 1T phase, leading to markedly improved performance [14, 15]. In addition, for Mo simple oxides, the higher HER activity of MoO_2 than MoO_3 is likely associated with their difference in electronic conductivity, as the bulk MoO_2 is metallic whereas MoO_3 is insulating [58]. In a similar fashion, the scheelite-to-perovskite phase change from $BaMoO_4$ to $BaMoO_3$ could give rise to a transition of the electrical conductivity property from insulating to metallic behavior. As presented in **Figure 4.4d**, four-probe DC measurements revealed an electrical

conductivity as low as 3.4×10^{-6} S cm^{-1} for $BaMoO_4$, which agrees with Maji et al.'s testing result [59]. In stark contrast, $BaMoO_3$ shows a drastic increase in the electrical conductivity by more than seven orders of magnitude (1.4×10^2 S cm^{-1}). Note that this value could be underestimated (with literature results approaching 10^3–10^4 S cm^{-1} [35-37]), due likely to the insufficient densification of the $BaMoO_3$ bar prepared from reducing the relatively more densified $BaMoO_4$ bar. Indeed, this metallic nature of $BaMoO_3$ is also supported by its narrow band gap (around 2 eV [39]), much smaller than that of $BaMoO_4$ (above 4 eV [60]). The metallicity of $BaMoO_3$ is closely related to the electronic configuration of the Mo^{4+} ion stabilized in the perovskite structure, which has two electrons filled in the d band, resulting in a large carrier density [37].

4.4 Conclusions

In summary, we have demonstrated how a facile scheelite-to-perovskite phase transition can lead to tremendously improved electrocatalytic properties in barium molybdate catalysts for the alkaline HER, with a reduction in the overpotential by more than 200 mV and a rise in the intrinsic activity by about one order of magnitude. We further show that the interconnected MoO_6 octahedra in the cubic-structured $BaMoO_3$ perovskite is intrinsically more active than the disconnected MoO_4 tetrahedra in the tetragonal-structured $BaMoO_4$ scheelite, which offers a reduced oxidation state of Mo, a larger presence of surface oxygen vacancies, and a higher electrical conductivity of the catalyst material, all favoring the proceeding of the Volmer step in the alkaline HER. Importantly, at this current stage, the promise of the target material researched here (i.e., $BaMoO_3$ perovskite with a bulk particle size) as alkaline HER electrocatalyst is fully showcased, rivaling many of the reported bulk-sized perovskite catalysts containing other transition metals as well as the intensively studied Mo-based catalysts, in particular, MoS_2. Looking back the history of the MoS_2 catalyst, one would find a dramatic growth in its electrocatalytic HER activity over the last decade or so, which is made possible through materials design strategies such as nanostructuring, elemental doping, defect engineering, and crystal phase tuning [12]. In fact, all these strategies can be implemented on the $BaMoO_3$ perovskite, given the versatility of the perovskite structure [51]. Therefore, further progress in promoting the alkaline HER performance of the $BaMoO_3$ perovskite is very much expected in the years to come.

4.5 References

[1] Mahmood N, Yao Y, Zhang J-W, Pan L, Zhang X, Zou J-J. Electrocatalysts for hydrogen evolution in alkaline electrolytes: mechanisms, challenges, and prospective solutions. Adv Sci 2018;5(2):1700464.

[2] Zheng Y, Jiao Y, Vasileff A, Qiao S-Z. The hydrogen evolution reaction in alkaline solution: from theory, single crystal models, to practical electrocatalysts. Angew Chem Int Ed 2018;57(26):7568-79.

[3] Wu C, Du Y, Fu Y, Wang W, Zhan T, Liu Y, et al. MOF-derived formation of nickel cobalt sulfides with multi-shell hollow structure towards electrocatalytic hydrogen evolution reaction in alkaline media. Compos B Eng 2019;177:107252.

[4] Subbaraman R, Tripkovic D, Strmcnik D, Chang K-C, Uchimura M, Paulikas AP, et al. Enhancing hydrogen evolution activity in water splitting by tailoring Li^+-$Ni(OH)_2$-Pt interfaces. Science 2011;334(6060):1256-60.

[5] Ramohlola KE, Monana GR, Hato MJ, Modibane KD, Molapo KM, Masikini M, et al. Polyaniline-metal organic framework nanocomposite as an efficient electrocatalyst for hydrogen evolution reaction. Compos B Eng 2018;137:129-39.

[6] Vrubel H, Hu X. Molybdenum boride and carbide catalyze hydrogen evolution in both acidic and basic solutions. Angew Chem Int Ed 2012;51(51):12703-6.

[7] An T-Y, Surendran S, Kim H, Choe W-S, Kim JK, Sim U. A polydopamine-mediated biomimetic facile synthesis of molybdenum carbide-phosphide nanodots encapsulated in carbon shell for electrochemical hydrogen evolution reaction with long-term durability. Compos B Eng 2019;175:107071.

[8] Zhu D, Liu J, Zhao Y, Zheng Y, Qiao S-Z. Engineering 2D metal–organic framework/MoS_2 interface for enhanced alkaline hydrogen evolution. Small 2019;15(14):1805511.

[9] Zhang L-F, Ke X, Ou G, Wei H, Wang L-N, Wu H. Defective MoS_2 electrocatalyst for highly efficient hydrogen evolution through a simple ball-milling method. Sci China Mater 2017;60(9):849-56.

[10] Zhao G, Lin Y, Rui K, Zhou Q, Chen Y, Dou SX, et al. Epitaxial growth of $Ni(OH)_2$ nanoclusters on MoS_2 nanosheets for enhanced alkaline hydrogen evolution reaction. Nanoscale 2018;10(40):19074-81.

[11] Jaramillo TF, Jørgensen KP, Bonde J, Nielsen JH, Horch S, Chorkendorff I. Identification of active edge sites for electrochemical H_2 evolution from MoS_2 nanocatalysts. Science 2007;317(5834):100-2.
[12] Ding Q, Song B, Xu P, Jin S. Efficient electrocatalytic and photoelectrochemical hydrogen generation using MoS_2 and related compounds. Chem 2016;1(5):699-726.
[13] Durst J, Siebel A, Simon C, Hasché F, Herranz J, Gasteiger HA. New insights into the electrochemical hydrogen oxidation and evolution reaction mechanism. Energy Environ Sci 2014;7(7):2255-60.
[14] Voiry D, Salehi M, Silva R, Fujita T, Chen M, Asefa T, et al. Conducting MoS_2 nanosheets as catalysts for hydrogen evolution reaction. Nano Lett 2013;13(12):6222-7.
[15] Anjum MAR, Jeong HY, Lee MH, Shin HS, Lee JS. Efficient hydrogen evolution reaction catalysis in alkaline media by all-in-one MoS_2 with multifunctional active sites. Adv Mater 2018;30(20):1707105.
[16] Chen D, Chen C, Baiyee ZM, Shao Z, Ciucci F. Nonstoichiometric oxides as low-cost and highly-efficient oxygen reduction/evolution catalysts for low-temperature electrochemical devices. Chem Rev 2015;115(18):9869-921.
[17] Gong M, Zhou W, Tsai M-C, Zhou J, Guan M, Lin M-C, et al. Nanoscale nickel oxide/nickel heterostructures for active hydrogen evolution electrocatalysis. Nat Commun 2014;5:4695.
[18] Ling T, Yan D-Y, Wang H, Jiao Y, Hu Z, Zheng Y, et al. Activating cobalt(II) oxide nanorods for efficient electrocatalysis by strain engineering. Nat Commun 2017;8:1509.
[19] Luo Z, Miao R, Huan TD, Mosa IM, Poyraz AS, Zhong W, et al. Mesoporous MoO_{3-x} material as an efficient electrocatalyst for hydrogen evolution reactions. Adv Energy Mater 2016;6(16):1600528.
[20] Xu X, Wang W, Zhou W, Shao Z. Recent advances in novel nanostructuring methods of perovskite electrocatalysts for energy-related applications. Small Methods 2018;2(7):1800071.
[21] Xu X, Zhong Y, Shao Z. Double perovskites in catalysis, electrocatalysis, and photo(electro)catalysis. Trends Chem 2019;1(4):410-24.
[22] Suntivich J, May KJ, Gasteiger HA, Goodenough JB, Shao-Horn Y. A perovskite oxide optimized for oxygen evolution catalysis from molecular orbital principles. Science 2011;334(6061):1383-5.

[23] Zhu Y, Zhou W, Chen Y, Yu J, Xu X, Su C, et al. Boosting oxygen reduction reaction activity of palladium by stabilizing its unusual oxidation states in perovskite. Chem Mater 2015;27(8):3048-54.

[24] Pan Y, Xu X, Zhong Y, Ge L, Chen Y, Veder J-PM, et al. Direct evidence of boosted oxygen evolution over perovskite by enhanced lattice oxygen participation. Nat Commun 2020;11:2002.

[25] Wang J, Gao Y, Chen D, Liu J, Zhang Z, Shao Z, et al. Water splitting with an enhanced bifunctional double perovskite. ACS Catal 2018;8(1):364-71.

[26] He B, Tan K, Gong Y, Wang R, Wang H, Zhao L. Coupling amorphous cobalt hydroxide nanoflakes on $Sr_2Fe_{1.5}Mo_{0.5}O_{5+\delta}$ perovskite nanofibers to induce bifunctionality for water splitting. Nanoscale 2020;12(16):9048-57.

[27] Dai J, Zhu Y, Zhong Y, Miao J, Lin B, Zhou W, et al. enabling high and stable electrocatalytic activity of iron-based perovskite oxides for water splitting by combined bulk doping and morphology designing. Adv Mater Interfaces 2019;6(1):1801317.

[28] Islam QA, Majee R, Bhattacharyya S. Bimetallic nanoparticle decorated perovskite oxide for state-of-the-art trifunctional electrocatalysis. J Mater Chem A 2019;7(33):19453-64.

[29] Zhang Z, Chen Y, Dai Z, Tan S, Chen D. Promoting hydrogen-evolution activity and stability of perovskite oxides via effectively lattice doping of molybdenum. Electrochim Acta 2019;312:128-36.

[30] Xu X, Chen Y, Zhou W, Zhu Z, Su C, Liu M, et al. A perovskite electrocatalyst for efficient hydrogen evolution reaction. Adv Mater 2016;28(30):6442-8.

[31] Oh NK, Kim C, Lee J, Kwon O, Choi Y, Jung GY, et al. In-situ local phase-transitioned $MoSe_2$ in $La_{0.5}Sr_{0.5}CoO_{3-\delta}$ heterostructure and stable overall water electrolysis over 1000 hours. Nat Commun 2019;10:1723.

[32] Zhang Z, He B, Chen L, Wang H, Wang R, Zhao L, et al. Boosting overall water splitting via FeOOH nanoflake-decorated $PrBa_{0.5}Sr_{0.5}Co_2O_{5+\delta}$ nanorods. ACS Appl Mater Interfaces 2018;10(44):38032-41.

[33] Li X, He L, Zhong X, Zhang J, Luo S, Yi W, et al. Evaluation of A-site Ba^{2+}-deficient $Ba_{1-x}Co_{0.4}Fe_{0.4}Zr_{0.1}Y_{0.1}O_{3-\delta}$ oxides as electrocatalysts for efficient hydrogen evolution reaction. Scanning. 2018;2018:1341608.

[34] Wang Y, Wang Z, Jin C, Li C, Li X, Li Y, et al. Enhanced overall water electrolysis on a bifunctional perovskite oxide through interfacial engineering. Electrochim Acta 2019;318:120-9.

[35] Brixner LH. X-ray study and electrical properties of system $Ba_xSr_{(1-x)}MoO_3$. J Inorg Nucl Chem 1960;14(3):225-30.

[36] Hayashi S, Aoki R, Nakamura T. Metallic conductivity in perovskite-type compounds $AMoO_3$ (A = Ba, Sr, Ca) down to 2.5K. Mater Res Bull 1979;14(3):409-13.

[37] Mizoguchi H, Fukumi K, Kitamura N, Takeuchi T, Hayakawa J, Yamanaka H, et al. Electronic structure of polycrystalline $AMoO_3$ (A=Sr or Ba). J Appl Phys 1999;85(9):6502-5.

[38] Kubo J, Ueda W. Catalytic behavior of $AMoO_x$ (A=Ba, Sr) in oxidation of 2-propanol. Mater Res Bull 2009;44(4):906-12.

[39] Hopper HA, Le J, Cheng J, Weller T, Marschall R, Bloh JZ, et al. An investigation of the optical properties and water splitting potential of the coloured metallic perovskites $Sr_{1-x}Ba_xMoO_3$. J Solid State Chem 2016;234:87-92.

[40] Toby BH. EXPGUI, a graphical user interface for GSAS. J Appl Cryst 2001;34:210-3.

[41] Gates-Rector S, Blanton T. The powder diffraction file: a quality materials characterization database. Powder Diffr 2019;34(4):352-60.

[42] Nassif V, Carbonio RE, Alonso JA. Neutron diffraction study of the crystal structure of $BaMoO_4$: a suitable precursor for metallic $BaMoO_3$ perovskite. J Solid State Chem 1999;146(1):266-70.

[43] Culver SP, Rabuffetti FA, Zhou S, Mecklenburg M, Song Y, Melot BC, et al. Low-temperature synthesis of $AMoO_4$ (A = Ca, Sr, Ba) scheelite nanocrystals. Chem Mater 2013;25(20):4129-34.

[44] Javaid S, Li Y, Chen D, Xu X, Pang Y, Chen W, et al. Spontaneous formation of heterodimer Au–Fe_7S_8 nanoplatelets by a seeded growth approach. J Phys Chem C 2019;123(16):10604-13.

[45] Benck JD, Hellstern TR, Kibsgaard J, Chakthranont P, Jaramillo TF. Catalyzing the hydrogen evolution reaction (HER) with molybdenum sulfide nanomaterials. ACS Catal 2014;4(11):3957-71.

[46] Guan D, Zhou J, Hu Z, Zhou W, Xu X, Zhong Y, et al. Searching general sufficient-and-necessary conditions for ultrafast hydrogen-evolving electrocatalysis. Adv Funct Mater 2019;29(20):1900704.
[47] Guan D, Zhou J, Huang Y-C, Dong C-L, Wang J-Q, Zhou W, et al. Screening highly active perovskites for hydrogen-evolving reaction via unifying ionic electronegativity descriptor. Nat Commun 2019;10:3755.
[48] Stamenkovic VR, Strmcnik D, Lopes PP, Markovic NM. Energy and fuels from electrochemical interfaces. Nat Mater 2017;16:57-69.
[49] Gong Q, Cheng L, Liu C, Zhang M, Feng Q, Ye H, et al. Ultrathin $MoS_{2(1-x)}Se_{2x}$ alloy nanoflakes for electrocatalytic hydrogen evolution reaction. ACS Catal 2015;5(4):2213-9.
[50] Wang H, Lu Z, Xu S, Kong D, Cha JJ, Zheng G, et al. Electrochemical tuning of vertically aligned MoS_2 nanofilms and its application in improving hydrogen evolution reaction. Proc Natl Acad Sci USA 2013;110(49):19701-6.
[51] Xu X, Pan Y, Ge L, Shao Z. Perovskite materials in electrocatalysis. In: Arul NS, Nithya VD, editors. Revolution of Perovskite: Synthesis, Properties and Applications. Singapore: Springer Singapore, 2020. p.209-50.
[52] Gou Y, Liu Q, Liu Z, Asiri AM, Sun X, Hu J. $FeMoO_4$ nanorod array: a highly active 3D anode for water oxidation under alkaline conditions. Inorg Chem Front 2018;5(3):665-8.
[53] Kibsgaard J, Chen Z, Reinecke BN, Jaramillo TF. Engineering the surface structure of MoS_2 to preferentially expose active edge sites for electrocatalysis. Nat Mater. 2012;11:963-9.
[54] Zhu Y, Xu X, Chen G, Zhong Y, Cai R, Li L, et al. Surfactant-free self-assembly of reduced graphite oxide-MoO_2 nanobelt composites used as electrode for lithium-ion batteries. Electrochim Acta 2016;211:972-81.
[55] Chen J, Wang H, Wang Z, Mao S, Yu J, Wang Y, et al. Redispersion of Mo-Based catalysts and the rational design of super small-sized metallic Mo species. ACS Catal 2019;9(6):5302-7.
[56] Craciun V, Singh RK. Characteristics of the surface layer of barium strontium titanate thin films deposited by laser ablation. Appl Phys Lett 2000;76(14):1932-4.
[57] Cao X, Zheng X, Sun Z, Jin C, Tian J, Sun S, et al. Oxygen defect-ridden molybdenum oxide-coated carbon catalysts for Li-O_2 battery cathodes. Appl Catal B-Environ 2019;253:317-22.

[58] Marcelli A, Spataro B, Sarti S, Dolgashev VA, Tantawi S, Yeremian DA, et al. Characterization of thick conducting molybdenum films: enhanced conductivity via thermal annealing. Surf Coat Technol 2015;261:391-7.
[59] Maji BK, Jena H, Asuvathraman R, Kutty KVG. Electrical conductivity and thermal expansion behavior of $MMoO_4$ (M=Ca, Sr and Ba). J Alloys Compd 2015;640:475-9.
[60] Sczancoski JC, Cavalcante LS, Marana NL, da Silva RO, Tranquilin RL, Joya MR, et al. Electronic structure and optical properties of $BaMoO_4$ powders. Curr Appl Phys 2010;10(2):614-24.

Chapter 5 Fe-based perovskites for catalyzing the hydrogen evolution reaction in alkaline solutions

5.1 Abstract

The hydrogen evolution reaction (HER) as the reaction occurring at the cathode of a water electrolyzer is important to the overall water splitting efficiency, but is limited by sluggish reaction kinetics. While perovskite-type oxides have seen application as the electrocatalysts to facilitate the HER reaction rate, most of the current research focuses on cobalt-containing perovskites. In this work, a series of Fe-based $La_{1-x}(Ba_{0.5}Sr_{0.5})_xFeO_{3-\delta}$ (x = 0.0, 0.2, 0.5, 0.8, and 1.0) perovskites, designed by substituting the alkaline-earth metals Ba and Sr for the rare-earth metal La, were evaluated as alternative candidates for catalyzing the HER in alkaline solutions. All the Ba/Sr substituted samples exhibited enhanced alkaline HER activity compared to the pristine $LaFeO_3$, with $La_{0.2}(Ba_{0.5}Sr_{0.5})_{0.8}FeO_{3-\delta}$ ($x = 0.8$) delivering the best activity with a 216-mV reduction in the overpotential to afford a current density of −10 mA cm_{geo}^{-2}. A comprehensive X-ray spectroscopic study indicates that the enhanced HER activity is correlated with the increased oxidation state of the Fe cation and the enhanced covalency of the Fe–O bond, which is closely related to the phase transition induced by Ba/Sr substation. The optimized activity of the Fe-based perovskite compares favorably to that of many other perovskites (e.g., those containing Co and Ni), highlighting the potential of Fe-based perovskites as HER catalysts.

5.2 Introduction

The electrochemical water splitting has recently been attracting growing attention worldwide because of its potential for large-scale production of clean hydrogen fuels.[1] However, its cathodic half reaction, namely hydrogen evolution reaction (HER), suffers from slow reaction kinetics that leads to inefficient energy conversion, especially in alkaline solutions.[2] To mitigate the energy penalty of this process, platinum group metal-based electrocatalysts, e.g., those containing platinum (Pt),[3] ruthenium (Ru),[4] or iridium (Ir),[5] have been developed with the highest catalytic activity, but the low abundance and high cost of these noble metals restrict their large-scale use. Therefore, research efforts should be devoted to exploring alternative catalytic materials that comprise inexpensive elements and exhibit competitive efficiency.

Over the past decade, a great variety of inorganic compounds have been explored as candidates for catalyzing the HER in alkaline media, including boride,[6] carbide,[7] nitride,[8] oxide,[9] phosphide,[10] sulfide,[11] and selenide.[12] Among these candidates, oxide materials have received increasing interest in the field of HER electrocatalysis due to their cost-effectiveness, simplicity of synthesis, and tunability of physicochemical properties. Of importance, oxides belonging to the perovskite family, for example, such as ABO_3 simple perovskites and $AA'B_2O_6$/$A_2BB'O_6$ double perovskites, A (or A′) being an alkaline-earth or rare-earth metal and B (or B′) a transition metal, have been demonstrated with promise as the alkaline HER catalysts.[13,14] For instance, one seminal work in this area reported that simple perovskite $Pr_{0.5}(Ba_{0.5}Sr_{0.5})_{0.5}Co_{0.8}Fe_{0.2}O_{3-\delta}$ as an electrocatalyst for the HER in a 1 M KOH solution required a 237-mV overpotential to produce a geometric current density of 10 mA cm_{geo}^{-2} (η_{10}, a generic metric for comparing catalytic activity),[15] comparing favorably to several other Co-based catalysts, such as metallic cobalt embedded in N-rich carbon nanotubes,[16] cobalt phosphide supported on carbon cloth,[17] and cobalt–cobalt oxide hybridized with N-doped carbon,[18] Taking advantage of the versatility of perovskite oxides in terms of chemical composition and structure, researchers have conducted a great number of investigations to further increase the HER performance of perovskite catalysts.[19-26] For example, Guan and coworkers screened more than ten Co-based perovskites and concluded that the A-site ionic electronegativity (AIE) can be utilized as a viable descriptor for predicting their HER activity, based on which the

double perovskite $(Gd_{0.5}La_{0.5})BaCo_2O_{5.5+\delta}$ having a suitable AIE value of about 2.33 was found to show optimum HER performance with a η_{10} of as low as 185 mV.[25,26]

However, most of the research to date is focused on perovskite oxides containing Co as the major active component, whereas less attention is given to those consisting mainly of Ni,[27] Mn,[28] and Fe.[29] The previous Chapter concerns the use of a Mo-based perovskite as the alkaline HER catalyst. In this Chapter, research attention is directed to a series of perovskite oxides that comprise solely Fe metal in the B-site as potential catalysts for the alkaline HER. The pristine lanthanum ferrite ($LaFeO_3$) was selected as the target perovskite host, into which alkaline-earth metals barium (Ba) and strontium (Sr) were dual-doped to replace the A-site La, yielding a continuous solid solution of $La_{1-x}(Ba_{0.5}Sr_{0.5})_xFeO_{3-\delta}$ (x = 0.0, 0.2, 0.5, 0.8, and 1.0; denoted as LFO, LBSFO82, LBSFO55, LBSFO28, and BSFO, respectively). Upon the inclusion of Ba/Sr, the iron-based perovskites experienced a phase transition from orthorhombic to cubic, along with changes in electronic structures including increased Fe valence and enhanced Fe–O covalency, which are correlated with a significant improvement in the HER electroactivity. The best-performing sample LBSFO28 needs a η_{10} value of approximately 300 mV, which surpasses or is on par with many of the reported perovskite electrocatalysts, suggesting its promise as alternative HER catalysts in alkaline solutions.

5.3 Results and discussion

5.3.1 Formation and characterizations of Fe-based perovskites

The Ba/Sr-substituted $La_{1-x}(Ba_{0.5}Sr_{0.5})_xFeO_{3-\delta}$ perovskites were prepared by a sol–gel process. As alkaline-earth metal-containing perovskites would generally require temperatures of around 1000 °C for phase formation, all the samples in this work are calcined at the temperature of 1100 °C to ensure good phase purity. The product changes color from yellow to dark/black, which provides visual support for the successful incorporation of Ba/Sr into the perovskite lattice. **Figure 5.1a** depicts the X-ray diffraction (XRD) profiles of the $La_{1-x}(Ba_{0.5}Sr_{0.5})_xFeO_{3-\delta}$ series with various doping contents. Well-defined, high-intensity diffraction peaks were observed for all the samples, indicating their high phase purity. The pristine LFO sample exhibited diffraction peaks typical of an orthorhombic structure (space group: *Pnma*), in accord with the standard pattern of ICDD PDF No. 01-088-0641.[30] Once a small proportion of Ba/Sr are doped into the system (x = 0.2), the structure evolves into a cubic structure

(space group: $Pm\bar{3}m$), which remains unchanged with further increasing the doping level to x = 1.0. The variation in the phase structure is more obviously evidenced by the absence of the diffraction peak at 2θ angle of about 34.2°, as seen in **Figure 5.1b**. With the increasing number of Ba/Sr dopants for all the doped samples, the main peak at about 32.3° first shifted to a higher angle and then to a lower angle, indicating first a lattice shrinkage and then a lattice expansion. This could be explained considering the operation of two major effects: i) substitution of Ba^{2+}/Sr^{2+} with a larger ionic radius for La^{3+} with a smaller ionic radius (1.61/1.44 Å vs. 1.36 Å) leads to expansion of lattice, and thus a shift to lower 2θ angles; ii) to maintain charge neutrality, increase of the Fe oxidation state (which has a reduced size, i.e., ionic radius of 0.645 Å and 0.585 Å for Fe^{3+} and Fe^{4+}) leads to shrinkage of lattice, and thus a shift to higher 2θ angles.[31] A more quantitative analysis regarding the phase structure and lattice parameters was conducted by Rietveld refinement, and the detailed results shown in **Figure 5.2** and **Table 5.1** consist with the discussion made here.

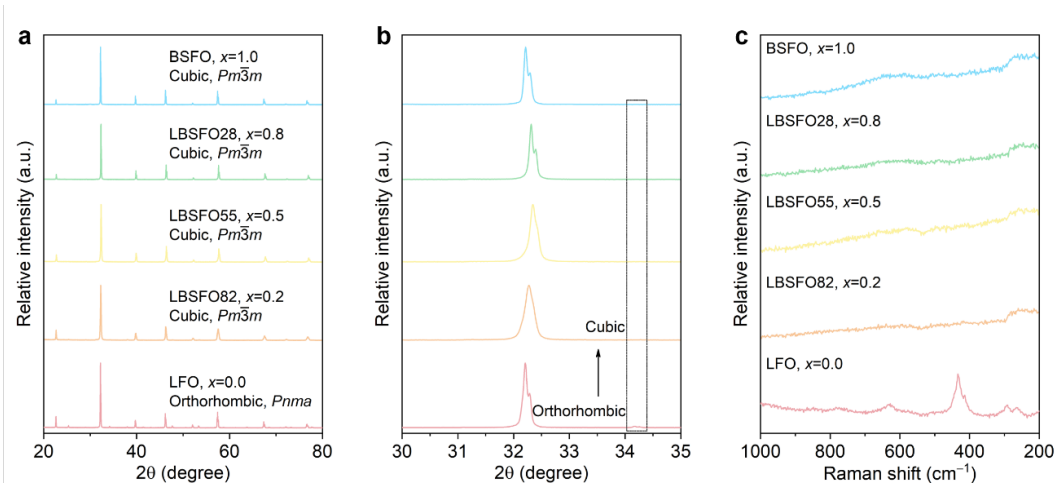

Figure 5.1 XRD and Raman data of $La_{1-x}(Ba_{0.5}Sr_{0.5})_xFeO_{3-\delta}$ (x = 0.0, 0.2, 0.5, 0.8, and 1.0). (a) XRD data presented in a broad 2θ range of 20–80°. (b) XRD data presented in a select 2θ range of 30–35°. (c) Raman data presented in a wavenumber range of 200–1000 cm^{-1}.

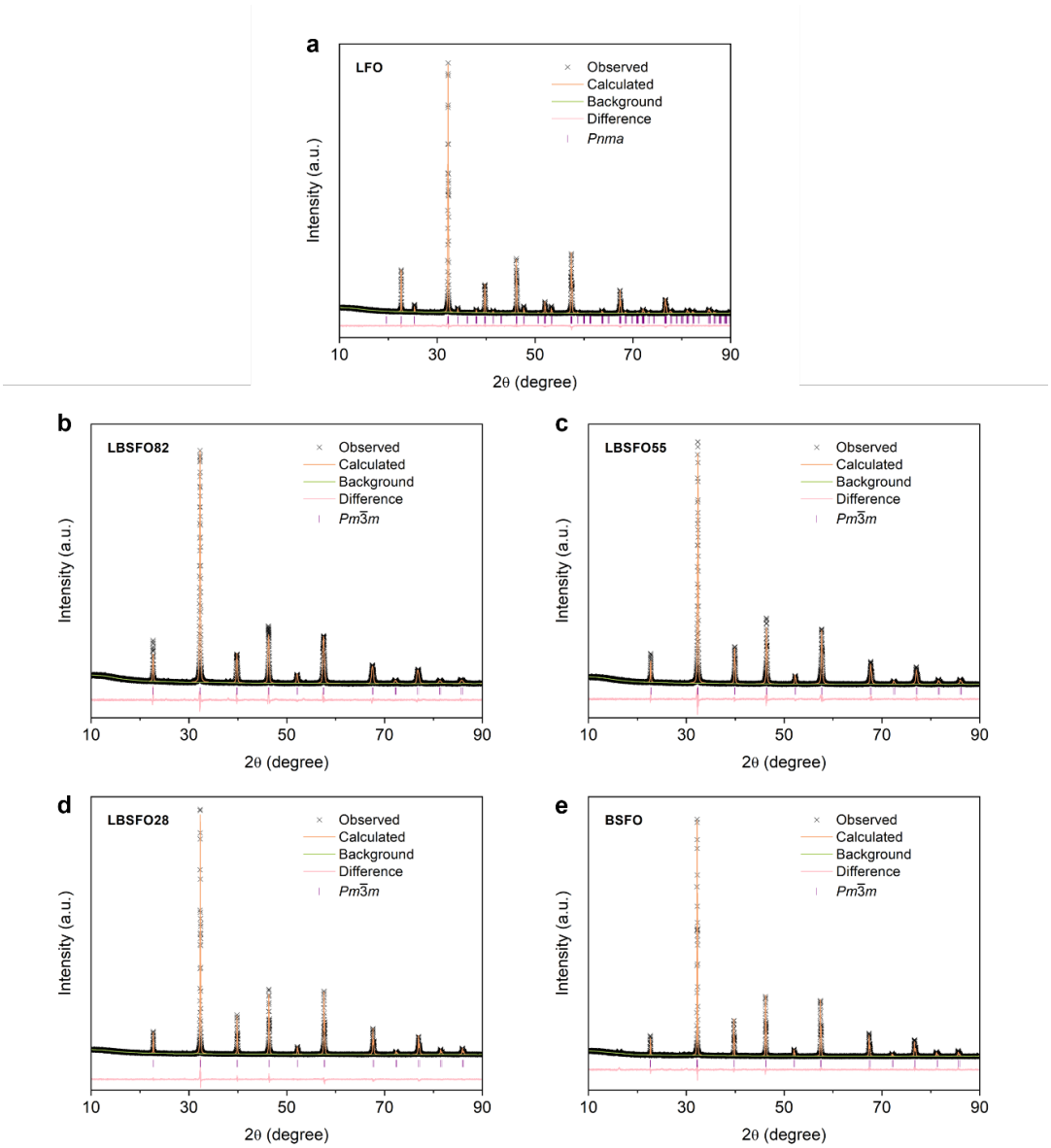

Figure 5.2 Rietveld refinement results for the XRD data of $La_{1-x}(Ba_{0.5}Sr_{0.5})_xFeO_{3-\delta}$ (x = 0.0, 0.2, 0.5, 0.8, and 1.0). (a) LFO. (b) LBSFO82. (c) LBSFO55. (d) LBSFO28. (e) BSFO.

Table 5.1 Rietveld refinement of the XRD data of $La_{1-x}(Ba_{0.5}Sr_{0.5})_xFeO_{3-\delta}$ (x = 0.0, 0.2, 0.5, 0.8, and 1.0), showing results of crystal symmetries, lattice parameters, and reliability factors.

Perovskite	Space group	Lattice parameter (Å)	χ^2	R_p (%)	R_{wp} (%)
LFO	*Pnma*	a = 5.5662, b = 7.8548, c = 5.5548	1.877	2.99	3.98
LBSFO82	$Pm\bar{3}m$	a = 3.9253	2.514	3.16	4.49
LBSFO55	$Pm\bar{3}m$	a = 3.9119	2.628	3.08	4.38
LBSFO28	$Pm\bar{3}m$	a = 3.9158	1.945	2.73	3.65
BSFO	$Pm\bar{3}m$	a = 3.9258	1.795	2.59	3.42

The phase transition of the samples after Ba/Sr substitution was also ascertained by Raman spectroscopy, a powerful tool for differentiating structural phases of perovskite oxides because different crystal symmetries will generally exhibit different Raman bands.[32] **Figure 5.1c** shows the Raman spectra in a wavenumber window of 200–1000 cm^{-1} recorded at room temperature. The pristine LFO displays Raman bands at wavenumbers of ~270, ~430, and ~630 cm^{-1}, which, consistent with those reported earlier,[33] is characteristic of the orthorhombic phase. In comparison, all the substituted samples exhibit no Raman-active bands, indicative of the presence of the cubic perovskite structure.[34]

The crystalline information of the cubic structure upon Ba/Sr doping was further provided by transmission electron microscopy (TEM) analysis, as exemplified by the LBSFO28 sample. **Figure 5.3a** and **c** show the high-resolution TEM (HRTEM) images taken in the zone axes of [100] and [111], respectively. Lattice fringes with interplanar distances of 0.39 and 0.28 nm were clearly detected, corresponding to the (010) and $(\bar{1}10)$ planes of the cubic-structured perovskite. The selected-area electron diffraction (SAED) patterns associated with these HRTEM images, as illustrated in **Figure 5.3b** and **d**, further support the formation of a cubic structure with the $Pm\bar{3}m$

space group. High-angle annular dark-field scanning TEM (HAADF-STEM) and energy-dispersive X-ray spectroscopy (EDS) mapping were conducted to prove the presence of the Ba and Sr dopants in the perovskite lattice. As shown in **Figure 5.3e**, a quite homogeneous distribution of all the constituent elements can be found, demonstrating the successful construction of a multi-element, perovskite-type solid solution.

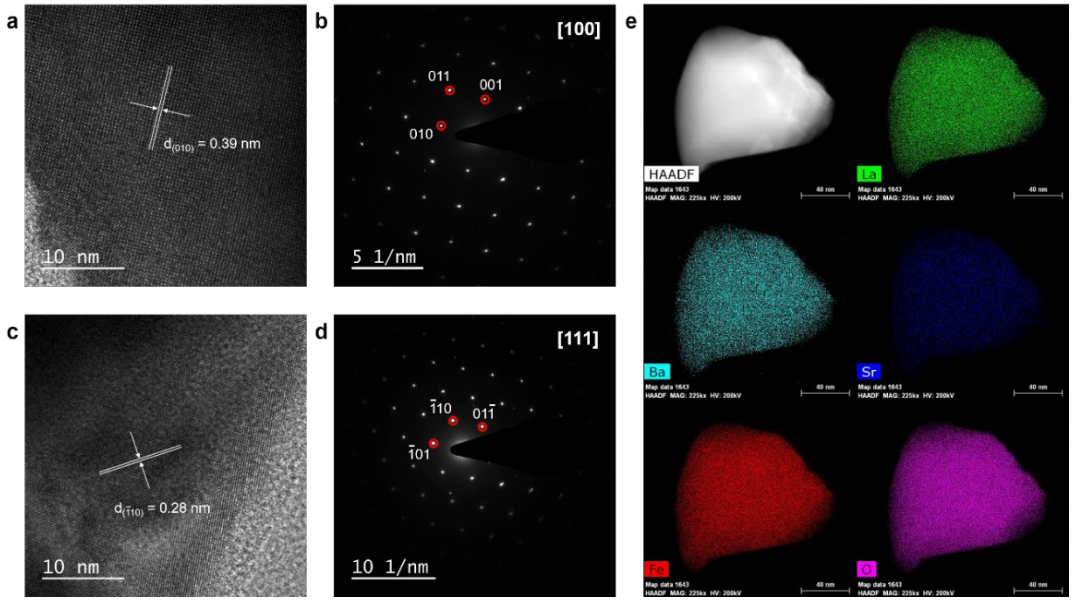

Figure 5.3 TEM characterization of the LBSFO28 sample. (a–b) HRTEM image and the associated SAED pattern in the [100] zone axis. (c–d) HRTEM image and the associated SAED pattern in the [111] zone axis. (e) HAADF-STEM image and the corresponding EDS mapping images of La, Ba, Sr, Fe, and O elements.

The morphology of the $La_{1-x}(Ba_{0.5}Sr_{0.5})_xFeO_{3-\delta}$ samples with various Ba/Sr doping contents was studied by scanning electron microscopy (SEM). All the samples possess similar morphological features, consisting of large particles in the size range from a few hundred nanometers to several micrometers (**Figure 5.4**). Due to the high calcination temperature used for phase formation (i.e., 1100 °C), the $La_{1-x}(Ba_{0.5}Sr_{0.5})_xFeO_{3-\delta}$ samples appear to be rather sintered with no presence of any pore structure. Of note, the particle size of the $La_{1-x}(Ba_{0.5}Sr_{0.5})_xFeO_{3-\delta}$ series becomes larger with the increasing amount of the alkaline-earth metal dopants, which is also verified by the decreasing trend of the Brunauer–Emmett–Teller (BET) surface areas (**Table 5.2**), as measured from nitrogen sorption measurements.

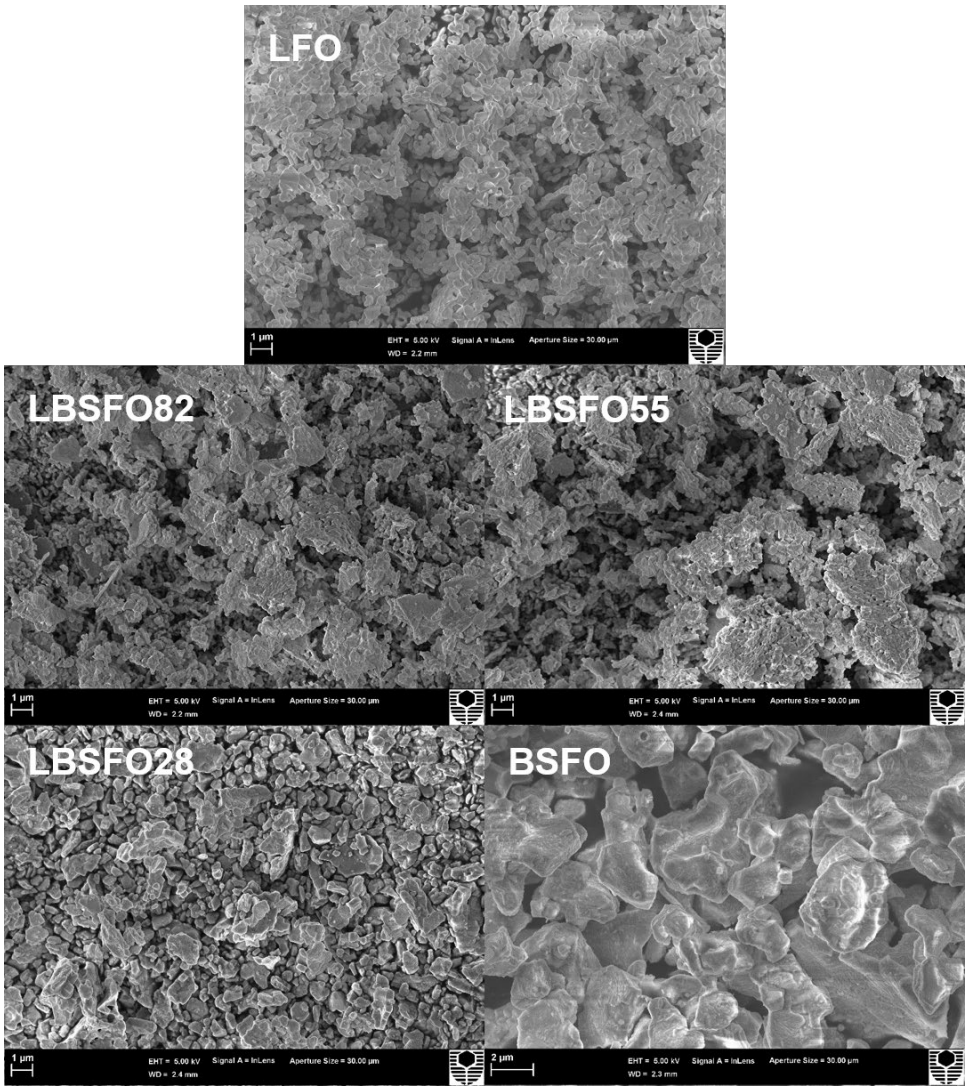

Figure 5.4 SEM images of $La_{1-x}(Ba_{0.5}Sr_{0.5})_xFeO_{3-\delta}$ (x = 0.0, 0.2, 0.5, 0.8, and 1.0).

Table 5.2 BET surface areas of $La_{1-x}(Ba_{0.5}Sr_{0.5})_xFeO_{3-\delta}$ (x = 0.0, 0.2, 0.5, 0.8, and 1.0).

Perovskite	Surface areas ($m^2\ g^{-1}$)
LFO	4.15
LBSFO82	2.97
LBSFO55	2.01
LBSFO28	1.25
BSFO	1.13

5.3.2 Electrocatalytic hydrogen evolution performance

The use of Fe-based $La_{1-x}(Ba_{0.5}Sr_{0.5})_xFeO_{3-\delta}$ perovskites as the HER electrocatalysts was evaluated at ambient conditions in an electrolyte of 1 M KOH aqueous solution. **Figure 5.5a** displays the apparent catalytic activity acquired from linear sweep voltammetry (LSV) collected at a slow scan rate of 5 mV s^{-1}, where the *iR*-corrected potential vs. the reversible hydrogen electrode (RHE) is plotted against the current normalized by the geometric area of the working electrode. It is found that upon the co-doping of Ba^{2+} and Sr^{2+} cations, the apparent activity showed a significant increase, as evidenced by a positive shift in the potential needed to reach a certain current output. More specifically, to afford an electrode activity of −10 mA cm_{geo}^{-2}, the LFO parent oxide requires a η_{10} value as large as 519 mV, whereas the doped samples require reduced values of 471, 394, 303, and 355 mV for LBSFO82, LBSFO55, LBSFO28, and BSFO, respectively (**Figure 5.5b**). Remarkably, LBSFO28 was found to be the most active toward the HER, with a drastic drop in η_{10} by 216 mV. Using the same metric, LBSFO28 was found to outperform previously reported Ni-, Mn-, and Fe-based perovskite-type HER electrocatalysts such as $La_{0.8}Sr_{0.2}Cr_{0.69}Ni_{0.31}O_{3-\delta}$ (η_{10} = 447 mV),[27] $NdBaMn_2O_{5.5+\delta}$ ($\eta_{10} \approx$ 500 mV),[28] and $LaFe_{0.8}Co_{0.2}O_{3-\delta}$ ($\eta_{10} \approx$ 400 mV).[29] More importantly, LBSFO28 compares favorably to many of the Co-based perovskite catalysts, including $SrCoO_{3-\delta}$ (η_{10} = 447 mV),[23] $La_{0.5}Sr_{0.5}CoO_{3-\delta}$ ($\eta_{10} \approx$ 420 mV),[22] $PrBa_{0.5}Sr_{0.5}Co_2O_{5+\delta}$ (η_{10} = 393 mV),[20] $SrCo_{0.7}Fe_{0.3}O_{3-\delta}$ (η_{10} = 378 mV),[24] $Ba_{0.95}Co_{0.4}Fe_{0.4}Zr_{0.1}Y_{0.1}O_{3-\delta}$ (η_{10} = 360 mV),[21] and $Ba_{0.5}Sr_{0.5}Co_{0.8}Fe_{0.2}O_{3-\delta}$ (η_{10} = 342 mV).[15] While there is still a gap when compared to the state-of-the-art Co-based perovskites, for instance, $Pr_{0.5}(Ba_{0.5}Sr_{0.5})_{0.5}Co_{0.8}Fe_{0.2}O_{3-\delta}$ (η_{10} = 237 mV) and $(Gd_{0.5}La_{0.5})BaCo_2O_{5.5+\delta}$ (η_{10} = 185 mV), these comparisons suggest that the Fe-based LBSFO28 catalyst has the potential for alkaline water splitting, especially when one further considers its lower cost relative to the Co-based counterpart.

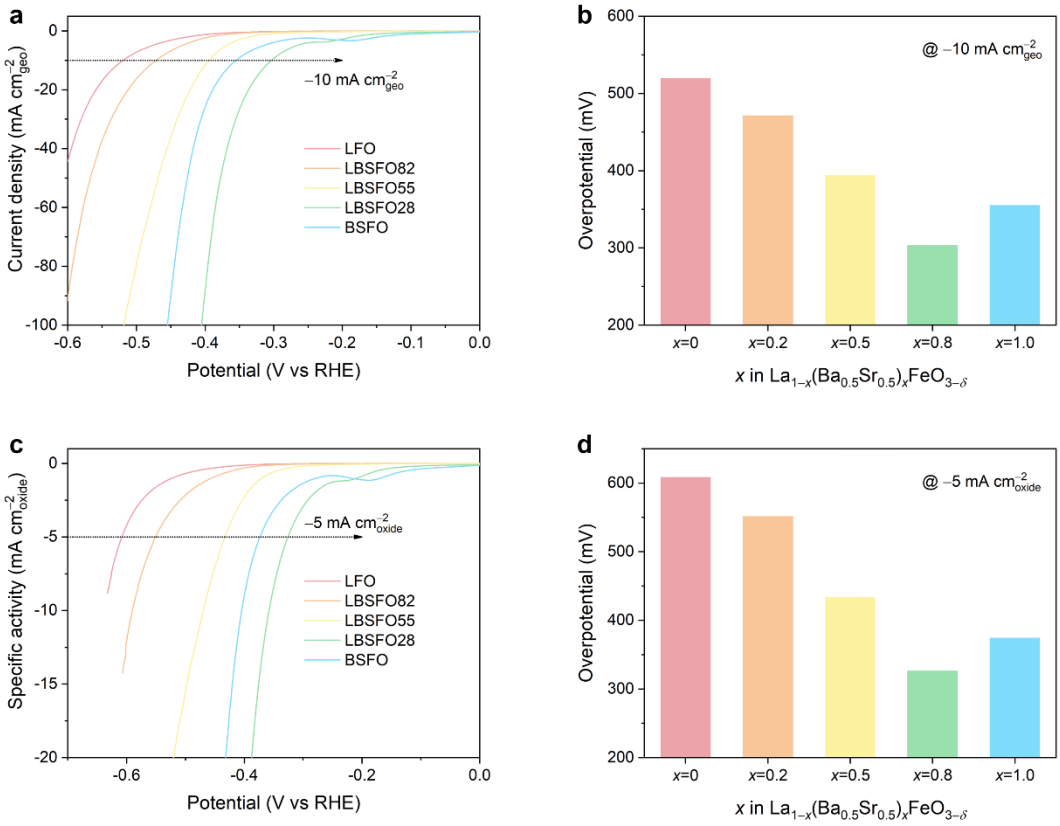

Figure 5.5 Electrocatalytic performance of $La_{1-x}(Ba_{0.5}Sr_{0.5})_xFeO_{3-\delta}$ (x = 0.0, 0.2, 0.5, 0.8, and 1.0) toward the hydrogen evolution reaction in a 1 M KOH electrolyte. (a) LSV curves where the current is normalized by the geometric area of the working electrode (in mA cm^{-2}_{geo}). The arrow indicates a decreasing trend in the potential required to deliver a current density of −10 mA cm^{-2}_{geo}. (b) A comparison of the overpotential required to deliver −10 mA cm^{-2}_{geo}. (c) LSV curves where the current is normalized by the BET surface area of the perovskite catalysts (in mA cm^{-2}_{oxide}). The arrow indicates a decreasing trend in the potential needed to deliver a specific activity of −5 mA cm^{-2}_{oxide}. (d) A comparison of the overpotential needed to deliver −5 mA cm^{-2}_{oxide}.

Taking into consideration of the surface area effect, **Figure 5.5c** reports the specific activity of the various Fe-based perovskites as a parameter for comparing their intrinsic activity.[26] Interestingly, the trend for the intrinsic activity follows the same as that for the apparent activity. As shown in **Figure 5.5d**, the LBSFO28 sample remains to be the most intrinsically active, requiring a lowest overpotential of 326 mV to afford a

specific activity of −5 mA cm_{oxide}^{-2}, lower than that of LBSFO82 (551 mV), LBSFO55 (433 mV), and BSFO (374 mV) and much smaller than that of the pristine LFO (608 mV).

It is noted that a minor cathodic peak was found at a potential preceding the HER, around −0.2 V vs. RHE, especially for the samples LBSFO28 and BSFO. This could be related to some certain electrochemical phenomena inherent to these Fe-based perovskite oxides, similar to that found on the $Pr_{0.5}(Ba_{0.5}Sr_{0.5})_{0.5}Co_{0.8}Fe_{0.2}O_{3-\delta}$ perovskite in which Fe is a minor constituent.[15] Detailed understanding of this electrochemical process is out of the scope of this study.

Figure 5.6 plots the logarithm of specific activity against the overpotential, from which Tafel slopes can be derived. As can be seen, the LFO parent oxide exhibits a Tafel slope of 137 mV dec^{-1}, while all the Ba/Sr doped samples exhibit a somewhat reduced Tafel slope, implying faster reaction kinetics. Again, the most active sample LBSFO28 has the smallest Tafel slope (i.e., 112 mV dec^{-1}). Nonetheless, all the samples, regardless of doping, show a Tafel slope value close to 120 mV dec^{-1}, which, according to previous research,[35] suggests that a Volmer–Heyrovsky reaction mechanism may be operative during the alkaline HER and that the reaction rate may be determined by the Volmer process. In the Volmer process water molecule is dissociated and electrochemically reduced to form the hydrogen atoms adsorbed on the catalyst surface, as can be described by the equation of $M + H_2O + e^- \leftrightarrow M–H + OH^-$, where M denotes a catalytically active surface site.[36]

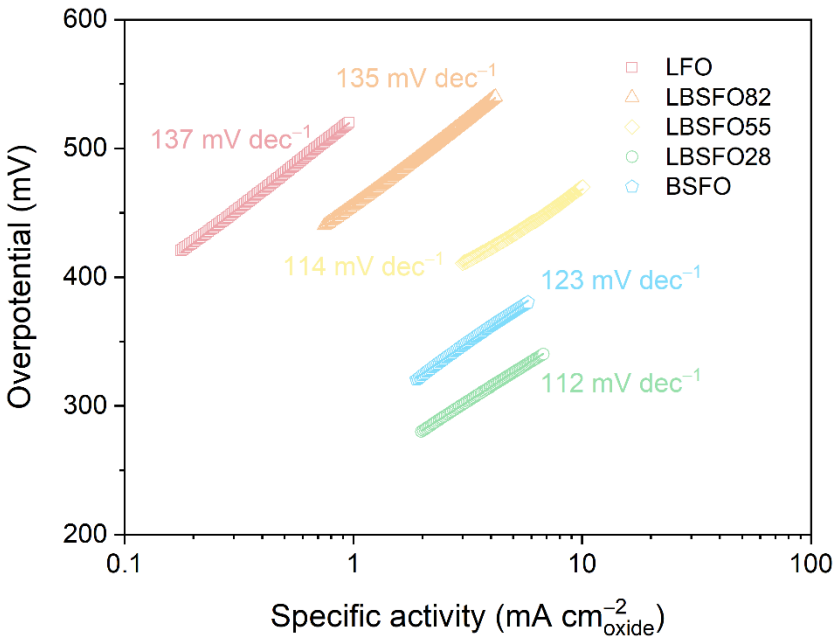

Figure 5.6 Tafel plots of $La_{1-x}(Ba_{0.5}Sr_{0.5})_xFeO_{3-\delta}$ (x = 0.0, 0.2, 0.5, 0.8, and 1.0).

5.3.3 Electronic origins for the activity enhancement

As the electrocatalytic performance is strongly correlated with the catalyst's electronic structures, a combined investigation of X-ray photoelectron spectroscopy (XPS) and soft X-ray absorption spectroscopy (XAS) was carried out to offer insights into the electronic origins for the enhancement of catalytic activity. **Figure 5.7a** displays the high-resolution XPS spectra of the Fe 2p core levels for the various Fe-based perovskite samples. A doublet at the binding energy of about 710.1 eV for $2p_{3/2}$ and about 723.8 eV for $2p_{1/2}$ was found for LFO, which, together with a shake-up contribution at about 718.4 eV, consists with reported Fe 2p features and suggests the dominant presence of trivalent Fe cations.[37] Interestingly, a gradual shift to higher binding energies was observed for samples with an increasing Ba/Sr dopant concentration, as indicated by a dotted line in **Figure 5.7a**. This observation suggests that partial oxidation from Fe^{3+} to Fe^{4+} occurred for all the doped samples[38] and that the extent of such oxidation strongly correlates with the doping level, that is, the higher the doping level, the greater the oxidation extent.

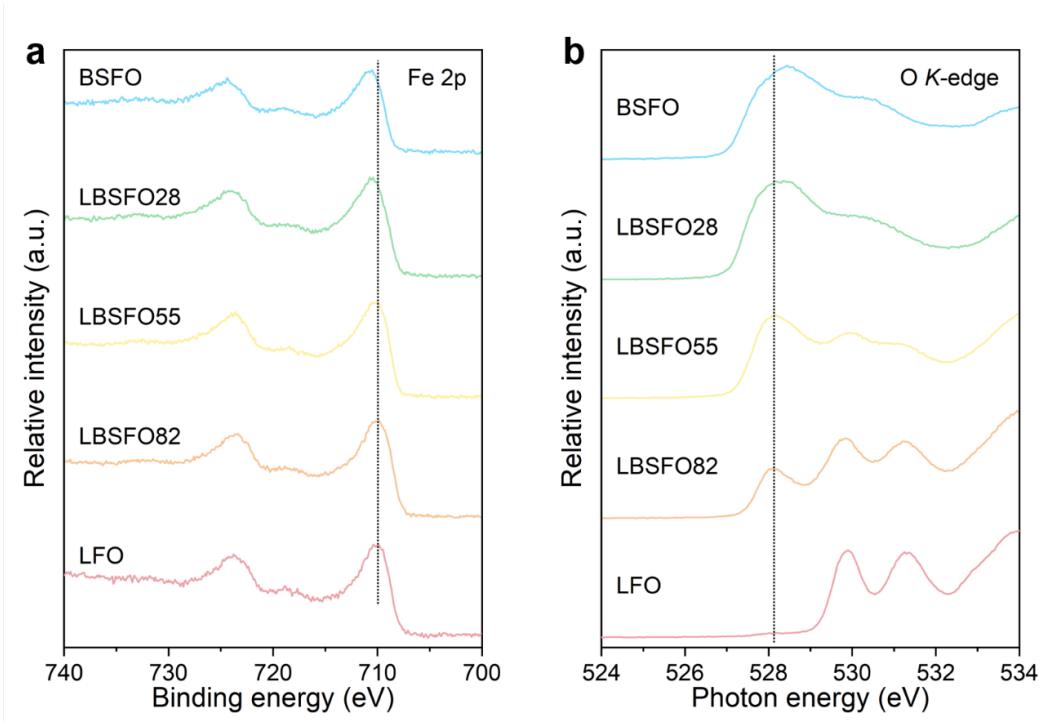

Figure 5.7 Electronic states of $La_{1-x}(Ba_{0.5}Sr_{0.5})_xFeO_{3-\delta}$ (x = 0.0, 0.2, 0.5, 0.8, and 1.0) as characterized by XPS and XAS. (a) Fe 2p XPS spectra. (b) O *K*-edge XAS spectra.

While the Fe 2p XPS result provides Fe^{3+}-to-Fe^{4+} oxidation information mainly of the catalyst surface, the O *K*-edge soft XAS data taken in the fluorescence yield mode, which are highly sensitive to the transition metal valence as well as transition metal–oxygen covalency,[39,40] further reveals the Fe valence changes in the bulk of the materials. As shown in **Figure 5.7b**, once Ba^{2+} and Sr^{2+} were incorporated into the LFO lattice, a pre-edge peak at the photon energy of about 528 eV appears, which continuously gains spectral weight and becomes dominant for high Ba/Sr concentrations. According to earlier publications,[25] this pre-edge peak is associated with the covalent mixing between transition metal 3d orbitals and O 2p states. Accompanying this evolution of the pre-edge peak is the suppression of the original pair of peaks sitting at the higher energy side, which merge completely into a shoulder peak for high Ba/Sr contents. These features are consistent with those found in the previously reported Sr single-doped $La_{1-x}Sr_xFeO_{3-\delta}$ series,[41,42] and are indicative of an increased overlap between the Fe 3d and O 2p states (i.e., enhanced Fe 3d–O 2p covalency) with the increasing doping of Ba/Sr, which is also correlated with the bulk oxidation of Fe^{3+} to Fe^{4+}.

The XPS and soft XAS investigations indicate that upon the inclusion of the Ba/Sr dopants, the oxidation state of the Fe cation increased steadily in the $La_{1-x}(Ba_{0.5}Sr_{0.5})_xFeO_{3-\delta}$ series and the Fe–O covalency enhanced concomitantly. However, the HER reactivity of the series did not increase monotonically. Instead, the best performance was achieved on LBSFO28 with a doping level of x = 0.8. This suggests that the HER performance of the Fe-based samples is optimized at a suitable Fe valence and Fe–O covalency (i.e., neither too high nor too low), which may lead to an appropriate binding state for the reaction intermediates and can thus result in an optimum activity, in line with the Sabatier's principle.[43] Note that a similar conclusion was also drawn for the research on a series of Co-based perovskites with different A-site compositions, in which the most active perovskite $(Gd_{0.5}La_{0.5})BaCo_2O_{5.5+\delta}$ with a suitable AIE value of about 2.33 also exhibited a moderate Co valence and Co–O covalency.[26]

5.4 Conclusions

To summarize, a series of Fe-based $La_{1-x}(Ba_{0.5}Sr_{0.5})_xFeO_{3-\delta}$ (x = 0.0, 0.2, 0.5, 0.8, and 1.0) perovskites were obtained by simultaneously doping alkaline-earth metals Ba and Sr into the A-site of $LaFeO_3$ and evaluated as the electroactive materials for catalyzing the hydrogen evolution under alkaline solutions. The replacement of La by Ba/Sr in $LaFeO_3$ leads to a phase transition from orthorhombic to cubic, along with electronic structure changes including partial oxidation of Fe valence from 3+ to 4+ as well as enhanced covalency between the Fe and O states, as revealed by a comprehensive X-ray spectroscopic study. Such changes in electronic structures contributed to increased HER kinetics, and the $La_{0.2}(Ba_{0.5}Sr_{0.5})_{0.8}FeO_{3-\delta}$ (LBSFO28) sample with a suitable Fe valence and Fe–O covalency was found to exhibit an optimum HER reactivity, requiring overpotentials of 303 and 326 mV to give a current density of −10 mA cm_{geo}^{-2} and a specific activity of −5 mA cm_{oxide}^{-2}, respectively. These results are expected to offer insights into the future development of cost-effective and efficient electrocatalytic materials for the alkaline HER.

5.5 References

(1) Li, L.; Wang, P.; Shao, Q.; Huang, X. Metallic nanostructures with low dimensionality for electrochemical water splitting. *Chem. Soc. Rev.* **2020**, *49*, 3072–3106.

(2) Zheng, Y.; Jiao, Y.; Vasileff, A.; Qiao, S.-Z. The hydrogen evolution reaction in alkaline solution: From theory, single crystal models, to practical electrocatalysts. *Angew. Chem. Int. Ed.* **2018**, *57*, 7568–7579.

(3) Zhang, H.; An, P.; Zhou, W.; Guan, B. Y.; Zhang, P.; Dong, J.; Lou, X. W. Dynamic traction of lattice-confined platinum atoms into mesoporous carbon matrix for hydrogen evolution reaction. *Sci. Adv.* **2018**, *4*, eaao6657.

(4) Mahmood, J.; Li, F.; Jung, S.-M.; Okyay, M. S.; Ahmad, I.; Kim, S.-J.; Park, N.; Jeong, H. Y.; Baek, J.-B. An efficient and pH-universal ruthenium-based catalyst for the hydrogen evolution reaction. *Nat. Nanotechnol.* **2017**, *12*, 441–446.

(5) Mahmood, J.; Anjum, M. A. R.; Shin, S.-H.; Ahmad, I.; Noh, H.-J.; Kim, S.-J.; Jeong, H. Y.; Lee, J. S.; Baek, J.-B. Encapsulating iridium nanoparticles inside a 3D cage-like organic network as an efficient and durable catalyst for the hydrogen evolution reaction. *Adv. Mater.* **2018**, *30*, 1805606.

(6) Gupta, S.; Patel, M. K.; Miotello, A.; Patel, N. Metal boride-based catalysts for electrochemical water-splitting: A review. *Adv. Funct. Mater.* **2020**, *30*, 1906481.

(7) Jun, H.; Kim, S.; Lee, J. Development strategies in transition metal carbide for hydrogen evolution reaction: A review. *Korean J. Chem. Eng.* **2020**, *37*, 1317–1330.

(8) Theerthagiri, J.; Lee, S. J.; Murthy, A. P.; Madhavan, J.; Choi, M. Y. Fundamental aspects and recent advances in transition metal nitrides as electrocatalysts for hydrogen evolution reaction: A review. *Curr. Opin. Solid State Mater. Sci.* **2020**, *24*, 100805.

(9) Ling, T.; Yan, D.-Y.; Wang, H.; Jiao, Y.; Hu, Z.; Zheng, Y.; Zheng, L.; Mao, J.; Liu, H.; Du, X.-W. et al. Activating cobalt(II) oxide nanorods for efficient electrocatalysis by strain engineering. *Nat. Commun.* **2017**, *8*, 1509.

(10) Weng, C.-C.; Ren, J.-T.; Yuan, Z.-Y. Transition metal phosphide-based materials for efficient electrochemical hydrogen evolution: A critical review. *ChemSusChem* **2020**, *13*, 3357–3375.

(11) Wang, P.; Zhang, X.; Zhang, J.; Wan, S.; Guo, S.; Lu, G.; Yao, J.; Huang, X. Precise tuning in platinum-nickel/nickel sulfide interface nanowires for synergistic hydrogen evolution catalysis. *Nat. Commun.* **2017**, *8*, 14580.

(12) Feng, W.; Pang, W.; Xu, Y.; Guo, A.; Gao, X.; Qiu, X.; Chen, W. Transition metal selenides for electrocatalytic hydrogen evolution reaction. *ChemElectroChem* **2020**, *7*, 31–54.

(13) Xu, X.; Wang, W.; Zhou, W.; Shao, Z. Recent advances in novel nanostructuring methods of perovskite electrocatalysts for energy-related applications. *Small Methods* **2018**, *2*, 1800071.

(14) Xu, X.; Zhong, Y.; Shao, Z. Double perovskites in catalysis, electrocatalysis, and photo(electro)catalysis. *Trends Chem.* **2019**, *1*, 410–424.

(15) Xu, X.; Chen, Y.; Zhou, W.; Zhu, Z.; Su, C.; Liu, M.; Shao, Z. A perovskite electrocatalyst for efficient hydrogen evolution reaction. *Adv. Mater.* **2016**, *28*, 6442–6448.

(16) Zou, X.; Huang, X.; Goswami, A.; Silva, R.; Sathe, B. R.; Mikmeková, E.; Asefa, T. Cobalt-embedded nitrogen-rich carbon nanotubes efficiently catalyze hydrogen evolution reaction at all pH values. *Angew. Chem. Int. Ed.* **2014**, *53*, 4372–4376.

(17) Tian, J.; Liu, Q.; Asiri, A. M.; Sun, X. Self-supported nanoporous cobalt phosphide nanowire arrays: An efficient 3D hydrogen-evolving cathode over the wide range of pH 0–14. *J. Am. Chem. Soc.* **2014**, *136*, 7587–7590.

(18) Jin, H.; Wang, J.; Su, D.; Wei, Z.; Pang, Z.; Wang, Y. In situ cobalt–cobalt oxide/N-doped carbon hybrids as superior bifunctional electrocatalysts for hydrogen and oxygen evolution. *J. Am. Chem. Soc.* **2015**, *137*, 2688–2694.

(19) Hua, B.; Li, M.; Pang, W.; Tang, W.; Zhao, S.; Jin, Z.; Zeng, Y.; Shalchi Amirkhiz, B.; Luo, J.-L. Activating p-blocking centers in perovskite for efficient water splitting. *Chem* **2018**, *4*, 2902–2916.

(20) Zhang, Z.; He, B.; Chen, L.; Wang, H.; Wang, R.; Zhao, L.; Gong, Y. Boosting overall water splitting via FeOOH nanoflake-decorated $PrBa_{0.5}Sr_{0.5}Co_2O_{5+\delta}$ nanorods. *ACS Appl. Mater. Interfaces* **2018**, *10*, 38032–38041.

(21) Li, X.; He, L.; Zhong, X.; Zhang, J.; Luo, S.; Yi, W.; Zhang, L.; Hu, M.; Tang, J.; Zhou, X. et al. Evaluation of A-Site Ba^{2+}-deficient $Ba_{1-x}Co_{0.4}Fe_{0.4}Zr_{0.1}Y_{0.1}O_{3-\delta}$ oxides as electrocatalysts for efficient hydrogen evolution reaction. *Scanning* **2018**, *2018*, 1341608.

(22) Oh, N. K.; Kim, C.; Lee, J.; Kwon, O.; Choi, Y.; Jung, G. Y.; Lim, H. Y.; Kwak, S. K.; Kim, G.; Park, H. In-situ local phase-transitioned $MoSe_2$ in $La_{0.5}Sr_{0.5}CoO_{3-\delta}$ heterostructure and stable overall water electrolysis over 1000 hours. *Nat. Commun.* **2019**, *10*, 1723.

(23) Islam, Q. A.; Majee, R.; Bhattacharyya, S. Bimetallic nanoparticle decorated perovskite oxide for state-of-the-art trifunctional electrocatalysis. *J. Mater. Chem. A* **2019**, *7*, 19453–19464.

(24) Zhang, Z.; Chen, Y.; Dai, Z.; Tan, S.; Chen, D. Promoting hydrogen-evolution activity and stability of perovskite oxides via effectively lattice doping of molybdenum. *Electrochim. Acta* **2019**, *312*, 128–136.

(25) Guan, D.; Zhou, J.; Hu, Z.; Zhou, W.; Xu, X.; Zhong, Y.; Liu, B.; Chen, Y.; Xu, M.; Lin, H.-J. et al. Searching general sufficient-and-necessary conditions for ultrafast hydrogen-evolving electrocatalysis. *Adv. Funct. Mater.* **2019**, *29*, 1900704.

(26) Guan, D.; Zhou, J.; Huang, Y.-C.; Dong, C.-L.; Wang, J.-Q.; Zhou, W.; Shao, Z. Screening highly active perovskites for hydrogen-evolving reaction via unifying ionic electronegativity descriptor. *Nat. Commun.* **2019**, *10*, 3755.

(27) Wang, Y.; Wang, Z.; Jin, C.; Li, C.; Li, X.; Li, Y.; Yang, R.; Liu, M. Enhanced overall water electrolysis on a bifunctional perovskite oxide through interfacial engineering. *Electrochim. Acta* **2019**, *318*, 120–129.

(28) Wang, J.; Gao, Y.; Chen, D.; Liu, J.; Zhang, Z.; Shao, Z.; Ciucci, F. Water splitting with an enhanced bifunctional double perovskite. *ACS Catal.* **2018**, *8*, 364–371.

(29) Dai, J.; Zhu, Y.; Zhong, Y.; Miao, J.; Lin, B.; Zhou, W.; Shao, Z. Enabling high and stable electrocatalytic activity of iron-based perovskite oxides for water splitting by combined bulk doping and morphology designing. *Adv. Mater. Interfaces* **2019**, *6*, 1801317.

(30) Falcón, H.; Goeta, A. E.; Punte, G.; Carbonio, R. E. Crystal structure refinement and stability of $LaFe_xNi_{1-x}O_3$ solid solutions. *J. Solid State Chem.* **1997**, *133*, 379–385.

(31) Shannon, R. Revised effective ionic radii and systematic studies of interatomic distances in halides and chalcogenides. *Acta Cryst. A* **1976**, *32*, 751–767.

(32) Dobal, P. S.; Katiyar, R. S. Studies on ferroelectric perovskites and Bi-layered compounds using micro-Raman spectroscopy. *J. Raman Spectrosc.* **2002**, *33*, 405–423.

(33) Paul Blessington Selvadurai, A.; Pazhanivelu, V.; Jagadeeshwaran, C.; Murugaraj, R.; Panneer Muthuselvam, I.; Chou, F. C. Influence of Cr substitution on structural, magnetic and electrical conductivity spectra of $LaFeO_3$. *J. Alloys Compd.* **2015**, *646*, 924–931.

(34) Granado, E.; Moreno, N. O.; García, A.; Sanjurjo, J. A.; Rettori, C.; Torriani, I.; Oseroff, S. B.; Neumeier, J. J.; McClellan, K. J.; Cheong, S. W. et al. Phonon Raman scattering in $R_{1-x}A_xMnO_{3+\delta}$ (R = La, Pr; A = Ca, Sr). *Phys. Rev. B* **1998**, *58*, 11435–11440.

(35) Mahmood, N.; Yao, Y.; Zhang, J.-W.; Pan, L.; Zhang, X.; Zou, J.-J. Electrocatalysts for hydrogen evolution in alkaline electrolytes: Mechanisms, challenges, and prospective solutions. *Adv. Sci.* **2018**, *5*, 1700464.

(36) Stamenkovic, V. R.; Strmcnik, D.; Lopes, P. P.; Markovic, N. M. Energy and fuels from electrochemical interfaces. *Nat. Mater.* **2017**, *16*, 57–69.

(37) Ghaffari, M.; Liu, T.; Huang, H.; Tan, O. K.; Shannon, M. Investigation of local structure effect and X-ray absorption characteristics (EXAFS) of Fe (Ti) K-edge on photocatalyst properties of $SrTi_{(1-x)}Fe_xO_{(3-\delta)}$. *Mater. Chem. Phys.* **2012**, *136*, 347–357.

(38) McIntyre, N. S.; Zetaruk, D. G. X-ray photoelectron spectroscopic studies of iron oxides. *Anal. Chem.* **1977**, *49*, 1521–1529.

(39) de Groot, F. M. F.; Grioni, M.; Fuggle, J. C.; Ghijsen, J.; Sawatzky, G. A.; Petersen, H. Oxygen 1s x-ray-absorption edges of transition-metal oxides. *Phys. Rev. B* **1989**, *40*, 5715–5723.

(40) Frati, F.; Hunault, M. O. J. Y.; de Groot, F. M. F. Oxygen K-edge X-ray absorption spectra. *Chem. Rev.* **2020**, *120*, 4056–4110.

(41) Abbate, M.; de Groot, F. M. F.; Fuggle, J. C.; Fujimori, A.; Strebel, O.; Lopez, F.; Domke, M.; Kaindl, G.; Sawatzky, G. A.; Takano, M. et al. Controlled-valence properties of $La_{1-x}Sr_xFeO_3$ and $La_{1-x}Sr_xMnO_3$ studied by soft-x-ray absorption spectroscopy. *Phys. Rev. B* **1992**, *46*, 4511–4519.

(42) Shen, Z.; Zhuang, Y.; Li, W.; Huang, X.; Oropeza, F. E.; Hensen, E. J. M.; Hofmann, J. P.; Cui, M.; Tadich, A.; Qi, D. et al. Increased activity in the oxygen evolution reaction by Fe^{4+}-induced hole states in perovskite $La_{1-x}Sr_xFeO_3$. *J. Mater. Chem. A* **2020**, *8*, 4407–4415.

(43) Sabatier, P. Hydrogénations et déshydrogénations par catalyse. *Ber. Dtsch. Chem. Ges.* **1911**, *44*, 1984–2001.

Chapter 6 An unusually stabilized Co-based perovskite for highly efficient oxygen evolution

6.1 Abstract

While electrochemical water splitting provides a green route to produce H_2 fuel, its efficiency is largely limited due to the intrinsically slow kinetics of the oxygen evolution reaction (OER) at the anode. Co-based perovskite oxides have been demonstrated excellent electrocatalytic activity toward the OER in an alkaline solution, yet not all of them show sufficient activity. In this work, a novel method based on thermal reduction in an inert atmosphere was applied to convert a hexagonal-structured perovskite ($BaCo_{0.7}Fe_{0.3}O_{3-\delta 1}$, denoted as *h*-BCF) with poor OER activity into a cubic-structured perovskite ($BaCo_{0.7}Fe_{0.3}O_{3-\delta 2}$, denoted as *c*-BCF) with highly efficient OER kinetics. This unusually stabilized *c*-BCF perovskite offers a significantly reduced Co valence as well as a greatly enhanced oxygen vacancy concentration, which leads to a twenty times higher intrinsic activity relative to the pristine *h*-BCF. The intrinsic activity of *c*-BCF also surpasses that of the state-of-the-art perovskites and noble metal-based standards. This work indicates that phase transformation can be utilized as an effective means to develop new and efficient OER electrocatalysts.

6.2 Introduction

While fossil fuels continue to be the major energy sources in our daily life, their impact on the environment cannot be neglected. To address environmental issues such as the global warming, humanity needs to develop cleaner energy sources to sustainably power our planet Earth. In this regard, hydrogen (H_2) has long been recognized as an alternative energy carrier with some highly desirable properties for use in the sustainable energy sectors.[1] For instance, H_2 possesses a mass-based energy content higher than any other fuels, i.e., nearly thrice that of gasoline (120 vs. 44 MJ kg^{-1}).[2] In the meantime, the consumption of H_2 in an internal combustion engine or a fuel cell generates water as the only product, which significantly reduces carbon emissions. Among various means of hydrogen production, the electrochemical water splitting ($H_2O \rightarrow 1/2O_2 + H_2$), also known as water electrolysis, has received growing interest nowadays owing to the large quantity of water resources on Earth, the simplicity of practical operation, and the high quality of the H_2 product.[3] Despite its high viability, the efficiency of the electrolysis of water is largely impeded by the sluggish kinetics of the electrode reactions, in particular, the oxygen evolution reaction (OER) on the anode side. Associated with the complexity of the four-electron oxidation process, this OER reaction requires a considerable overpotential to occur at moderate rates, leading to a large energy loss.[4] To overcome this energy barrier, electrocatalysts comprising precious metals like ruthenium (Ru) and iridium (Ir) are widely used,[5] which show one of the best catalytic performances. Unfortunately, the scarcity and expensiveness of these catalysts have greatly hindered their industrial-scale use. Therefore, the development of cost-effective and highly efficient alternatives has been a very popular research topic central to the realization of the water splitting technology.

Over the recent years, transition metal-based (e.g., Co, Fe, Ni) materials have been extensively studied for electrocatalyzing the OER in an alkaline solution ($4OH^- \rightarrow O_2 + 2H_2O + 4e^-$), including metal or metal alloys,[6] oxides and (oxy)hydroxides,[7,8] and non-oxides such as nitrides,[9] sulfides,[10] and phosphides.[11] Among these candidates, oxide compounds featuring an ABO_3 perovskite structure have received tremendous research attention due to their cost-effectiveness and high reactivity.[12,13] For example, $Ba_{0.5}Sr_{0.5}Co_{0.8}Fe_{0.2}O_{3-\delta}$ (BSCF, here δ denotes oxygen vacancy) was demonstrated with a high intrinsic activity surpassing that of iridium dioxide (IrO_2) by more than two orders of magnitude.[14] The high activity is correlated with the electronic state of

the active Co cation having an e_g occupancy close to unity (Co valence: ~2.8; e_g occupancy: ~1.2), which can lead to an optimum binding state between the oxygen intermediates and the surface active sites.[14] This e_g parameter has led to the discovery of several other Co-based perovskites with superior catalytic activity, for example, $SrNb_{0.1}Co_{0.7}Fe_{0.2}O_{3-\delta}$,[15] $BaCo_{0.7}Fe_{0.2}Sn_{0.1}O_{3-\delta}$ (BCFSn),[16] and $SrCo_{0.9}Ti_{0.1}O_{3-\delta}$,[17] all having a Co valence in the range of 2.8–3.0, leading to near-unity e_g occupancy. Later research suggested that lowering the Co valence of BSCF could further contribute to enhanced OER performance.[18,19] Notably, nanosized BSCF prepared from a flame spray method delivered an exceptional OER activity, which was closely related to a significantly reduced Co oxidation state.[20] The ability to stabilize low-valent Co state in the BSCF perovskite is strongly associated with its extraordinary structural flexibility to accommodate a large number of oxygen vacancies, with δ ranging from 0.2 to 0.8.[21]

In fact, BSCF can be regarded as a derivative of $BaCo_{1-x}Fe_xO_{3-\delta}$ (BCF). Due to a considerable size mismatch between the A-site Ba cation and the B-site Co/Fe cations, BCF generally crystalizes in the low-symmetry hexagonal phase at room temperature.[22] The partial replacement of A-site Ba with a smaller-sized Sr dopant represents one means to sustain a simple cubic structure, as seen in the example of BSCF.[14,23] On the other hand, the incorporation of cations having a large size and a high valence at the B-site, as seen in the example of BCFSn,[16,24] represents another strategy to stabilize the cubic structure. While capable of promoting the formation of a cubic perovskite structure, these doping strategies cannot not bring about a sufficiently low Co valence, thus limiting the activity enhancement for BCF-based OER catalysts.

In this work, a novel strategy based on thermal reduction under an inert atmosphere was proposed to convert BCF perovskite from the hexagonal phase to cubic phase. As a proof-of-concept, $BaCo_{0.7}Fe_{0.3}O_{3-\delta}$ with a Co/Fe molar ratio of 7:3 was selected as a representative of the BCF series. Through the introduction of a reductive driving force provided by an inert atmosphere (e.g., nitrogen or argon) at elevated temperatures, hexagonal-structured $BaCo_{0.7}Fe_{0.3}O_{3-\delta 1}$ (denoted as *h*-BCF) successfully transitioned to cubic-structured $BaCo_{0.7}Fe_{0.3}O_{3-\delta 2}$ (denoted as *c*-BCF), following the below equation:

$$BaCo_{0.7}Fe_{0.3}O_{3-\delta 1}\ (\text{hexagonal}) \rightarrow BaCo_{0.7}Fe_{0.3}O_{3-\delta 2}\ (\text{cubic}) + 1/2(\delta 2 - \delta 1)O_2 \quad (1)$$

where $\delta 1$ and $\delta 2$ ($\delta 1 < \delta 2$) are used to represent the different amounts of oxygen vacancies in these two different structures. The formation of the cubic perovskite structure is likely due to the stabilization of low-valent Co^{2+} species which has higher ionic radius relative to Co^{3+} and Co^{4+}.[25] Simultaneously, the phase transition led to a greatly increased oxygen vacancy concentration, which, along with the considerably reduced Co valence, contributed to a remarkable enhancement in OER reactivity. When evaluated for the OER electrocatalysis in a 0.1 M KOH electrolyte, the cubic-structured *c*-BCF was found to show an intrinsic activity that is about 20-fold higher than the hexagonal structured *h*-BCF. Of significance, *c*-BCF was demonstrated to be one of the most active perovskite-type catalysts reported until now, showing intrinsic activity much better than the state-of-the-art perovskites such as BSCF and BCFSn as well as the noble metal standards IrO_2 and RuO_2. These results highlight the potential of the unusually stabilized, cubic-phase *c*-BCF perovskite for accelerating the electrocatalytic oxygen evolution.

6.3 Results and discussion

6.3.1 Stabilization of the cubic-structured *c*-BCF

The pristine hexagonal $BaCo_{0.7}Fe_{0.3}O_{3-\delta 1}$ oxide (*h*-BCF) was crystallized after calcination of a sol–gel made precursor at 1000 °C in air. To probe any potential phase change of *h*-BCF, in situ X-ray diffraction (XRD) was performed under an air atmosphere at temperatures ranging from room temperature to 900 °C. As displayed in **Figure 6.1a**, the XRD patterns exhibit identical peak features within the temperature window studied, indicating the high thermal stability of *h*-BCF. The diffraction peaks gradually shifted to smaller 2θ angels upon heating and then shifted back to the original 2θ angels upon cooling (**Figure 6.1b**), implying lattice expansion and shrinkage induced mainly by the thermal reduction. These results suggest that under the air atmosphere the pristine *h*-BCF is rather stable and undergoes no obvious phase transition at temperatures up to 900 °C. Note that phase structure at temperatures higher than 900 °C was not investigated due to the temperature limit of the XRD instrument.

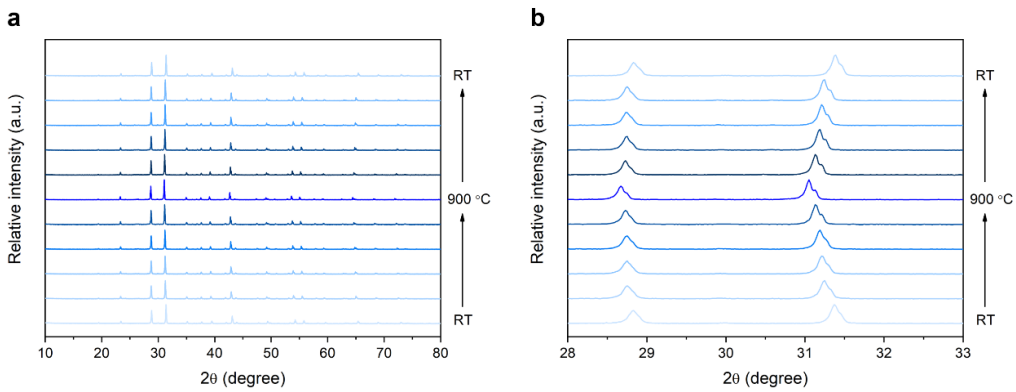

Figure 6.1 In situ XRD profiles of *h*-BCF. (a) XRD profiles presented in a broad 2*θ* range of 10–80°. (b) XRD data presented in a select 2*θ* range of 28–33°.

A more reductive condition, i.e., a N_2 atmosphere, was then employed to realize the phase transformation from *h*-BCF to the cubic-structured $BaCo_{0.7}Fe_{0.3}O_{3-\delta 2}$ (*c*-BCF). As depicted in **Figure 6.2a**, the pristine *h*-BCF possessed an XRD profile typical of the hexagonal structure as reported earlier.[26] After thermal reduction in N_2 at 900 °C, the structure completely evolved into a new one whose XRD peaks are characteristic of the ideal cubic structure (space group: $Pm\bar{3}m$).[16] This phase change was also verified by Raman spectra recorded at room temperature. As illustrated in **Figure 6.2b**, the pristine *h*-BCF displays several Raman bands at wavenumbers of ~320, ~400, ~600, and ~690 cm^{-1}. In general, these Raman shifts are consistent with those reported for the hexagonal phase,[27] although the peak intensities may appear different, which is likely caused by the inhomogeneity of the *h*-BCF sample in the laser spot area during Raman testing. By comparison, *c*-BCF exhibits a featureless Raman spectrum, which, according to literature,[28] is associated with the presence of the ideal cubic structure as perovskites with such structure do not present any Raman active modes. The combined XRD and Raman characterizations reveal that with calcination at 900 °C under the N_2 atmosphere, the hexagonal-structured $BaCo_{0.7}Fe_{0.3}O_{3-\delta 1}$ successfully transitioned into the cubic-structured $BaCo_{0.7}Fe_{0.3}O_{3-\delta 2}$. The phase transition is most likely facilitated by the effect of a much lower oxygen partial pressure, as enabled by a more reductive atmosphere (i.e., N_2 versus air), providing a driving force strong enough for the transition to occur.

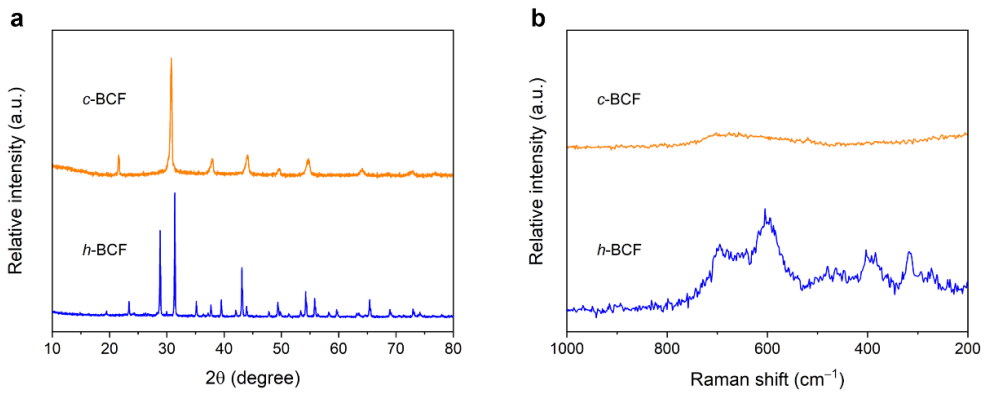

Figure 6.2 XRD profiles and Raman spectra of *h*-BCF and *c*-BCF. (a) XRD profiles presented in a 2θ range of 10–80°. (b) Raman spectra presented in a wavenumber range of 200–1000 cm^{-1}.

To further investigate the phase transformation of *h*-BCF, a combined thermogravimetric and differential scanning calorimetry analysis (TG-DSC) was conducted under an argon (Ar) atmosphere, with the results presented in **Figure 6.3a**. A progressive weight loss was observed after the temperature reached 400 °C until a more drastic weight loss took place at about 800 °C. Concomitant with this drastic weight loss is an endothermic peak appearing at the temperature of about 825 °C, which can be ascribed to the phase transformation from hexagonal to cubic.[29] The sample weight became unchanged after the settling period at 900 °C, leading to a total weight loss of 2.28 wt%. The phase transition process of *h*-BCF was also examined by oxygen temperature-programmed desorption (O_2-TPD) experiment conducted in an Ar atmosphere. As shown in **Figure 6.3b**, a broad peak that initiated at about 550 °C and peaked at about 740 °C is assignable to the reduction of tetravalent Co^{4+}/Fe^{4+} to trivalent Co^{3+}/Fe^{3+}, and another sharp peak at about 865 °C is related to the further reduction of trivalent Co^{3+} to divalent Co^{2+}.[24] Note that the overall result of O_2-TPD accords with that of TG-DSC, while the minor inconsistency in temperatures is likely due to the variations in the sample mass and sample form used in the two different analysis instruments (about 30 mg of powder in TG-DSC and about 0.15 g of 150-mesh granule in O_2-TPD).

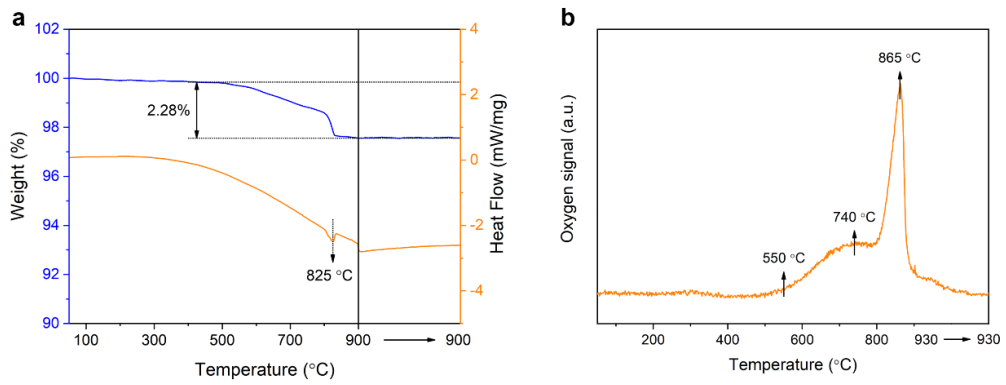

Figure 6.3 TG-DSC and O_2-TPD profiles of *h*-BCF. (a) TG-DSC profile. (b) O_2-TPD profile.

The *h*-BCF sample after the O_2-TPD experiment in Ar atmosphere was further subjected to XRD analysis. As shown in **Figure 6.4**, XRD diffraction peaks identical to those of the *c*-BCF sample obtained in N_2 atmosphere were observed, suggesting the reproducibility of the phase transition in two different inert atmospheres. The above experiments indicate that the stabilization of the cubic structure of *c*-BCF is likely due to the generation of Co^{2+} species which has higher ionic radius than Co^{3+}/Co^{4+}.[25] Additional experimental trials on another hexagonal perovskite with a similar composition, namely $BaCo_{0.8}Fe_{0.2}O_{3-\delta}$ (BCF82), did not give rise to the stabilization of a pure cubic phase, as revealed in **Figure 6.5**. This suggests that the hexagonal to cubic phase transition could also be dependent on the relevant content of the constituent metals.

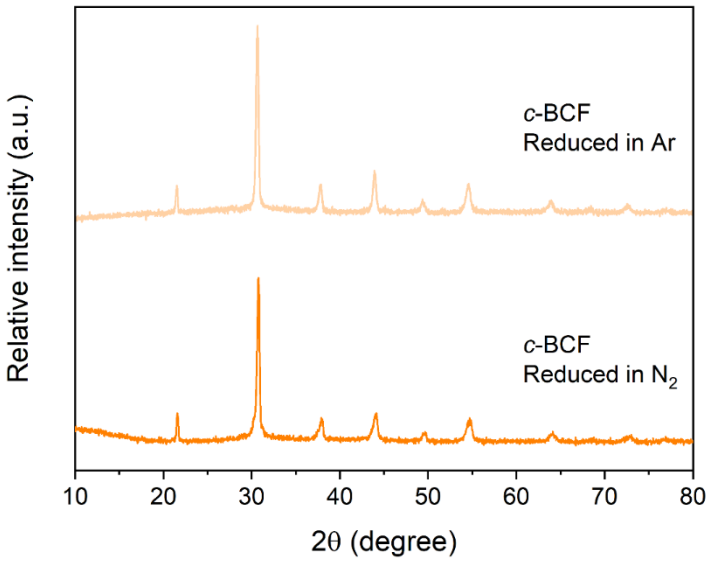

Figure 6.4 XRD profiles of *c*-BCF obtained by reducing *h*-BCF in N_2 (during synthesis) and in Ar (during O_2-TPD experiment).

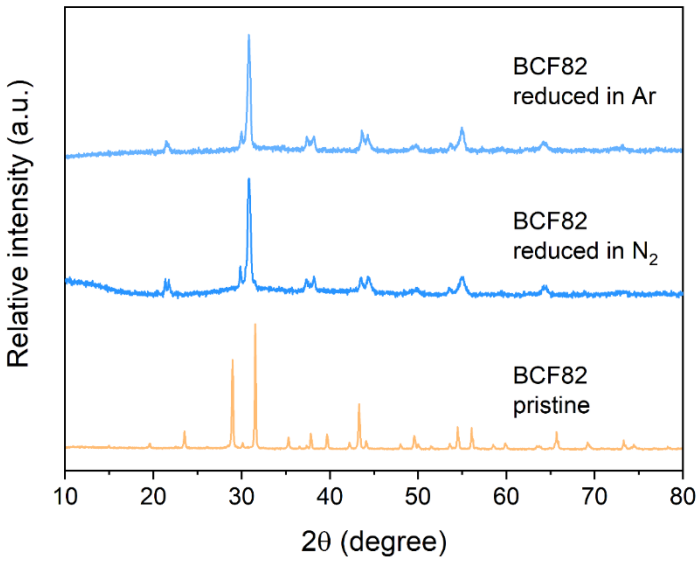

Figure 6.5 XRD profiles of the pristine $BaCo_{0.8}Fe_{0.2}O_{3-\delta}$ (BCF82) sample, BCF82 after reduction in N_2 (during synthesis), and BCF82 after reduction in Ar (during O_2-TPD experiment).

6.3.2 Electrocatalytic oxygen evolution performance

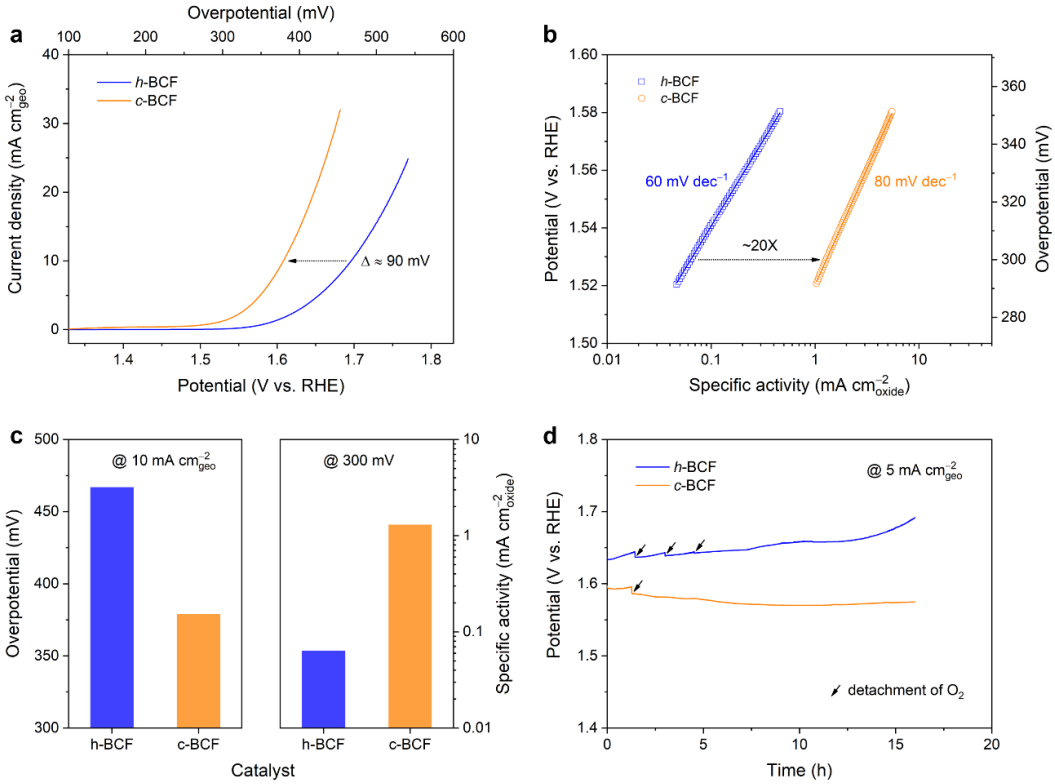

Figure 6.6 Electrocatalytic performance of *h*-BCF and *c*-BCF toward the oxygen evolution reaction in a 0.1 M KOH electrolyte. (a) OER kinetic currents. The arrow shows a decreasing trend in the potential required to produce a current density of 10 mA cm^{-2}_{geo}. (b) Tafel plot where the OER currents are normalized by the catalyst surface areas to obtain the specific activity. The arrow shows an increasing trend in the specific activity at an overpotential of 300 mV. (c) Comparisons of the overpotential at a current density of 10 mA cm^{-2}_{geo} and the specific activity at an overpotential of 300 mV. (d) Electrochemical stability recorded by chronopotentiometry tests at a steady current density of 5 mA cm^{-2}_{geo}. The arrows indicate the detachment of O_2 bubbles generated on the electrode surface.

The electrocatalytic OER performance was measured at room temperature in an O_2-saturated 0.1 M KOH electrolyte. Both the pristine *h*-BCF and the reduced *c*-BCF were loaded on a glassy carbon rotating disk electrode to act as the working electrode. **Figure 6.6a** shows the OER kinetic currents based on the geometric area of the working electrode, which were obtained by averaging and *iR*-correcting the as-

recorded cyclic voltammograms to eliminate distractions from the capacitive current and the electrolyte resistance, respectively.[14,30] As is obvious, the OER on the reduced *c*-BCF sample initiated at a much earlier potential than the pristine *h*-BCF did, indicating significantly improved OER activity after the phase transition. More specifically, *c*-BCF produced a current density of 10 mA cm_{geo}^{-2} at an overpotential of 379 mV (η_{10} = 379 mV, here η_{10} is a solar-fuel synthesis related parameter used for comparing OER activity),[31] which is approximately 90 mV smaller compared to *h*-BCF (η_{10} = 467 mV). These reductions in (over)potentials are indicative of a boost in the geometric electrode activity (also known as the apparent activity) induced by the phase transformation.

To rule out the contribution of the catalyst surface area to the observed electrode activity, the OER kinetic currents were then normalized by the Brunauer–Emmett–Teller (BET) surface area estimated using N_2 sorption measurements (0.62 and 0.38 $m^2\ g^{-1}$ for *h*-BCF and *c*-BCF, respectively), which yielded specific activity as a metric for comparing the intrinsic activity.[14,32] **Figure 6.6b** plots the logarithm of specific activity as a function of the potential. It was found that *c*-BCF consistently outperformed *h*-BCF in terms of the specific activity within the entire potential window of 1.52–1.58 V vs. the reversible hydrogen electrode (RHE). For example, at an overpotential of 300 mV, *c*-BCF delivered a specific activity approximately twenty times that of *h*-BCF (1.30 vs. 0.064 mA cm_{oxide}^{-2}), implying that enhancement in the OER intrinsic activity was also observed after the phase transition. The data in **Figure 6.6b** were further fitted to obtain the Tafel slope. *c*-BCF exhibited a Tafel slope value that is somewhat higher than that of *h*-BCF (80 vs. 60 mV dec^{-1}), which might suggest an alteration in the OER reaction mechanism. **Figure 6.6c** illustrates the comparisons regarding the discussion made in **Figure 6.6a** and **b**, further highlighting the improved OER reactivity resulting from the phase transformation. A comparison was also made with the state-of-the-art perovskite OER catalysts in terms of the specific activity at a 300-mV overpotential, as tabulated in **Table 6.1**. Remarkably, the *c*-BCF sample showed a higher intrinsic activity than several other BCF-based perovskites, for example BSCF (~0.53 mA cm_{oxide}^{-2})[14] and BCFSn (~0.14 mA cm_{oxide}^{-2}),[16] demonstrating the high efficacy of the unusually stabilized *c*-BCF perovskite in catalyzing the OER. Of importance, *c*-BCF was found to exhibit one of the best performances reported to date, surpassing that of single perovskite

$Cs_{0.4}La_{0.6}Mn_{0.25}Co_{0.75}O_3$ (~0.79 mA cm_{oxide}^{-2}),[33] double perovskite $PrBaCo_2O_{5+\delta}$ (~0.74 mA cm_{oxide}^{-2}),[34] Ruddlesden–Popper perovskite $La_{0.5}Sr_{1.5}Ni_{0.7}Fe_{0.3}O_{4+\delta}$ (~0.76 mA cm_{oxide}^{-2}),[35] and quadruple perovskite $CaCu_3Fe_4O_{12}$ (~0.17 mA cm_{oxide}^{-2}).[36] More importantly, *c*-BCF displayed an intrinsic activity almost two orders of magnitude higher than the noble metal-based benchmarking catalysts, IrO_2 (~0.015 mA cm_{oxide}^{-2}) and RuO_2 (~0.011 mA cm_{oxide}^{-2}).[37] These comparisons underscore the good OER activity of the cubic-structured *c*-BCF sample.

Table 6.1 A comparison of the OER activity (in terms of the specific activity at an overpotential of 300 mV) of *c*-BCF with other state-of-the-art perovskite catalysts and noble metal oxides tested on a glassy carbon electrode in 0.1 M KOH.

Catalyst	Loading (mg cm^{-2})	Catalyst/carbon mass ratio	Specific activity[a] (mA cm_{oxide}^{-2})	Ref.
c-BCF	0.255	5:1	1.30	This work
IrO_2	0.050	No carbon[b]	~0.015[c]	37
RuO_2	0.050	No carbon	~0.011	37
$Ba_{0.5}Sr_{0.5}Co_{0.8}Fe_{0.2}O_{3-\delta}$	0.250	5:1	~0.53	14
$BaCo_{0.7}Fe_{0.2}Sn_{0.1}O_{3-\delta}$	0.232	1:1	~0.14	16
$Cs_{0.4}La_{0.6}Mn_{0.25}Co_{0.75}O_3$	0.168	No carbon	~0.79	33
$PrBaCo_2O_{5+\delta}$	0.250	5:1	~0.74	34
$La_{0.5}Sr_{1.5}Ni_{0.7}Fe_{0.3}O_{4+\delta}$	0.0153	3:7	~0.76	35
$CaCu_3Fe_4O_{12}$	0.250	5:1	~0.17	36

[a] The specific activity was compared at an overpotential of 300 mV (i.e., a potential of 1.529 V vs. RHE).

[b] The catalyst was loaded on the glassy carbon electrode without the addition of conductive carbon.

[c] The activity data in this column were obtained from published results using the software WebPlotDigitizer.[38]

The stability of *h*-BCF and *c*-BCF as the OER electrocatalysts was tested by chronopotentiometry at a steady current density of 5 mA cm_{geo}^{-2} for 16 h. During these tests, O_2 bubbles were accumulated on the electrode surface due to the continuous oxidation of water, which were then detached under the constant rotation of the electrode, as indicated by the arrows in **Figure 6.6d**. For *h*-BCF, the potential to maintain 5 mA cm_{geo}^{-2} began to increase after a 10-hour period, indicating relatively poor stability. By contrast, a more stable behavior was observed for the *c*-BCF sample, which required an almost unchanged voltage to sustain 5 mA cm_{geo}^{-2} after the initial O_2 detachment at about 1 h. These chronopotentiometry tests suggest that aside from activity, *c*-BCF also demonstrated better electrochemical stability than *h*-BCF.

6.3.3 Understanding the enhancement in catalytic performance

The OER activity of an electrocatalytic is strongly correlated with its electronic structure. As described by Equation (1), the transition from *h*-BCF to *c*-BCF not only alters the phase structure of the material but also changes the oxygen stoichiometry and the transition metal valence. As reported earlier, the pristine *h*-BCF has an average valence of 3.73 for Co and Fe,[24] from which the oxygen non-stoichiometry is calculated to be $\delta 1$ = 0.135 based on charge neutrality. In addition, the phase transition led to a total mass loss of 2.28 wt% (**Figure 6.3a**), which can be used to compute the oxygen non-stoichiometry ($\delta 2$ = 0.478) and accordingly the average transition metal valence (3.04). By assuming that the Fe cation has a valence of 4+ or 3+, the lower and upper limit for the Co valence was also approximated, as presented in **Table 6.2**. Overall, an increase in oxygen vacancy concentration as well as a reduction in the transition meatal valence were observed after the phase transition.

Table 6.2 Oxygen vacancy, average metal valence, and Co valence of *h*-BCF and *c*-BCF.

Perovskite	Oxygen vacancy, δ	Average metal valence	Co valence (for Fe^{4+})[a]	Co valence (for Fe^{3+})[a]
$BaCo_{0.7}Fe_{0.3}O_{3-\delta 1}$ (*h*-BCF)	$\delta 1 = 0.135$	3.73[b]	3.61	4.04[c]
$BaCo_{0.7}Fe_{0.3}O_{3-\delta 2}$ (*c*-BCF)	$\delta 2 = 0.478$	3.04	2.63	3.06

[a] Lower and upper limit for the Co valence, as estimated by assuming that Fe is of tetravalent or trivalent, respectively.

[b] Data reported earlier, as obtained from chemical titration.[24]

[c] While this value exceeds 4.00, it is just an estimation of the upper limit for the Co valence.

Previous publications on oxygen-deficient perovskites suggest that incorporating oxygen vacancies can promote the OER electrocatalysis.[30,39,40] For instance, A-site La-deficient $La_{0.95}FeO_{3-\delta}$ was reported with an increased number of oxygen vacancies as compared to the stoichiometric $LaFeO_3$,[39] showing a ~6-fold enhancement in the OER intrinsic activity under the conventional adsorbate evolution mechanism (AEM).[14] In another work, Sr substitution for La in the $La_{1-x}Sr_xCoO_{3-\delta}$ series significantly boosted the OER reaction kinetics, and the $SrCoO_{3-\delta}$ sample with the highest Sr content possessed the largest oxygen vacancy content and exhibited the best OER activity, which is likely associated with the functioning of a novel lattice-oxygen mediated mechanism (LOM).[40] In contrast to the AEM pathway where the OER takes place primarily on the surface metal site,[14] the LOM mechanism involves the lattice oxygen as an additional active site.[40] Later research further suggests that the extent to which the lattice oxygen participates in the OER is related to the oxygen-ion diffusivity, the higher the oxygen-ion diffusivity, the higher the OER activity.[30] It is therefore reasonable to suggest that the more than three-fold increase in the oxygen vacancy

concentration is critical to the enhanced OER activity of *c*-BCF relative to *h*-BCF. Furthermore, *c*-BCF with a crystal symmetry higher than *h*-BCF is expected to offer faster oxygen-ion mobility and thus facilitate the proceeding of the OER under the LOM reaction scheme.[41]

In addition, the reduced Co oxidation state may also be beneficial to the OER. For perovskites utilizing the AEM mechanism, those that contain transition metal with a suitable e_g orbital filling number near unity were reported to show optimum OER reactivity, as exemplified by the BSCF perovskite (with a valence of ~2.8 and an e_g filling of ~1.2 for Co).[14] Based on the assumption that Co in both *h*-BCF and *c*-BCF is in an intermediate spin state, the e_g occupancy can be estimated from the Co valence to be 0–0.4 for *h*-BCF and 1–1.4 for *c*-BCF, with the latter closer to unity. This approximation suggests that under the AEM scheme, the reduced Co valence in *c*-BCF is more favorable to the OER.

It should be noted that strictly speaking, the determination of the real spin state of the Co cation in these perovskites would require experimental inputs from spectroscopic tools such as X-ray absorption spectroscopy (XAS) and Mössbauer spectroscopy.[42,43] The advantageous role of reduced Co valence for the OER is also supported by two recent studies based on the BSCF catalyst: one modifies BSCF by compositing with reductive carbon and the other by altering the synthetic approach,[18,19] both leading to a lower Co oxidation state and a higher OER performance. In another report, nanosized BSCF was prepared by a flame spray method,[20] which stabilized the Co cation at an even lower valence between 2.13 and 2.38, estimated from the oxygen vacancy of ~0.75 utilizing a similar approximation demonstrated in **Table 6.2**. Interestingly, the LOM mechanism is likely operative during the OER on this nanosized BSCF, leading to growth of an oxy(hydroxide) surface layer with high activity, as evidenced by operando XAS measurements.[20] The dynamic generation of the OER-active surface layer is favored by the large quantity of oxygen vacancy, which is generated due to the essential role of the reduced Co valence.[20] While whether the surface of *c*-BCF can undergo a similar reconstruction remains to be an open question, it is believed that the reduced oxidation state of Co is likely to aid the complex OER process.

As the electrochemical reaction occurs mostly near the catalyst surface, X-ray photoelectron spectroscopy (XPS) was performed to probe the surface chemical state

of the samples. **Figure 6.7** compares the XPS spectra of *h*-BCF and *c*-BCF. Due to an overlap between the Co 2p and Ba 3d core levels at the binding energies of about 780 eV for Co $2p_{3/2}$ and Ba $3d_{5/2}$ and about 795 eV for Co $2p_{1/2}$ and Ba $3d_{3/2}$,[44] a quantitative analysis of the Co valence appears to be quite challenging. However, a shift of the doublet to lower binding energies can be found for the *c*-BCF sample compared to *h*-BCF, which according to previous literature,[45,46] may indicate a decrease in the surface Co valence.

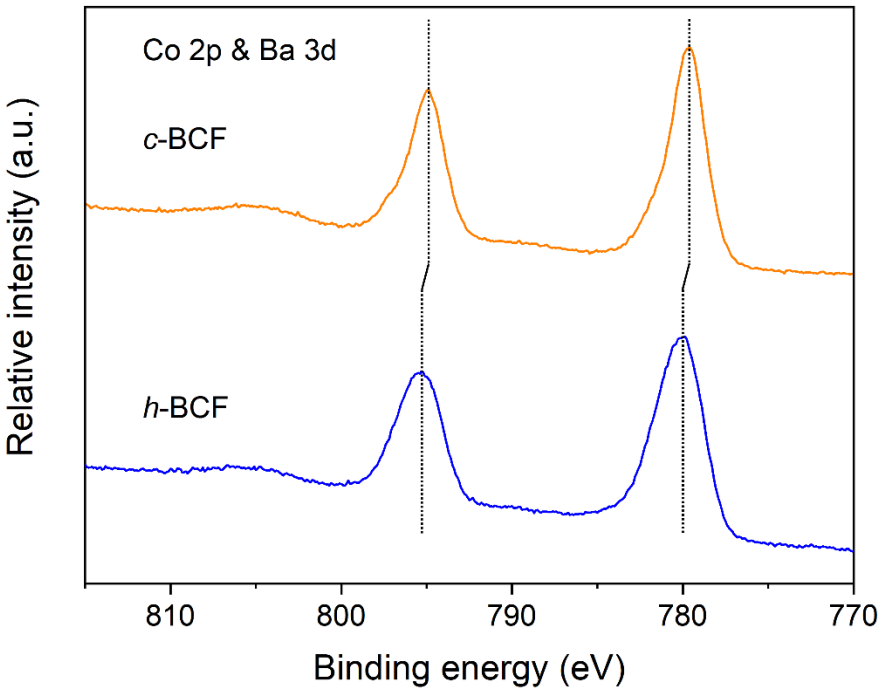

Figure 6.7 XPS spectra of the Co 2p and Ba 3d core levels for *h*-BCF and *c*-BCF.

The above discussion suggests that an increase in the oxygen vacancy amount and a decrease in the Co valence, which accompany the phase transition from *h*-BCF to *c*-BCF, may collectively account for the improved OER activity. The observation that compared to the BSCF perovskite, *c*-BCF with a higher oxygen vacancy concentration and a smaller Co valence exhibited a better OER intrinsic activity (**Table 6.1**) may further support this conclusion. It should be noted that while the other transition metal, Fe, could also undergo a reduction after the phase transition, this effect contributes insignificantly to the overall OER electrocatalysis. On the one hand, compared to Co,

Fe in general is less OER-active and constitutes a much smaller fraction of the B-site.[47] On the other hand, tetravalent Fe^{4+} is often more active than trivalent Fe^{3+} when incorporated in perovskites,[36,39] although the Fe^{4+}-to-Fe^{3+} reduction may be more difficult to occur than the Co^{4+}-to-Co^{3+} reduction.[48]

6.4 Conclusions

In conclusion, cubic-structured *c*-BCF was stabilized by reducing hexagonal-structured *h*-BCF in an inert atmosphere at elevated temperatures. The hexagonal-to-cubic phase transformation resulted in both a reduction in Co valence and an increase in oxygen vacancy concentration, which contributed to a 20-fold rise in the OER intrinsic activity in alkaline solutions. Importantly, *c*-BCF turned out to be one of the most active perovskite-type electrocatalysts reported till date, comparing favorably to the state-of-the-art perovskites while surpassing the noble metal-based standards. Additionally, *c*-BCF also presented good electrocatalytic stability. These results suggest that the unusually stabilized, cubic-structured *c*-BCF perovskite has the promise for accelerating the electrochemical water splitting kinetics. A next step would be to thoroughly investigate the reaction mechanism by which *c*-BCF catalyzes the OER.

6.5 References

(1) Hosseini, S. E.; Wahid, M. A. Hydrogen production from renewable and sustainable energy resources: Promising green energy carrier for clean development. *Renew. Sustain. Energy Rev.* **2016**, *57*, 850–866.

(2) Wang, W.; Xu, M.; Xu, X.; Zhou, W.; Shao, Z. Perovskite oxide based electrodes for high-performance photoelectrochemical water splitting. *Angew. Chem. Int. Ed.* **2020**, *59*, 136–152.

(3) Darband, G. B.; Aliofkhazraei, M.; Shanmugam, S. Recent advances in methods and technologies for enhancing bubble detachment during electrochemical water splitting. *Renew. Sustain. Energy Rev.* **2019**, *114*, 109300.

(4) Suen, N.-T.; Hung, S.-F.; Quan, Q.; Zhang, N.; Xu, Y.-J.; Chen, H. M. Electrocatalysis for the oxygen evolution reaction: recent development and future perspectives. *Chem. Soc. Rev.* **2017**, *46*, 337–365.

(5) Shi, Q.; Zhu, C.; Du, D.; Lin, Y. Robust noble metal-based electrocatalysts for oxygen evolution reaction. *Chem. Soc. Rev.* **2019**, *48*, 3181–3192.

(6) Wang, C.; Yang, H.; Zhang, Y.; Wang, Q. NiFe alloy nanoparticles with hcp crystal structure stimulate superior oxygen evolution reaction electrocatalytic activity. *Angew. Chem. Int. Ed.* **2019**, *58*, 6099–6103.

(7) Chung, D. Y.; Lopes, P. P.; Farinazzo Bergamo Dias Martins, P.; He, H.; Kawaguchi, T.; Zapol, P.; You, H.; Tripkovic, D.; Strmcnik, D.; Zhu, Y. et al. Dynamic stability of active sites in hydr(oxy)oxides for the oxygen evolution reaction. *Nat. Energy* **2020**, *5*, 222–230.

(8) Sun, Y.; Liao, H.; Wang, J.; Chen, B.; Sun, S.; Ong, S. J. H.; Xi, S.; Diao, C.; Du, Y.; Wang, J.-O. et al. Covalency competition dominates the water oxidation structure–activity relationship on spinel oxides. *Nat. Catal.* **2020**, *3*, 554–563.

(9) Zhu, Y.; Chen, G.; Zhong, Y.; Chen, Y.; Ma, N.; Zhou, W.; Shao, Z. A surface-modified antiperovskite as an electrocatalyst for water oxidation. *Nat. Commun.* **2018**, *9*, 2326.

(10) Li, P.; Zhao, X.; Duan, X.; Li, Y.; Kuang, Y.; Sun, X. A multiphase nickel iron sulfide hybrid electrode for highly active oxygen evolution. *Sci. China Mater.* **2020**, *63*, 356–363.

(11) Yang, S.; Chen, G.; Ricciardulli, A. G.; Zhang, P.; Zhang, Z.; Shi, H.; Ma, J.; Zhang, J.; Blom, P. W. M.; Feng, X. Topochemical synthesis of two-dimensional transition-metal phosphides using phosphorene templates. *Angew. Chem. Int. Ed.* **2020,** *59*, 465–470.

(12) Hwang, J.; Rao, R. R.; Giordano, L.; Katayama, Y.; Yu, Y.; Shao-Horn, Y. Perovskites in catalysis and electrocatalysis. *Science* **2017**, *358*, 751–756.

(13) Xu, X.; Wang, W.; Zhou, W.; Shao, Z. Recent advances in novel nanostructuring methods of perovskite electrocatalysts for energy-related applications. *Small Methods* **2018**, *2*, 1800071.

(14) Suntivich, J.; May, K. J.; Gasteiger, H. A.; Goodenough, J. B.; Shao-Horn, Y. A perovskite oxide optimized for oxygen evolution catalysis from molecular orbital principles. *Science* **2011**, *334*, 1383–1385.

(15) Zhu, Y.; Zhou, W.; Chen, Z.-G.; Chen, Y.; Su, C.; Tadé, M. O.; Shao, Z. $SrNb_{0.1}Co_{0.7}Fe_{0.2}O_{3-\delta}$ perovskite as a next-generation electrocatalyst for oxygen evolution in alkaline solution. *Angew. Chem. Int. Ed.* **2015**, *54*, 3897–3901.

(16) Xu, X.; Su, C.; Zhou, W.; Zhu, Y.; Chen, Y.; Shao, Z. Co-doping strategy for developing perovskite oxides as highly efficient electrocatalysts for oxygen evolution reaction. *Adv. Sci.* **2016**, *3*, 1500187.

(17) Su, C.; Wang, W.; Chen, Y.; Yang, G.; Xu, X.; Tadé, M. O.; Shao, Z. $SrCo_{0.9}Ti_{0.1}O_{3-\delta}$ as a new electrocatalyst for the oxygen evolution reaction in alkaline electrolyte with stable performance. *ACS Appl. Mater. Interfaces* **2015**, *7*, 17663–17670.

(18) Fabbri, E.; Nachtegaal, M.; Cheng, X.; Schmidt, T. J. Superior bifunctional electrocatalytic activity of $Ba_{0.5}Sr_{0.5}Co_{0.8}Fe_{0.2}O_{3-\delta}$/carbon composite electrodes: Insight into the local electronic structure. *Adv. Energy Mater.* **2015,** *5*, 1402033.

(19) Xu, X.; Pan, Y.; Zhou, W.; Chen, Y.; Zhang, Z.; Shao, Z. Toward enhanced oxygen evolution on perovskite oxides synthesized from different approaches: A case study of $Ba_{0.5}Sr_{0.5}Co_{0.8}Fe_{0.2}O_{3-\delta}$. *Electrochim. Acta* **2016**, *219*, 553–559.

(20) Fabbri, E.; Nachtegaal, M.; Binninger, T.; Cheng, X.; Kim, B.-J.; Durst, J.; Bozza, F.; Graule, T.; Schäublin, R.; Wiles, L. et al. Dynamic surface self-reconstruction is the key of highly active perovskite nano-electrocatalysts for water splitting. *Nat. Mater.* **2017**, *16*, 925–931.

(21) McIntosh, S.; Vente, J. F.; Haije, W. G.; Blank, D. H. A.; Bouwmeester, H. J. M. Oxygen stoichiometry and chemical expansion of $Ba_{0.5}Sr_{0.5}Co_{0.8}Fe_{0.2}O_{3-\delta}$ measured by in situ neutron diffraction. *Chem. Mater.* **2006**, *18*, 2187–2193.

(22) Yoshiya, M.; Fisher, C. A. J.; Iwamoto, Y.; Asanuma, M.; Ishii, J.; Yabuta, K. Phase stability of $BaCo_{1-y}Fe_yO_{3-\delta}$ by first principles calculations. *Solid State Ionics* **2004**, *172*, 159–163.

(23) Shao, Z.; Haile, S. M. A high-performance cathode for the next generation of solid-oxide fuel cells. *Nature* **2004**, *431*, 170–173.

(24) Zhang, Z.; Chen, Y.; Tade, M. O.; Hao, Y.; Liu, S.; Shao, Z. Tin-doped perovskite mixed conducting membrane for efficient air separation. *J. Mater. Chem. A* **2014**, *2*, 9666–9674.

(25) Shannon, R. Revised effective ionic radii and systematic studies of interatomic distances in halides and chalcogenides. *Acta Cryst. A* **1976**, *32*, 751–767.

(26) Cheng, Y.; Zhao, H.; Teng, D.; Li, F.; Lu, X.; Ding, W. Investigation of Ba fully occupied A-site $BaCo_{0.7}Fe_{0.3-x}Nb_xO_{3-\delta}$ perovskite stabilized by low concentration of Nb for oxygen permeation membrane. *J. Membr. Sci.* **2008**, *322*, 484–490.

(27) Martín-Carrón, L.; de Andrés, A.; Martínez-Lope, M. J.; Casais, M. T.; Alonso, J. A. Raman phonons and light scattering in $RMnO_3$ (R=La, Pr, Nd, Ho, Er Tb and Y) orthorhombic and hexagonal manganites. *J. Alloys Compd.* **2001**, *323–324*, 494–497.

(28) Granado, E.; Moreno, N. O.; García, A.; Sanjurjo, J. A.; Rettori, C.; Torriani, I.; Oseroff, S. B.; Neumeier, J. J.; McClellan, K. J.; Cheong, S. W. et al. Phonon Raman scattering in $R_{1-x}A_xMnO_{3+\delta}$ (R = La, Pr; A = Ca, Sr). *Phys. Rev. B* **1998**, *58*, 11435–11440.

(29) Zhao, H.; Xu, N.; Cheng, Y.; Wei, W.; Chen, N.; Ding, W.; Lu, X.; Li, F. Investigation of mixed conductor $BaCo_{0.7}Fe_{0.3-x}Y_xO_{3-\delta}$ with high oxygen permeability. *J. Phys. Chem. C* **2010**, *114*, 17975–17981.

(30) Pan, Y.; Xu, X.; Zhong, Y.; Ge, L.; Chen, Y.; Veder, J.-P. M.; Guan, D.; O'Hayre, R.; Li, M.; Wang, G. et al. Direct evidence of boosted oxygen evolution over perovskite by enhanced lattice oxygen participation. *Nat. Commun.* **2020**, *11*, 2002.

(31) Gorlin, Y.; Jaramillo, T. F. A bifunctional nonprecious metal catalyst for oxygen reduction and water oxidation. *J. Am. Chem. Soc.* **2010**, *132*, 13612–13614.

(32) Wei, C.; Sun, S.; Mandler, D.; Wang, X.; Qiao, S. Z.; Xu, Z. J. Approaches for measuring the surface areas of metal oxide electrocatalysts for determining their intrinsic electrocatalytic activity. *Chem. Soc. Rev.* **2019**, *48*, 2518–2534.

(33) Weng, B.; Song, Z.; Zhu, R.; Yan, Q.; Sun, Q.; Grice, C. G.; Yan, Y.; Yin, W.-J. Simple descriptor derived from symbolic regression accelerating the discovery of new perovskite catalysts. *Nat. Commun.* **2020**, *11*, 3513.

(34) Grimaud, A.; May, K. J.; Carlton, C. E.; Lee, Y.-L.; Risch, M.; Hong, W. T.; Zhou, J.; Shao-Horn, Y. Double perovskites as a family of highly active catalysts for oxygen evolution in alkaline solution. *Nat. Commun.* **2013**, *4*, 2439.

(35) Forslund, R. P.; Hardin, W. G.; Rong, X.; Abakumov, A. M.; Filimonov, D.; Alexander, C. T.; Mefford, J. T.; Iyer, H.; Kolpak, A. M.; Johnston, K. P. et al. Exceptional electrocatalytic oxygen evolution via tunable charge transfer interactions in $La_{0.5}Sr_{1.5}Ni_{1-x}Fe_xO_{4\pm\delta}$ Ruddlesden-Popper oxides. *Nat. Commun.* **2018**, *9*, 3150.

(36) Yagi, S.; Yamada, I.; Tsukasaki, H.; Seno, A.; Murakami, M.; Fujii, H.; Chen, H.; Umezawa, N.; Abe, H.; Nishiyama, N. et al. Covalency-reinforced oxygen evolution reaction catalyst. *Nat. Commun.* **2015**, *6*, 8249.

(37) Lee, Y.; Suntivich, J.; May, K. J.; Perry, E. E.; Shao-Horn, Y. Synthesis and activities of rutile IrO_2 and RuO_2 nanoparticles for oxygen evolution in acid and alkaline solutions. *J. Phys. Chem. Lett.* **2012**, *3*, 399–404.

(38) Rohatgi, A.; Austin, Texas, USA, **2017**.

(39) Zhu, Y.; Zhou, W.; Yu, J.; Chen, Y.; Liu, M.; Shao, Z. Enhancing electrocatalytic activity of perovskite oxides by tuning cation deficiency for oxygen reduction and evolution reactions. *Chem. Mater.* **2016**, *28*, 1691–1697.

(40) Mefford, J. T.; Rong, X.; Abakumov, A. M.; Hardin, W. G.; Dai, S.; Kolpak, A. M.; Johnston, K. P.; Stevenson, K. J. Water electrolysis on $La_{1-x}Sr_xCoO_{3-\delta}$ perovskite electrocatalysts. *Nat. Commun.* **2016**, *7*, 11053.

(41) Chen, Y.; Qian, B.; Shao, Z. Tin and iron co-doping strategy for developing active and stable oxygen reduction catalysts from $SrCoO_{3-\delta}$ for operating below 800 °C. *J. Power Sources* **2015**, *294*, 339–346.

(42) Harvey, A. S.; Yang, Z.; Infortuna, A.; Beckel, D.; Purton, J. A.; Gauckler, L. J. Development of electron holes across the temperature-induced semiconductor–metal transition in $Ba_{1-x}Sr_xCo_{1-y}Fe_yO_{3-\delta}$ (x, y = 0.2–0.8): a soft x-ray absorption spectroscopy study. *J. Phys. Condens. Matter* **2008**, *21*, 015801.

(43) Russo, U.; Nodari, L.; Faticanti, M.; Kuncser, V.; Filoti, G. Local interactions and electronic phenomena in substituted $LaFeO_3$ perovskites. *Solid State Ionics* **2005**, *176*, 97–102.

(44) Norman, C.; Leach, C. In situ high temperature X-ray photoelectron spectroscopy study of barium strontium iron cobalt oxide. *J. Membr. Sci.* **2011**, *382*, 158–165.

(45) Dupin, J. C.; Gonbeau, D.; Benqlilou-Moudden, H.; Vinatier, P.; Levasseur, A. XPS analysis of new lithium cobalt oxide thin-films before and after lithium deintercalation. *Thin Solid Films* **2001**, *384*, 23–32.

(46) Luo, X. G.; Chen, X. H.; Liu, X.; Wang, R. T.; Xiong, Y. M.; Wang, C. H.; Wang, G. Y.; Qiu, X. G. Magnetic and transport properties in $CoSr_2Y_{1-x}Ca_xCu_2O_7$ (x=0–0.4). *Phys. Rev. B* **2004**, *70*, 054520.

(47) Trasatti, S. Electrocatalysis in the anodic evolution of oxygen and chlorine. *Electrochim. Acta* **1984**, *29*, 1503–1512.

(48) Tai, L. W.; Nasrallah, M. M.; Anderson, H. U.; Sparlin, D. M.; Sehlin, S. R. Structure and electrical properties of $La_{1-x}Sr_xCo_{1-y}Fe_yO_3$. Part 1. The system $La_{0.8}Sr_{0.2}Co_{1-y}Fe_yO_3$. *Solid State Ionics* **1995**, *76*, 259–271.

Chapter 7 Alkali-metal-doped perovskites for efficient oxygen evolution in alkaline solutions

7.1 Abstract

Perovskite oxides are widely researched as the oxygen evolution reaction (OER) electrocatalysts in alkaline water splitting, due to their cost-effectiveness and high activity. To date, the majority of research concentrates on Co-containing perovskites and a range of highly efficient perovskite catalysts have been developed by applying a simple cation doping strategy. This work reports a doping strategy rarely adopted previously, that is alkali-metal doping. By selecting Fe-containing $LaFeO_3$ as the model catalyst, aliovalent Na^+ was partially doped into the A-site to replace the La^{3+}. While the alkali-metal incorporation did not alter the orthorhombic phase structure, it did lead to changes in the perovskite electronic structure, including an increased Fe oxidation state, an enhanced Fe–O covalency, and an enlarged oxygen vacancy concentration. These changes were further found to promote the OER activity of the Fe-based perovskites, with $La_{0.9}Na_{0.1}FeO_{3-\delta}$ (x = 0.1) showing a ~90-mV drop in the overpotential to afford a current density of 10 mA cm_{geo}^{-2} and a 8-fold growth in the intrinsic activity. These results suggest that the alkali-metal doping could open up a new avenue for the design of efficient perovskite OER catalysts.

7.2 Introduction

The electrochemical water splitting represents a clean pathway to the production of high-purity hydrogen (H_2) for powering our planet without carbon emissions into the environment. While the electrolysis of water appears to be a quite simple reaction ($H_2O \rightarrow 1/2O_2 + H_2$), it does not proceed at its thermodynamic voltage (1.229 V) and requires additional energy input to occur at appreciable rates.[1] Most of this extra energy is used to overcome the large energy barriers of the two half-reactions involved, of which the anodic oxygen evolution reaction (OER), a complex multistep four-electron process also referred to as water oxidation, accounts for a major share.[2] To drive the OER more efficiently, noble metal-based materials, for example, those containing iridium (Ir) and ruthenium (Ru), have been demonstrated with one of the best catalytic activities.[3] Unfortunately, as these noble metals are scarce in natural resources and high in cost,[4] their practical use is largely limited. Therefore, alternative electrocatalysts that are made of Earth-abundant elements and have competitive catalytic capability are highly desirable.

During the past years, a multitude of candidate materials have been screened for catalyzing the OER in alkaline media ($4OH^- \rightarrow O_2 + 2H_2O + 4e^-$), among which nonprecious-metal-based perovskite oxides have attracted increasing research attention.[5,6] Having a general chemical formula of ABO_3 (A is often a rare-earth or alkaline-earth metal, B is a transition metal, and O is oxygen), perovskite oxides can offer a high degree of freedom in cation arrangement, allowing the incorporation of foreign elements into both the A- and B-sites. For example, the multi-cation perovskite $Ba_{0.5}Sr_{0.5}Co_{0.8}Fe_{0.2}O_{3-\delta}$ (BSCF) was reported with an excellent intrinsic activity more than two orders of magnitude higher than that of iridium dioxide (IrO_2).[7] Based on molecular orbital principles, the high intrinsic activity of BSCF is rationalized by the electronic state of the major active Co component which has a suitable near-unity e_g filling number ($e_g^{\sim 1.2}$), leading to an optimized binding with the oxygen intermediates under the conventional adsorbate evolution mechanism scheme.[7] In addition, substitution of Sr for La in $La_{1-x}Sr_xCoO_{3-\delta}$ perovskites contributed to a significant increase in the OER reactivity, due to an increased number of oxygen vacancy in parallel with an enhanced Co–O covalency, which likely promotes the activation of oxygen anions in the perovskite lattice to participate in the OER through a so-called lattice-oxygen mediated mechanism.[8]

Despite these advances, most of the research efforts are focused on perovskite oxides that contain Co as the primary active center and La/Ba/Sr as the partner cations.[7-10] To further increase activity, transition metal Fe, which has a much higher abundance than Co in the Earth's crust, is often doped into the Co-based perovskite electrocatalysts.[11-13] A recent study reveals that Fe serves a major role of stabilizing the Co-based perovskite structure without formation of any impurity oxide phase.[14] However, much less attention is directed to Fe-based perovskite oxides for catalyzing the OER, due likely to their insufficient activity and unsatisfactory stability.[15-17] It was reported that silicon doping at the B-site of $SrFeO_{3-\delta}$ could lead to a threefold increase in OER reactivity, but the stability was not good enough.[15] Such instability is related to the amorphization of the catalyst surface after OER measurements, as suggested by Han et al.'s work on the $Sr_xCa_{1-x}FeO_{3-\delta}$ series.[16] Shao and coworkers reported that A-site Sr doping in $LaFeO_3$ could increase the OER activity, which, however, still degraded to some extent after a continuous cycling test.[17]

In this work, a new strategy based on alkali-metal doping was utilized to increase the OER performance of perovskite catalysts. As a proof-of-concept, the iron-based $LaFeO_3$ was selected as the host perovskite and sodium (Na), which has an ionic radius similar to that of La,[18] was chosen as the alkali-metal dopant. The Na substitution was found to modify the electronic structure of the perovskites, leading to a more oxidized Fe state and an increased number of oxygen vacancy, while maintaining the crystalline structure, as described by the following equation:

$$LaFe^{3+}O_3 + xNa^+ - xLa^{3+} \rightarrow La_{1-x}Na_xFe^{3+}{}_{1-y}Fe^{4+}{}_yO_{3-\delta} + \delta/2O_2 \quad (1)$$

In the meantime, the Fe–O covalency was also enhanced to some extent. Such electronic modulation substantially facilitated the OER kinetics, with the optimized sample $La_{0.9}Na_{0.1}FeO_{3-\delta}$ showing both enhanced activity and stability (i.e., an overpotential of 421 mV at 10 mA cm_{geo}^{-2}, a small Tafel slope of 61 mV dec^{-1}, and a stable operation at 5 mA cm_{geo}^{-2} for 10 hours).

7.3 Results and discussion

7.3.1 Formation and characterizations of Na-doped perovskites

Alkali-metal-doped lanthanum ferrites ($La_{1-x}Na_xFeO_{3-\delta}$, $x = 0$, 0.05, 0.1, and 0.2) were prepared by a modified sol–gel process with a reduced calcination temperature for phase formation.[19] With the increase of the Na dopant amount, the as-prepared samples

show a gradual color change from yellow to brownish (**Figure 7.1**), which is a direct evidence for the successful incorporation of sodium into the perovskite lattice. As sodium may experience partial volatilization under high-temperature conditions,[20] it is likely that the stoichiometries of the as-synthesized samples can deviate from the intended ones. To evaluate this issue, inductively coupled plasma-optical emission spectrometry (ICP-OES) was carried out to analyze the bulk composition of a select sample, $La_{0.8}Na_{0.2}FeO_{3-\delta}$ ($x = 0.2$), and an atomic ratio of 0.80:0.21:1.00 was obtained for La/Na/Fe. This suggests that sodium volatilization is very much unlikely during the synthesis of Na-doped perovskites, which is not unexpected given the relatively low temperature used for phase formation, i.e., 600 °C vs. 800 °C or even higher.[6,21]

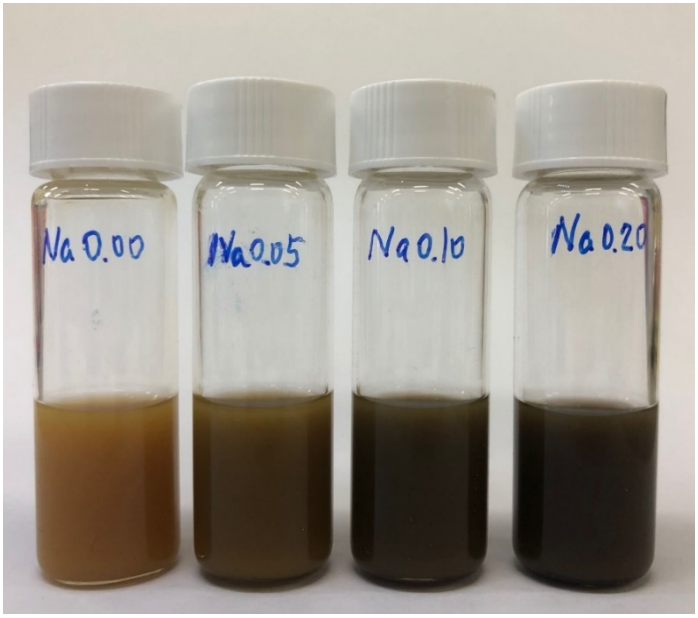

Figure 7.1 Photographs of $La_{1-x}Na_xFeO_{3-\delta}$ (x = 0, 0.05, 0.1, and 0.2) powders dispersed in absolute ethanol. The dispersions were prepared by ultrasonicating a mixture of about 6 mg of the perovskite oxide and 3 ml of absolute ethanol for a duration of 5 min.

The formation of Na-substituted perovskites was further corroborated by X-ray diffraction (XRD) studies. As illustrated in **Figure 7.2a**, the samples doped with Na^+ exhibit a similar phase structure to that of the pristine $LaFeO_3$, all having a pure orthorhombic structure (space group: *Pnma*) which aligns with the standard pattern of ICDD PDF No. 01-088-0641.[22] In addition, as more La^{3+} was replaced by Na^+ (with x in $La_{1-x}Na_xFeO_{3-\delta}$ ranging from 0.05 to 0.2), a slight shift to higher 2θ angles was

observed for the main diffraction peaks (**Figure 7.2b**), indicative of a lattice shrinkage. This observation suggests that the B-site Fe cation is likely to be partially oxidized from 3+ to 4+ (with an ionic radius of 0.645 Å and 0.585 Å, respectively) after Na-doping, because should the Fe oxidation state remain unchanged then a lattice expansion would be expected due to the larger size of Na^{+} than La^{3+} (1.39 Å vs. 1.36 Å).[18]

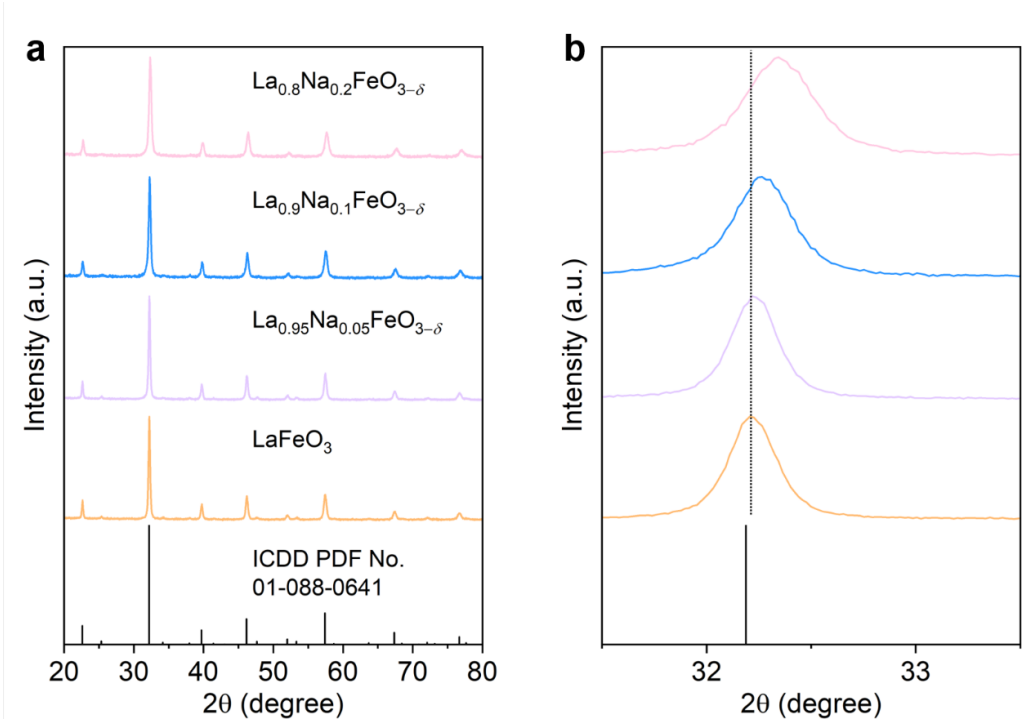

Figure 7.2 XRD data of $La_{1-x}Na_xFeO_{3-\delta}$ (x = 0, 0.05, 0.1, and 0.2). (a) XRD data presented in a broad 2θ range of 20–80°. (b) XRD data presented in a select 2θ range of 31.5–33.5°.

When the Na-doping level was further increased to 30% (x = 0.3), impurity peaks, associated with a Fe_2O_3 phase and some unidentified phases,[23] began to appear, as seen in **Figure 7.3**. To avoid any possible interference caused by the effect of impurity phases, the following investigations were carried out using samples with a Na doping range of $0 \leq x \leq 0.2$, i.e., samples having nominal compositions of $La_{1-x}Na_xFeO_{3-\delta}$ (x = 0, 0.05, 0.1, and 0.2).

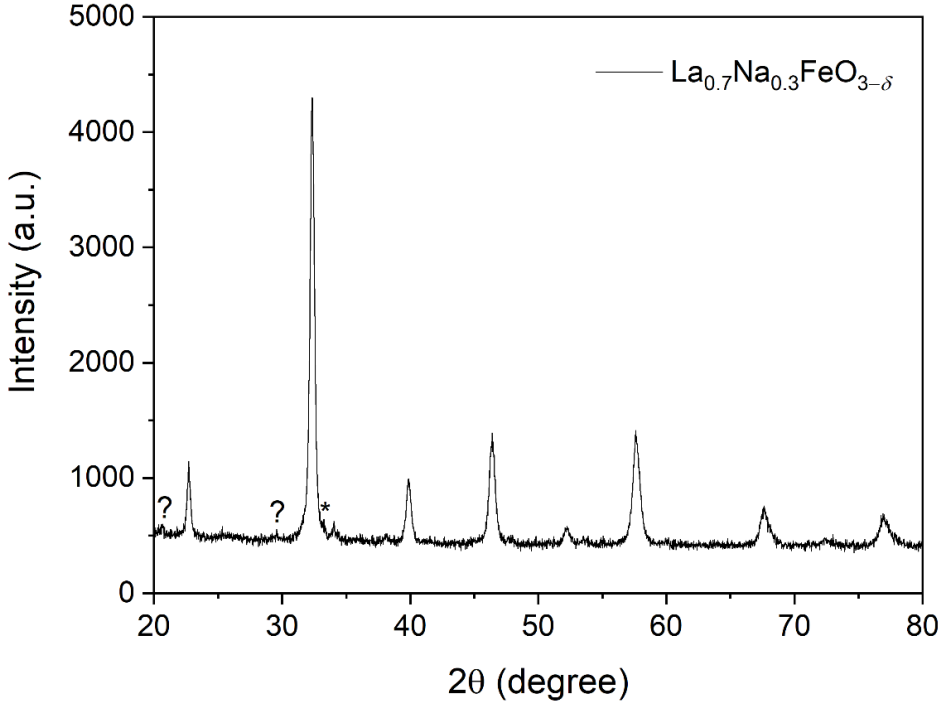

Figure 7.3 XRD pattern of the sample $La_{0.7}Na_{0.3}FeO_{3-\delta}$ ($x = 0.3$) with an excessive Na doping amount. The asterisk indicates a phase likely of Fe_2O_3, whereas the question marks indicate unknown phase(s).

High-resolution transmission electron microscopy (HRTEM) was also used to examine the crystalline structure information. **Figure 7.4** displays the HRTEM images of the undoped $LaFeO_3$ and the Na-doped $La_{0.9}Na_{0.1}FeO_{3-\delta}$, both captured with the electron beam in the direction of the $[\bar{1}\bar{1}1]$ zone axis. A similar lattice spacing of 0.39 nm was observed for both structures, in good accord with the (101) plane of the orthorhombic-structured perovskites. It should be noted that while a variation in the (101) interplanar spacing should exist between $LaFeO_3$ and $La_{0.9}Na_{0.1}FeO_{3-\delta}$, as previously suggested by the XRD analysis, such variation is not large enough to be differentiated by the HRTEM technique. **Figure 7.4** insets show the corresponding fast Fourier transform (FFT) patterns, which are characteristic of the orthorhombic phase structure. Further, **Figure 7.5** displays HRTEM images of $La_{0.9}Na_{0.1}FeO_{3-\delta}$ recorded in another two different zone axes, i.e., $[3\bar{1}\bar{1}]$ and $[1\bar{2}1]$, providing

additional support to the formation of an orthorhombic perovskite structure after the incorporation of Na into $LaFeO_3$.

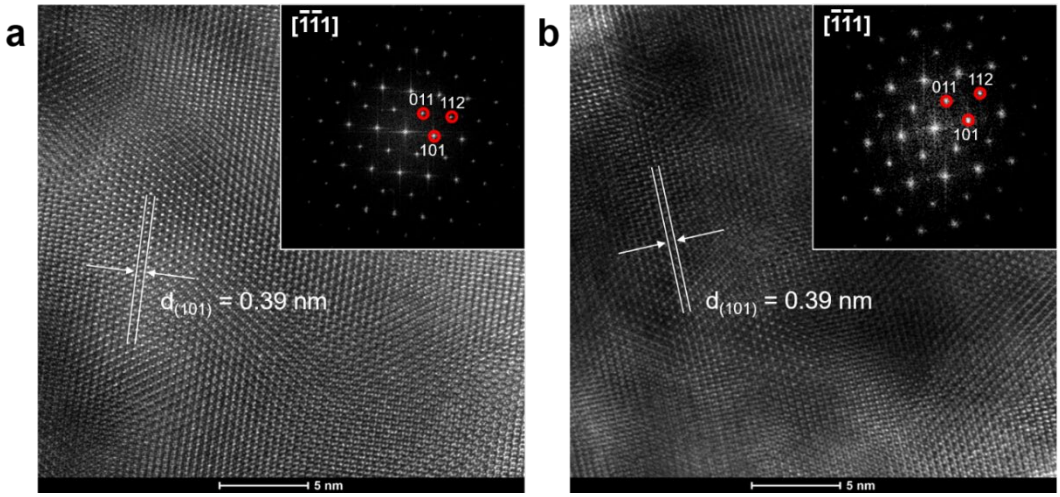

Figure 7.4 HRTEM images of $La_{1-x}Na_xFeO_{3-\delta}$ (x = 0 and 0.1) in the [$\bar{1}\bar{1}1$] zone axis. (a) $LaFeO_3$ (x = 0). (b) $La_{0.9}Na_{0.1}FeO_{3-\delta}$ (x = 0.1). The insets show the corresponding FFT patterns.

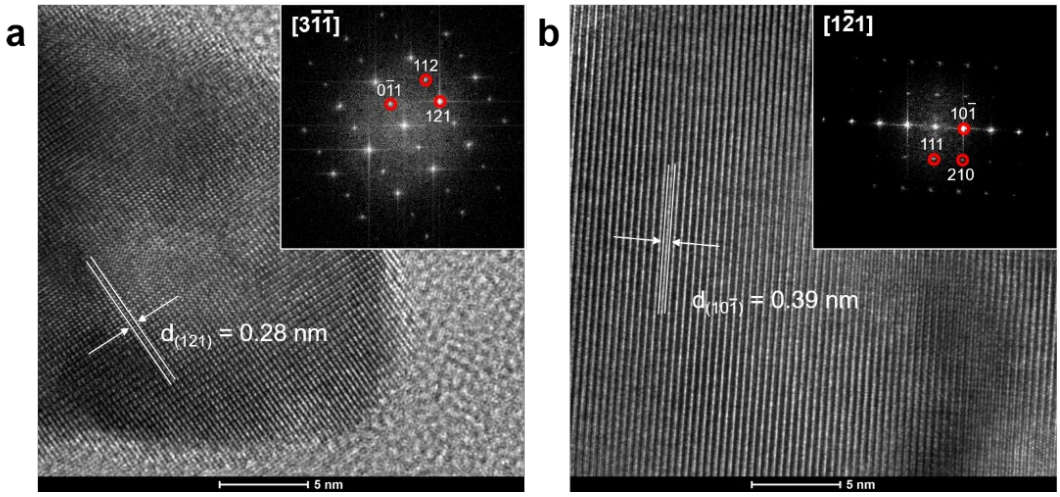

Figure 7.5 HRTEM images of $La_{0.9}Na_{0.1}FeO_{3-\delta}$ (x = 0.1) in another two zone axes. (a) In the [$3\bar{1}\bar{1}$] zone axis. (b) In the [$1\bar{2}1$] zone axis. The insets show the corresponding FFT patterns.

The morphology of the $La_{1-x}Na_xFeO_{3-\delta}$ series was revealed by scanning electron microscopy (SEM) observations. As depicted in **Figure 7.6**, all the samples possess

similar morphological features, with chunks of varying sizes from several hundred nanometers to a few micrometers. A closer look at the SEM images (**Figure 7.6b, d, f, h**) suggests that each large chunk is made of particles of a much smaller size. This is more obviously noticed in the high-angle annular dark-field scanning TEM (HAADF-STEM) imaging of the sample $La_{0.9}Na_{0.1}FeO_{3-\delta}$ (**Figure 7.7a**), where nanoparticles in the scale of approximately 30–60 nm agglomerated into larger aggregates. **Figure 7.7b** shows the energy-dispersive X-ray spectroscopy (EDS) mapping images, which indicate that the Na dopant, along with other constituent elements, was homogeneously distributed within the perovskite framework.

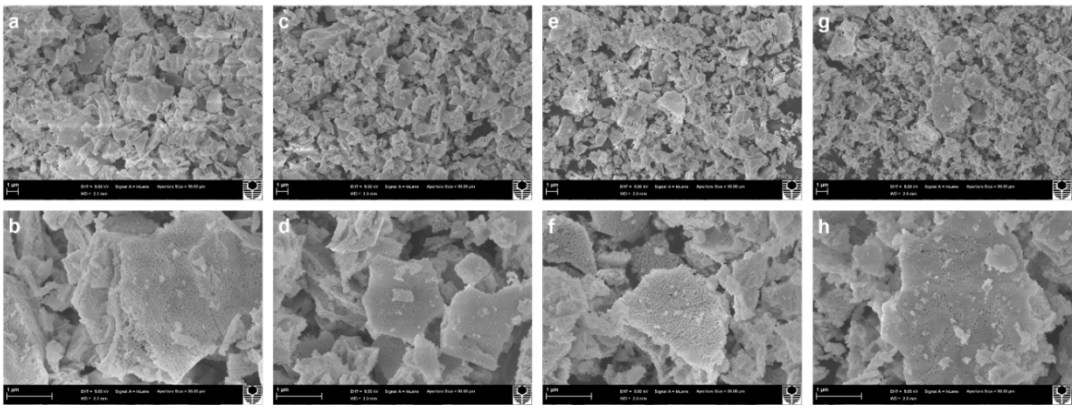

Figure 7.6 SEM images of $La_{1-x}Na_xFeO_{3-\delta}$ (x = 0, 0.05, 0.1, and 0.2) at two different magnifications. (a–b) $LaFeO_3$. (c–d) $La_{0.95}Na_{0.05}FeO_{3-\delta}$. (e–f) $La_{0.9}Na_{0.1}FeO_{3-\delta}$. (g–h) $La_{0.8}Na_{0.2}FeO_{3-\delta}$.

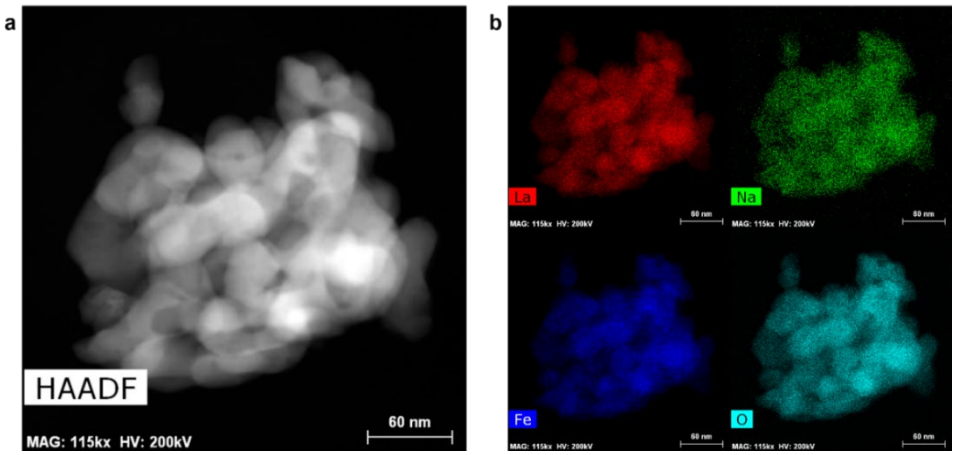

Figure 7.7 HAADF-STEM image and the corresponding EDS mapping images of $La_{0.9}Na_{0.1}FeO_{3-\delta}$. (a) HAADF-STEM image. (b) EDS mapping images of La, Na, Fe, and O elements.

The similarity in the samples' morphology was also validated by their analogous Brunauer–Emmett–Teller (BET) surface areas (S_{BET}), ranging from 11.7 m^2 g^{-1} to 16.9 m^2 g^{-1}, as determined by nitrogen adsorption-desorption measurements. However, it should be noted that with the introduction of the Na dopant, the surface areas become somewhat smaller, due likely to the fact that the nanoparticles were sintered to a larger extent for doped samples than for the undoped $LaFeO_3$ (**Figure 7.6b, d, f, h**). **Figure 7.8** presents the nitrogen sorption isotherms for $La_{1-x}Na_xFeO_{3-\delta}$ (x = 0, 0.05, 0.1, and 0.2), which can be categorized into the Type V isotherms, suggesting the existence of mesopores.[24] The mesoporous structure is also discernible from the SEM and STEM images (**Figure 7.6 and 7.7**). It is worth mentioning that compared to perovskites prepared from a similar sol–gel method, for instance, BSCF (S_{BET} <2 m^2 g^{-1}),[25,26] the Na-doped lanthanum ferrites reported here have much larger surface areas (S_{BET} >10 m^2 g^{-1}), which is associated with the nature of the lanthanum-containing samples as well as the reduced calcination temperature during synthesis.[21,27] Overall, the high surface areas as well as the presence of porous structure can increase the amount and accessibility of active sites and are thus expected to facilitate the electrocatalytic oxygen evolution.

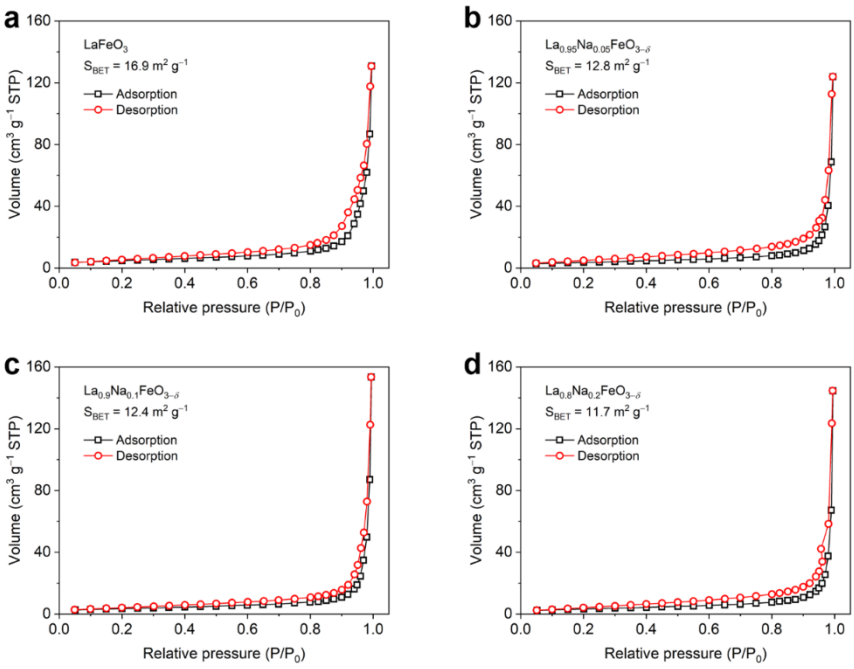

Figure 7.8 Nitrogen adsorption-desorption isotherms of $La_{1-x}Na_xFeO_{3-\delta}$ (x = 0, 0.05, 0.1, and 0.2). (a) $LaFeO_3$. (b) $La_{0.95}Na_{0.05}FeO_{3-\delta}$. (c) $La_{0.9}Na_{0.1}FeO_{3-\delta}$. (d) $La_{0.8}Na_{0.2}FeO_{3-\delta}$.

7.3.2 Electrocatalytic oxygen evolution performance

The electrochemical measurements were performed in an electrolyte of 0.1 M KOH saturated with oxygen under ambient conditions. The OER activity was assessed by running cyclic voltammetry (CV) experiments at a slow scan rate of 10 mV s^{-1}, with the working electrode being held at 2000 revolutions per minute (rpm) to efficiently prevent the accumulation of the O_2 bubbles generated. To eliminate the effects from the capacitive current and the electrolyte resistance, the CV data were taken average and then corrected for *iR* drop to allow the reporting of the OER kinetic current,[7,9] as exemplified by the data processing of the sample $La_{0.9}Na_{0.1}FeO_{3-\delta}$ (**Figure 7.9**).

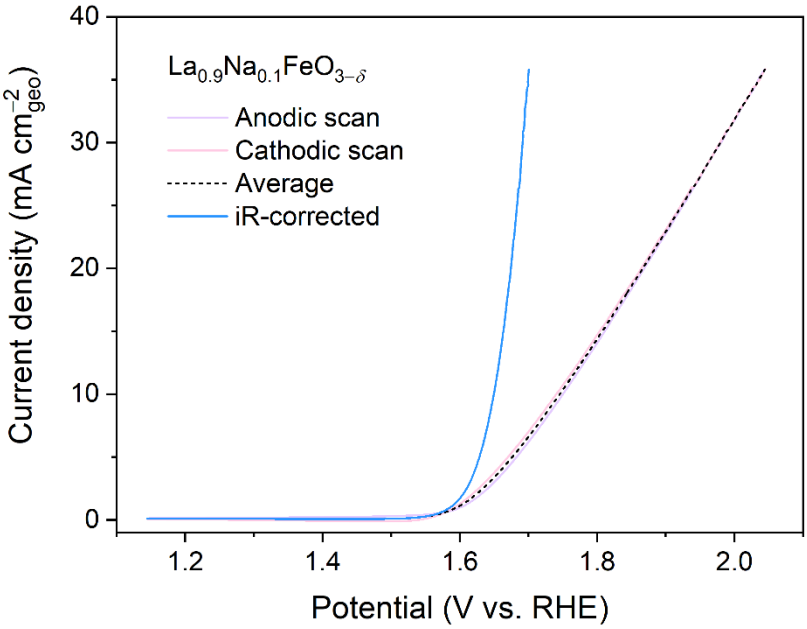

Figure 7.9 An example of the processing of the electrochemical CV data of $La_{0.9}Na_{0.1}FeO_{3-\delta}$ to allow the reporting of the OER kinetic current.

Figure 7.10a shows the kinetic currents normalized by the geometric area of the working electrode, from which it is clearly seen that compared with the pristine $LaFeO_3$, all the Na-doped samples required reduced (over)potentials to deliver a certain current output, indicating improved apparent activity toward the OER. This becomes more obvious when comparison is made in regard to the overpotential to reach a 10 mA cm_{geo}^{-2} current density (η_{10}), a solar-fuel production related metric that is often used for benchmarking different OER catalysts.[28] As presented in **Figure**

7.10b, $LaFeO_3$ gives a η_{10} value of 512 mV, in consistency with previous reports.[23] By comparison, $La_{0.95}Na_{0.05}FeO_{3-\delta}$, $La_{0.9}Na_{0.1}FeO_{3-\delta}$, and $La_{0.8}Na_{0.2}FeO_{3-\delta}$ show considerably reduced η_{10} values of 449, 421, and 464 mV, respectively, with $La_{0.9}Na_{0.1}FeO_{3-\delta}$ demonstrating the highest apparent activity.

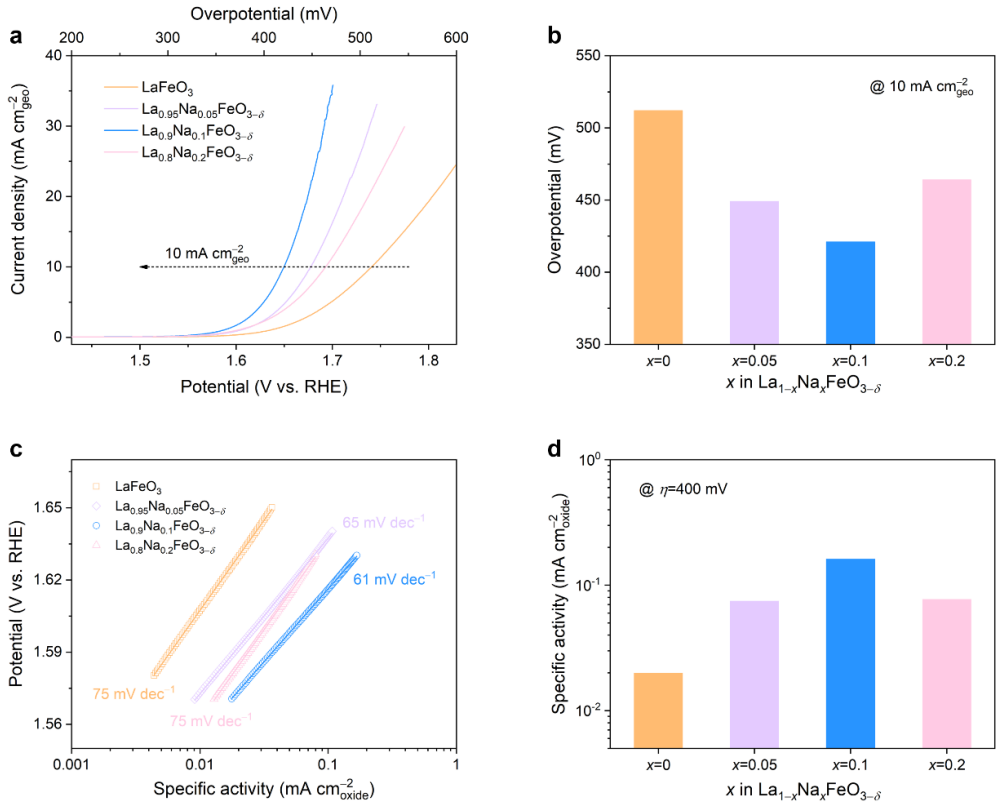

Figure 7.10 Electrocatalytic performance of $La_{1-x}Na_xFeO_{3-\delta}$ (x = 0, 0.05, 0.1, and 0.2) toward the oxygen evolution reaction in a 0.1 M KOH electrolyte. (a) OER kinetic current. The arrow indicates a decreasing trend in the potential required to produce a current density of 10 mA cm^{-2}_{geo}. (b) A comparison of the overpotential required to reach 10 mA cm^{-2}_{geo}. (c) Tafel plot where the OER current is normalized by the catalyst surface areas to obtain the specific activity. (d) A comparison of the specific activity at an overpotential of 400 mV.

It is generally acknowledged that the apparent activity is strongly associated with the catalyst surface area, that is, a higher surface area often means a larger number of active sites and thus greater apparent activity.[29] Therefore, to allow for the comparison of the intrinsic activity, the OER kinetic current was also normalized by the catalysts' BET surface areas to obtain specific activity, which has been recommended as a viable

means to represent the intrinsic activity for oxide electrocatalysts.[7,30] **Figure 7.10c** shows the logarithm of specific activity versus the potential, a figure also known as the Tafel plot. Still, all the Na-substituted samples exhibit improved intrinsic activity than the pristine $LaFeO_3$ does, as evidenced by a larger specific activity at a given (over)potential. Notably, at a 400 mV overpotential, the best-performing sample $La_{0.9}Na_{0.1}FeO_{3-\delta}$ delivers a specific activity almost one order of magnitude larger than that of $LaFeO_3$ (0.16 vs. 0.02 mA cm_{oxide}^{-2}), implying its significantly enhanced OER activity (**Figure 7.10d**). In addition, $La_{0.9}Na_{0.1}FeO_{3-\delta}$ has a smallest Tafel slope (61 mV dec^{-1}) among all the samples, further suggesting its increased OER kinetics. These results indicate that the Na substitution for La in $La_{1-x}Na_xFeO_{3-\delta}$ facilitates the proceeding of the electrocatalytic water oxidation and that a suitable level of substitution (i.e., $x = 0.1$) can lead to the best electrocatalytic activity.

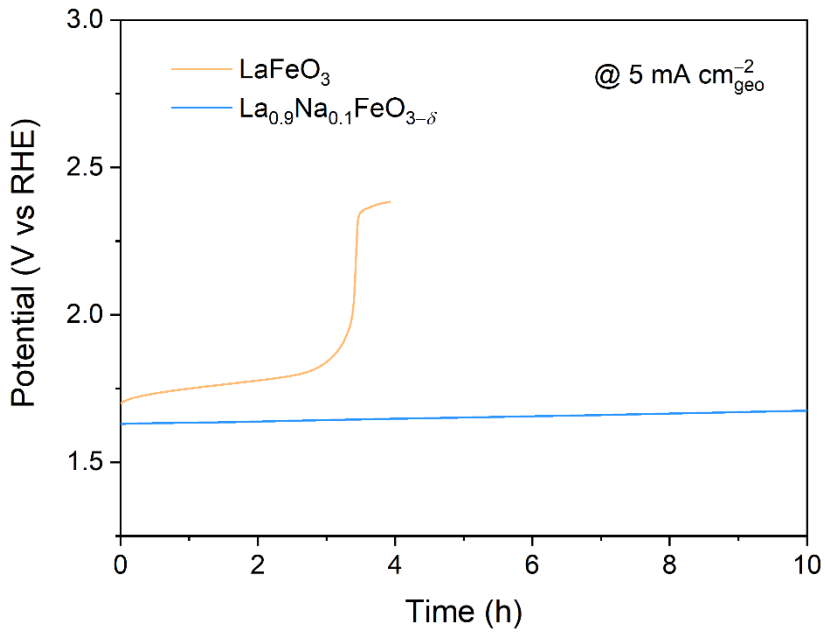

Figure 7.11 Electrochemical stability of $LaFeO_3$ and $La_{0.9}Na_{0.1}FeO_{3-\delta}$ recorded by chronopotentiometry tests at a steady current density of 5 mA cm_{geo}^{-2}.

It is of equal importance to appraise the capability for catalysts to sustain prolonged oxidation of water. To address this, the electrochemical stability was characterized by chronopotentiometry during which the electrode was held at a steady current density

of 5 mA cm_{geo}^{-2}. As displayed in **Figure 7.11**, the pristine $LaFeO_3$ quickly lost its activity during the first four-hour test, whereas $La_{0.9}Na_{0.1}FeO_{3-\delta}$ was able to maintain a rather stable performance for ten hours. This observation suggests that Na incorporation in the $LaFeO_3$ lattice is also beneficial to the electrochemical stability.

7.3.3 Understanding the enhancement in catalytic performance

Understanding the origins of the improved OER activity facilitated by A-site alkali-metal substitution can provide guidelines for the development of improved electrocatalysts. Generally, the pristine $LaFeO_3$ has a Fe nominal valence of 3+. Once a proportion of trivalent La^{3+} is replaced by monovalent Na^{+}, the Fe valence would increase to compensate for any likely charge imbalance triggered by the doping and in the meantime oxygen vacancy may be generated to further maintain the charge balance. As shown in **Figure 7.12a**, a pair of 2p doublet, i.e., $2p_{3/2}$ at the binding energy (BE) of ~710.2 and $2p_{1/2}$ at the BE of ~723.9 eV, along with a satellite peak at the BE of ~718.3 eV, was observed for the X-ray photoelectron spectroscopy (XPS) spectrum of the undoped $LaFeO_3$, in agreement with the dominance of Fe^{3+}.[31] The doublet for the Fe 2p XPS spectrum of $La_{0.9}Na_{0.1}FeO_{3-\delta}$ was found to shift slightly to more positive BE positions, indicating a partial oxidation of the Fe species.

The change in the Fe electronic state is also verified by the soft X-ray absorption spectra (XAS) at the O *K*-edge, a highly sensitive technique that can reflect the extent to which the transition metal state hybridizes with the oxygen state in oxide compounds.[32,33] As displayed in **Figure 7.12b**, when Na was introduced into the $LaFeO_3$ lattice, a pre-edge peak at the photon energy of ~528 eV was detected. This feature, as also found in the divalent alkaline-earth metal-doped $La_{1-x}A_xFeO_{3-\delta}$ series (A = Ca or Sr),[34-36] indicates an increased mixing between the Fe 3d state and O 2p state and thus an enhanced Fe 3d–O 2p covalency, which is associated with the partial oxidation from Fe^{3+} to Fe^{4+}. These modifications in the transition-metal valence and transition metal–oxygen covalency are likely beneficial to the OER electrocatalysis. On the one hand, considering that the Fe cations in unsubstituted and substituted $LaFeO_3$ generally adopt a high spin state at room temperature,[36] the Fe^{4+} cation has a preferable electronic configuration of $t_{2g}^3e_g^1$ compared to that of Fe^{3+} (with a $t_{2g}^3e_g^2$ configuration). According to Shao-Horn et al.'s guiding principle, perovskites with transition metal cations having a near-unity e_g occupancy can lead to optimum OER activity in alkaline solutions.[7] From this perspective, the Na-substituted

$La_{0.9}Na_{0.1}FeO_{3-\delta}$ with an e_g^1 configuration for a fraction of the Fe^{4+} species is expected to show improved OER activity than the unsubstituted $LaFeO_3$ where the Fe^{3+} cation is dominant. On the other hand, the enhanced Fe 3d–O 2p covalency can promote the OER kinetics. A previous report suggests that Fe doping in $LaCo_{1-x}Fe_xO_3$ increased the Co–O hybridization, which brings about improved OER currents.[13] In another research, Sr substitution enhanced the Co–O covalency in the $La_{1-x}Sr_xCoO_{3-\delta}$ perovskites, which activated the lattice-oxygen in participating in the OER and thus led to significantly increased OER activity.[8] While whether lattice-oxygen participation in the Na-substituted $La_{1-x}Na_xFeO_{3-\delta}$ is possible remains to be testified, the enhanced Fe 3d–O 2p covalency in $La_{0.9}Na_{0.1}FeO_{3-\delta}$ relative to that of $LaFeO_3$ likely accounts for the increased activity. In addition, the quadruple perovskite $CaCu_3Fe_4O_{12}$ with Fe at the tetravalent state was reported with both high activity and stability, due to the Fe^{4+}-based covalent bonding network.[37] The enhanced electrochemical stability of the Na-doped $La_{0.9}Na_{0.1}FeO_{3-\delta}$ may also be related with the enhanced Fe–O covalency.

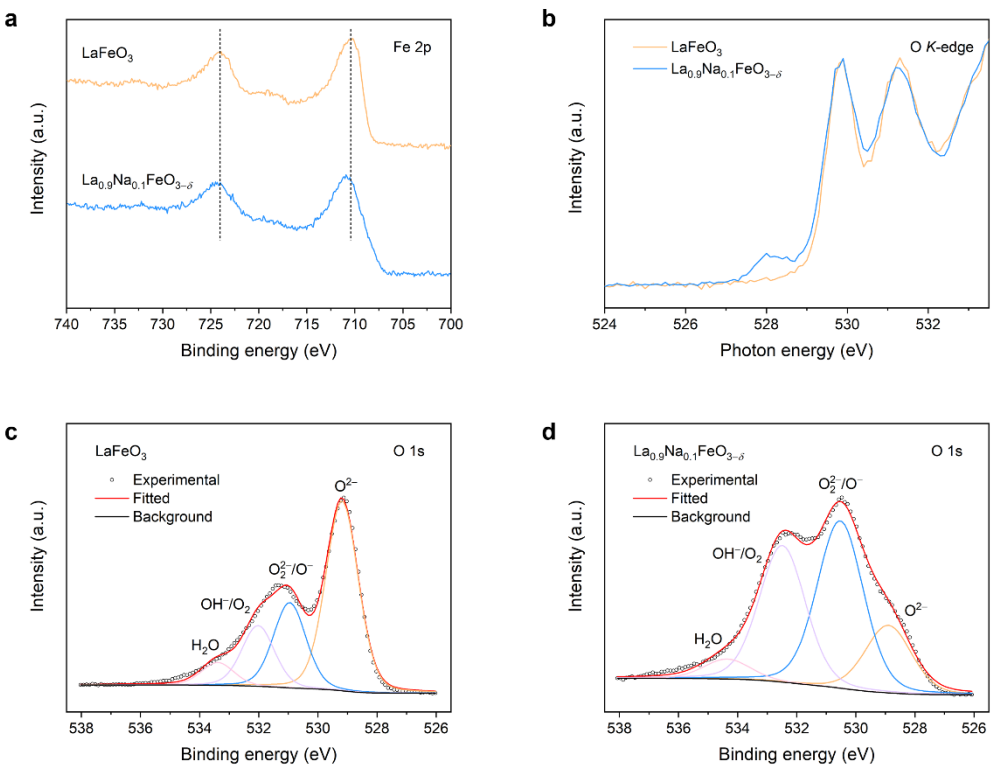

Figure 7.12 Electronic states of $LaFeO_3$ and $La_{0.9}Na_{0.1}FeO_{3-\delta}$ as characterized by XPS and XAS. (a) Fe 2p XPS spectra. (b) O *K*-edge XAS spectra. (c–d) O 1s XPS spectra.

The presence of oxygen vacancy is supported by the XPS analysis of the O 1s core level. **Figure 7.12 c** and **d** demonstrate the O 1s XPS spectra of $LaFeO_3$ and $La_{0.9}Na_{0.1}FeO_{3-\delta}$, respectively. Based on previous literature,[19,38] these spectra can be fitted by four major components, namely lattice oxygen (O^{2-}) at the BE of ~529 eV, highly oxidative oxygen (O_2^{2-}/O^-) at the BE of ~531 eV, hydroxide or adsorbed oxygen (OH^-/O_2) at the BE of ~532 eV, and adsorbed water (H_2O) at the BE of ~534 eV. As seen from the detailed fitting results shown in **Table 7.1**, a much larger presence of O_2^{2-}/O^- was observed on $La_{0.9}Na_{0.1}FeO_{3-\delta}$ than on $LaFeO_3$, indicating a higher concentration of the surface oxygen vacancy.[39] Earlier studies have revealed that creating oxygen vacancies on metal oxide surfaces can effectively boost the OER electrocatalysis.[8,9,23,40] It is reasonable to believe that the increased amount of defective oxygen, as induced by the Na incorporation, is another parameter crucial to the improved OER catalysis over $La_{0.9}Na_{0.1}FeO_{3-\delta}$.

Table 7.1 XPS peak fitting results of the O 1s core level of $LaFeO_3$ and $La_{0.9}Na_{0.1}FeO_{3-\delta}$.

Catalyst	O^{2-}		O_2^{2-}/O^-		OH^-/O_2		H_2O	
	BE (eV)	Content (%)	BE (eV)	Content (%)	BE (eV)	Content (%)	BE (eV)	Content (%)
$LaFeO_3$	529.2	52.9	531.0	23.7	532.0	17.0	533.4	6.4
$La_{0.9}Na_{0.1}FeO_{3-\delta}$	528.9	17.3	530.5	42.7	532.5	34.9	534.4	5.1

7.4 Conclusions

To conclude, a series of alkali-metal-doped perovskites $La_{1-x}Na_xFeO_{3-\delta}$ (x = 0, 0.05, 0.1, and 0.2) were prepared by partially substituting Na for La at the A-site of $LaFeO_3$ and assessed as the catalytic materials for the water oxidation in alkaline electrolytes. The introduction of alkali-metal dopant did not alter the orthorhombic phase structure but did modify the electronic structure to some extent by oxidizing the Fe species,

enhancing the Fe–O covalency, and increasing the oxygen vacancy concentration. This electronic modulation was found to substantially promote the OER performance, as evidenced by the sample with a suitable level of Na-doping (i.e., $La_{0.9}Na_{0.1}FeO_{3-\delta}$) which shows an optimum performance with an overpotential of 421 mV at 10 mA cm_{geo}^{-2}, a small Tafel slope of 61 mV dec^{-1}, and a stable operation at 5 mA cm_{geo}^{-2} for 10 hours. The results from this research could shed light to the development of other types of electrocatalyst materials by means of alkali-metal doping.

7.5 References

(1) Roger, I.; Shipman, M. A.; Symes, M. D. Earth-abundant catalysts for electrochemical and photoelectrochemical water splitting. *Nat. Rev. Chem.* **2017**, *1*, 0003.

(2) Darband, G. B.; Aliofkhazraei, M.; Shanmugam, S. Recent advances in methods and technologies for enhancing bubble detachment during electrochemical water splitting. *Renew. Sustain. Energy Rev.* **2019**, *114*, 109300.

(3) Lee, Y.; Suntivich, J.; May, K. J.; Perry, E. E.; Shao-Horn, Y. Synthesis and activities of rutile IrO_2 and RuO_2 nanoparticles for oxygen evolution in acid and alkaline solutions. *J. Phys. Chem. Lett.* **2012**, *3*, 399–404.

(4) Bullock, R. M.; Chen, J. G.; Gagliardi, L.; Chirik, P. J.; Farha, O. K.; Hendon, C. H.; Jones, C. W.; Keith, J. A.; Klosin, J.; Minteer, S. D. et al. Using nature's blueprint to expand catalysis with Earth-abundant metals. *Science* **2020**, *369*, eabc3183.

(5) Hwang, J.; Rao, R. R.; Giordano, L.; Katayama, Y.; Yu, Y.; Shao-Horn, Y. Perovskites in catalysis and electrocatalysis. *Science* **2017**, *358*, 751–756.

(6) Xu, X.; Wang, W.; Zhou, W.; Shao, Z. Recent advances in novel nanostructuring methods of perovskite electrocatalysts for energy-related applications. *Small Methods* **2018**, *2*, 1800071.

(7) Suntivich, J.; May, K. J.; Gasteiger, H. A.; Goodenough, J. B.; Shao-Horn, Y. A perovskite oxide optimized for oxygen evolution catalysis from molecular orbital principles. *Science* **2011**, *334*, 1383–1385.

(8) Mefford, J. T.; Rong, X.; Abakumov, A. M.; Hardin, W. G.; Dai, S.; Kolpak, A. M.; Johnston, K. P.; Stevenson, K. J. Water electrolysis on $La_{1-x}Sr_xCoO_{3-\delta}$ perovskite electrocatalysts. *Nat. Commun.* **2016**, *7*, 11053.

(9) Pan, Y.; Xu, X.; Zhong, Y.; Ge, L.; Chen, Y.; Veder, J.-P. M.; Guan, D.; O'Hayre, R.; Li, M.; Wang, G. et al. Direct evidence of boosted oxygen evolution over perovskite by enhanced lattice oxygen participation. *Nat. Commun.* **2020**, *11*, 2002.

(10) Su, C.; Wang, W.; Chen, Y.; Yang, G.; Xu, X.; Tadé, M. O.; Shao, Z. $SrCo_{0.9}Ti_{0.1}O_{3-\delta}$ as a new electrocatalyst for the oxygen evolution reaction in

alkaline electrolyte with stable performance. *ACS Appl. Mater. Interfaces* **2015**, *7*, 17663–17670.

(11) Zhu, Y.; Zhou, W.; Chen, Z.-G.; Chen, Y.; Su, C.; Tadé, M. O.; Shao, Z. $SrNb_{0.1}Co_{0.7}Fe_{0.2}O_{3-\delta}$ perovskite as a next-generation electrocatalyst for oxygen evolution in alkaline solution. *Angew. Chem. Int. Ed.* **2015**, *54*, 3897–3901.

(12) Xu, X.; Su, C.; Zhou, W.; Zhu, Y.; Chen, Y.; Shao, Z. Co-doping strategy for developing perovskite oxides as highly efficient electrocatalysts for oxygen evolution reaction. *Adv. Sci.* **2016**, *3*, 1500187.

(13) Duan, Y.; Sun, S.; Xi, S.; Ren, X.; Zhou, Y.; Zhang, G.; Yang, H.; Du, Y.; Xu, Z. J. Tailoring the Co 3d-O 2p covalency in $LaCoO_3$ by Fe substitution to promote oxygen evolution reaction. *Chem. Mater.* **2017**, *29*, 10534–10541.

(14) Kim, B.-J.; Fabbri, E.; Abbott, D. F.; Cheng, X.; Clark, A. H.; Nachtegaal, M.; Borlaf, M.; Castelli, I. E.; Graule, T.; Schmidt, T. J. Functional role of Fe-doping in Co-based perovskite oxide catalysts for oxygen evolution reaction. *J. Am. Chem. Soc.* **2019**, *141*, 5231–5240.

(15) Xu, X.; Chen, Y.; Zhou, W.; Zhong, Y.; Guan, D.; Shao, Z. Earth-abundant silicon for facilitating water oxidation over iron-based perovskite electrocatalyst. *Adv. Mater. Interfaces* **2018**, *5*, 1701693.

(16) Han, B.; Grimaud, A.; Giordano, L.; Hong, W. T.; Diaz-Morales, O.; Yueh-Lin, L.; Hwang, J.; Charles, N.; Stoerzinger, K. A.; Yang, W. et al. Iron-based perovskites for catalyzing oxygen evolution reaction. *J. Phys. Chem. C* **2018**, *122*, 8445–8454.

(17) She, S.; Yu, J.; Tang, W.; Zhu, Y.; Chen, Y.; Sunarso, J.; Zhou, W.; Shao, Z. Systematic study of oxygen evolution activity and stability on $La_{1-x}Sr_xFeO_{3-\delta}$ perovskite electrocatalysts in alkaline media. *ACS Appl. Mater. Interfaces* **2018**, *10*, 11715–11721.

(18) Shannon, R. Revised effective ionic radii and systematic studies of interatomic distances in halides and chalcogenides. *Acta Cryst. A* **1976**, *32*, 751–767.

(19) Xu, X.; Chen, Y.; Zhou, W.; Zhu, Z.; Su, C.; Liu, M.; Shao, Z. A perovskite electrocatalyst for efficient hydrogen evolution reaction. *Adv. Mater.* **2016**, *28*, 6442–6448.

(20) Torres-Martínez, L. M.; Cruz-López, A.; Juárez-Ramírez, I.; Meza-de la Rosa, M. E. Methylene blue degradation by $NaTaO_3$ sol–gel doped with Sm and La. *J. Hazard. Mater.* **2009**, *165*, 774–779.

(21) Jung, J.-I.; Risch, M.; Park, S.; Kim, M. G.; Nam, G.; Jeong, H.-Y.; Shao-Horn, Y.; Cho, J. Optimizing nanoparticle perovskite for bifunctional oxygen electrocatalysis. *Energy Environ. Sci.* **2016**, *9*, 176–183.

(22) Falcón, H.; Goeta, A. E.; Punte, G.; Carbonio, R. E. Crystal structure refinement and stability of $LaFe_xNi_{1-x}O_3$ solid solutions. *J. Solid State Chem.* **1997**, *133*, 379–385.

(23) Zhu, Y.; Zhou, W.; Yu, J.; Chen, Y.; Liu, M.; Shao, Z. Enhancing electrocatalytic activity of perovskite oxides by tuning cation deficiency for oxygen reduction and evolution reactions. *Chem. Mater.* **2016**, *28*, 1691–1697.

(24) Sing, K. S. W. Reporting physisorption data for gas/solid systems with special reference to the determination of surface area and porosity (Recommendations 1984). *Pure Appl. Chem.* **1985**, *57*, 603–619.

(25) Xu, X.; Pan, Y.; Zhou, W.; Chen, Y.; Zhang, Z.; Shao, Z. Toward enhanced oxygen evolution on perovskite oxides synthesized from different approaches: A case study of $Ba_{0.5}Sr_{0.5}Co_{0.8}Fe_{0.2}O_{3-\delta}$. *Electrochim. Acta* **2016**, *219*, 553–559.

(26) Jung, J.-I.; Jeong, H. Y.; Kim, M. G.; Nam, G.; Park, J.; Cho, J. Fabrication of $Ba_{0.5}Sr_{0.5}Co_{0.8}Fe_{0.2}O_{3-\delta}$ catalysts with enhanced electrochemical performance by removing an inherent heterogeneous surface film layer. *Adv. Mater.* **2015**, *27*, 266–271.

(27) Zhou, S.; Miao, X.; Zhao, X.; Ma, C.; Qiu, Y.; Hu, Z.; Zhao, J.; Shi, L.; Zeng, J. Engineering electrocatalytic activity in nanosized perovskite cobaltite through surface spin-state transition. *Nat. Commun.* **2016**, *7*, 11510.

(28) Gorlin, Y.; Jaramillo, T. F. A bifunctional nonprecious metal catalyst for oxygen reduction and water oxidation. *J. Am. Chem. Soc.* **2010**, *132*, 13612–13614.

(29) Seh, Z. W.; Kibsgaard, J.; Dickens, C. F.; Chorkendorff, I.; Nørskov, J. K.; Jaramillo, T. F. Combining theory and experiment in electrocatalysis: Insights into materials design. *Science* **2017**, *355*, eaad4998.

(30) Wei, C.; Sun, S.; Mandler, D.; Wang, X.; Qiao, S. Z.; Xu, Z. J. Approaches for measuring the surface areas of metal oxide electrocatalysts for determining their intrinsic electrocatalytic activity. *Chem. Soc. Rev.* **2019**, *48*, 2518–2534.

(31) Ghaffari, M.; Liu, T.; Huang, H.; Tan, O. K.; Shannon, M. Investigation of local structure effect and X-ray absorption characteristics (EXAFS) of Fe (Ti) K-edge on photocatalyst properties of $SrTi_{(1-x)}Fe_xO_{(3-\delta)}$. *Mater. Chem. Phys.* **2012**, *136*, 347–357.

(32) de Groot, F. M. F.; Grioni, M.; Fuggle, J. C.; Ghijsen, J.; Sawatzky, G. A.; Petersen, H. Oxygen 1s x-ray-absorption edges of transition-metal oxides. *Phys. Rev. B* **1989**, *40*, 5715–5723.

(33) Frati, F.; Hunault, M. O. J. Y.; de Groot, F. M. F. Oxygen K-edge X-ray absorption spectra. *Chem. Rev.* **2020**, *120*, 4056–4110.

(34) Abbate, M.; de Groot, F. M. F.; Fuggle, J. C.; Fujimori, A.; Strebel, O.; Lopez, F.; Domke, M.; Kaindl, G.; Sawatzky, G. A.; Takano, M. et al. Controlled-valence properties of $La_{1-x}Sr_xFeO_3$ and $La_{1-x}Sr_xMnO_3$ studied by soft-x-ray absorption spectroscopy. *Phys. Rev. B* **1992**, *46*, 4511–4519.

(35) Suntivich, J.; Hong, W. T.; Lee, Y.-L.; Rondinelli, J. M.; Yang, W.; Goodenough, J. B.; Dabrowski, B.; Freeland, J. W.; Shao-Horn, Y. Estimating hybridization of transition metal and oxygen states in perovskites from O K-edge X-ray absorption spectroscopy. *J. Phys. Chem. C* **2014**, *118*, 1856–1863.

(36) Shen, Z.; Zhuang, Y.; Li, W.; Huang, X.; Oropeza, F. E.; Hensen, E. J. M.; Hofmann, J. P.; Cui, M.; Tadich, A.; Qi, D. et al. Increased activity in the oxygen evolution reaction by Fe^{4+}-induced hole states in perovskite $La_{1-x}Sr_xFeO_3$. *J. Mater. Chem. A* **2020**, *8*, 4407–4415.

(37) Yagi, S.; Yamada, I.; Tsukasaki, H.; Seno, A.; Murakami, M.; Fujii, H.; Chen, H.; Umezawa, N.; Abe, H.; Nishiyama, N. et al. Covalency-reinforced oxygen evolution reaction catalyst. *Nat. Commun.* **2015**, *6*, 8249.

(38) Wang, Y.; Ren, J.; Wang, Y.; Zhang, F.; Liu, X.; Guo, Y.; Lu, G. Nanocasted synthesis of mesoporous $LaCoO_3$ perovskite with extremely high surface area and excellent activity in methane combustion. *J. Phys. Chem. C* **2008**, *112*, 15293–15298.

(39) Merino, N. A.; Barbero, B. P.; Eloy, P.; Cadús, L. E. $La_{1-x}Ca_xCoO_3$ perovskite-type oxides: Identification of the surface oxygen species by XPS. *Appl. Surf. Sci.* **2006**, *253*, 1489–1493.

(40) Hirai, S.; Morita, K.; Yasuoka, K.; Shibuya, T.; Tojo, Y.; Kamihara, Y.; Miura, A.; Suzuki, H.; Ohno, T.; Matsuda, T. et al. Oxygen vacancy-originated highly

active electrocatalysts for the oxygen evolution reaction. *J. Mater. Chem. A* **2018**, *6*, 15102–15109.

Every reasonable effort has been made to acknowledge the owners of copyright material. I would be pleased to hear from any copyright owner who has been omitted or incorrectly acknowledged.

Chapter 8 Conclusions and perspectives

8.1 Conclusions

In this thesis, a range of new perovskite-type oxide materials made of non-precious transition metals Mo, Co, and Fe are designed, synthesized, characterized, and evaluated as the electrocatalysts for facilitating the reaction kinetics of the water-splitting half-reactions, i.e., the hydrogen evolution reaction (HER) at the cathode and the oxygen evolution reaction (OER) at the anode. These perovskite oxides are prepared using facile chemical methods such as high-temperature reduction and sol–gel process. Their physicochemical properties are investigated using a set of diffraction, microscopy, and spectroscopy characterizations including X-ray diffraction, scanning electron microscopy, transmission electron microscopy, X-ray photoelectron spectroscopy, X-ray absorption spectroscopy, and Raman spectroscopy, as well as a number of testing or analysis methods such as N_2 sorption measurements, inductively coupled plasma-optical emission spectrometry, thermogravimetric and differential scanning calorimetry analysis, oxygen temperature-programmed desorption, and electrical conductivity measurement. The electrocatalytic performance is evaluated in a rotating disk electrode-based, three-electrode setup using electrochemical techniques ranging from cyclic voltammetry, linear sweep voltammetry, to chronopotentiometry. By fine-tuning the chemical compositions and structures, perovskite oxides with improved HER/OER catalytic performance are developed. More importantly, correlations are established between the electrocatalytic activity and the perovskite electronic structure (e.g., crystal symmetry, transition metal oxidation state, oxygen vacancy, and metal–oxygen covalency). Overall, these studies are expected to offer a deepened understanding of the structure–activity relationship of the perovskite oxide electrocatalysts. The general conclusions derived from each study are also summarized as the following.

8.1.1 From scheelite $BaMoO_4$ to perovskite $BaMoO_3$: Enhanced electrocatalysis toward the hydrogen evolution in alkaline media

- A Mo-based $BaMoO_3$ perovskite oxide was synthesized by reducing the $BaMoO_4$ scheelite oxide under a reductive H_2 atmosphere at elevated temperatures.
- Compared to scheelite $BaMoO_4$, perovskite $BaMoO_3$ showed significantly higher catalytic activity toward the alkaline HER, with the overpotential to

afford a current density of −10 mA cm_{geo}^{-2} lowered by more than 200 mV and the intrinsic activity at the select overpotentials of 350–450 mV increased by about one order of magnitude.

- The improved HER activity is due to the intrinsically higher activity of the interconnected MoO_6 octahedra in the cubic-structured $BaMoO_3$ perovskite as compared to the disconnected MoO_4 tetrahedra in the tetragonal-structured $BaMoO_4$ scheelite. The former offers a reduced Mo oxidation state, an increased number of surface oxygen vacancies, and a larger electrical conductivity.

8.1.2 Fe-based perovskites for catalyzing the hydrogen evolution reaction in alkaline solutions

- A series of Fe-based $La_{1-x}(Ba_{0.5}Sr_{0.5})_xFeO_{3-\delta}$ (x = 0.0, 0.2, 0.5, 0.8, and 1.0) perovskites were obtained by simultaneously substituting the alkaline-earth metals Ba and Sr for the rare-earth metal La at the A-site of $LaFeO_3$. The substitution leads to a phase transition from orthorhombic to cubic.
- The substituted samples all exhibited enhanced alkaline HER activity compared to the pristine $LaFeO_3$, with the best activity observed on $La_{0.2}(Ba_{0.5}Sr_{0.5})_{0.8}FeO_{3-\delta}$ (x = 0.8) showing a 216-mV drop in the overpotential to afford a current density of −10 mA cm_{geo}^{-2}. This activity compares favorably to that of many of the other reported perovskite-type HER catalysts.
- A comprehensive X-ray spectroscopic study suggests that the enhanced HER activity is related to the increased oxidation state of the Fe cation and the enhanced covalency of the Fe–O bond, which is closely associated with the phase change induced by Ba/Sr co-doping.

8.1.3 An unusually stabilized Co-based perovskite for highly efficient oxygen evolution

- A cubic-structured perovskite ($BaCo_{0.7}Fe_{0.3}O_{3-\delta 2}$, denoted as *c*-BCF) was prepared through the thermal reduction of a hexagonal-structured perovskite ($BaCo_{0.7}Fe_{0.3}O_{3-\delta 1}$, denoted as *h*-BCF) under an inert atmosphere.
- This unusually stabilized *c*-BCF perovskite exhibited a twenty times higher OER intrinsic activity relative to the pristine *h*-BCF. *c*-BCF also outperforms many of the state-of-the-art perovskites and noble metal-based benchmark catalysts. Additionally, *c*-BCF presented good electrocatalytic stability.

- The substantial increase in the OER activity is closely related to the stabilized cubic perovskite structure, which provides a significantly reduced Co valence as well as a greatly enhanced oxygen vacancy concentration.

8.1.4 Alkali-metal-doped perovskites for efficient oxygen evolution in alkaline solutions

- A series of alkali-metal-doped perovskites $La_{1-x}Na_xFeO_{3-\delta}$ (x = 0, 0.05, 0.1, and 0.2) were prepared by replacing a proportion of rare-earth metal La with alkali metal Na at the A-site of $LaFeO_3$. The introduction of alkali-metal dopant did not alter the orthorhombic phase structure.
- The Na-doped samples all displayed enhanced OER activity compared to the pristine $LaFeO_3$, with the highest activity observed on $La_{0.9}Na_{0.1}FeO_{3-\delta}$ (x = 0.1) showing a ~90-mV reduction in the overpotential to afford a current density of 10 mA cm_{geo}^{-2} and a 8-fold increase in the intrinsic activity. $La_{0.9}Na_{0.1}FeO_{3-\delta}$ also exhibited improved electrocatalytic stability compared to $LaFeO_3$.
- The incorporation of low-valent Na cation into the $LaFeO_3$ perovskite caused a partially oxidized Fe state, an enhanced Fe–O covalency, and an increased oxygen vacancy content, which are responsible for the enhanced OER activity observed.

8.2 Perspectives

Despite the results obtained in this thesis, there is much that can be done to further our understanding in the water-splitting reactions catalyzed by perovskite oxides. In this section personal perspectives are provided as an effort to underline some important areas of research interest in the future.

8.2.1 From bulk-sized to nanosized perovskite electrocatalysts

Most of the studies in this thesis are focused on perovskite oxides having a particle size in the (sub-)micron scale. As the electrode activity (i.e., based on the current per electrode surface area) is strongly correlated with the catalyst surface area, developing nanosized perovskite oxides appears to be a promising approach to further increasing catalytic activity. One way to attain nanoscale perovskites is through lowering the calcination temperature in conventional synthesis. For example, in the case of $La_{1-x}Na_xFeO_{3-\delta}$, a heating temperature as low as 600 °C was used to produce

perovskites with specific surface area larger than 10 m^2 g^{-1}, in contrast to $La_{1-x}(Ba_{0.5}Sr_{0.5})_xFeO_{3-\delta}$ calcined at a higher temperature of 1100 °C showing surface area smaller than 5 m^2 g^{-1}. However, this method has its own limitations. On the one hand, it may only apply to perovskites comprising mainly lanthanides at the A-site which can crystallize at a relatively low temperature,[1,2] whereas alkaline-earth metal-containing perovskites often require a much higher temperature for phase formation.[3,4] On the other hand, while this method can produce nanosized particles, these particles are prone to agglomerate into larger aggregates (as observed for $La_{1-x}Na_xFeO_{3-\delta}$), which is not beneficial to the electrocatalysis.

Alternatively, the downsizing of perovskite catalysts can be achieved by adopting other chemical synthesis methodologies, such as precipitation method, template-assisted synthesis, and electrospinning, to name a few.[5] With nanosized perovskites, it remains interesting to delve into the size effect on electrocatalysis. For instance, $LaCoO_3$ with a particle size below 100 nm was found to exhibit a more favorable e_g orbital filling compared to that observed in the bulk form of $LaCoO_3$, thus leading to an enhanced intrinsic activity.[1] The change in the Co electronic configuration was likely due to the presence of a surface spin-state transition which occurred for smaller-sized $LaCoO_3$ nanoparticles.[1]

8.2.2 From *ex-situ* characterizations to *in-situ*/operando analysis

This thesis has correlated the electrocatalytic HER/OER performance collected from electrochemical measurements with the perovskite oxide properties gathered *ex situ* from physicochemical characterizations. A further step to understand the structure–activity relationship is through the utilization of *in-situ*/operando techniques, which can probe real-time changes over the perovskite catalysts during water electrolysis. The *in-situ*/operando analysis is useful in that it could provide a better picture of the real active sites operative in the perovskite electrocatalysts. For example, nanosized $Ba_{0.5}Sr_{0.5}Co_{0.8}Fe_{0.2}O_{3-\delta}$ (BSCF) perovskite was found to dynamically self-reconstruct at the surface region during the OER in alkaline solutions, forming an active layer made of (oxy)hydroxide which was proposed to be the real catalytic site.[6] Additionally, studies utilizing *in-situ*/operando characterizations can facilitate a better understanding of the stability of perovskite electrocatalysts under operating conditions,[7] which is critical to the design of both active and stable perovskite catalysts. Currently, a great many *in-situ*/operando techniques have been employed in water-splitting related

electrocatalysis, such as X-ray absorption spectroscopy, X-ray photoelectron spectroscopy, Mössbauer spectroscopy, and transmission electron microscopy, which can provide information about the crystal structure, metal oxidation state, and coordination environment of the catalysts of interest.[8] Very often, collaboration is needed to conduct electrocatalysis research using *in-situ*/operando tools.

8.2.3 From fundamental research to practical applications

This thesis provides fundamental understanding of the structure–activity relationship of the perovskite oxide electrocatalysts and proposes materials design strategies toward the development of new perovskite oxides with improved electrocatalytic HER/OER activity. From the perspective of applied research, the as-developed perovskite catalysts are expected to be evaluated for overall water splitting based on practical water electrolyzers. Most of the current research evaluates the overall water splitting performance of an electrocatalyst in a single-chamber electrochemical cell.[9,10] While this practice could allow the assessment of a potential catalyst for water electrolysis, it cannot begin to compare with the conduct involved in real-world water electrolysis. A more realistic configuration for this purpose would be one that is based on the membrane electrode assembly (MEA). Another comment is that practical water splitting operates at a temperature higher than ambient temperature (e.g., around 80 °C) to achieve enhanced kinetics, which in turn places higher requirement on the catalyst stability. A recent report demonstrated that a MEA made of nanosized BSCF perovskite could steadily operate at 50 °C and 200 mA cm^{-2} for 5 h, requiring a voltage much lower than that made of the noble metal IrO_2 catalyst.[6] While this appears promising, there remains much to be done to realize the water electrolysis over perovskite electrocatalysts with improved efficiency and for extended durations.

8.3 References

(1) Zhou, S.; Miao, X.; Zhao, X.; Ma, C.; Qiu, Y.; Hu, Z.; Zhao, J.; Shi, L.; Zeng, J. Engineering electrocatalytic activity in nanosized perovskite cobaltite through surface spin-state transition. *Nat. Commun.* **2016**, *7*, 11510.

(2) Jung, J.-I.; Risch, M.; Park, S.; Kim, M. G.; Nam, G.; Jeong, H.-Y.; Shao-Horn, Y.; Cho, J. Optimizing nanoparticle perovskite for bifunctional oxygen electrocatalysis. *Energy Environ. Sci.* **2016**, *9*, 176–183.

(3) Xu, X.; Pan, Y.; Zhou, W.; Chen, Y.; Zhang, Z.; Shao, Z. Toward enhanced oxygen evolution on perovskite oxides synthesized from different approaches: A case study of $Ba_{0.5}Sr_{0.5}Co_{0.8}Fe_{0.2}O_{3-\delta}$. *Electrochim. Acta* **2016**, *219*, 553–559.

(4) Jung, J.-I.; Jeong, H. Y.; Kim, M. G.; Nam, G.; Park, J.; Cho, J. Fabrication of $Ba_{0.5}Sr_{0.5}Co_{0.8}Fe_{0.2}O_{3-\delta}$ catalysts with enhanced electrochemical performance by removing an inherent heterogeneous surface film layer. *Adv. Mater.* **2015**, *27*, 266–271.

(5) Xu, X.; Wang, W.; Zhou, W.; Shao, Z. Recent advances in novel nanostructuring methods of perovskite electrocatalysts for energy-related applications. *Small Methods* **2018**, *2*, 1800071.

(6) Fabbri, E.; Nachtegaal, M.; Binninger, T.; Cheng, X.; Kim, B.-J.; Durst, J.; Bozza, F.; Graule, T.; Schäublin, R.; Wiles, L. et al. Dynamic surface self-reconstruction is the key of highly active perovskite nano-electrocatalysts for water splitting. *Nat. Mater.* **2017**, *16*, 925–931.

(7) Guan, D.; Ryu, G.; Hu, Z.; Zhou, J.; Dong, C.-L.; Huang, Y.-C.; Zhang, K.; Zhong, Y.; Komarek, A. C.; Zhu, M. et al. Utilizing ion leaching effects for achieving high oxygen-evolving performance on hybrid nanocomposite with self-optimized behaviors. *Nat. Commun.* **2020**, *11*, 3376.

(8) Zhu, Y.; Wang, J.; Chu, H.; Chu, Y.-C.; Chen, H. M. In situ/operando studies for designing next-generation electrocatalysts. *ACS Energy Lett.* **2020**, *5*, 1281–1291.

(9) Oh, N. K.; Kim, C.; Lee, J.; Kwon, O.; Choi, Y.; Jung, G. Y.; Lim, H. Y.; Kwak, S. K.; Kim, G.; Park, H. In-situ local phase-transitioned $MoSe_2$ in $La_{0.5}Sr_{0.5}CoO_{3-\delta}$ heterostructure and stable overall water electrolysis over 1000 hours. *Nat. Commun.* **2019**, *10*, 1723.

(10) Sun, H.; Xu, X.; Chen, G.; Zhou, Y.; Lin, H.-J.; Chen, C.-T.; Ran, R.; Zhou, W.; Shao, Z. Smart control of composition for double perovskite electrocatalysts toward enhanced oxygen evolution reaction. *ChemSusChem* **2019**, *12*, 5111–5116.

Every reasonable effort has been made to acknowledge the owners of copyright material. I would be pleased to hear from any copyright owner who has been omitted or incorrectly acknowledged.

Appendix A From scheelite $BaMoO_4$ to perovskite $BaMoO_3$: Enhanced electrocatalysis toward the hydrogen evolution in alkaline media

Supplementary Information for Chapter 4

A.1 Supplementary figures

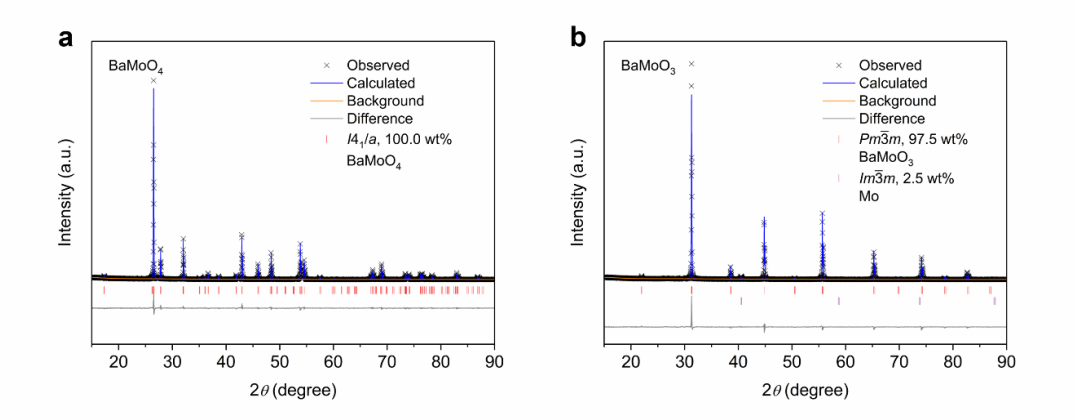

Figure A.1 Rietveld refinement analysis of the XRD patterns of (a) $BaMoO_4$ scheelite and (b) $BaMoO_3$ perovskite.

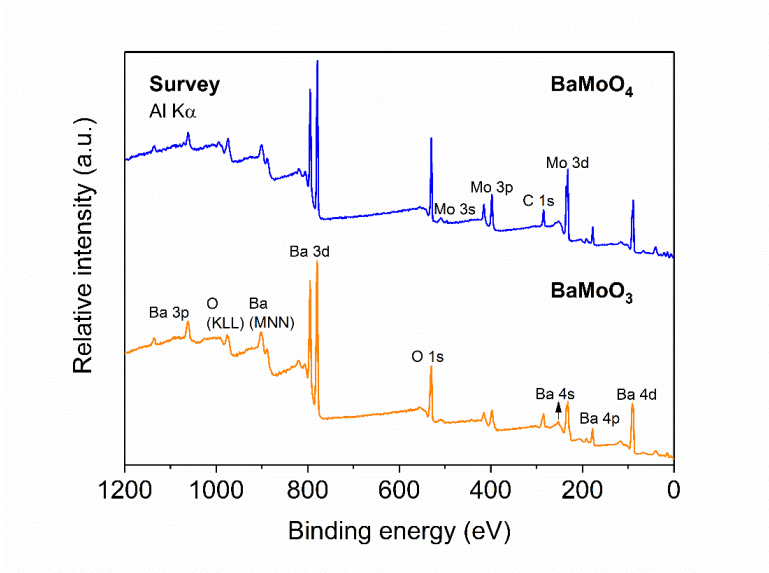

Figure A.2 XPS survey spectra of $BaMoO_4$ scheelite and $BaMoO_3$ perovskite.

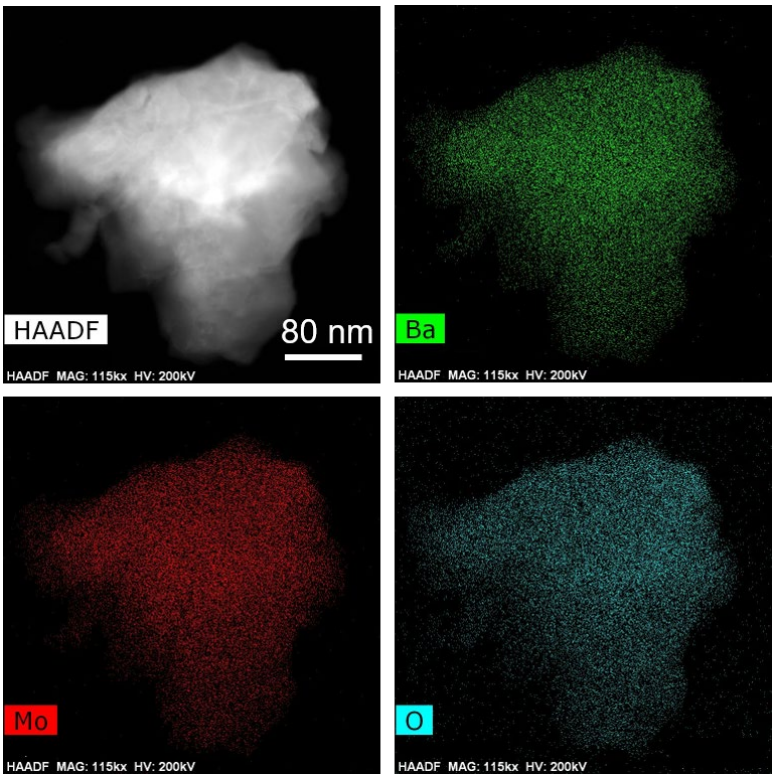

Figure A.3 HAADF-STEM image of $BaMoO_3$ perovskite and the corresponding EDS mapping images of Ba, Mo, and O.

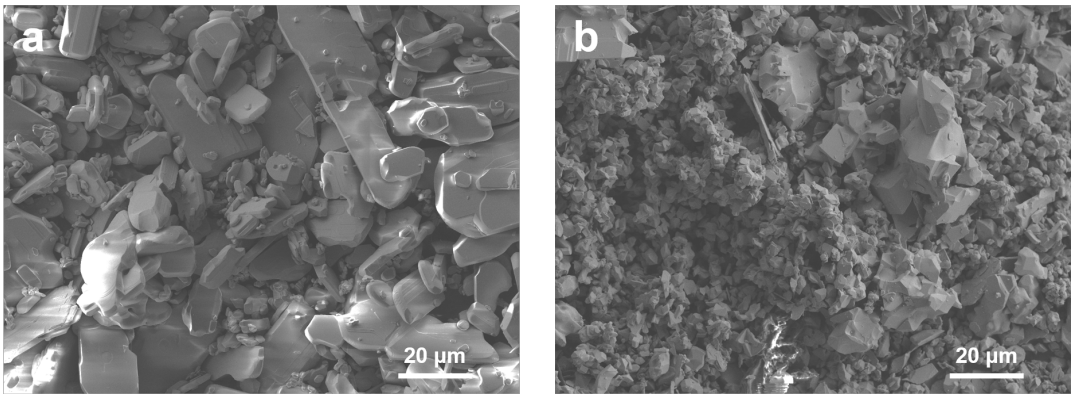

Figure A.4 SEM images of the commercial molybdenum oxides showing their bulk particle size. (a) MoO_3, (b) MoO_2.

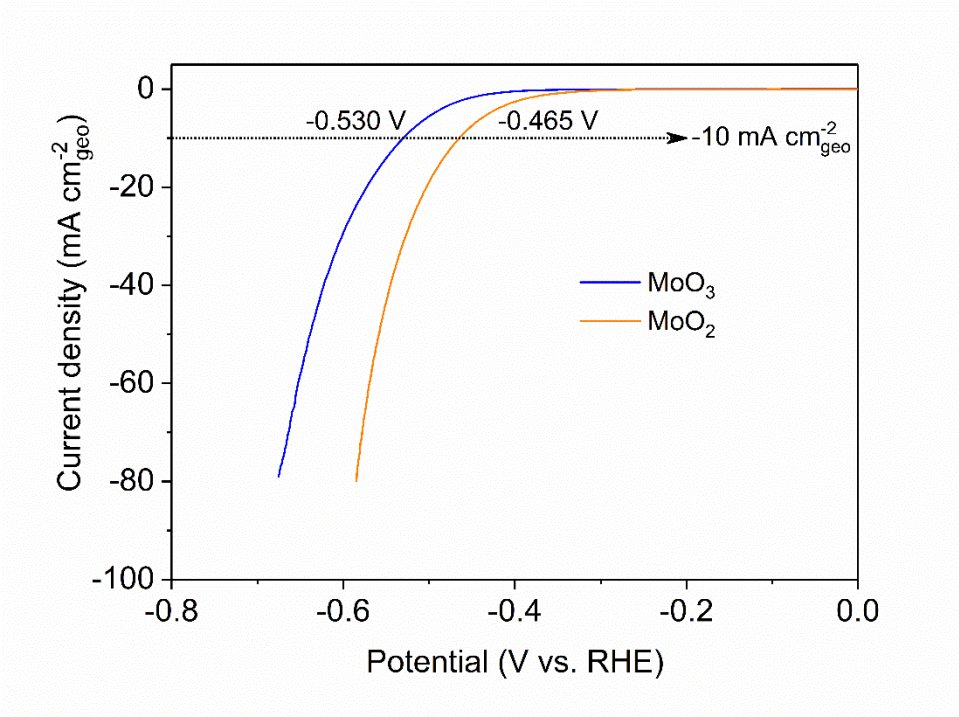

Figure A.5 LSV curves of the commercial molybdenum oxides MoO_3 and MoO_2.

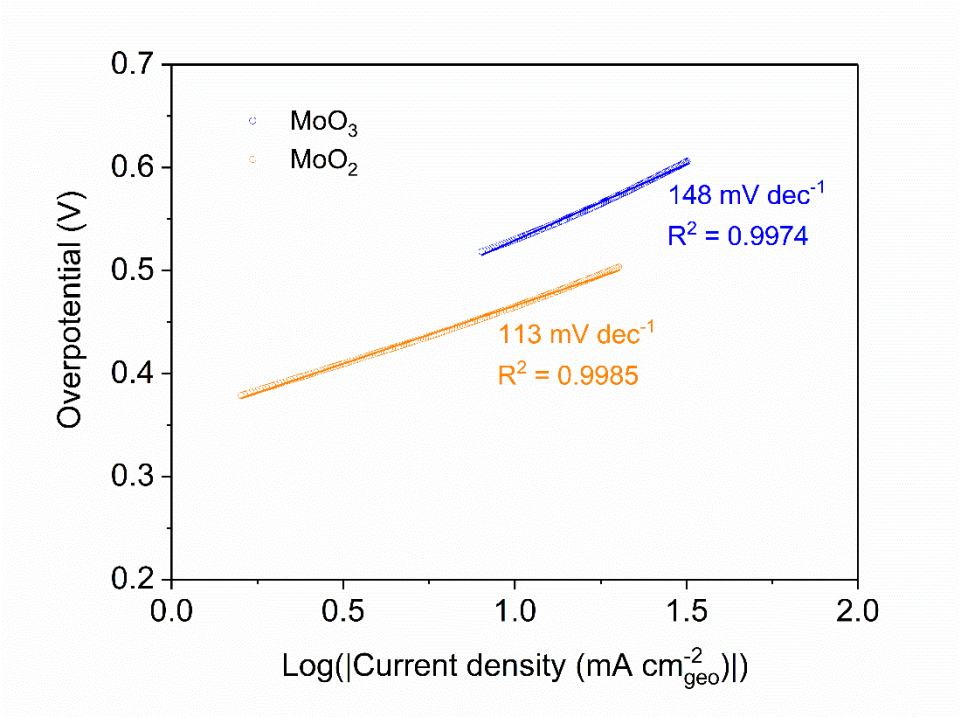

Figure A.6 Tafel plots of the commercial molybdenum oxides MoO_3 and MoO_2.

A.2 Supplementary tables

Table A.1 Rietveld refinement results of the XRD patterns of the as-prepared $BaMoO_4$ scheelite and $BaMoO_3$ perovskite.

Catalyst	Phase composition	Phase structure	Space group	Lattice parameters (Å)	χ^2	R_p (%)	R_{wp} (%)
$BaMoO_4$	$BaMoO_4$ (100.0 wt%)	Tetragonal	$I4_1/a$	a = 5.58234(3) c = 12.8219(1)	2.420	7.99	10.37
$BaMoO_3$	$BaMoO_3$ (97.5 wt%)	Cubic	$Pm\overline{3}m$	a = 4.04103(2)	2.560	8.35	10.59
	Mo (2.5 wt%)	Cubic	$Im\overline{3}m$	a = 3.1468(2)			

Table A.2 A comparison of the HER activity of $BaMoO_4$ scheelite and $BaMoO_3$ perovskite with other bulk-sized, Mo-containing catalysts (e.g., Mo oxide and sulfide) and perovskite catalysts (e.g., Mn-, Fe-, Co-, and Ni-based) tested in 1 M KOH.

Catalyst	Substrate	Loading ($mg_{catalyst}$ cm^{-2})	Catalyst/carbon mass ratio	η_{10}[a] (mV)	Tafel slope (mV dec^{-1})	Ref.
$BaMoO_3$	GCE[b]	0.253	No carbon	336	110	This work
$BaMoO_4$	GCE	0.253	No carbon	561	189	This work
MoO_2	GCE	0.253	No carbon	465	113	This work
MoO_3	GCE	0.253	No carbon	530	148	This work
MoO_2	CPE[c]	N.A.[d]	N.A.	~440	N.A.	[1]
MoO_3	CPE	N.A.	N.A.	~660	N.A.	[1]
MoS_2	GCE	0.159	5:1	349	109	[2]
MoS_2	GCE	2.8	No carbon	~360	153	[3]
MoS_2	GCE	0.204	No carbon	370	124	[4]
$NdBaMn_2O_{5.5+\delta}$	GCE	0.4	1:1	~500	138	[5]
$Nd_{0.5}Ba_{0.5}MnO_{3-\delta}$	GCE	0.4	1:1	~610	132	[5]
$Sr_2Fe_{1.5}Mo_{0.5}O_{6-\delta}$	GCE	0.234	4:1	443	105	[6]
$LaFeO_{3-\delta}$	GCE	0.232	1:1	~480	140	[7]
$LaFe_{0.8}Co_{0.2}O_{3-\delta}$	GCE	0.232	1:1	~400	113	[7]
$SrCoO_{3-\delta}$	CP[e]	1	10:1	447	157	[8]
$SrCo_{0.9}Nb_{0.1}O_{3-\delta}$	CP	1	10:1	427	142	[8]
$SrCo_{0.7}Fe_{0.3}O_{3-\delta}$	GCE	0.362	1:1	378	190	[9]
$Ba_{0.5}Sr_{0.5}Co_{0.8}Fe_{0.2}O_{3-\delta}$	GCE	0.232	1:1	342	75	[10]
$La_{0.5}Sr_{0.5}CoO_{3-\delta}$	GCE	0.385	No carbon	~420	95	[11]
$PrBa_{0.5}Sr_{0.5}Co_2O_{5+\delta}$	GCE	0.226	4:1	393	101	[12]
$Ba_{0.95}Co_{0.4}Fe_{0.4}Zr_{0.1}Y_{0.1}O_{3-\delta}$	GCE	0.255	5:1	360	80	[13]
$La_{0.8}Sr_{0.2}Cr_{0.69}Ni_{0.31}O_{3-\delta}$	GCE	0.401	1:1	447	116	[14]

[a] The overpotential required to reach a current density of 10 mA cm_{geo}^{-2}.

[b] Glassy carbon electrode.

[c] Carbon-paste electrode.

[d] Not available.

[e] Carbon paper.

Table A.3 A comparison of the HER specific activity of $BaMoO_4$ scheelite and $BaMoO_3$ perovskite at select overpotentials.

Catalyst	Specific activity at select overpotentials ($mA\ cm_{oxide}^{-2}$)		
	0.35 V	0.40 V	0.45 V
$BaMoO_4$	0.56	0.80	1.41
$BaMoO_3$	4.52	12.98	37.19

Table A.4 XPS peak fitting results of the O 1s core levels of $BaMoO_4$ scheelite and $BaMoO_3$ perovskite.

Catalyst	Lattice oxygen		Defective oxygen		Chemisorbed oxygen	
	Binding energy (eV)	Concentration (%)	Binding energy (eV)	Concentration (%)	Binding energy (eV)	Concentration (%)
$BaMoO_4$	530.1	79.2	531.1	15.5	532.4	5.3
$BaMoO_3$	530.0	53.3	531.5	27.3	533.0	19.4

A.3 Supplementary references

[1] Vrubel H, Hu X. Molybdenum boride and carbide catalyze hydrogen evolution in both acidic and basic solutions. Angew Chem Int Ed 2012;51(51):12703-6.

[2] Zhu D, Liu J, Zhao Y, Zheng Y, Qiao S-Z. Engineering 2D metal–organic framework/MoS_2 interface for enhanced alkaline hydrogen evolution. Small 2019;15(14):1805511.

[3] Zhang L-F, Ke X, Ou G, Wei H, Wang L-N, Wu H. Defective MoS_2 electrocatalyst for highly efficient hydrogen evolution through a simple ball-milling method. Sci China Mater 2017;60(9):849-56.

[4] Zhao G, Lin Y, Rui K, Zhou Q, Chen Y, Dou SX, et al. Epitaxial growth of $Ni(OH)_2$ nanoclusters on MoS_2 nanosheets for enhanced alkaline hydrogen evolution reaction. Nanoscale 2018;10(40):19074-81.

[5] Wang J, Gao Y, Chen D, Liu J, Zhang Z, Shao Z, et al. Water splitting with an enhanced bifunctional double perovskite. ACS Catal 2018;8(1):364-71.

[6] He B, Tan K, Gong Y, Wang R, Wang H, Zhao L. Coupling amorphous cobalt hydroxide nanoflakes on $Sr_2Fe_{1.5}Mo_{0.5}O_{5+\delta}$ perovskite nanofibers to induce bifunctionality for water splitting. Nanoscale 2020.

[7] Dai J, Zhu Y, Zhong Y, Miao J, Lin B, Zhou W, et al. enabling high and stable electrocatalytic activity of iron-based perovskite oxides for water splitting by combined bulk doping and morphology designing. Adv Mater Interfaces 2019;6(1):1801317.

[8] Islam QA, Majee R, Bhattacharyya S. Bimetallic nanoparticle decorated perovskite oxide for state-of-the-art trifunctional electrocatalysis. J Mater Chem A 2019;7(33):19453-64.

[9] Zhang Z, Chen Y, Dai Z, Tan S, Chen D. Promoting hydrogen-evolution activity and stability of perovskite oxides via effectively lattice doping of molybdenum. Electrochim Acta 2019;312:128-36.

[10] Xu X, Chen Y, Zhou W, Zhu Z, Su C, Liu M, et al. A perovskite electrocatalyst for efficient hydrogen evolution reaction. Adv Mater 2016;28(30):6442-8.

[11] Oh NK, Kim C, Lee J, Kwon O, Choi Y, Jung GY, et al. In-situ local phase-transitioned $MoSe_2$ in $La_{0.5}Sr_{0.5}CoO_{3-\delta}$ heterostructure and stable overall water electrolysis over 1000 hours. Nat Commun 2019;10:1723.

[12] Zhang Z, He B, Chen L, Wang H, Wang R, Zhao L, et al. Boosting overall water splitting via FeOOH nanoflake-decorated $PrBa_{0.5}Sr_{0.5}Co_2O_{5+\delta}$ nanorods. ACS Appl Mater Interfaces 2018;10(44):38032-41.

[13] Li X, He L, Zhong X, Zhang J, Luo S, Yi W, et al. Evaluation of A-site Ba^{2+}-deficient $Ba_{1-x}Co_{0.4}Fe_{0.4}Zr_{0.1}Y_{0.1}O_{3-\delta}$ oxides as electrocatalysts for efficient hydrogen evolution reaction. Scanning. 2018;2018:1341608.

[14] Wang Y, Wang Z, Jin C, Li C, Li X, Li Y, et al. Enhanced overall water electrolysis on a bifunctional perovskite oxide through interfacial engineering. Electrochim Acta 2019;318:120-9.

Appendix B Copyright permissions

JOHN WILEY AND SONS LICENSE
TERMS AND CONDITIONS

Aug 27, 2020

This Agreement between Curtin University -- Xiaomin Xu ("You") and John Wiley and Sons ("John Wiley and Sons") consists of your license details and the terms and conditions provided by John Wiley and Sons and Copyright Clearance Center.

License Number	4896800163590
License date	Aug 26, 2020
Licensed Content Publisher	John Wiley and Sons
Licensed Content Publication	Small Methods
Licensed Content Title	Recent Advances in Novel Nanostructuring Methods of Perovskite Electrocatalysts for Energy-Related Applications
Licensed Content Author	Zongping Shao, Wei Zhou, Wei Wang, et al
Licensed Content Date	May 28, 2018
Licensed Content Volume	2
Licensed Content Issue	7
Licensed Content Pages	35
Type of Use	Dissertation/Thesis
Requestor type	Author of this Wiley article
Format	Print and electronic
Portion	Text extract
Number of Pages	2
Will you be translating?	No
Title	Engineering of Perovskite Oxides for Electrochemical Water Splitting
Institution name	Curtin University
Expected presentation date	Jan 2021
Portions	Text extract from Page 1 and Page 19
Requestor Location	Curtin University Kent Street Bentley Perth, Western Australia 6102 Australia Attn: Curtin University
Publisher Tax ID	EU826007151
Total	**0.00 USD**
Terms and Conditions	

TERMS AND CONDITIONS

This copyrighted material is owned by or exclusively licensed to John Wiley & Sons, Inc. or one of its group companies (each a"Wiley Company") or handled on behalf of a society with which a Wiley Company has exclusive publishing rights in relation to a particular work (collectively "WILEY"). By clicking "accept" in connection with completing this licensing transaction, you agree that the following terms and conditions apply to this transaction (along with the billing and payment terms and conditions established by the Copyright Clearance Center Inc., ("CCC's Billing and Payment terms and conditions"), at the time that you opened your RightsLink account (these are available at any time at http://myaccount.copyright.com).

Terms and Conditions

SPRINGER NATURE LICENSE
TERMS AND CONDITIONS

Aug 27, 2020

This Agreement between Curtin University -- Xiaomin Xu ("You") and Springer Nature ("Springer Nature") consists of your license details and the terms and conditions provided by Springer Nature and Copyright Clearance Center.

License Number	4896990438062
License date	Aug 27, 2020
Licensed Content Publisher	Springer Nature
Licensed Content Publication	Springer eBook
Licensed Content Title	Perovskite Materials in Electrocatalysis
Licensed Content Author	Xiaomin Xu, Yangli Pan, Lei Ge et al
Licensed Content Date	Jan 1, 2020
Type of Use	Thesis/Dissertation
Requestor type	non-commercial (non-profit)
Format	print and electronic
Portion	full article/chapter
Will you be translating?	no
Circulation/distribution	50000 or greater
Author of this Springer Nature content	yes
Title	Engineering of Perovskite Oxides for Electrochemical Water Splitting
Institution name	Curtin University
Expected presentation date	Jan 2021
Requestor Location	Curtin University Kent Street Bentley Perth, Western Australia 6102 Australia Attn: Curtin University
Total	**0.00 USD**

Terms and Conditions

Springer Nature Customer Service Centre GmbH
Terms and Conditions

This agreement sets out the terms and conditions of the licence (the **Licence**) between you and **Springer Nature Customer Service Centre GmbH** (the **Licensor**). By clicking 'accept' and completing the transaction for the material (**Licensed Material**), you also confirm your acceptance of these terms and conditions.

1. Grant of License

1. 1. The Licensor grants you a personal, non-exclusive, non-transferable, world-wide licence to reproduce the Licensed Material for the purpose specified in your order only. Licences are granted for the specific use requested in the order and for no other use, subject to the conditions below.

1. 2. The Licensor warrants that it has, to the best of its knowledge, the rights to license reuse of the Licensed Material. However, you should ensure that the material you are requesting is original to the Licensor and does not carry the copyright of another entity (as credited in the published version).

Appendix C Co-author attribution statement

1. Part of Chapter 1 contains text extracts form the below publication. The co-author attribution statement for this paper is given in the following table.

Publication detail: *Xiaomin Xu, Yangli Pan, Yijun Zhong, Ran Ran, Zongping Shao, Ruddlesden–Popper perovskites in electrocatalysis, Materials Horizons, 2020, 7, 2519–2565.*

Co-author attribution statement:

Co-author	Conception and design	Methodology & data acquisition	Data processing & analysis	Interpretation & discussion	Manuscript writing, revision & finalization	Final approval
Ms. Yangli Pan				×	×	×
	I acknowledge that these represent my contribution to the above result output.				Signed.	[redacted]
Mr. Yijun Zhong				×	×	×
	I acknowledge that these represent my contribution to the above result output.				Signed.	[redacted]
Dr. Ran Ran				×	×	×
	I acknowledge that these represent my contribution to the above result output.				Signed.	[redacted]
Dr. Zongping Shao	×			×	×	×
	I acknowledge that these represent my contribution to the above result output.				Signed.	[redacted]

2. Part of Chapter 1 contains text extracts form the below publication. The co-author attribution statement for this paper is given in the following table.

Publication detail: *Xiaomin Xu, Wei Wang, Wei Zhou, Zongping Shao, Recent advances in novel nanostructuring methods of perovskite electrocatalysts for energy-related applications, Small Methods, 2018, 2, 1800071.*

Co-author attribution statement:

Co-author	Conception and design	Methodology & data acquisition	Data processing & analysis	Interpretation & discussion	Manuscript writing, revision & finalization	Final approval
Dr. Wei Wang				×	×	×
	I acknowledge that these represent my contribution to the above result output.				Signed.	[redacted]
Dr. Wei Zhou				×	×	×
	I acknowledge that these represent my contribution to the above result output.				Signed.	[redacted]
Dr. Zongping Shao	×			×	×	×
	I acknowledge that these represent my contribution to the above result output.				Signed.	[redacted]

3. Chapter 2 is reprinted (adapted) form the below publication. The co-author attribution statement for this work is given in the following table.

Publication detail: *Xiaomin Xu, Yangli Pan, Lei Ge, Zongping Shao, (2020) Perovskite Materials in Electrocatalysis. In: Arul N., Nithya V. (eds) Revolution of Perovskite. Materials Horizons: From Nature to Nanomaterials. Springer, Singapore. DOI: 10.1007/978-981-15-1267-4_8.*

Co-author attribution statement:

Co-author	Conception and design	Methodology & data acquisition	Data processing & analysis	Interpretation & discussion	Manuscript writing, revision & finalization	Final approval
Ms. Yangli Pan				×	×	×
	I acknowledge that these represent my contribution to the above result output.				Signed.	[redacted]
Dr. Lei Ge				×	×	×
	I acknowledge that these represent my contribution to the above result output.				Signed.	[redacted]
Dr. Zongping Shao	×			×	×	×
	I acknowledge that these represent my contribution to the above result output.				Signed:	[redacted]

4. Part of Chapter 3 and the whole of Chapter 4 are reprinted (adapted) from the below publication. The co-author attribution statement for this paper is given in the following table.

Publication detail: *Xiaomin Xu, Yangli Pan, Yijun Zhong, Lei Ge, San Ping Jiang, Zongping Shao, From scheelite $BaMoO_4$ to perovskite $BaMoO_3$: Enhanced electrocatalysis toward the hydrogen evolution in alkaline media, Composites Part B: Engineering, 2020, 198, 108214.*

Co-author attribution statement:

Co-author	Conception and design	Methodology & data acquisition	Data processing & analysis	Interpretation & discussion	Manuscript writing, revision & finalization	Final approval
Ms. Yangli Pan			×	×		×
	I acknowledge that these represent my contribution to the above result output.				Signed.	[redacted]
Mr. Yijun Zhong			×	×		×
	I acknowledge that these represent my contribution to the above result output.				Signed.	[redacted]
Dr. Lei Ge				×	×	×
	I acknowledge that these represent my contribution to the above result output.				Signed.	[redacted]
Dr. San Ping Jiang				×	×	×
	I acknowledge that these represent my contribution to the above result output.				Signed.	[redacted]
Dr. Zongping Shao	×			×	×	×
	I acknowledge that these represent my contribution to the above result output.				Signed.	[redacted]